Università degli Studi di Padova

Dipartimento di Ingegneria Civile, Edile ed Ambientale

Department Of Civil, Environmental and Architectural Engineering

---

Corso di dottorato in Scienze dell'Ingegneria Civile e Ambientale

XXXII ciclo

Titolo Tesi

MODELLING THE PLANO-ALTIMETRIC EQUILIBRIUM OF A TIDAL CHANNEL

Tesi redatta con il contributo finanziario del Dipartimento ICEA e dell'Ateneo di Università degli studi di Padova

Supervisore:
Ch.mo Prof. Stefano Lanzoni
Co-Supervisore:
Prof. Andrea D'Alpaos

Coordinatore:
Ch.mo Prof. Marco Marani

Revisori esterni:
Prof.ssa Nicoletta Tambroni
Prof. Luca Solari

Dottorando:
Alessandro Sgarabotto

Anno accademico 2018-2019

There are few things more liberating in this life than having your worst fear realized. Disappointment will come. The beauty is that through disappointment you can gain clarity, and with clarity comes conviction and true originality.

Conan O'Brien

Abstract

Tidal channels are ubiquitous features of the tidal landscape which play a critical role in the morphodynamic evolution of these landscapes. In addition, tidal channels represent a substantial ecological and economic value, being however vulnerable to climate changes and increasing anthropogenic pressures. Improving current knowledge on tidal channel form and function is therefore key step to model and predict the evolution of tidal systems.

A number of studies have analyzed the evolution and equilibrium configuration of tidal channels, focusing on the equilibrium profile of the channel bed for a given channel-width distribution as well as on channel equilibrium cross-sectional shape. However, the role that vegetation growth on the marsh platform plays on the equilibrium morphology of salt-marsh channels has received less attention. Here we developed a model which analyzes the equilibrium configuration of a channel and the adjacent salt-marsh platform and provides a useful tool for quantitative analyses of long-term eco-morphodynamic studies in tidal landscapes. The open channel flow is studied by a 1D hydrodynamic model developed to describe the flow field within the channel and, if present, on the lateral shoals. The 1D hydrodynamics was "validated" considering some test cases comparing the results obtained with a full-fledged 2D model as a reference.

The tidal channel evolution can be sought using three different setups which single out landforming effects: purely erosional model, in which the erosion is the only effect shaping the channel; depositional model, in which erosion, sea level rise and settling deposition scour and promote the vertical accretion of the basin; depositional model with vegetation, in which vegetation effects are included in the previous setup.

Model results reproduce several observed channel characteristics which are deemed to be relevant from a geomorphological point of view. Model results also show that vegetation encroachment on the marsh surface produces two competing effects. Enhanced marsh accretion associated with the increased particle trapping and with the organic production by halophytic plants, increases marsh elevation in the tidal frame, thus reducing

the landscape forming tidal prism and the channel cross-sectional area. However, the increased flow resistance on the canopy promotes flow concentration within the channel, leading to more incised cross sections characterized by smaller width-to-depth ratios. Our simulations indicate that the second process is more important in marshes which are lower in the tidal frame, whereas the first process is more important in marshes higher in the tidal frame when most of the tidal fluxes are already confined within the channel.

Sommario

I canali a marea innervano gli ambienti a marea costituendo dei percorsi preferenziali per il trasporto di acqua, sedimenti e nutrimenti. Inoltre, i canali a marea rappresentano un sostanziale valore ecologico ed economico, essendo tuttavia vulnerabili ai cambiamenti climatici e alle crescenti pressioni antropiche. La comprensione dei meccanismi che regolano la forma ed il funzionamento dei canali a marea è cruciale per migliorare la previsione delle tendenze evolutive degli ambienti a marea.

Numerosi studi hanno analizzato l'evoluzione e la configurazione dell'equilibrio dei canali di marea, concentrandosi sul profilo di equilibrio del letto di canale per una data distribuzione della larghezza del canale e sulla forma della sezione trasversale di equilibrio del canale. Tuttavia, il ruolo che la crescita della vegetazione sulla piattaforma di barena svolge sulla morfologia di equilibrio dei canali a marea ha ricevuto meno attenzione. In questa tesi è stato sviluppato un modello che analizza la configurazione di equilibrio di un canale e l'adiacente barena e fornisce uno strumento utile per analisi quantitative di tipo eco-morfodinamico a lungo termine in ambienti a marea. L'idrodinamica è studiata attraverso un modello idrodinamico 1D sviluppato per descrivere il campo di moto all'interno di un canale e, dove presenti, sui bassofondali laterali. L'idrodinamica 1D è stata validata considerando alcuni casi test e confrontando i risultati ottenuti con un modello 2D scelto come riferimento. L'evoluzione del canale a marea può essere analizzata utilizzando tre diverse impostazioni che consentono di considerare separatamente o congiuntamente gli effetti responsabili della formazione del canale: modello puramente erosivo, l'erosione è l'unico effetto che modella il canale; modello deposizionale, in cui gli effetti considerati sono erosione, innalzamento del livello del mare e deposito per sedimentazione; modello con vegetazione, in cui si aggiungono alla precedente configurazione gli effetti di vegetazione.

I risultati del modello riproducono diverse caratteristiche osservate del canale ritenute rilevanti dal punto di vista geomorfologico. I risultati del modello mostrano anche che la presenza della vegetazione sulla

superficie di barena produce due effetti contrastanti. La crescita della vegetazione associata ad un incremento dell'effetto di intrappolamento di particelle di sedimento e della produzione organica da parte di piante alofite, aumenta la quota della superficie di barena rispetto all'escursione di marea, riducendo così il prisma di marea e l'area della sezione trasversale del canale. Tuttavia, la maggiore resistenza al flusso sulle piattaforme laterali promuove la concentrazione del flusso all'interno del canale, portando a sezioni trasversali più incise caratterizzate da rapporti larghezza-profondità più piccoli. Le nostre simulazioni indicano che il secondo processo è più importante sulle superfici di barena a quote più basse rispetto all'escursione di marea, mentre il primo processo è più importante sulle superfici di barena a quote più alte rispetto all'escursione di marea quando la maggior parte dei flussi di marea sono già confinati all'interno del canale.

Ringraziamenti

Giunge al termine un'avventura incredibile e difficile, più di quanto mi sarei mai immaginato. Vorrei ringraziare il prof. Stefano Lanzoni per avermi incoraggiato e aiutato nello sviluppo di un modello matematico la cui formulazione è sempre stata una dura lotta. Ringrazio il prof. Andrea D'Alpaos per avermi supportato, motivato e aiutato sempre, specialmente quando nulla sembrava funzionare. Desidero ringraziare anche il prof. Luca Carniello per la gentilezza, la disponibilità e la professionalità dimostrata nello sciogliere i dubbi riguardanti alcuni problemi incontrati nel percorso di dottorato. Devo poi ringraziare i compagni di viaggio di questo dottorato per aver addolcito e rallegrato le giornate, dentro e fuori il dipartimento, con inestimabili momenti di leggerezza, in ordine sparso: Mattia, Sergio, Marta, Luigi, Giulia, Mara, Tommaso, Arianna, Giovanni, Nico e nell'ultimo periodo Davide, Nicola, Leonardo e Luigi B. .

Dedico un ringraziamento speciale a Dino, Valeria e Camilla. Il loro costante aiuto è stato essenziale per portare a termine questo percorso.

Padova, 30/11/2019

Alessandro

Contents

1 Introduction **1**

1.1 Who cares? . . . 1
1.2 Objectives . . . 3
1.3 Background . . . 3
1.4 Overview . . . 10

2 Hydrodynamics **11**

2.1 One-dimensional shallow water equations . . . 11
2.2 3D domain schematization . . . 21
2.3 Wetting and drying processes . . . 22
2.3.1 Local estimation of energy losses . . . 25
2.3.2 Phase-averaged Coriolis factors . . . 28
2.3.3 Phase-averaged one dimensional equations . . . 28
2.3.4 The numerical scheme of 1D shallow water equations . . . 29
2.3.5 Modeling flow transitions . . . 33
2.3.6 Double-sweep method . . . 37
2.4 Results . . . 41
2.5 Concluding remarks . . . 55

3 Morphodynamics **57**

3.1 Modeling suspended sediment transport . . . 57
3.2 Results . . . 64
3.2.1 Morphodynamic equilibrium considerations . . . 64
3.3 Concluding remarks . . . 67

4 The plano-altimetric equilibrium configuration **69**

4.1 Stable cross sections . . . 70
4.2 The shear stress distribution across the channel section . . . 72
4.2.1 The turbulence model . . . 74

4.2.2 Vegetation effects on velocity and shear stress distribution . . 76
4.3 Numerical approach 78
4.3.1 The computational domain 78
4.3.2 The Exner equation finite difference scheme 80
4.3.3 The shear-stress distribution finite difference scheme 84
4.3.4 Cross-sectional geometry issues 86
4.3.5 Numerical code flowchart 87
4.4 Model sensitivity to the acceleration of the morphological factor . . 88
4.5 Model validation 90
4.5.1 General features of the morphodynamic evolution 91
4.5.2 Sensitivity analysis 92
4.6 Concluding remarks 96

5 Results **101**
5.1 Purely erosive effects on initial conditions 101
5.2 Depositional model 104
5.2.1 Sediment settling and sea level rise 104
5.2.2 Effects of SSC and SLR variations 106
5.3 Vegetation effects 108
5.3.1 Comparison with the test case $I2$. 109
5.3.2 SSC and SLR variations 111
5.4 Overall comparison of the results 112
5.5 Endangering the survival of the tidal landscapes 116
5.6 Concluding remarks 118

6 Conclusions **121**
Appendix 123

A 1D model validation: additional results **125**

B Shear stress distribution equation derivation **133**

Bibliography **137**

List of Figures

1.1 Eco-morphodynamic approach (**Image from** Coco et al. [2013]). . . 2
1.2 Triangular diagram for coastal systems evolution (adapted from Dalrymple et al. [1992]). 2
1.3 Tidal networks across the world. On panel a) the tidal channels at Cook Inlet in Alaska (US, Photo by Ingo Arndt); on panel b) tidal channel of Guadalquivir at Isla Minima in Seville (ES, Photo by Hector Garrido); on panel c) the tidal channel dissecting San Felice salt marsh in the north-eastern portion of the Venice Lagoon (IT). . 5
1.4 Tidal-network classification [Hughes, 2012]. 5
1.5 The Jarrett-O'Brien-Marchi law [D'Alpaos et al., 2009a]. 7
1.6 Channel morphology within salt marsh and tidal flats [Marani et al., 2002], where $\mathcal{B}$ is the channel width and D its depth. 7

2.1 The control volume for deriving the 1D shallow water equations, coinciding with a channel reach of length dx (Adapted from Cunge et al. [1980]). a) Lateral view; b) Top view; c) Cross-sectional view of the control volume. 15
2.2 Tidal channel geometry 17
2.3 Channel from the mouth (a) to the head (d). Jiangsu Province (China). 19
2.4 a) Compact cross section of an intertidal transect; b) compound cross section cross sections. 20
2.5 Sketch of the criterion adopted to distinguish channeled and unchanneled regions. 22
2.6 Wetting and drying approach applied to compact and compound cross sections. 29
2.7 Four point box scheme 30
2.8 The LPI Filter [Fread et al., 1996]. 34
2.9 A bathymetry with an abrupt change in the cross section. 35

2.10 Abrupt change of width. 36
2.11 Different iterative procedure depending on the choice of first cross section. 39
2.12 Different iterative procedure depending on the choice of first cross section. 41
2.13 Water level oscillations on a linearly sloping beach with or without intermediate irregularities, as suggested by Balzano [1998]. Left panels: ebb phase; right panels: flood phase. Input data are: $\Delta x = 1200$ m, Δt=600 s, k_s=50 $m^{1/3}s^{-1}$, $a_0 = 2.0$ m, $T = 43\,200$ s. The roughness parameter e_s in equations (2.43), (2.44) has been set to 0.3 m. Thin lines denote water levels at every time step; thick lines correspond to water level plotted every 5 time steps (i.e., 50 min). 43
2.14 Outflow from a 1D basin with reservoir by sinusoidal depletion (reference case suggested in Balzano [1998]) for different e_s values from left to right 0.003, 0.3, 0.6, 2.0 m. These are the run input data: $\Delta x = 1200$ m, Δt=600 s, k_s=50 $m^{1/3}s^{-1}$, $a_0 = 2.0$ m, $T_{run} = 100$ h. 44
2.15 The three bathymetries used to test the present 1D model: a) channel with compact cross sections; b) channel with compound cross sections; c) channel with both compact and compound cross sections. 46
2.16 Water level oscillations computed for bathymetry 1 ($z_{tf} = 0.0$ m). a) landward section; b) halfway cross section; c) seaward section. The water levels are tracked on the channel axis (black), on the tidal flat edge (red) and on the lateral boundary of the tidal domain (green). . 47
2.17 Temporal distribution of the cross-sectional discharge Q computed for bathymetry 1 ($z_{tf} = 0.0$ m). a) landward section; b) halfway cross section; c) seaward section. 47
2.18 The cross sectional discharge Q is plotted as a function of the water stage h for bathymetry 1 ($z_{tf} = 0.0$ m) a) landward section; b) halfway cross section; c) seaward section. 48
2.19 a) Maximum shear stress τ_{max} and b) velocity U_{max} computed during a tidal cycle along the longitudinal axis fo the tidal basin with bathymetry 1 ($z_{tf} = 0.0$ m). 48
2.20 Behavior of the 1D model energy slope S_f along the channel in the bathymetry 1 a) in ebb and b) in flood phase. 49
2.21 Water level oscillations computed for bathymetry 2 ($z_{tf} = 0.0$ m). a) landward section; b) halfway cross section; c) seaward section. The water levels are tracked on the channel axis (black), on the tidal flat edge (red) and on the lateral boundary of the tidal domain (green). . 50

2.22 Temporal distribution of the cross-sectional discharge Q computed for bathymetry 2 (z_{tf} = 0.0 m). a) landward section; b) halfway cross section; c) seaward section. 50
2.23 The cross sectional discharge Q is plotted as a function of the water stage h for bathymetry 2 (z_{tf} = 0.0 m) a) landward section; b) halfway cross section; c) seaward section. 51
2.24 a) Maximum shear stress τ_{max} and b) velocity U_{max} computed during a tidal cycle along the longitudinal axis for the tidal basin with bathymetry 2 (z_{tf} = 0.0 m). 51
2.25 Behavior of the 1D model energy slope S_f along the channel in the bathymetry 2 a) in ebb and b) in flood phase. 52
2.26 Water level oscillations computed for bathymetry 3 (z_{tf} = 0.0 m). a) landward section; b) halfway cross section; c) seaward section. The water levels are tracked on the channel axis (black), on the tidal flat edge (red) and on the lateral boundary of the tidal domain (green). . 53
2.27 Temporal distribution of the cross-sectional discharge Q computed for bathymetry 3 (z_{tf} = 0.0 m). a) landward section; b) halfway cross section; c) seaward section. 53
2.28 The cross sectional discharge Q is plotted as a function of the water stage h for bathymetry 3 (z_{tf} = 0.0 m) a) landward section; b) halfway cross section; c) seaward section. 54
2.29 a) Maximum shear stress τ_{max} and b) velocity U_{max} computed during a tidal cycle along the longitudinal axis for the tidal basin with bathymetry 3 (z_{tf} = 0.0 m). 54
2.30 Behavior of the 1D model energy slope S_f along the channel in the bathymetry 3 a) in ebb and b) in flood phase. 55

3.1 Sketch of the sediment fluxes in the main channel and on its lateral shoals (adapted from Di Silvio [1978a]). 59
3.2 The sediment fluxes considered in the morphodynamic model, with $C_0(\boldsymbol{x}, t) = const.$ the concentration of the externally imposed input of sediment. 60
3.3 Erosion rate curves as a function of the bed shear stress. Original formulation based on a well defined threshold for incipient erosion (continuous line) and gradual transition from an immobile bed to an eroding bed as proposed by Carniello et al. [2012]. 61
3.4 Deposition rate curve as a function of the bed shear stress. 62
3.5 Plant biomass curve as a function of the bed elevation z_b 63

3.6 Possible combinations of erosion/deposition thresholds. a) The critical bed shear stress for deposition is higher than critical bed shear stress for erosion. An intermediate interval of shear stresses then exists, such that the bed does not experience erosion nor deposition. b) The critical bed shear stress for deposition is higher than that for erosion. An intermediate interval of shear stresses then exists, such that both processes can occur at the same time. 66

4.1 Network of isovels and their orthogonal rays (Adapted from [Leighly, 1932]). 71

4.2 Sketch of a typical cross-section of the tidal basin, formed by a main channel flanked by intertidal areas, and notations. 73

4.3 Dispersive and energy slope contributions to the cross sectional distribution of bed shear stresses as they peak during a tidal cycle. . . 76

4.4 Overall framework for computing the cross-sectional distribution of bed shear stresses in the main channel and in the presence of intertidal platforms encroached by saltmarsh vegetation. Here, S is the energy slope, dn is the elementary wetted perimeter delimited by two normals to the sediment bed, d$\mathcal{A}$ is the infinitesimal area between the two normals, $\mathcal{K}$ is the factor that drives the momentum exchange between the normals. 78

4.5 Sketch of the computational domain. 79

4.6 The q_b finite difference issue. 81

4.7 Discretization stencil. L:left; R:right. 84

4.8 Examples of interceptions between normal rays (blue lines) and approximations used (red lines) to manage these situations. 87

4.9 Code flowchart. 89

4.10 Effects on the equilibrium channel configuration of different values of the morphological factor f_{MOR}. a) Temporal evolution of the channel axis elevation at the seaward cross-section; b) Equilibrium elevation of the seaward channel axis for different f_{MOR} values. 90

4.11 Evolution of a 2000 m long and 200 m wide tidal basin computed for purely erosional conditions. The reference case depicted here corresponds to a sinusoidal tidal forcing of amplitude 0.5 m; the initial elevation of the tidal flats flanking the main channel is -0.5 m a.m.s.l. 92

4.12 a) Longitudinal profiles obtained at different times with the purely erosional model. b) Temporal evolution of channel axis elevation and tidal flat elevation computed at the seaward boundary. Reference case as explained in the caption of Figure 4.11. 93
4.13 Width and bed profiles obtained using a purely erosional model. The red line denotes the reference test (see test I3 in Table 4.2). The ranges of the investigated paramenters are those reported in Table 4.2. 97
4.14 a) The cross-sectional area, A, is plotted versus the tidal prism, P, emphasizing the compliance with the O'Brien-Jarret-Marchi law; b) the mean flow depth, D, of the main channel cross section is plotted versus the corresponding width, B; c) the main channel width-to-depth, β, is plotted versus the main channel width, B relation. . . . 98
4.15 Comparison between the present computations, LD15's model and the field data measured in the Venice lagoon [Marani et al., 2002]. Red circles represent the present model results considering purely erosional effects (bottom panel). Black circles represent LD15's model results considering purely erosional effects (top panel). Field cross sectional data in Marani et al. [2002] are represented as crosses, if referred to channels dissecting salt marshes, as pluses, if referred to channels dissecting tidal flats. 99

5.1 Examples of initial cross-sectional shapes used to trigger the formation of a main channel within a rectangular tidal basin. a) Cosine function; b) Gaussian function; c) *Witch of Agnesi*. 102
5.2 Longitudinal distribution of a,c,e) main channel with; b,d,f) channel depth at the axis. Initial channel incision prescribed through: a,b) cosine function; c,d) gaussian function; e,f) width of Agnesi. All simulations have been carried out with the purely erosional model. Parameters are those of the Test Case $I3$ in Table 4.2. 103
5.3 a) The cross-sectional area, A, is plotted versus the tidal prism, P; b) the mean flow depth, D, of the main channel cross section is plotted versus the corresponding width, B; c) the main channel width-to-depth, β, is plotted versus the main channel width, B relation. Simulation conditions are the same of Figure 5.2. 104
5.4 Three-dimensional view of the morphodynamic evolution of a rectangular tidal domain computed with the depositional model. Relevant parameters are those corresponding to the Test Case $I2$ of Table 4.2 and to Table 4.1. In addition, SLR =3.5 mm/yrs, SSC =7.5 mg/l). 105

5.5 a) Longitudinal bed profiles at different stages of the tidal basin evolution; b) temporal trajectories of the elevations of two points located at the seaward boundary on the channel bed (red line) and the adjacent tidal flat (green line). The simulation is that referred to in Figure 5.4. 106

5.6 Longitudinal distributions of main channel width and bed profiles computed using depositional model for different values of the SLR. (a) $SLR = 2.5$ mm/yrs; (b) $SLR = 3.5$ mm/yrs; (c) $SLR = 4.5$ mm/yrs. 107

5.7 a) The cross-sectional area, A, is plotted versus the tidal prism, P; b) the mean flow depth, D, of the main channel cross section is plotted versus the corresponding width, B; c) the main channel width-to-depth, β, is plotted versus the main channel width, B relation. Simulation conditions are the same of Figure 5.6. 108

5.8 Three-dimensional view of the morphodynamic evolution of a rectangular tidal domain computed with the depositional model and allowing the growth of vegetation. Relevant parameters are those corresponding to the Test Case $I3$ of Table 4.2. In addition, SLR =3.5 mm/yrs, SSC =7.5 mg/l). 110

5.9 a) Longitudinal bed profiles at different stages of the tidal basin evolution; b) temporal trajectories of the elevations of two points located at the seaward boundary on the channel bed (red line) and the adjacent tidal flat (green line). The simulation is that referred to in Figure 5.8. 110

5.10 Longitudinal channel width and bed profiles obtained adding vegetation growth to the depositional model. (a) SLR=2.5 mm/yrs; (b) SLR=3.5 mm/yrs; (c) SLR=4.5 mm/yrs. 111

5.11 a) The cross-sectional area, A, is plotted versus the tidal prism, P; b) the mean flow depth, D, of the main channel cross section is plotted versus the corresponding width, B; c) the main channel width-to-depth, β, is plotted versus the main channel width, B. Simulation conditions are the same of Figure 5.10. 112

5.12 Longitudinal channel width and bed profile computed with reference to the erosional (black line), depositional (red line) and vegetated (blue line) scenarios, for different values of suspended sediment availability: (a) SSC=5.0 mg/l; (b) SSC=7.5 mg/l; (c) SSC=10.0 mg/l. . 114

5.13 The relations $A-P$, $D-B$ and $\beta-B$ are plotted for the equilibrium channel bed topographies computed with reference to the erosional (black line), depositional (red line) and vegetated (blue line) scenarios, for different values of suspended sediment availability: (a) SSC=5.0 mg/l; (b) SSC=7.5 mg/l; (c) SSC=10.0 mg/l. 115

5.14 Comparison between the present computations and the field data measured in the Venice lagoon [Marani et al., 2002]. Black circles represent the results obtained considering the purely erosional setup, red circles represent the results obtained considering the depositional setup (SSC+SLR), blue circles represent the results obtained considering the vegetated setup (SSC+SLR+vegetation). Field cross sectional data in Marani et al. [2002] are represented as crosses, if referred to channel dissecting salt marshes, as pluses, if referred to channel dissecting tidal flats. 116

5.15 Seaward cross section evolution under a sudden change in SSC after 300 yrs: (a) SSC=22.5 mg/l; (b) SSC=22.5 mg/l; (c) SSC=2.5 mg/l; (d) SSC=2.5 mg/l. 117

5.16 Seaward cross section evolution under a sudden change in RSLR. (a) RSLR=10.5 mm/yrs; (b) RSLR=10.5 mm/yrs; (c) RSLR=1.2 mm/yrs; (d) SSC=1.2 mg/l. 118

A.1 The three bathymetries tested: in the panel A prismatic channel with compact cross sections, in the pannel B non-prismatic channel with compound cross sections and in the pannel C a non-prismatic channel with both compact and compound cross sections. 125

A.2 Water level oscillations computed for bathymetry 1 ($z_{tf} = -0.45$ m). a) landward section; b) halfway cross section; c) seaward section. The water levels are tracked on the channel axis (black), on the tidal flat edge (red) and on the lateral boundary of the tidal domain (green). . 126

A.3 Temporal distribution of the cross-sectional discharge Q computed for bathymetry 1 ($z_{tf} = -0.45$ m). a) landward section; b) halfway cross section; c) seaward section. 126

A.4 The cross sectional discharge Q is plotted as a function of the water stage h for bathymetry 1 ($z_{tf} = -0.45$ m) a) landward section; b) halfway cross section; c) seaward section. 127

A.5 a) Maximum shear stress τ_{max} and b) velocity U_{max} computed during a tidal cycle along the longitudinal axis fo the tidal basin with bathymetry 1 ($z_{tf} = -0.45$ m). 127

A.6 Water level oscillations computed for bathymetry 2 ($z_{tf} = -0.45$ m). a) landward section; b) halfway cross section; c) seaward section. The water levels are tracked on the channel axis (black), on the tidal flat edge (red) and on the lateral boundary of the tidal domain (green). . 128
A.7 Temporal distribution of the cross-sectional discharge Q computed for bathymetry 2 ($z_{tf} = -0.45$ m). a) landward section; b) halfway cross section; c) seaward section. 128
A.8 The cross sectional discharge Q is plotted as a function of the water stage h for bathymetry 2 ($z_{tf} = -0.45$ m) a) landward section; b) halfway cross section; c) seaward section. 129
A.9 a) Maximum shear stress τ_{max} and b) velocity U_{max} computed during a tidal cycle along the longitudinal axis fo the tidal basin with bathymetry 2 ($z_{tf} = -0.45$ m). 129
A.10 Water level oscillations computed for bathymetry 3 ($z_{tf} = -0.45$ m). a) landward section; b) halfway cross section; c) seaward section. The water levels are tracked on the channel axis (black), on the tidal flat edge (red) and on the lateral boundary of the tidal domain (green). . 130
A.11 Temporal distribution of the cross-sectional discharge Q computed for bathymetry 2 ($z_{tf} = -0.45$ m). a) landward section; b) halfway cross section; c) seaward section. 130
A.12 The cross sectional discharge Q is plotted as a function of the water stage h for bathymetry 3 ($z_{tf} = -0.45$ m) a) landward section; b) halfway cross section; c) seaward section. 131
A.13 a) Maximum shear stress τ_{max} and b) velocity U_{max} computed during a tidal cycle along the longitudinal axis fo the tidal basin with bathymetry 3 ($z_{tf} = -0.45$ m). 131

List of Tables

2.1 Compact and compound cross section coefficients. 29

4.1 Parameters adopted in the runs carried out for validating the model: ρ_s sediment density; w_s settling velocity; D_{50} mean sediment grain size; τ_{cd} critical threshold for deposition; τ_{ce} critical threshold for erosion; $\mathcal{E}_0$ empirically-based erosion rate due to sediment features. . 91

4.2 Runs used to validate the purely erosional model, as described in Lanzoni and D'Alpaos [2015]. 94

5.1 Parameters adopted to model biomass production by vegetation: z_{max} maximum stem height within the vegetation pattern; z_{min} minimum stem height within the vegetation pattern; b_{max} max biomass value; Q_{b0} max organic production rate; c_{D0} drag coefficient without vegetation; α_{c_D} fitting parameter linking drag coefficient to biomass; U_0 is a characteristic velocity value of the flow trough vegetation. 109

Chapter 1

Introduction

1.1 Who cares?

People like living on the coast. The coastline provides resources for economy and leisure activities attracting people and improving their health [Bowen et al., 2006]. Consequently, the coastline has become densely populated having 15 of 20 megacities (population $>$ 10 millions) sited on the coast [Luijendijk et al., 2018]. However, there are some issues. Set at the boundary between land and sea, the coastline is subjected to natural forcings, such as rivers, winds, tides, and anthropogenic pressure making it a highly dynamic system (Coco et al. [2013], Figure 1.1). The mutual relations only between these agents drive the evolution of such systems starting from their geomorphology, sediment sources and climatic conditions. The feedback loops that can be positive, if promoting a change in state, or negative, if self-regulating, lead coastal systems to different outcomes (Figure 1.2). The physical processes occurring in the system and mediated by the presence of vegetation may offset each other leading the system to an ephemeral equilibrium state before the evolution starts again as the system becomes off balance [D'Alpaos et al., 2016; Zhou et al., 2017].

Since many people live along the coasts and many economical activities take place there, coastal landscapes and their fate are hot topics. In this regard the effects of climate change has increased the variability of forcings acting on the environment. According to the most recent data and global projections from the IPCC [Church et al., 2013], in 2100 for the best case scenario the global mean sea level (GMSL) is likely [1] to range between $0.3 - 0.6$ m, whereas in the worst case scenario these estimates rise up to $0.5 - 1.0$ m. Hence, large areas along the coast

[1] Likely refers to a likelihood of outcome of 66-100 % [Church et al., 2013].

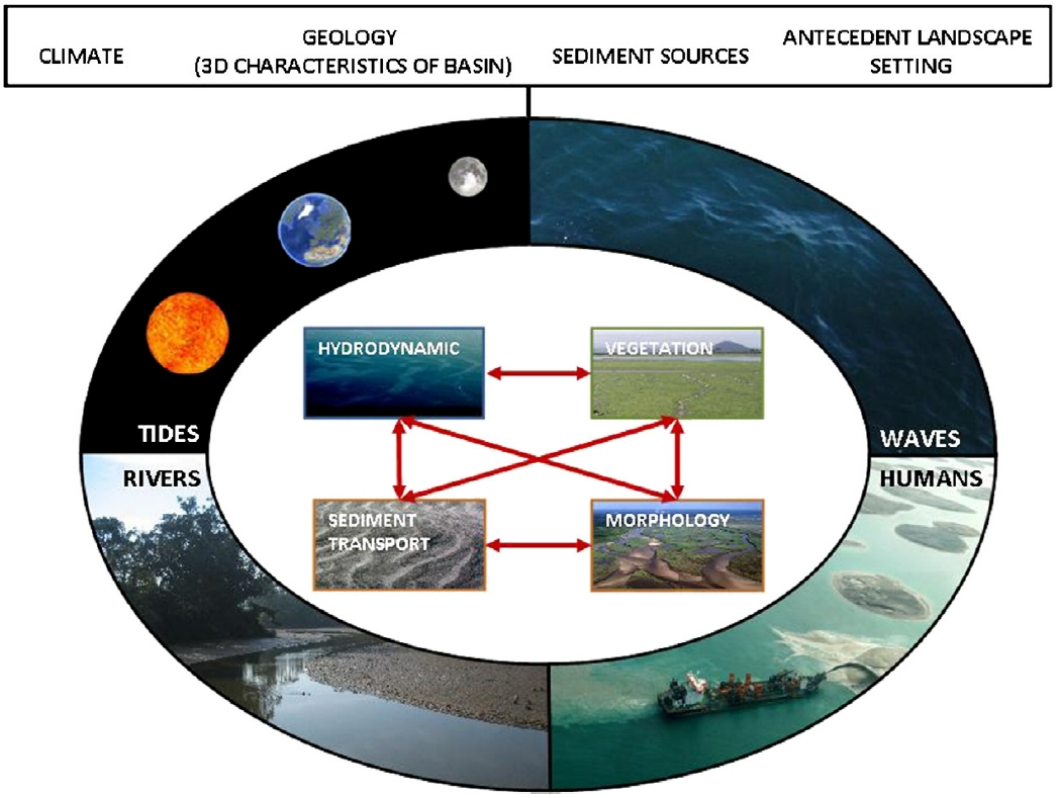

Figure 1.1: Eco-morphodynamic approach (**Image from** Coco et al. [2013]).

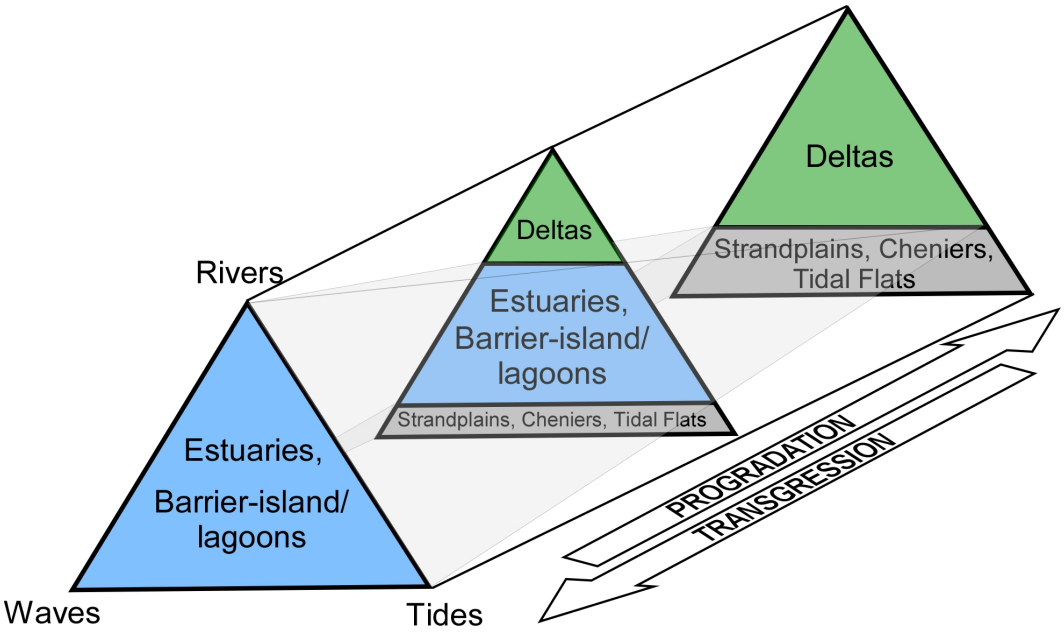

Figure 1.2: Triangular diagram for coastal systems evolution (adapted from Dalrymple et al. [1992]).

are likely to be flooded by the end of this century. Moreover, a rise in the mean sea level will promote more frequent extreme sea-level events, namely any event, storm surges of surface waves, exceeding a threshold level. Finally, because it extends the wave action, sea level rise will enhance the erosion on the coasts causing the shoreline to retreat.

Facing threatening physical impacts of climate change, long-term predictions about coastal system become an urgent need [de Vriend et al., 1993]. In truth long-term predictions are not absolute but, by the use of different models, the constant signatures of the evolutionary trends outlined become of utmost importance to coastal managements. Among coastal systems, tidal environments are systems whose ephemeral equilibrium is the subject matter of this thesis.

1.2 Objectives

Early investigations on tide propagation over simple geometrical domains paved the way for the development of the modern numerical models widely spread and used nowadays. The need for predictions on the long term has challenged scientists to implement robust package tools to be added in the numerical models library at any user's hand (Delft3D [Deltares, 2014], MIKE [DHI, 2017a,b], Telemac-Mascaret [Tassi and Villaret, 2017], HEC-RAS [USACE, 2016]). Despite the increasing computer performances, it is still unsure what feedback on a short time scale will drive the system evolution on the long run [de Vriend et al., 1993]. Under this perspective, simple geometrical domains have been brushed up to give insight about the physical mechanisms that may drive to stable or unstable equilibrium.

The problem we seek to solve is the open channel flow in a schematical lagoon formed by a rectangular basin cut through by a straight channel connected with the sea just at one end. Specifically, we want to investigate the effects of sedimentation, sea level rise and vegetation growth on the long-term configuration of a tidal channel assuming non-negligible tidal propagation effects. The objectives of this thesis are to answer multiple questions. What is the role exerted by sea level rise, sedimentation and vegetation in the final configuration of a tidal channel flanked by lateral shoals? Is the final configuration an equilibrium state? If so, which kind of equilibrium? Is there evidence of any pattern in the synthetic cross sectional morphologies?

1.3 Background

Tidal environments are dissected by networks of channels which act as the preferable routes for the tidal propagation and the transport of sediments, nutrients and pollutants [Coco et al., 2013]. The network branches from a tidal inlet spreading

out in different sites and driving the exchange between the sea and the tidal ecosystem [Friedrichs and Perry, 2001; Hughes, 2012]. Depending on their bathymetric distribution and functions, characteristic morphological features are recognizable in tidal basins. Firstly, salt marshes are located above the MSL, they are periodically submerged by the tide, typically every 12 hours in systems with semidiurnal tides. These morphological structures are approximately flat areas, concave upward, cut by small channels that feed and drain the surface. The periodic submergence allows the growth of halophitic vegetation, resistant in brackish waters [Marani et al., 2004; Silvestri and Marani, 2004]. Since the surface is not completely flat, vegetation encroaches salt marshes distributing in patches [Marani et al., 2004; Pennings et al., 2005]. Vegetation has been proven to shield and stabilize salt marshes preventing erosion [Marani et al., 2004; Mariotti and Fagherazzi, 2010] and mitigating sediment suspension. Set below the MSL, tidal flats are always submerged except for extreme low tides. The almost perpetual submergence hinders the growth of vegetation except for seagrass, algae and mycrophitobenthos which create a thin bio-film. The absence of vegetation makes tidal flats more vulnerable to erosion and suspension of sediments that are carried away by the channels. Finally, tidal channels dissect tidal flats and salt marshes exerting a chief control on the morphodynamic evolution of tidal environments [DAlpaos et al., 2005; Lanzoni and D'Alpaos, 2015]. The channels indeed connect far and close sites together creating a network where multiple branches concur to form different outlines, such as linear, dendritic, superimposed, reticulate, meandering (Figures 1.3 and 1.4). The tidal channels have a funnel shape with lateral shoals which allow the flow, confined in straight conduit at low tide, to expand in multiple directions at high tide. Flooded and drained frequently during the tidal period, the lateral shoals make therefore wetting and drying processes ubiquitous [Fagherazzi and Furbish, 2001].

Similarly to their fluvial counterparts, tidal networks have tree-like structures. However, differently from their river relatives, tidal networks do not behave as scaling invariant features [Fagherazzi et al., 1999]. Indeed, a number of studies showed that the geomorphological relationships valid for fluvial networks do not hold in tidal environments as the spatial scale changes [Rinaldo et al., 1999]. The abscence of free-scale behaviour for tidal networks prompted to search for geomorphic (scaling) relationships able to give insights about landforming processes. The study of different tidal networks highlighted that geometric features as widths and wavelengths have a large variability increasing toward the seaward end [Marani et al., 2002]. Notwithstanding, the curvature seems constant throughout the basin allowing an analytical formulation of the morphodynamic problem [Solari et al., 2002]. Another important feature of tidal channels is the width-to-depth ratio β, defined as the ratio between the width B and the depth D. Looking at the width-to-depth

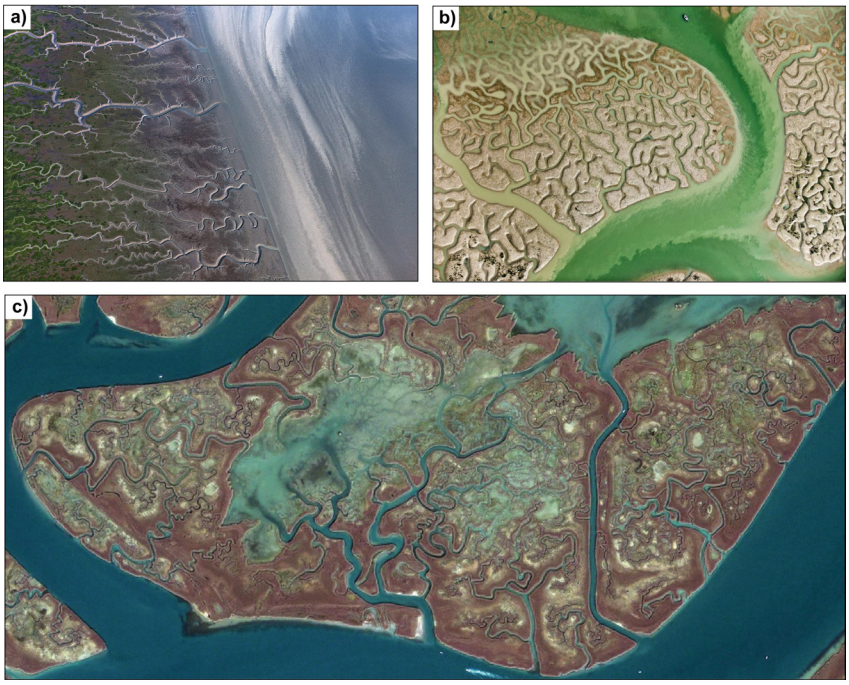

Figure 1.3: Tidal networks across the world. On panel a) the tidal channels at Cook Inlet in Alaska (US, Photo by Ingo Arndt); on panel b) tidal channel of Guadalquivir at Isla Minima in Seville (ES, Photo by Hector Garrido); on panel c) the tidal channel dissecting San Felice salt marsh in the north-eastern portion of the Venice Lagoon (IT).

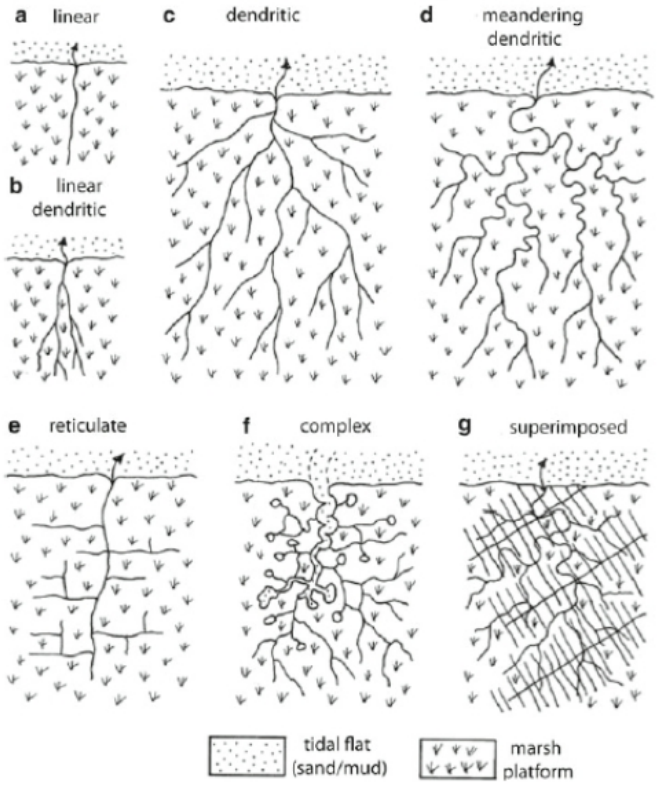

Figure 1.4: Tidal-network classification [Hughes, 2012].

ratio of tidal channels, two different behaviors were detected on the marshes and on the tidal flats in the Venice lagoon. The channel dissecting marshes are deeper and narrower with β ranging between 5 and 7 because of vegetation which increases friction on the platform favoring the flow within the channel. On the other hand, channels dissecting tidal flats, where vegetation is absent, display higher width-to-depth ratios with β ranging between 8 and 50, similarly to fluvial cross sections. The two different behaviors are shown in figure 1.6.

Despite the variety of tidal networks, it is possible to bridge the gap between the hydrodynamics and the morphology by the use of geomorphic relations. The relationship between the tidal prism, P (which is the volume of water that flows through a given cross section during flood or ebb) and the wetted cross-sectional area, $\mathcal{A}$, is described by the O'Brien-Jarrett-Marchi law (denoted as OBJM law hereafter) [D'Alpaos et al., 2009a,b], empirically discovered studying harbor and estuary inlets [Jarrett, 1976; O'Brien, 1931] and then theoretically derived [Marchi, 1990] and verified in the case of tidal channels [D'Alpaos et al., 2009b; Rinaldo et al., 1999]. According to this relationship, the tidal prism and the cross sectional area at the inlet are related through the following power law:

$$\mathcal{A} \propto aP^b \tag{1.1}$$

where $\mathcal{A}$ is the minimum cross sectional area at the inlet, P is tidal prism at spring tide, a and b coefficients empirically set at 0.0025 and 6/7 respectively. Many authors have proven that OBJM law is verified not only for the inlets but also for the other cross sections along the channel except for those cross sections very far from the inlet, where the quasi-static assumption, fundamental for the theoretical derivation, does not hold [Di Silvio, 1992] and for those small cross sections highly subjected to wetting and drying phenomena [Lanzoni and D'Alpaos, 2015; Marani et al., 2002].

In tidal environments, as in all open systems, the existence of a morphodynamic equilibrium is often questioned. The concept is elusive since it refers to the real world, where all physical processes involved may balance out in a transient equilibrium state, and, on the other hand, to the virtual world, reproduced by the mathematical model under assumptions and approximations [Zhou et al., 2017]. All in all, the equilibrium has to be conceived as a preferable state a system is tending to given certain forcings with respect to the model in use [Rinaldo, 1997]. Long-term predictions are hampered by uncertainties about boundary conditions and lack of understanding about phenomena; hence simplified approaches are favored to study the problem. In this regard, the equilibrium in tidal networks has been

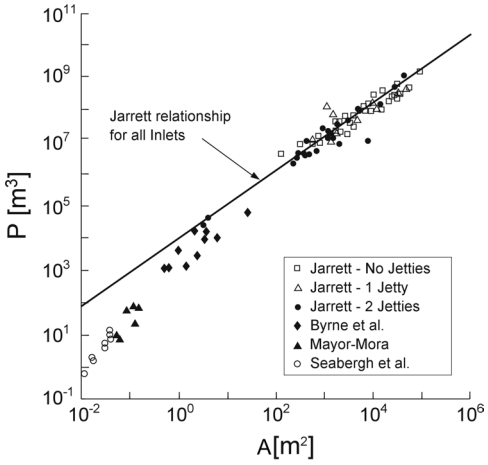

Figure 1.5: The Jarrett-O'Brien-Marchi law [D'Alpaos et al., 2009a].

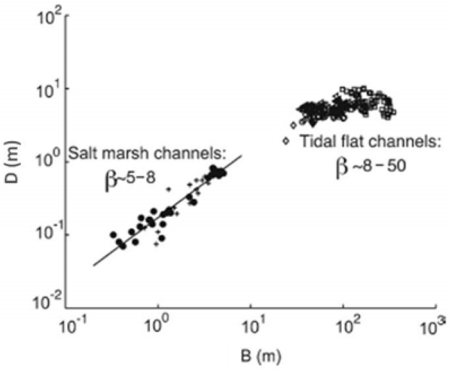

Figure 1.6: Channel morphology within salt marsh and tidal flats [Marani et al., 2002], where $\mathcal{B}$ is the channel width and D its depth.

investigated singling out their morphological features, the channel and its lateral platforms, whether marshes, if vegetated, or tidal flats, if not.

Set at the fringe between land and sea and above MSL, marshes are highly exposed to natural forcings offering a brief outlook of the health of tidal environments. Marsh morphodynamics has been investigated both vertically, with respect to their accretion/erosion, and horizontally, with respect to their progradation/retreat. The vertical evolution of marshes has been widely modeled using 0D approaches accounting for sea level rise, sediment supply and vegetation encroachment [Allen, 1996; French and Spencer, 1996; Kirwan and Temmerman, 2009; Krone, 1987; Marani et al., 2007; Temmerman et al., 2007]. Despite the simple semblance, point models capture the significant feedbacks driving marsh vertical evolution. As the marsh rises, it is less flooded so that the accretion rate dwindles until it reaches an equilibrium. If the marsh is not able to keep up with the sea level rise because the sediment supply is scarcely available, it drowns. The presence of vegetation affects depositional processes by trapping and organic production affecting the ability to keep up with sea level rise. A tight coupling between physical and biological processes allows the coexistence of multiple equilibrium states within tidal environment, one for the subtidal plane and one for the marsh region [Marani et al., 2007, 2010]. By comparing different model outputs, Kirwan et al. [2010] highlighted how the coupled processes described in point models are able to catch crucial evolutionary trends without demanding cumbersome numerical formulations. Moreover, some steps were made also to introduce within this simple approach feedbacks triggered by algae mat coverage which shields submerged regions reducing erosion occurrence [Pivato et al., 2019; Tambroni et al., 2015; Venier et al., 2012]. On the other hand,

the marsh migration has been studied focusing on the fate of the scarp between marsh platform and tidal flats under different scenarios which include sea level rise, sediment supply and wind waves [Marani et al., 2011; Mariotti and Fagherazzi, 2010, 2013a,b; van de Koppel et al., 2005]. Set the sediment supply, the scarp shifts depending on the rate of sea level rise: if the rate is low, the marsh edge progrades becoming shallower, conversely, if the rate is high, the marsh edge retreats deepening the channel. The physical mechanisms retained in the marsh migration were verified in lab works [Bendoni et al., 2014] and in the field [Bendoni et al., 2016].

Given the fundamental control on morphodynamics exerted by tidal channels, many authors have analyzed tidal-channel morphodynamics focusing on the evolution of the longitudinal bed profile for a given channel-width distribution. Keeping a constant width as in tidal flat conceived as a channel, the analytical equilibrium profile tends to adjust in a tide dominated environment along a convex-linear trend [Friedrichs and Aubrey, 1996]: linear profile throughout the basin except in the landward part of the basin where a convex profile controlled by a sinusoidal elevation curve is established. This seminal theoretical framework was derived posing peak uniform velocity, and thus shear stress, across the flat as condition for stability. This constrain was then proved to be reasonable since it leads to cancel out non-uniformity in the hydrodynamic field and therefore in the sediment settling [Pritchard and Hogg, 2003]. Numerical models have then managed to follow the analytical results with constant width [Lanzoni and Seminara, 2002; Pritchard et al., 2002] and to introduce channel convergence by a width distribution function [Todeschini et al., 2008].

Analytical and theoretical results concerning straight channel morphodynamics were confirmed by experimental works [Tambroni et al., 2005]. The experimental set-up consisted in a tank, acting as a sea basin, attached to a straight channel with a sharp or smooth inlet. The equilibrium profile is slightly concave except at the landward end where a convex beach completes the channel. The landward beach is the result of the landward net transport acting at the start of the runs; this is the result of flood dominance at early stages of the experiments as confirmed by other authors. Afterward, sediment begins to rearrange in the inner part while at the seaward end the channel loses sediments creating an outer-delta. This experimental work was used as validation data set for the development of a 2D-1D hydrodynamic model coupled with a morphodynamic model to investigate the inlet dynamics [Tambroni et al., 2004]. Specifically, a 2D model copes with the dynamics in the sea basin, while a 1D model, matched with the 2D model at the inlet, drives the evolution in the rectangular channel. The longitudinal bed profile observed at the seaward end was better predicted by the 1D-2D model than by a full 1D approach; however, landward the scouring effect has prevailed shaping a dip which was

not observed nor predicted by the 1D model. Moreover, the outer-delta evolution has been reproduced just qualitatively since turbulent structures issuing the inlet edges turn out to play a significant role that cannot be simulated by the model. The runs end up to be hefty and costly to long term predictions. Considering the 1D model, Tambroni and Seminara [2005] investigated the effects of vegetation, wind and sea level rise on the long term evolution of a straight channel without lateral shoals. As soon as the channel bed emerged, vegetation started to encroach the landward portion of the channel. The landward marsh platform aggraded and prograded retreating only when the vegetation growth was not enough to keep up with sea level rise. Wind effects triggered resuspension events that do not cancel out the sea level rise action. In this framework morphodynamic equilibrium proved to be hard to achieve.

In Seminara et al. [2010] the equilibrium length of a straight tidal channel has been sought analytically considering or neglecting the funneling and presence of tidal flats. Constant width channels develop a convergence length that depends on the critical velocity, which assesses the erosional potential of the channel. Moreover, the tapered shape of the channel acts on the downstream profile which becomes more concave. The presence of adjacent embayments may reduce considerably the convergence length (since the channel becomes more incised reducing the critical velocity).

Besides the profile, the evolution of channel cross sections has also been investigated. Draining a rectangular tidal basin, the flow at the inlet was studied by a quasi-static model accounting just for the purely erosive effects [Fagherazzi and Furbish, 2001]. Aiming to reach a dynamic equilibrium, depositional effects were introduced considering sediment supply, constant in space and time, and vegetation [D'Alpaos et al., 2006]. Moreover, a complete modeling framework assessing both altimetric and plani-metric equilibrium channel features has recently been proposed [Lanzoni and D'Alpaos, 2015; Xu et al., 2019] aiming to numerically match theoretical results [Seminara et al., 2010]. The tidal basin was built by a succession of cross sections intending to create a straight channel cutting through a rectangular basin. Proceeding seaward, each cross section subtends a larger basin surface which is flooded and drained by the use of a quasi-static hydrodynamics under the assumption of a short channel [Lanzoni and D'Alpaos, 2015]. However, while a link in terms of discharge is evident between cross sections, the cross sections do not engage with each other in terms of momentum, in other words cross sections are hydraulically disconnected one from the other. Despite this shortcoming, the static equilibrium channel morphology matched roughly the cross sectional data measured on field [Marani et al., 2002], derived analytically [D'Alpaos et al., 2009a] or computed by other numerical models [Canestrelli et al., 2007]. The previous results prompted to

numerically obtain a dynamic equilibrium by introducing depositional effects on the same computational domain [Xu et al., 2019]. Differently from single cross section equilibrium, the dynamic equilibrium was reached only relaxing the assumption of sediment supply constant in space and time [Xu et al., 2019]. Synthetic morphology proved to match real cross sectional data in spite of hydraulic cross-sectional disconnection.

1.4 Overview

The thesis is structured in five chapters. Chapter 2 focuses on the hydrodynamics of a rectangular tidal basin dissected by a straight channel. The problem is tackled using different models: a two-dimensional model, which has been developed in the ICEA Department for studying open channel flow in fluvial or tidal systems and a one-dimensional model, which introduces further approximations to cut the cumbersome bits in order to use it for long-term predictions. Conversely, Chapter 3 deals with the sediment transport mathematical model, whose equations are solved separately from the hydrodynamic problems. Moreover, Chapter 4 describes the bottom shear stress distribution used across the tidal basin putting into effect the one-dimensional model described before. The new model configuration is tested by repeating the runs in Lanzoni and D'Alpaos [2015]. The central core of the thesis is in Chapter 5 which aims to put the hydrodinamic model and the mophodynamic model described in the previous chapters to make long-term predictions on the final configuration of a tidal channel subjected to different forcings. Finally, in Chapter 6 the conclusions are drawn. Two appendixes are attached in the back matter of the thesis: appendix A groups additional results for the validation of the one-dimensional model developed, while appendix B focuses on the mathematical derivation of the bottom shear stress distribution along a cross section.

Chapter 2

Hydrodynamics

This chapter focuses on the flow in a rectangular tidal basin, dissected by a straight channel flanked by two lateral shoals. The objective is to develop a one dimensional (1D) model that reproduces the main features of the flow that establishes within the tidal channel. The 1D model is then "validated" by considering some reference tests and comparing the results with those of a two dimensional (2D) full-fledged finite element model.

2.1 One-dimensional shallow water equations

The one-dimensional De Saint Venant equations hold provided the following assumptions are satisfied:

- The fluid can be treated as incompressible, i.e. such that $d\varrho/dt = 0$ and, consequently, $\nabla \cdot \boldsymbol{u} = 0$, with ϱ the fluid density, $\boldsymbol{u}$ the turbulence averaged velocity vector with components u_x, u_y, u_z;

- The longitudinal scale of the flow is much larger that the cross section width and depth; this implies that the flow is essentially one-dimensional, i.e., the streamlines of the depth averaged flow deviate only very weakly from the longitudinal direction and the water level across a given section is almost horizontal;

- The local value of the vertical component of the velocity is much smaller than the longitudinal component and, therefore, the mean pressure is hydrostatically distributed in the vertical direction;

- The average bed slope is small, such that the direction normal to the flow can be approximated with the vertical;

- The effects of boundary friction and turbulence can be accounted for through resistance laws analogous to those developed for uniform flow conditions.

The one-dimensional DSV equations can be easily obtained by depth integrating the 2D continuity and x-y momentum equations [Vreugdenhil, 1992]:

$$\frac{\partial D}{\partial t} + \frac{\partial}{\partial x}(D\,U_x) + \frac{\partial}{\partial y}(D\,U_y) = 0, \tag{2.1}$$

$$\frac{\partial}{\partial t}(D\,U_x) + \frac{\partial}{\partial x}(D\,U_x^2) + \frac{\partial}{\partial y}(D\,U_x\,U_y) + gD\frac{\partial h}{\partial x} - \frac{1}{\varrho}(\tau_x^h + \tau_x^\eta) = \frac{1}{\varrho}\frac{\partial}{\partial x}(D\,\mathcal{T}_{xx}) + \frac{1}{\varrho}\frac{\partial}{\partial x}(D\,T_{xx}^{(disp)}) + \frac{1}{\varrho}\frac{\partial}{\partial y}(D\,\mathcal{T}_{xy}) + \frac{1}{\varrho}\frac{\partial}{\partial y}(D\,T_{xy}^{(disp)}), \tag{2.2}$$

$$\frac{\partial}{\partial t}(D\,U_y) + \frac{\partial}{\partial x}(D\,U_x\,U_y) + \frac{\partial}{\partial y}(D\,U_y^2) + g\,D\,\frac{\partial h}{\partial y} - \frac{1}{\varrho}(\tau_y^h + \tau_y^\eta) = \frac{1}{\varrho}\frac{\partial}{\partial x}(D\,\mathcal{T}_{yx}) + \frac{1}{\varrho}\frac{\partial}{\partial x}(D\,T_{yx}^{(disp)}) + \frac{1}{\varrho}\frac{\partial}{\partial y}(D\,\mathcal{T}_{yy}) + \frac{1}{\varrho}\frac{\partial}{\partial y}(D\,T_{yy}^{(disp)}), \tag{2.3}$$

Here x is the longitudinal coordinate, y is the lateral coordinate, $D(x,y)$ is the local flow depth, $h(x,y,t)$ is the water surface elevation, τ_x^h, τ_y^h are components of the shear stress at the free surface, τ_x^η, τ_y^η are the components of the shear stress at the bed interface,

$$U(x,y,t) = \frac{1}{D}\int_\eta^h u_x(x,y,z,t)\,dz, \qquad U_y(x,y,t) = \frac{1}{D}\int_\eta^h u_y(x,y,z,t)\,dz, \tag{2.4}$$

$$\mathcal{T}_{xx} = \frac{1}{D}\int_\eta^h 2(\mu+\mu_T)\frac{\partial u_x}{\partial x}\,dz, \qquad \mathcal{T}_{yy} = \frac{1}{D}\int_\eta^h 2(\mu+\mu_T)\frac{\partial u_y}{\partial y}\,dz, \tag{2.5}$$

$$\mathcal{T}_{xy} = \mathcal{T}_{yx} = \frac{1}{D}\int_\eta^h (\mu+\mu_T)\left(\frac{\partial u_x}{\partial y} + \frac{\partial u_y}{\partial x}\right)\,dz, \tag{2.6}$$

$$T_{xx}^{(disp)} = -\frac{\varrho}{D}\int_\eta^h (u_x - U_x)^2 dz, \qquad T_{yy}^{(disp)} = -\frac{\varrho}{D}\int_\eta^h (u_y - U_y)^2 dz, \tag{2.7}$$

$$T_{xy}^{(disp)} = T_{yx}^{(disp)} = -\frac{\varrho}{D}\int_\eta^h (u_x - U_x)(u_y - U_y) dz, \tag{2.8}$$

with μ the viscosity of water and μ_T the turbulent viscosity. The dispersive stresses, denoted by a superscript "disp", are a sort of *macro-Reynolds stresses* associated with the deviations of the distribution along z of the local mean velocity from its depth averaged value.

Under the assumption that the coordinate axis z normal to the flow nearly coincides with the vertical direction (small bed slopes), the integration of the continuity

equation (2.1) between $\mathcal{B}_L$ and $\mathcal{B}_R$ yields:

$$\int_{-\mathcal{B}_R}^{\mathcal{B}_L} \left[\frac{\partial D}{\partial t} + \frac{\partial}{\partial x}(D\,U_x) + \frac{\partial}{\partial y}(D\,U_y)\right] dy = \\ \frac{\partial}{\partial t}\int_{-\mathcal{B}_R}^{\mathcal{B}_L} D\,dy + \frac{\partial}{\partial x}\int_{-\mathcal{B}_R}^{\mathcal{B}_L} (D\,U_x)\,dy + (DU_y)|_{\mathcal{B}_L} - (DU_y)|_{\mathcal{B}_R}, \tag{2.9}$$

where the terms deriving from the application of Leibnitz rule have not been included because at the channel banks ($y = -\mathcal{B}_R$ and $y = \mathcal{B}_L$) we have that $U_y(x, \mathcal{B}_L, t) = U_y(x, -\mathcal{B}_R, t) = 0$ and $D(x, \mathcal{B}_L, t) = D(x, -\mathcal{B}_L, t) = 0$. Noting that:

$$\int_{-\mathcal{B}_R}^{\mathcal{B}_L} D(x, y, t)\,dy = A(x, t), \qquad \int_{-\mathcal{B}_R}^{\mathcal{B}_L} (D\,U_x)\,dy = Q(x, t), \tag{2.10}$$

where A is the cross sectional area and Q the flow discharge, the 1D continuity equation eventually takes the form:

$$\frac{\partial A}{\partial t} + \frac{\partial Q}{\partial x} = 0. \tag{2.11}$$

The lateral averaging of the the $y-$component of the shallow water equations shows that the free surface elevation is constant in the $y-$direction, i.e. $h = h(x, t)$. On the other hand, the averaging of the $x-$momentum equation (2.2) leads to:

$$\int_{-\mathcal{B}_R}^{\mathcal{B}_L} \left[\frac{\partial}{\partial t}(D\,U_x)\right] dy = \frac{\partial Q}{\partial t}, \\ \int_{-\mathcal{B}_R}^{\mathcal{B}_L} \left[\frac{\partial}{\partial x}(D\,U_x^2) - \frac{1}{\varrho}\frac{\partial}{\partial x}(D\,T_{xx}^{(disp)})\right] dy = \frac{\partial}{\partial x}\left[\int_{-\mathcal{B}_R}^{\mathcal{B}_L} dy \int_{\eta}^{h} u_x^2\,dz\right] = \frac{\partial}{\partial x}\left(\beta_{cor}\,U^2\,A\right), \\ \int_{-\mathcal{B}_R}^{\mathcal{B}_L} \left[\frac{\partial}{\partial y}(D\,U_x\,U_y) - \frac{1}{\varrho}\frac{\partial}{\partial y}(D\,T_{xy}^{(disp)}) - \frac{1}{\varrho}\frac{\partial}{\partial y}(D\,\mathcal{T}_{xy})\right] dy = 0, \\ \int_{-\mathcal{B}_R}^{\mathcal{B}_L} \left[g\,D\,\frac{\partial h}{\partial x}\right] dy = g\,A\,\frac{\partial h}{\partial x}, \\ \int_{-\mathcal{B}_R}^{\mathcal{B}_L} \left[-\frac{1}{\varrho}(\tau_x^h + \tau_x^\eta)\right] dy = -\frac{1}{\varrho}(\mathcal{B}\,\tau_w + c\,\tau_b), \\ \int_{-\mathcal{B}_R}^{\mathcal{B}_L} \left[\frac{1}{\varrho}\frac{\partial}{\partial x}(D\,\mathcal{T}_{xx})\right] dy = \frac{\partial A\,\mathcal{T}}{\partial x}, \tag{2.12}$$

where τ_b is the average shear stress along the wetted perimeter c, τ_w is the average wind stress across the water surface of width $\mathcal{B}$, and $U, \mathcal{T}$ are the cross sectionally averages of the flow speed u_x and Reynolds stress T_{xx}, respectively. Moreover, β_{cor} is a correction (Coriolis) coefficient which represents the ratio between the actual momentum flux of the stream and the momentum flux of a stream characterized by the same cross sectional area and a constant velocity distribution equal to the cross

sectionally averaged speed $U = Q/A$ of the actual stream. Hence:

$$\beta_{cor} = \frac{\int_{-\mathcal{B}_R}^{\mathcal{B}_L} dy \int_{\eta}^{h} u_x^2 \, dz}{A \, U^2}. \tag{2.13}$$

In general, the corrective coefficient β_{cor} incorporates also the effect of dispersive stresses $T_{xx}^{(disp)}$. The coefficient β_{cor} is $\simeq 1$ for sufficiently compact cross sections, whereas it may significantly differ from 1 in composite sections treated as a single section.

Eventually, the 1D momentum equation reads:

$$\frac{\partial Q}{\partial t} + \frac{\partial}{\partial x}\left(\frac{\beta_{cor} Q^2}{A}\right) + g\,A\,\frac{\partial h}{\partial x} - \frac{1}{\varrho}(\mathcal{B}\,\tau_w + c\,\tau_b) - \frac{\partial (A\,\mathcal{T})}{\partial x} = 0. \tag{2.14}$$

In order to close the 1D problem described by equations (2.11) and (2.14) closure relationships are required for $\bar{\tau}_w$, $\bar{\tau}_0$ and $\mathcal{T}$.

Denoting by C_f the cross sectionally averaged value of the friction coefficient of the water flow and by C_{fw} the wind friction coefficient, we write:

$$\tau_b = -\varrho C_f \, U \, |U|, \qquad \tau_w = \varrho_a \, C_{fw} \, U_w \, |U_w|. \tag{2.15}$$

with ϱ_a and U_w the density and mean velocity of the wind flowing over the water surface.

As far as $\mathcal{T}$ is concerned, typically this contribution is neglected and semiempirical closures are necessary only when the 1D formulation is employed to investigate processes characterized by fairly short spatial scales (e.g., roll wave formation).

Adopting (2.15) and setting $\mathcal{T} = 0$, the 1D form of the momentum equation takes the form:

$$\frac{\partial Q}{\partial t} + \frac{\partial}{\partial x}\left(\frac{\beta_{cor} Q^2}{A}\right) + g\,A\,\frac{\partial h}{\partial x} - \mathcal{B}\frac{\varrho_a}{\varrho} C_{fw} U_w |U_w| + c\,C_f \frac{Q\,|Q|}{A^2} = 0. \tag{2.16}$$

A simplified version of this equation, often employed in fluvial contexts, is obtained setting $\beta_{cor} = 1$, introducing the hydraulic radius $R_H = A/c$, neglecting the wind contribution and using the continuity equation (2.11), to find:

$$\frac{\partial U}{\partial t} + U\frac{\partial U}{\partial x} + g\,\frac{\partial h}{\partial x} + C_f \, \frac{U|U|}{R_H} = 0. \tag{2.17}$$

The system formed by the partial differential equations (2.11) and (2.16) (or 2.17) is quasi-linear and hyperbolic. It needs suitable boundary and initial conditions to be solved. Boundary conditions consist of known time dependent relationships between h and U (or h and Q) at the end sections of the channel reach. In

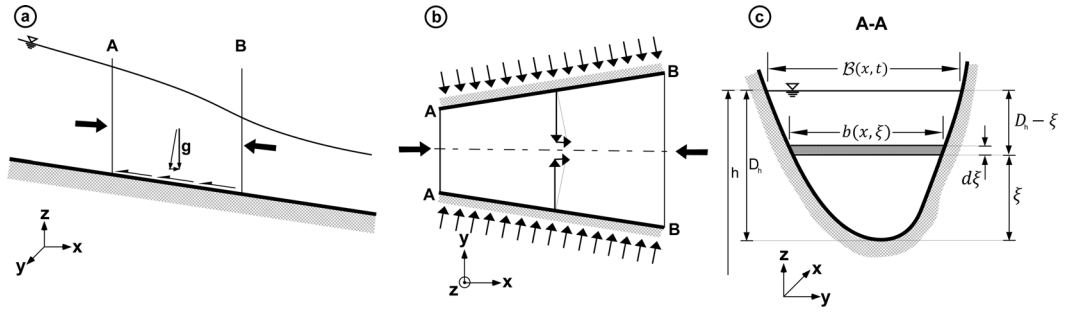

Figure 2.1: The control volume for deriving the 1D shallow water equations, coinciding with a channel reach of length dx (Adapted from Cunge et al. [1980]). a) Lateral view; b) Top view; c) Cross-sectional view of the control volume.

particular, two of such relationships must be assigned at the upstream boundary under supercritical flow conditions, while one relationship must be assigned at each boundary under subcritical conditions. Initial conditions for h and U (or h and Q) at each cross section must also be assigned within the investigated reach.

The structure of the gravitational term $g\,A\,\partial h/\partial x$ does not allow one to write the system (2.11) and (2.16) in conservative form, i.e. such that:

$$\frac{\partial \boldsymbol{Q}}{\partial t} + \frac{\partial \boldsymbol{F}}{\partial x} = \boldsymbol{R} \tag{2.18}$$

with $\boldsymbol{Q}$ the unknown variable vector (e.g., A, Q), $\boldsymbol{F}$ the flux vector, and $\boldsymbol{R}$ a source term vector.

Nevertheless, the gravitational term can be rewritten observing that (Figure 2.1):

$$h(x,t) = z_b(x) + D_h(x,t) = z_b(x) + \xi + d_h(x,\xi,t), \tag{2.19}$$

$$\frac{dz_b}{dx} = -sin\theta \sim -\tan\theta = -S_0 \tag{2.20}$$

$$A = \int_\eta^h D(x,y,t)\,dy = \int_0^{D_h} b(x,\xi)\,d\xi \tag{2.21}$$

with $z_b(x)$ the elevation of the lower point of the section (thalweg), coinciding with the intersection of the $x-$axis with the cross section, $D_h(x,t)$ the distance of this point from the free surface, ξ a dummy variable (independent of x and t), θ the angle that the $x-$axis forms with the horizontal, S_0 the channel bed slope, $b(\xi)$ the cross sectional with at a distance ξ from the thalweg.

Further noting that $\partial h/\partial x$ and $\partial z_b/\partial x$ keep constant across a given section, we

write:

$$A\frac{\partial h}{\partial x} = \int_0^{D_h} b(x,\xi)\frac{\partial h}{\partial x}\,d\xi = A\frac{dz_b}{dx} + \int_0^{D_h} b\frac{\partial d_h}{\partial x}\,d\xi \tag{2.22}$$

$$= -\,A\,S_0 + \int_0^{D_h} \frac{\partial[b(x,\xi)\,d_h(x,\xi,t)]}{\partial x}\,d\xi - \int_0^{D_h} d_h(x,\xi,t)\frac{\partial b(x,\xi)}{\partial x}\,d\xi \tag{2.23}$$

with $d_h(x,\xi,t) = D_h(x,t) - \xi$. Using the Leibnitz derivation rule and observing that $d_h(x,D_h,t) = 0$, it is straightforward to show that

$$\int_0^{D_h} \frac{\partial[b(x,\xi)\,d_h(x,\xi,t)]}{\partial x}\,d\xi = \frac{\partial}{\partial x}\int_0^{D_h}[b(x,\xi)\,d_h(x,\xi,t)]\,d\xi, \tag{2.24}$$

Setting:

$$I_1 = \int_0^{D_h}[b(x,\xi)\,d_h(x,\xi,t)]\,d\xi \qquad I_2 = \int_0^{D_h} d_h(x,\xi,t)\frac{\partial b(x,\xi)}{\partial x}\,d\xi \tag{2.25}$$

the gravitational term is eventually rewritten as:

$$g\,A\,\frac{\partial h}{\partial x} = \frac{\partial}{\partial x}(g\,I_1) - g\,I_2 - gAS_o \tag{2.26}$$

The integral I_1 is the static moment of the cross-sectional area referred to the water surface and the corresponding contribution accounts for the difference in pressures acting on the upstream and downstream cross sections of the streamtube formed by a channel reach of length dx. The integral I_2 is related to the resultant of the pressure acting on the lateral area of this streamtube, projected along the longitudinal direction.

With the above findings, the conservative form of the cross-sectionally averaged momentum equation turns out to be [Cunge et al., 1980]:

$$\frac{\partial Q}{\partial t} + \frac{\partial}{\partial x}\left(\frac{\beta_{cor}Q^2}{A} + gI_1\right) = g\,A(S_0 - S_f) + g\,I_2, \tag{2.27}$$

where the energy slope S_f reads

$$S_f = c\,\frac{C_f}{g}\frac{Q|Q|}{A^3}, \qquad \frac{C_f}{g} = \frac{1}{\chi^2} = \frac{1}{k_s^2}\,R_H^{-1/3} \tag{2.28}$$

Here χ and k_s are the Chezy and Gauckler-Strickler resistance coefficients, respectively. In the following we will use the Gauckler-Strickler resistance relations and rewrite the energy slope in terms of the conveyance K_T:

$$S_f = \frac{Q|Q|}{K_T^2}, \qquad K_T = k_s\,A\,R_H^{2/3} \tag{2.29}$$

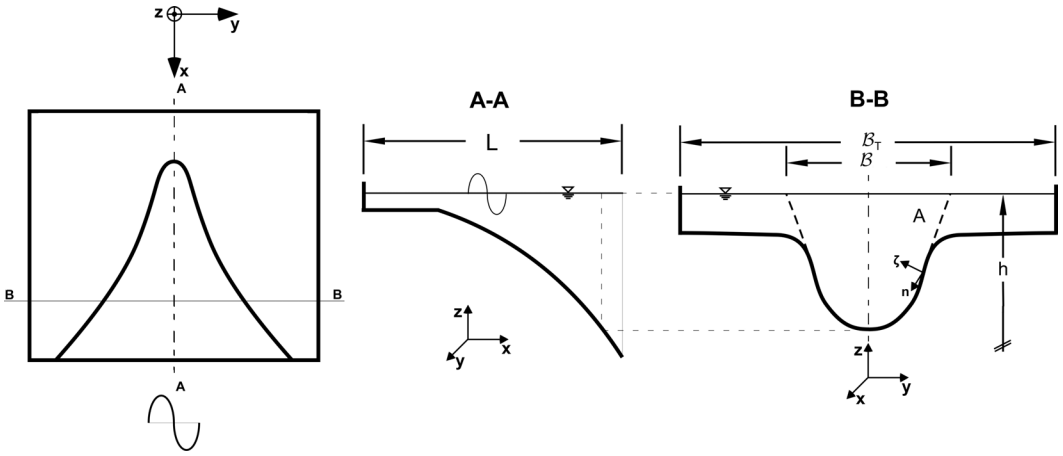

Figure 2.2: Tidal channel geometry

As long as all the unknowns (e.g., Q and A) are differentiable, there is no difference between the systems of partial differential equation formed by mass conservation (2.11) and the momentum equation written in either non-conservative (2.16) or conservative (2.27) form. Conversely, when discontinuities (e.g., hydraulic jumps or bores) come into play, the two systems of PDE differ from each other. The system written in conservative form, solved with suitable numerical techniques, allows one to reproduce correctly the position and shape of the discontinuity, while this is not the case when the non-conservative form is adopted.

In tidal environments channel cross sections are often compound (Figure 2.2): two adjacent intertidal areas flank a main channel providing the flow additional storage volumes. While within the channel region the 1D assumptions hold, on intertidal areas the stream may show a two-dimensional behavior (curvature of longitudinal streamlines is no longer negligible). On the other hand, during each tidal cycle intertidal areas flanking the main channel can be involved or not in the channel flow, depending on whether the tide inundates or not the intertidal platform. When the tidal flow is confined within the channel, the flow has a preferable direction and the cross section can be usually treated as compact (1D flow). Conversely, as overbank tide spills onto the intertidal (marsh or tidal flat) surface, the flow may assume a two-dimensional character and, in any case, within a 1D framework the cross section hosting the flow has to be treated as compound.

The intertidal areas flanking the main channel can be treated as additional storage volumes with still water, without the need of tracking the flow over them [Cunge et al., 1980; Dronkers, 1964; Toffolon and Lanzoni, 2010]. Equations (2.11)

and (2.16) can then be rewritten as:

$$\mathcal{B}\, r_s \frac{\partial h}{\partial t} + \frac{\partial Q}{\partial x} = 0 \tag{2.30}$$

$$\frac{\partial Q}{\partial t} + \frac{\partial}{\partial x}\Big(\beta_{cor}\frac{Q^2}{A}\Big) + g\, A \frac{\partial h}{\partial x} + g\, A\, S_f = \mathcal{F} \tag{2.31}$$

where $\mathcal{B}$ is the main channel width at the water surface (Figure 2.2), A is the main channel area, β_{cor} is the Coriolis coefficient, while K_T is the conveyance of the whole cross section, including the lateral intertidal areas. Moreover the coefficients r_s and the term $\mathcal{F}$ read:

$$r_s = \left(1 + \frac{\mathcal{B}_T - \mathcal{B}}{\mathcal{B}}\right) \tag{2.32}$$

$$\mathcal{F} = \left(\frac{Q}{A} - U_{in}\cos\delta\right)\mathcal{B}\,(r_s - 1)\,\frac{\partial h}{\partial t} \tag{2.33}$$

with $\mathcal{B}_T$ the width of the entire tidal transect (Figure 2.2), U_{in} the velocity of the flow entering the channel from the intertidal areas, and δ the angle between this flow and the direction of the channel axis.

The coefficient r_s accounts for the static effect of the intertidal areas when they are inundated by the tide. The term $\mathcal{F}$ [Toffolon and Lanzoni, 2010] takes into account the additional pressure forces acting at the interface with the main channel (dotted lines in Figure 2.2c) when the water spills onto the intertidal areas or, viceversa, goes into the channel. Note that, the direction of the flow on the floodplain (i.e., the angle δ) has to be imposed *a priori* (i.e., it is not a result of the hydrodynamic model) and generally varies during the tidal cycle depending on bathymetry and friction [Lawrence et al., 2004]. In the presence of a quite rough intertidal surfaces, $\delta \simeq \pi/2$ [e.g., see Figure 9b of Lawrence et al., 2004] and equation (2.33) becomes $\mathcal{F} = \left(\frac{Q}{A}\right)\mathcal{B}(r_s - 1)\frac{\partial h}{\partial t}$. For the sake of simplicity, in the following the term $\mathcal{F}$ is neglected.

For 1D modeling purposes, the case of a tidal channel head merging with a landward intertidal areas has to be considered (Figure 2.3). Therefore, the 1D equations governing the mass and momentum balance must hold for both the compact cross section characterizing an intertidal transect (Figure 2.4a), and compound cross sections as those typical of a channelized region flanked by two intertidal areas (Figure 2.4b). In the former case, the cross section covers the entire tidal basin width and, hence, the storage coefficient r_s is equal to 1. Conversely, in the presence of a main channel flow incised in the intertidal platform, the storage ensured by the lateral intertidal areas increases r_s, which becomes greater than 1. The friction in the momentum equation (i.e., the conveyance coefficient K_T) is always computed

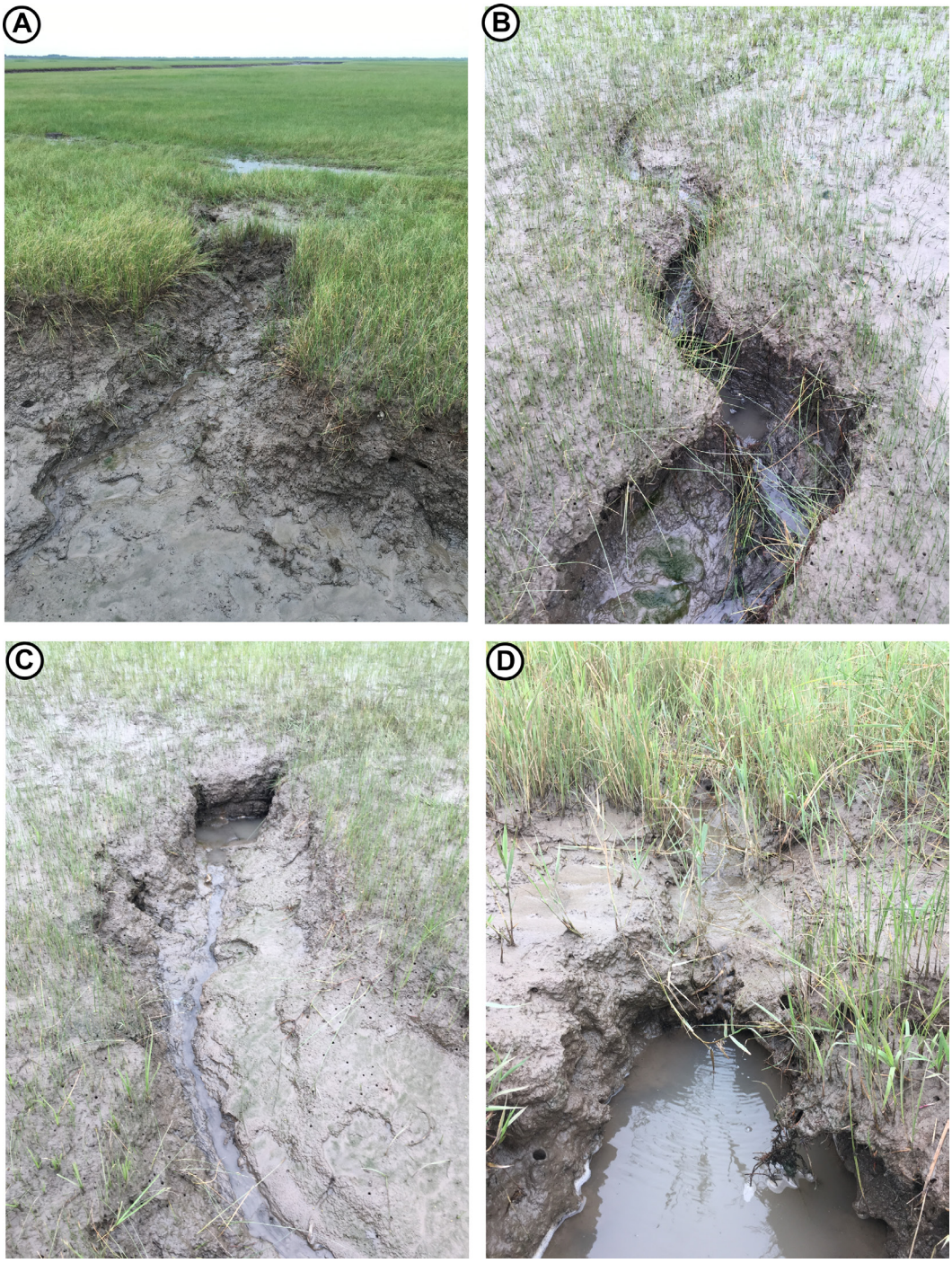

Figure 2.3: Channel from the mouth (a) to the head (d). Jiangsu Province (China).

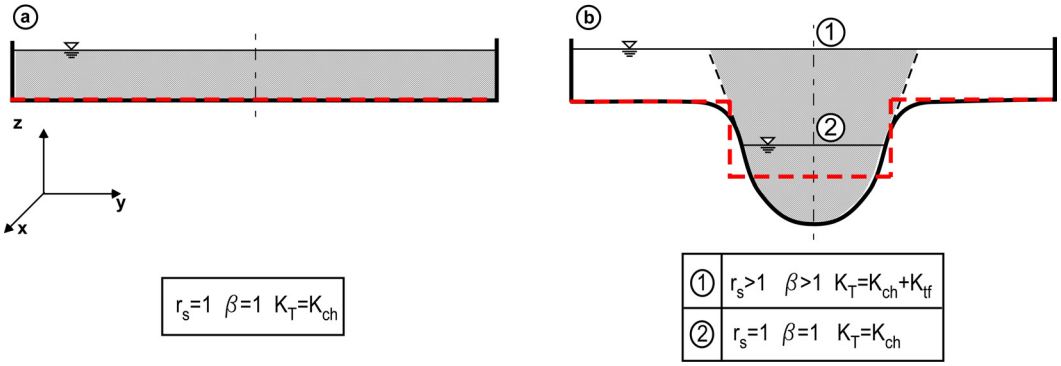

Figure 2.4: a) Compact cross section of an intertidal transect; b) compound cross section cross sections.

considering the whole cross section [1]. In compact intertidal transects, modeled as a rectangular cross section of with $\mathcal{B}_T$, the channel bed acts as the only source of friction and $\beta_{cor} \sim 1$; in compound cross sections both tidal flats and channel bed concur to the flow resistance such that $\beta_{cor} > 1$.

In order to consider in the 1D model a unique type of cross section throughout the entire length of the computational domain, in the following the compact cross section characterizing any intertidal transect located upstream of the main channel head is treated as a compound section with a rectangular main channel and two small adjacent tidal flats with elevation equal to that of the main channel bed (Figure 2.4a). This modeling choice allows one to treat each cross section of the 1D model as compound, facilitating the computations of the coefficients r_s, β_{cor} and K_T (Figure 2.4b).

The system formed by the PDE equations (2.30) and (2.31) (with $\mathcal{F} = 0$) needs to be complemented with suitable initial and boundary conditions for the water discharge $Q(x,t)$ and the water surface elevation $h(x,t)$. At the beginning of each simulation, the computational domain is supposed to be still and fully wet:

$$\begin{aligned} h(x,0) &= a_0 \\ Q(x,0) &= 0 \end{aligned} \tag{2.34}$$

Assuming that the flow is subcritical, according to Figure 2.2, a no-flux condition

[1] The Gauckler-Strickler coefficient in a compact and compound cross section respectively are [Cunge et al., 1980] :

$$k_{s,eq} = \frac{p^{2/3}}{\left(\sum_i \frac{p_i}{k_{si}^{2/3}}\right)^{2/3}} \qquad k_{s,eq} = \frac{\sum_i k_{si} A_i^{5/3}/p_i^{2/3}}{A^{5/3}/p^{2/3}}$$

where p_i is the i-part of the wet perimeter p, A_i is the i-part of the area A, k_{si} is Gauckler-Strickler coefficient. If k_{si} is constant, $k_{eq} = k_s$.

is imposed at the upstream boundary ($x = 0$) of the computational domain while downstream ($x = L$), at the channel mouth, the water stage is set equal to the tidal oscillation:

$$\begin{aligned} h(L,t) &= a_0 \cos\omega t \\ Q(0,t) &= 0 \end{aligned} \tag{2.35}$$

where a_0 is the tidal amplitude and $\omega = 2\,\pi/T$ is the wave number, with T the tidal period.

2.2 3D domain schematization

The tidal domain to be investigated consists of a 3D schematical rectangular basin incised symmetrically by a tidal channel along the longitudinal axis. The basin geometry is described through M cross sections, each of which is a function of the coordinates (y, z). In order to study the tide propagation over the domain using a 1D model, each cross section is approximated by using the compact/compound framework described in the previous section. Hence, the width $\mathcal{B}$, the bed height z_b and the conveyance K_T are computed for each cross section. In the computation of K_T the same value of the Gauckler-Strickler coefficient k_s is assigned to the channel and, if present, to the lateral shoals; as we will see in the next Chapters, only when the vegetation encroaches the lateral platforms, different values of k_s are assigned to channel and, if present, to the lateral platforms. In this latter case, the region pertaining to the main channel needs to be identified.

In general, a methodology to unambiguously separate the main channel area from the lateral flow region does not exist. Approximately, the channel region occupies the portion of basin where the streamlines are roughly straight, while the streamlines over the intertidal areas are nearly straight only for a certain interval of the tidal period, and tend to be deflected towards the channel during the initial phases of the flooding phase and the final phase of the ebb. Actually, different tidal forcings and degree of bed roughness may produce a certain flow exchange between the main channel and the adjacent tidal flats. This exchange is likely minimized ($\mathcal{F} \sim 0$ in equation (2.31)) for rough intertidal surfaces [Lawrence et al., 2004]. We thus assume that the tidal flats concur only to water storage in the continuity equation and use a simple geometrically-based criterion to identify the main channel region. Specifically, a given bed point of a transect is assumed to belong to the main channel when the angle between the normal to the bed and the vertical exceeds a given threshold (say 1°), or in other words, when the local traversal slope exceeds $1 \div 2$ (Figure 2.5).

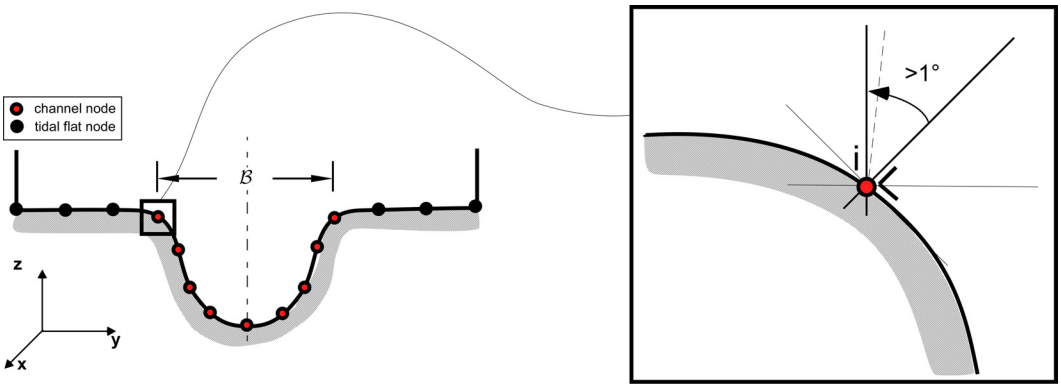

Figure 2.5: Sketch of the criterion adopted to distinguish channeled and unchanneled regions.

The channel cross-sectional width is then computed considering the position of the first and the last channelized point. Simple weighting average of the bed elevations $z_b(x_i, y_i)$ are then used to compute mean height $z_{b,tf}(x_i)$ of the tidal flat region and of the channel cross section $z_{b,ch}(x_i)$. By analogy, given the friction coefficients $k_{si}(x_i, y_i)$ at each bed point, the mean average friction coefficients are computed for the tidal flats $k_{s,tf}(x_i)$ and the channel region $k_{s,ch}(x_i)$.

2.3 Wetting and drying processes

Tidal environments are subjected to wetting and drying processes as a consequence of the tidal cycle. Intertidal areas are flooded when the tide rise, spilling out water on them, and are drained when the tide recedes. On areas subjected to cyclic wetting and drying numerical issues may arise. Specifically, the flow depth becomes quite small or vanishes in certain regions thus leading to unrealistically too large values of the conveyance K_T as well as to abrupt changes in the cross sectional area A. These problems have been addressed by many numerical techniques, developed to handle the wetting and drying problem ensuring mass conservation globally and locally.

Focusing on tidal hydrodynamics and storm surges, Medeiros and Hagen [2013] classified wetting and drying algorithms in four groups: thin film, element removal, depth extrapolation and negative depth algorithms. The first type includes models which assumes the existence of a thin fluid layer on all the computational domain, that it is always wet; therefore the mass and momentum equations are computed over the entire domain. The second category concerns algorithms that check if computational elements are wet/dry or partially dry and remove dry elements from the domain. Further considerations are then needed to include partially dry elements, typically by checking if the bed roughness or the depth of the surrounding elements is large enough to claim a dry element to be wet. The third category groups mod-

els that extrapolate depth from wet elements into dry elements at the boundary between wet and dry regions. The new depths are then used to compute the velocities. The last category concerns algorithms that manage water levels also below the ground surface. Regions with negative depths are considered dry and they become wet if depths, increasing, turn again positive. Independently from the classification, these algorithms are highly tailored to the model they are coupled to. In this regards, benchmarks have been suggested to test 1D and 2D models when small depths or wetting and drying processes come into play [Balzano, 1998]. Specifically, for 1D models the typical reference case consists of a sloping beach profile where some convex contour are inserted, or the depletion of a 1D reservoir. In the case of 2D models, test cases exist for which analytical solutions are available, such as the oscillations of a fluid mass contained within a paraboloid surface.

Another approach adopted to handle wetting and drying processes is based on the observation that there is no sharp transition from wet to dry elements since the terrain irregularities, negligible at high stages, drive the flow when the depths are small, mitigating the wet-dry transition [Defina, 2000]. This approach introduces a subgrid model to describe the ground elevation unevenness, whose mean distribution is defined by roughness parameter e_s. Averaging over bed irregularities allows one to smooth the transition between wet and dry. Specifically, Defina [2000] derived a new set of 2D equations by phase-averaging the Reynolds averaged Navier Stokes equations (RANS) over the bed unevenness of a reference area element ($\mathcal{REA}$-$\mathcal{R}$eference $\mathcal{E}$lement $\mathcal{A}$rea). The resulting set of PDEs are then integrated over the flow depth to obtain a form of the shallow water equations (SWEs) embedding directly the wetting/drying processes. This new set of SWE is equal to the classic 2D SWE for high depths, while they slightly differ for small or negative depths. A similar procedure can be applied to derive the phase-averaged 1D shallow water equations [Lanzoni and Seminara, 2002] and also the phase-averaged 2D Exner equations [Lanzoni, 2008].

Following this phase-averaging approach, let us introduce the phase function $\psi(\boldsymbol{X})$:

$$\psi(\boldsymbol{X}) = \begin{cases} 1 & z > z_b(\boldsymbol{X}) \\ 0 & z \leq z_b(\boldsymbol{X}) \end{cases} \tag{2.36}$$

where $\boldsymbol{X} = x\,\boldsymbol{i}_x + y\,\boldsymbol{i}_y + z\,\boldsymbol{i}_z$ is a coordinate vector ($\boldsymbol{i}_j$ being the unit vector of the $j-$th axis) and $z_b(\boldsymbol{X})$ is the local bed elevation. The variable ψ detects the ground points and behaves as a Dirac delta; the variable $\Delta\psi$ has the direction of the unit normal to the ground $\boldsymbol{i}_z$. Denoting with $\langle\cdot\rangle$ the phase-average procedure, the phase-averaged value of a generic function $f(\boldsymbol{X}, t)$ is computed integrating the

function over $\mathcal{REA}$ as follows:

$$\langle \psi(\boldsymbol{X}) f(\boldsymbol{X},t) \rangle = \frac{1}{\mathcal{A}} \int_{\mathcal{A}} \psi(\boldsymbol{X}) f(\boldsymbol{X},t)\, d\mathcal{A} \tag{2.37}$$

where $\mathcal{A}$ is the $\mathcal{REA}$ area. Two functions Ψ and Ψ_h can be defined as follows:

$$\Psi(\boldsymbol{X}) = \langle \psi(x,y,z) \rangle = \frac{1}{\mathcal{A}} \int \psi(x,y,z)\, d\mathcal{A} \tag{2.38}$$

$$\Psi_h(x,y,h) = \langle \psi(x,y,H) \rangle = \frac{1}{\mathcal{A}} \int \psi(x,y,h)\, d\mathcal{A} \tag{2.39}$$

The quantity $\Psi(\boldsymbol{X})$ represents the area laying over the bed in a $\mathcal{REA}$ while $\Psi_h(x,y,h)$ detects the corresponding wetted area. Integrating $\Psi(\boldsymbol{X})$ along the depth, the phase-averaged depth is obtained:

$$D(\boldsymbol{X},t) = \int_{-\infty}^{h} \Psi(\boldsymbol{X},t) d\zeta \tag{2.40}$$

Assuming a statistical distribution of bed unevenness, the function $\Psi(\boldsymbol{X})$ can be interpreted as the cumulative non-exceedance probability (PDF) that the bed elevation $z_b(x,y)$ is lower than the generic elevation $h(x,y)$:

$$\Psi(\boldsymbol{X}) = \mathscr{P}(z_b \leq h) \tag{2.41}$$

Under the approximation that the PDF is Gaussian, Ψ_h and Φ_h can be expressed as [Defina, 2000]:

$$\Psi_h(x,y) = \frac{1}{2}\,\mathrm{erfc}(\xi_h); \quad \xi = -2\,\frac{z - z_b(x,y)}{e_s}; \quad \xi_h = -2\frac{h(x,y) - z_b(x,y)}{e_s} \tag{2.42}$$

$$\Phi_h = \frac{e_s}{4} \int_{\xi_H}^{\infty} \mathrm{erfc}(\xi)\, d\xi = \frac{e_s}{4} \left[\frac{1}{\sqrt{\pi}} \exp(-\xi_h^2) - \xi_h\, \mathrm{erfc}(\xi_h) \right] \tag{2.43}$$

Finally, on the $\mathcal{REA}$ it is useful to define an equivalent water depth $\mathcal{H}$ whose value reads [Defina, 2000] :

$$\mathcal{H} = e_s\, \mathscr{F}\left(\frac{D}{e_s}\right); \quad \mathscr{F} \approx \frac{D}{e_s} + 0.27\sqrt{\frac{D}{e_s}}\, e^{-2\,D/e_s} \tag{2.44}$$

2.3.1 Local estimation of energy losses

For an infinitely wide rectangular cross section, the uniform flow reads $U = k_s\, D\, S_f^{1/2}$. In the presence of wetting and drying this relation can be generalized as:

$$U = k_s \int_{-\infty}^{h} (h - z_b)^{2/3} \frac{\partial \Psi}{\partial z}\, dz\, S_f^{1/2} \tag{2.45}$$

hence

$$S_f^{1/2} = \frac{U}{k_s \int_{-\infty}^{h} (h - z_b)^{2/3}\, (\partial \Psi / \partial z)\, dz} \tag{2.46}$$

The above integral can be approximated observing that:

$$\frac{\partial \Psi}{\partial z} = \frac{2}{e_s} \frac{\partial \Psi}{\partial \xi} = -\frac{2}{e_s}\left(-\frac{1}{\sqrt{\pi}}\, e^{-\xi}\right) = \frac{2}{e_s} \frac{1}{\sqrt{\pi}}\, e^{-\xi}$$

$$\xi = -2\, \frac{z - z_b}{e_s}, \quad \xi_h = -2\, \frac{h - z_b}{e_s}$$

Consequently, it results:

$$\int_{-\infty}^{h} (h - z_b)^{2/3}\, \frac{\partial \Psi}{\partial \xi}\, dz = \left(\frac{e_s}{2}\right)^{2/3} \frac{1}{\sqrt{\pi}} \int_{\xi_h}^{\infty} (\xi - \xi_h)^{2/3}\, e^{\xi^2}\, d\xi \tag{2.47}$$

$$= e_s^{2/3} \left[\frac{D}{e_s} + a_1 \sqrt{\frac{D}{e_s}}\, e^{-a_2 D / e_s}\right]^{2/3} \tag{2.48}$$

The uniform flow velocity is eventually computed as:

$$U = k_s\, \Phi_{(2/3)}\, S_f$$

with

$$\Phi_{(a)} = \int_{-\infty}^{h} (h - z_b)^a \frac{\partial \Psi}{\partial z}\, dz = \left(\frac{e_s}{2}\right)^a \int_{\xi_h}^{\infty} (\xi - \xi_h)^a\, e^{-\xi^2}\, d\xi$$

In the case of an always wet rectangular section, the uniform flow velocity is $U = k_s\, R_H^{2/3}\, S_f^{1/2}$ with:

$$R_H^{2/3} = \left(\frac{A}{\mathcal{B} + 2D}\right)^{2/3} = \frac{D^{2/3}}{(1 + 2D/\mathcal{B})^{2/3}} \underbrace{\cong}_{D/\mathcal{B} << 1} D^{2/3} \tag{2.49}$$

In the presence of wetting and drying the latter expression changes as:

$$R_H^{2/3} = \int_{-\infty}^{h} \left(\frac{H - z_b}{1 + 2(H - z_b/\mathcal{B})} \right)^{2/3} \frac{\partial \Psi}{\partial z}\, dz \cong \int_{-\infty}^{h} (h - z_b)^{2/3} \frac{\partial \Psi}{\partial z}\, dz \tag{2.50}$$

$$\mathcal{A} = \int_{-\infty}^{h} (h - z_b) \frac{\partial \Psi}{\partial z}\, dz \tag{2.51}$$

namely

$$R_H^{2/3} \cong \Phi_{(2/3)}, \tag{2.52}$$

Moreover,

$$\mathcal{A} \cong \mathcal{B}\, \Phi_{(1)} \tag{2.53}$$

while the flow discharge is:

$$Q = \int_{-\infty}^{h} k_s\, (h - z_b)^{2/3}\, S_f^{1/2} \mathcal{B}(h - z_b) \frac{\partial \Psi}{\partial z}\, dz$$

namely

$$Q = \mathcal{B}\, k_s\, \Phi_{(5/3)}\, S_f^{1/2} \tag{2.54}$$

In the case of a compound cross section, the uniform flow velocity within the overall cross section is $U = k_{s,eq}\, R_H^{2/3}\, S_f^{1/2}$ while that corresponding to the $i-$th sub-section is $U = k_{si}\, R_{Hi}^{2/3}\, S_f^{1/2}$, with $k_{s,eq}$ and k_{si} the corresponding values of the Gauckler-Strickles roughness coefficient. Hence, the overall discharge can be written as:

$$Q = k_{s,eq}\, \mathcal{A}\, R_H^{2/3}\, S_f^{1/2} = \sum_i k_{si}\, R_{Hi}^{2/3}\, S_f^{1/2} \tag{2.55}$$

Assuming that the energy slope keeps constant across the section, the overall (equivalent) friction coefficient $k_{s,eq}$ reads:

$$k_{s,eq} = \frac{\sum_i k_{si}\, \mathcal{A}_i\, R_{Hi}^{2/3}}{\mathcal{A}\, R_H^{2/3}} \tag{2.56}$$

In the case of wetting and drying, the above relations need to be modified as follows:

$$Q = k_{s,eq}\, \mathcal{B}_T\, \Phi_{(5/3)} = \sum_1^3 k_{si}\, R_{Hi}^{2/3}\, S_f^{1/2}$$

Hence:

$$
\begin{aligned}
k_{s,eq}\,\mathcal{B}_T\,\Phi_{(5/3)} &= \int_{-\infty}^{h} \sum k_{si}\,\underbrace{R_{Hi}^{2/3}}_{\mathcal{A}_i^{5/3}/c_i}\,\frac{\partial \Psi}{\partial z}\,dz = \sum_1^3 k_{si}\,\mathcal{B}_i^{5/3} \int_{-\infty}^{h} \frac{(h-z_b)^{5/3}}{c_i^{2/3}}\,\frac{\partial \Psi}{\partial z}\,dz \\
&= k_s \left\{ \mathcal{B}^{5/3} \int_{-\infty}^{h} \frac{(h-z_b)^{5/3}}{\mathcal{B}^{2/3}} \frac{\partial \Psi}{\partial z}\,dz \right. \\
&\left. + 2\left(\frac{\mathcal{B}_T-\mathcal{B}}{2}\right)^{5/3} \int_{-\infty}^{h} \frac{(h-z_b)^{5/3}}{\left[(\mathcal{B}_T-\mathcal{B})/2+(h-z_b)\right]^{2/3}} \frac{\partial \Psi}{\partial z}\,dz \right\} \\
&= k_s \left\{ \mathcal{B}\,\Phi_{(5/3)} + (\mathcal{B}_T-\mathcal{B}) \int_{-\infty}^{h} \frac{(h-z_b)^{5/3}}{\left[1+(h-z_b)/(\mathcal{B}_T-\mathcal{B})\right]^{2/3}} \frac{\partial \Psi}{\partial z}\,dz \right\}
\end{aligned}
$$

and, if $\underbrace{2\,(h-z_b)}_{D} \ll \mathcal{B}_T - \mathcal{B}$:

$$
\begin{aligned}
k_{s,eq}\,\mathcal{B}_T\,\Phi_{(5/3)} &= k_s\left[\mathcal{B}\,\Phi_{(5/3)} + (\mathcal{B}_T-\mathcal{B})\,\Phi_{(5/3)}\right] \\
&= k_s\,\mathcal{B}_T\,\Phi_{(5/3)}
\end{aligned}
$$

i.e.,

$$
k_{s,eq} = k_s
$$

In other words, when $2\,(h-z_{bi}) \ll \mathcal{B}_T - \mathcal{B}$, we can write:

$$
k_{s,eq}\,\mathcal{B}_T\,\Phi_{(5/3)} = \sum_1^3 k_{si}\,\mathcal{B}_i\,\Phi_{i(5/3)}
$$

and, hence:

$$
k_{s,eq} = \frac{\sum_1^3 k_{si}\,\mathcal{B}_i\,\Phi_{i(5/3)}}{\mathcal{B}_T\,\Phi_{(5/3)}} \tag{2.57}
$$

In conclusion, the friction term:

$$
\frac{c\,\tau_b}{\varrho} = g\,\frac{\mathcal{A}}{c}\,S_f\,c = g\,\mathcal{A}\,S_f \tag{2.58}
$$

can be computes estimating S_f considering the contribution to resistance of the entire section (main channel and lateral tidal flats):

$$
S_f = \frac{Q\,|Q|}{\left[k_{s,eq}\,\mathcal{A}^{5/3}/c^{2/3}\right]}, \qquad \mathcal{A} = \sum_1^3 \mathcal{A}_i \tag{2.59}
$$

with $\mathcal{A}$ the total cross section and c the corresponding wetted perimeter.

2.3.2 Phase-averaged Coriolis factors

The phase-averaged Coriolis coefficient in (2.13) turns in [Defina, 2000]:

$$\beta_{cor} = \frac{\int_{-\mathcal{B}_R}^{\mathcal{B}_L} dy \int_{\eta}^{h} \left(\frac{U}{\Psi_h}\right)^2 dz}{\mathcal{A}\, U^2}. \tag{2.60}$$

In a compact cross section the velocity is uniform ($u_x \cong U$) and, as a consequence, the correction coefficient $\beta_{cor} \sim 1$. Conversely, in a compound cross section, instead of performing the cumbersome computations in (2.60), an heuristic approach is used to approximate the correction coefficient as follows:

$$\beta_{cor} = \frac{\mathcal{A}_T}{K_T^2}\left(\frac{K_{ch}^2}{\mathcal{A}} + \frac{K_{tf}^2}{\mathcal{A}_{tf}}\right) \tag{2.61}$$

where $\mathcal{A}_T$, K_T, K_{ch}, $\mathcal{A}$, K_{tf}, $\mathcal{A}_{tf}$ are phase-averaged variables whose values are shown in the following section. Using this procedure the coefficient β_{cor} ranges between 1.0 and 1.15 as commonly reported in literature [Henderson, 1966].

2.3.3 Phase-averaged one dimensional equations

Let us consider a generally compound cross section in which wetting and drying phenomena may affect both the lateral tidal flats and main channel (Figure 2.6). A phase-averaged version of the governing equations (2.30) and (2.31) (with $\mathcal{F} = 0$) has to be used, similarly to [Lanzoni and Seminara, 2002]. However, the functions Ψ_h, D, and Φ_h derived above to deal with wetting and drying have to be defined for both the tidal flats and the main channel, choosing the appropriate bed elevation z_b. Eventually, the storage coefficient r_s, the channel cross-sectional area $\mathcal{A}$ and the overall conveyance K_T take the expressions reported in Table 2.1, where the corresponding relationships for a compact cross section are also shown.

Recalling that the coefficient r_s accounts for the storage capacity of the lateral intertidal areas, we note that when the floodplains are dry ($D_{tf} \approx e_s$), this additional storage capacity vanishes and r_s is equal to 1. Conversely, when the intertidal areas are flooded ($D_{tf} >> e_s$), the value of r_s is greater than 1 implying that the whole cross section contributes to the mass balance. Wetting and drying effects on intertidal areas are embedded in r_s through $\Psi_{h,tf}$ and $\Psi_{h,ch}$. Conversely, these intertidal areas have no effects in the momentum equation, since the additional storage they provide is assumed to be made of still water. On the other hand, wetting

Compact	*Compound*
$r_s = 1$	$r_s = \Psi_{h,ch}\left(1 + \frac{\Psi_{h,tf}}{\Psi_{h,ch}}\frac{\mathcal{B}_T - \mathcal{B}}{\mathcal{B}}\right)$
$\mathcal{A} = \mathcal{B}_T D_{ch}$ $\mathcal{A}_{tf} = 0$ $\mathcal{A}_T = \mathcal{A} + \mathcal{A}_{tf}$	$\mathcal{A} = \mathcal{B} D_{ch}$ $\mathcal{A}_{tf} = (\mathcal{B}_T - \mathcal{B}) D_{tf}$ $\mathcal{A}_T = \mathcal{A} + \mathcal{A}_{tf}$
$K = k_{s,ch}\mathcal{B}\Phi_{h,ch}$ $K_{tf} = 0$ $K_T = K_{ch} + K_{tf}$	$K = k_{s,ch}\mathcal{B}\Phi_{h,ch}$ $K_{tf} = k_{s,tf}(\mathcal{B}_T - \mathcal{B})\Phi_{h,tf}$ $K_T = K_{ch} + K_{tf}$
$\beta_{cor} = 1$	$\beta_{cor} = \frac{\mathcal{A}_T}{K_T^2}\left(\frac{K_{ch}^2}{\mathcal{A}} + \frac{K_{tf}^2}{\mathcal{A}_{tf}}\right)$

Table 2.1: Compact and compound cross section coefficients.

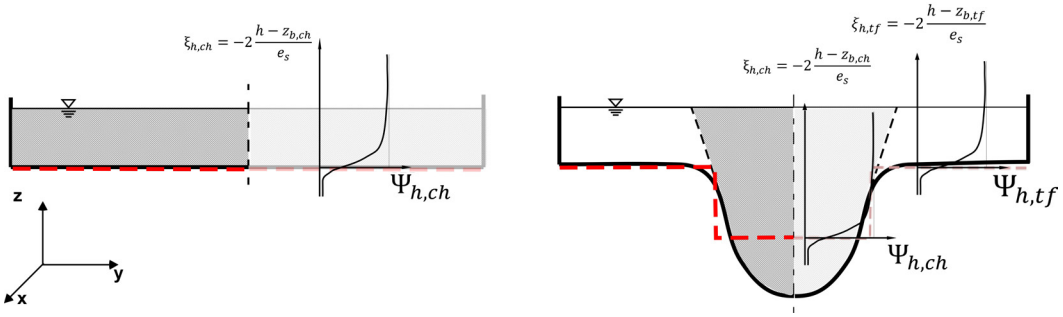

Figure 2.6: Wetting and drying approach applied to compact and compound cross sections.

and drying can affect the conveyance K_T appearing in the momentum equation, allowing the friction to significantly increase for small or negative depths.

2.3.4 The numerical scheme of 1D shallow water equations

The system of PDEs (2.30) and (2.31) (with $\mathcal{F} = 0$) is solved using the Preissman method, an implicit finite difference scheme. The Preissman method is based on approximating each term of the PDEs by a weighted average on a four-point box, whereby a given variable f and its derivatives are discretized as follows (Figure 2.7, Abbott and Basco [1989]; Cunge et al. [1980]):

$$f(x,t) = (1-\nu)[(1-\theta)f_j^n + \theta f_j^{n+1}] + \nu[(1-\theta)f_{j+1}^n + \theta f_{j+1}^{n+1}] \tag{2.62}$$

$$\frac{\partial f(x,t)}{\partial x} = (1-\theta)\frac{f_{j+1}^n - f_j^n}{\Delta x} + \theta\frac{f_{j+1}^{n+1} - f_j^{n+1}}{\Delta x} \tag{2.63}$$

$$\frac{\partial f(x,t)}{\partial t} = (1-\nu)\frac{f_j^{n+1} - f_j^n}{\Delta t} + \nu\frac{f_{j+1}^{n+1} - f_{j+1}^n}{\Delta t} \tag{2.64}$$

Here, θ and ν are time and space weighting coefficients, respectively, subscript indexes denote spatial nodes and superscript indexes represent time steps.

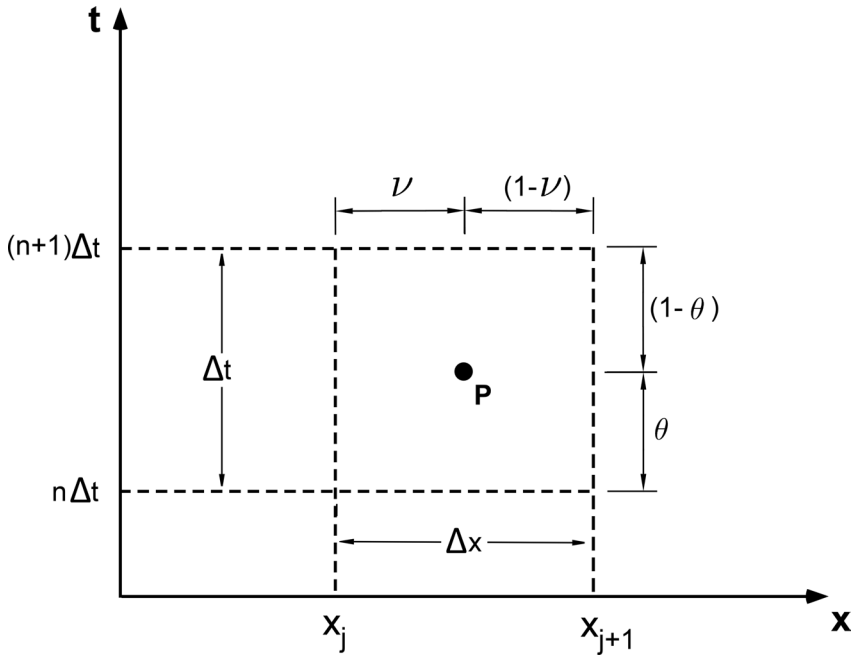

Figure 2.7: Four point box scheme

Crucial to the model stability is how inertial and resistance terms are discretized. Following Verwey's variant of Preissman scheme [Cunge et al., 1980; Gibbons, 1986], those terms are treated as follows:

$$\frac{\partial}{\partial x}\left(\beta_{cor}\frac{Q^2}{\mathcal{A}}\right) \approx \frac{1}{\Delta x}\left(\beta_{cor,j+1}^{n+1/2}\frac{Q_{j+1}^{n}Q_{j+1}^{n+1}}{\mathcal{A}_{j+1}^{n+1/2}} - \beta_{cor,j}^{n+1/2}\frac{Q_{j}^{n}Q_{j}^{n+1}}{\mathcal{A}_{j}^{n+1/2}}\right) \tag{2.65}$$

$$\frac{Q|Q|}{K_T^2} \approx \frac{1}{2}\left[\frac{|Q_{j+1}^{n}|Q_{j+1}^{n+1}}{(K_{T,j+1}^{n+1/2})^2} + \frac{|Q_{j}^{n}|Q_{j}^{n+1}}{(K_{T,j}^{n+1/2})^2}\right] \tag{2.66}$$

$$\mathcal{A} \approx \frac{\mathcal{A}_{j+1}^{n+1/2} + \mathcal{A}_{j}^{n+1/2}}{2} \tag{2.67}$$

$$\mathcal{B} \approx \frac{\mathcal{B}_{j+1}^{n+1/2} + \mathcal{B}_{j}^{n+1/2}}{2} \tag{2.68}$$

$$r_s \approx \frac{r_{s,j+1}^{n+1/2} + r_{s,j}^{n+1/2}}{2} \tag{2.69}$$

On substituting these approximations into the continuity equation (2.30) leads to:

$$\begin{aligned}&\nu\,\mathcal{B}\,r_s\,\frac{h_{j+1}^{n+1} - h_{j+1}^{n}}{\Delta t} + (1-\nu)\,\mathcal{B}\,r_s\frac{h_{j}^{n+1} - h_{j}^{n}}{\Delta t}\\ &+\theta\,\frac{Q_{j+1}^{n+1} - Q_{j}^{n+1}}{\Delta x} + (1-\theta)\,\frac{Q_{j+1}^{n} - Q_{j}^{n}}{\Delta x} = 0\end{aligned} \tag{2.70}$$

Grouping the variables at time $n+1$ on the left hand side of the equation, multiplying by Δx and rearranging, the discretized continuity equation becomes:

$$A1_j\, Q_j^{n+1} + B1_j\, h_j^{n+1} + C1_j\, Q_{j+1}^{n+1} + D1_j\, h_{j+1}^{n+1} = E1_j \tag{2.71}$$

where

$$\begin{aligned}
A1_j &= -\theta \\
B1_j &= (1-\nu)\mathcal{B}r_s\frac{\Delta x}{\Delta t} \\
C1_j &= \theta \\
D1_j &= \nu\mathcal{B}r_s\frac{\Delta x}{\Delta t} \\
E1_j &= (1-\theta)\,(Q_j^n - Q_{j+1}^n) + B1_j h_j^n + D1_j h_{j+1}^n
\end{aligned}$$

On the other hand, the discretization of the momentum equation (2.31) equations implies:

$$\begin{aligned}
&\nu\,\frac{Q_{j+1}^{n+1}-Q_{j+1}^n}{\Delta t} + (1-\nu)\,\frac{Q_j^{n+1}-Q_j^n}{\Delta t} + \left[\beta_{cor,j+1}^{n+1/2}\,\frac{Q_{j+1}^n\,Q_{j+1}^{n+1}}{\mathcal{A}_{j+1}^{n+1/2}} - \beta_{cor,j}^{n+1/2}\,\frac{Q_j^n\,Q_j^{n+1}}{\mathcal{A}_j^{n+1/2}}\right]\frac{1}{\Delta x} \\
&+ g\,\mathcal{A}\,\frac{\theta(h_{j+1}^{n+1}-h_j^{n+1}) + (1-\theta)(h_{j+1}^n - h_j^n)}{\Delta x} + \frac{g\,\mathcal{A}}{2}\left[\frac{|Q_{j+1}^n|Q_{j+1}^{n+1}}{(K_{T,j+1}^{n+1/2})^2} + \frac{|Q_j^n|Q_j^{n+1}}{(K_{T,j}^{n+1/2})^2}\right] = 0
\end{aligned} \tag{2.72}$$

Grouping the variables at time $n+1$ on the left hand side of the equation, multiplying by Δx and rearranging, the discretized form of the momentum equation becomes:

$$A2_j\, Q_j^{n+1} + B2_j\, h_j^{n+1} + C2_j\, Q_{j+1}^{n+1} + D2_j\, h_{j+1}^{n+1} = E2_j \tag{2.73}$$

where

$$\begin{aligned}
A2_j &= (1-\nu)\,\frac{\Delta x}{\Delta t} - \beta_{cor,j}^{n+1/2}\,\frac{Q_j^n}{\mathcal{A}_j^{n+1/2}} + \frac{g\mathcal{A}}{2}\,\frac{|Q_j^n|}{(K_{T,j}^{n+1/2})^2}\,\Delta x \\
B2_j &= -g\,\theta\,\mathcal{A} \\
C2_j &= \nu\,\frac{\Delta x}{\Delta t} + \beta_{cor,j+1}^{n+1/2}\,\frac{Q_{j+1}^n}{\mathcal{A}_{j+1}^{n+1/2}} + \frac{g\,\mathcal{A}}{2}\,\frac{|Q_{j+1}^n|}{(K_{T,j+1}^{n+1/2})^2}\,\Delta x \\
D2_j &= -B2_j \\
E2_j &= \frac{\Delta x}{\Delta t}[(1-\nu)\,Q_j^n + \nu Q_{j+1}^n] - (1-\theta)\,g\,\mathcal{A}\,(h_{j+1}^n - h_j^n)
\end{aligned}$$

In domain discretized by means of M cross sections, a system composed by

$2M-2$ equations in $2M$ unknowns is obtained:

$$\begin{bmatrix} L_1 & L2 & & & & & \\ A1_1 & B1_1 & C1_1 & D1_1 & & & \\ A2_1 & B2_1 & C2_1 & D2_1 & & & \\ & \ddots & \ddots & \ddots & \ddots & & \\ & & \ddots & \ddots & \ddots & \ddots & \\ & & & A1_{M-1} & B1_{M-1} & C1_{M-1} & D1_{M-1} \\ & & & A2_{M-1} & B2_{M-1} & C2_{M-1} & D2_{M-1} \\ & & & & & R_1 & R2 \end{bmatrix} \begin{bmatrix} Q_1^{n+1} \\ h_1^{n+1} \\ Q_2^{n+1} \\ \vdots \\ \vdots \\ h_{M-1}^{n+1} \\ Q_M^{n+1} \\ h_M^{n+1} \end{bmatrix} = \begin{bmatrix} L_3 \\ E1_1 \\ E2_1 \\ \vdots \\ \vdots \\ E1_{M-1} \\ E2_{M-1} \\ R_3 \end{bmatrix} \tag{2.74}$$

where $L_1\,Q_1^{n+1} + L_2\,h_1^{n+1} = L_3$ and $R_1\,Q_1^{n+1} + R_2\,h_1^{n+1} = R_3$ are the boundary conditions at the landward and seaward ends, respectively, necessary for defining a well-posed problem.

Setting both the weighting coefficients θ and ν equal 0.5, the finite difference approximation is equivalent to a centered-difference scheme of second order accuracy [Cunge et al., 1980]. However, for Courant number C_r ($c\Delta t/\Delta x$) greater than 1, spurious oscillations may appear in the solution. Setting θ between 0.6 and 1.0 avoids this inconvenience [Abbott and Basco, 1989]. In all runs, the time weighting coefficient θ has been set equal to 0.7, while space weighting coefficient equal to 0.5.

An important quantity to be discretized is the energy slope S_f which, as it will be seen in Chapter 4, plays a fundamental role in determining the shape of cross sections. It can be computed using different averaging methods [French, 1986], such as arithmetic mean, geometric mean, harmonic mean, and conveyance mean. Even considering a 1D steady, gradually varied flow, different averaging methods can give different approximations, depending on the test case considered [Artichowicz and Mikos-Studnicka, 2014; Artichowicz and Prybytak, 2015]. For a drop-down profile, the harmonic mean fits better; conversely, for a backwater curve, the more suitable averaging technique is the conveyance average. Finally, for the spillway case, the arithmetic average performs better. For these reasons in the HEC-RAS code the energy slope is averaged differently along the channel depending on the investigated water surface profile [USACE, 2016].

Since it will be cumbersome to implement energy slope computations depending on the hydraulic conditions, here S_f is computed by using the conveyance mean, implemented in the four point Preissman box as [Wu, 2008]:

$$S_f = \left\{ \frac{(1-\nu)\left[(1-\theta)\,Q_j^n + \theta\,Q_j^{n+1}\right] + \nu\left[(1-\theta)\,Q_{j+1}^n + \theta\,Q_{j+1}^{n+1}\right]}{(1-\nu)\left[(1-\theta)\,K_{T,j}^n + \theta K_{T,j}^{n+1}\right] + \nu\left[(1-\theta)\,K_{T,j+1}^n + \theta\,K_{T,j+1}^{n+1}\right]} \right\}^2 \tag{2.75}$$

2.3.5 Modeling flow transitions

The mathematical problem provided by the PDEs (2.30) and (2.31), subject to the upstream and downstream boundary conditions (2.35) is well-posed only for sub-critical flow conditions. Indeed, for super-critical flows two conditions must be applied at the upstream boundary. On the other hand, when a transition is encountered in the domain, the external boundary conditions result in being too many or not enough making the problem ill-posed. In the transition from supercritical to subcritical, for example, two conditions are needed upstream and one condition is required downstream for a total of three boundary conditions. Differently, in the transition from subcritical to supercritical, one condition has to be set upstream and none downstream. Meselhe and Holly Jr. [1997] have shown by linear stability analysis that Preissman scheme is marginally stable when the flow is approaching critical conditions. Nevertheless, the simplicity retained in this bi-diagonal implicit finite difference scheme has encouraged several authors to find adaptations to the method suitable for transcritical flows [Freitag and Morton, 2007; Johnson et al., 2002; Sart et al., 2010]. The key idea of these adaptations applied to equations (2.30) and (2.27) consists of introducing internal boundary conditions in each section depending on the local direction of characteristics. Despite the changes, the algebraic system to be solved keeps the simple diagonal form, typical of Preissman discretization, but allows one to handle flow transitions without suffering from instability. This approach avoids tracking of the critical interfaces in the domain to include internal conditions.

Another practical approach for achieving stability of the classical Preissman scheme when transcritical flows occur consists of reducing or dropping selectively the convective term (or the whole inertia term) in the momentum equation. The Local Partial Inertia (LPI) filter, developed by Fread et al. [1996], introduces a γ coefficient that multiplies the convective term in the momentum equation (2.31), defined as:

$$\gamma = \begin{cases} 1 - F_r^m & F_r > F_{rm} \\ 0 & F_r \leq F_{rm} \end{cases} \tag{2.76}$$

where F_r is the Froude number, F_{rm} and m are tuning parameters. The parameter F_{rm} is the Froude number threshold over which the inertia is dropped, while m is the parameter that drives the magnitude of the inertia reduction when the Froude number is below the threshold (Figure 2.8). The closer F_r is to F_{rm}, the greater is the inertia reduction. Well known 1D models, such as MIKE11 [DHI, 2017a] and HEC-RAS [USACE, 2016], have implemented LPI filter to deal robustly with internal transitions. Here we follow this practical approach and set $F_{rm} = 1$ and

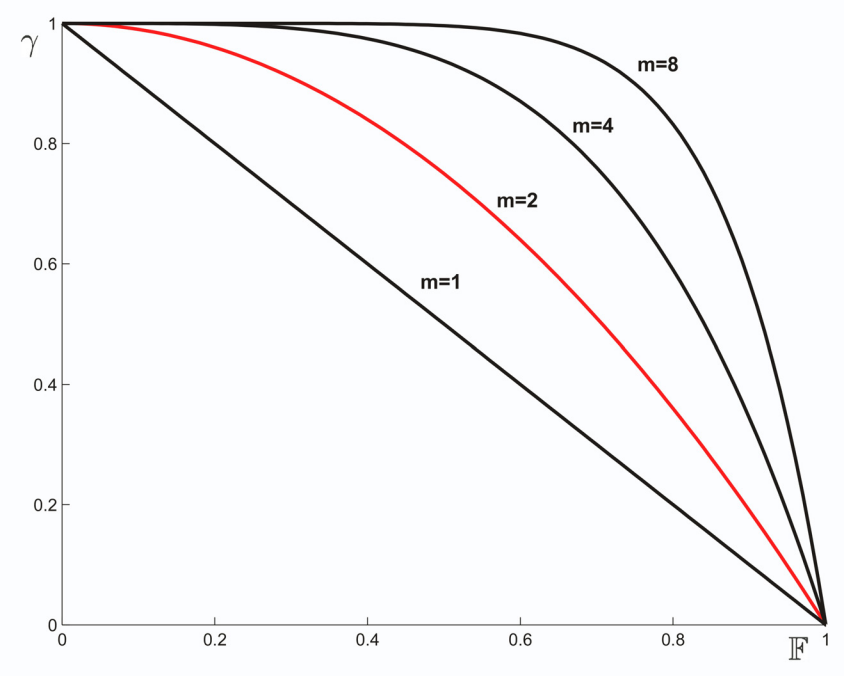

Figure 2.8: The LPI Filter [Fread et al., 1996].

$m = 2$. Besides the LPI filter, to ensure stability to the model, some care must be paid to treat geometry discontinuities, such as the transition from a compound to a compact cross section. This is for example the case (Figure 2.9) of a main channel that undergoes a progressive deepening due to the concomitant aggradation of the intertidal areas flanking it. As a result, the main channel head, characterized by a compound section, tends to merge with the compact cross section of the landward intertidal region.

The discontinuity when easily detectable can be handled by means of interior boundary conditions whereby the discretized equations (2.71) and (2.73) are substituted by compatibility conditions. One of this conditions ensures the mass continuity; the other may specify the water stage or the energy grade line [Cunge, 1975]. Typical examples are as follows.

- Abrupt change in the cross section (Figure 2.10):

  a) $Q_j = Q_{j+1}$

  b) $h_j + \alpha_{cor,j} Q_j/(2\,g\,A_j) = h_{j+1} + \alpha_{cor,j} Q_{j+1}/(2\,g\,A_{j+1})$ neglecting head loss, or simply $h_j = h_{j+1}$ [2]

- Free flow weir separating a given channel reach into two independent parts:

[2] $\alpha_{cor,j+1}$ is a correction (Coriolis) coefficient which represents the ratio between the actual kinetic energy of the stream and the kinetic energy of a stream characterized by the same cross sectional area and a constant velocity distribution equal to the cross sectionally averaged speed

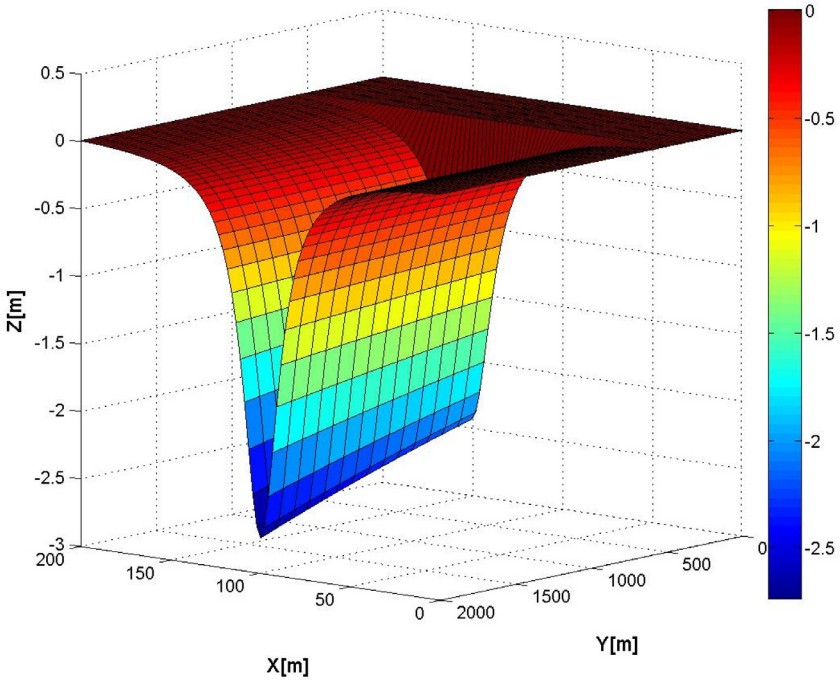

Figure 2.9: A bathymetry with an abrupt change in the cross section.

a) $Q_j = Q_{j+1}$

b) none

- Submerged weir;

a) $Q_j = Q_{j+1}$

b) $f(h_j, h_{sill}, h_{j+1}) = 0$

Specifically, in the case of an abrupt change in the cross section, the above internal conditions, discretized using the Preissman approach, lead to:

$U = Q/A$ of the actual stream. Hence:

$$\alpha_{cor} = \frac{\int_{-\mathcal{B}_R}^{\mathcal{B}_L} dy \int_{\eta}^{h} U^3 \, dz}{A \ \mathcal{U}^3}. \tag{2.77}$$

The coefficient α_{cor} is equal to 1 in a compound cross section, while in a compound cross section, by analogy with β_{cor}, is computed as follows:

$$\alpha_{cor} = \frac{\mathcal{A}_T}{K_T^3} \left(\frac{K_{ch}^3}{\mathcal{A}} + \frac{K_{tf}^3}{\mathcal{A}_{tf}} \right) \tag{2.78}$$

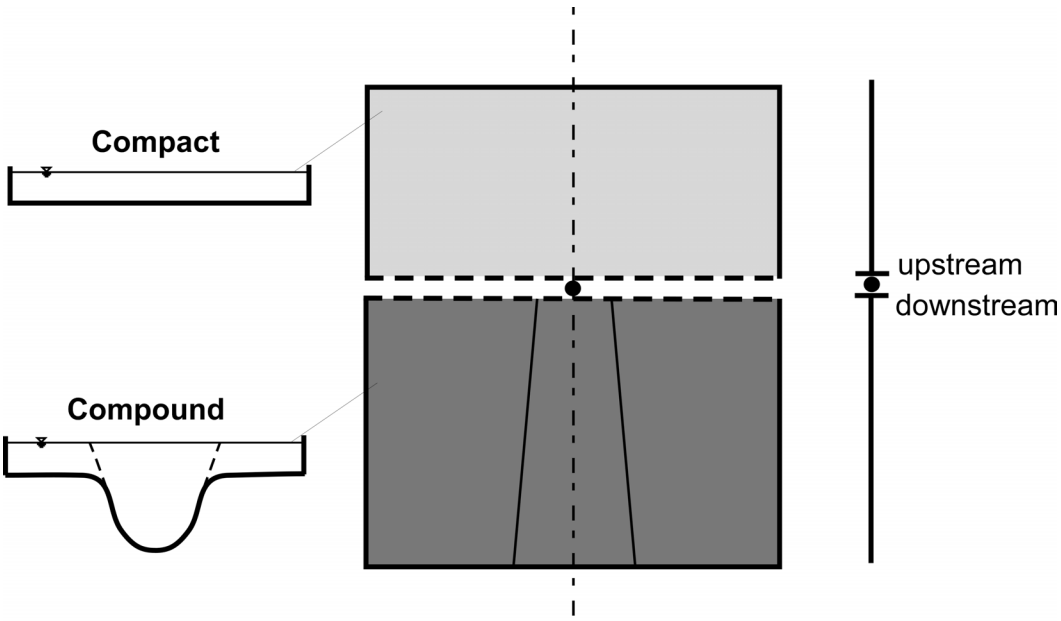

Figure 2.10: Abrupt change of width.

$$(1-\theta)\,Q_j^n + \theta\,Q_j^{n+1} = (1-\theta)\,Q_{j+1}^n + \theta\,Q_{j+1}^{n+1} \tag{2.79}$$

$$(1-\theta)\,h_j^n + \theta\,h_j^{n+1} + \frac{\alpha_{cor,j}^{n+1/2}}{2g}\,\frac{|Q_j^n|\,Q_j^{n+1}}{(\mathcal{A}_{j+1}^{n+1/2})^2} \tag{2.80}$$

$$= (1-\theta)\,h_{j+1}^n + \theta\,h_{j+1}^{n+1} + \frac{\alpha_{cor,j+1}^{n+1/2}}{2g}\,\frac{|Q_{j+1}^n|\,Q_{j+1}^{n+1}}{(\mathcal{A}_{j+1}^{n+1/2})^2}$$

Grouping together the variables at time $n+1$ on the left hand side of the equation, these algebraic equations become:

$$A1_j\,Q_j^{n+1} + B1_j\,h_j^{n+1} + C1_j\,Q_{j+1}^{n+1} + D1_j\,h_{j+1}^{n+1} = E1_j \tag{2.81}$$

$$A2_j Q_j^{n+1} + B2_j h_j^{n+1} + C2_j Q_{j+1}^{n+1} + D2_j h_{j+1}^{n+1} = E2_j \tag{2.82}$$

where

$$
\begin{aligned}
A1_j &= -\theta \\
B1_j &= 0 \\
C1_j &= \theta \\
D1_j &= 0 \\
E1_j &= (1-\theta)\,(Q_j^n - Q_{j+1}^n) \\
A2_j &= -\frac{\alpha_{cor,j}^{n+1/2}}{2g}\,\frac{|Q_j^n|}{(\mathcal{A}_j^{n+1/2})^2} \\
B2_j &= -\theta \\
C2_j &= \frac{\alpha_{cor,j+1}^{n+1/2}}{2g}\,\frac{|Q_{j+1}^n|}{(\mathcal{A}_{j+1}^{n+1/2})^2} \\
D2_j &= -B2_j \\
E2_j &= (1-\theta)\,(h_j^n - h_{j+1}^n)
\end{aligned}
$$

However, when the basin bathymetry is evolving in a long term simulation, the discontinuity could not be easy to localize and thus using internal boundary conditions may become cumbersome to implement. Hence, despite the approximation introduced, the LPI filter is a preferable option since it can be applied in all the domain without the need to detect, classify and treat the discontinuity with suitable internal boundary conditions.

2.3.6 Double-sweep method

The set of algebraic equations (2.71) and (2.73) implies a tridiagonal system than can be solved using an iterative procedure such as the double sweep method (or Thomas algorithm). This algorithm can be set up making a first sweep from seaward to landward and then a second sweep from landward to seaward (or inverting the direction of both the steps). In present applications, the first procedure was implemented.

1st sweep: from seaward to landward - 2nd sweep: from landward to seaward

The double sweep method is based on this initial relation:

$$Q_j^{n+1} = F_j\, h_j^{n+1} + G_j \tag{2.83}$$

where F_j and G_j are variables whose values are determined later. By substituting the relation (2.83) in (2.71) and (2.73), we obtain:

$$(B2_j + A2_j\, F_j)\, h_j^{n+1} + C2_j\, Q_{j+1}^{n+1} + D2_j\, h_{j+1}^{n+1} = E2_j - A2_j\, G_j \tag{2.84}$$

From the first equation, it is straightforward to derive h_j^{n+1}:

$$h_j^{n+1} = H_j\, Q_{j+1}^{n+1} + I_j\, h_{j+1}^{n+1} + J_j \tag{2.85}$$

where H_j, I_j, J_j are defined as follows:

$$H_j = -\frac{C1_j}{B1_j + A1_j\, F_j}, \quad I_j = -\frac{D1_j}{B1_j + A1_j\, F_j}, \quad J_j = \frac{E1_j - A1_j\, G_j}{B1_j + A1_j\, F_j} \tag{2.86}$$

To eliminate h_i^{n+1}, we multiply equation (2.84) by $(B2_j + A2_j F_j)$ and, viceversa, equation (2.84) by $(B1_j + A1_j F_j)$ and subtract them side by side:

$$\begin{aligned}[C1_j\,(B2_j + A2_j\, F_j) - C2_j\,(B1_j + A1_j\, F_j)]Q_{j+1}^{n+1} \\ + [D1_j\,(B2_j + A2_j\, F_j) - D2_j\,(B1_j + A1_j\, F_j)]h_{j+1}^{n+1} \\ = (B2_j + A2_j\, F_j)(E1_j - A1_j\, G_j) - (B1_j + A1_j\, F_j)(E2_j - A2_j\, G_j)\end{aligned} \tag{2.87}$$

From the previous equation, putting $\varepsilon_j = (B1_j + A1_j\, F_j)$, it follows:

$$Q_{j+1}^{n+1} = -\frac{\varepsilon_j\, I_j + D2_j}{\varepsilon_j\, H_j + C2_j}\, h_{j+1}^{n+1} + \frac{E2_j - A2_j\, G_j - \varepsilon_j\, J_j}{\varepsilon_j\, H_j + C2_j} \tag{2.88}$$

and:

$$F_{j+1} = -\frac{\varepsilon_j\, I_j + D2_j}{\varepsilon_j\, H_j + C2_j}, \qquad G_{j+1} = \frac{E2_j - A2_j\, G_j - \varepsilon_j\, J_j}{\varepsilon_j\, H_j + C2_j} \tag{2.89}$$

Equations (2.83) and (2.85) are used to compute upwardly values of F_j, G_j, H_j, J_j and I_j. The procedure consists of four steps:

- By the definition of the upstream boundary condition (j=0), G_0 and F_0 are computed;
- In the first sweep is upstrem-downstream and allows one to compute F_{j+1} and G_{j+1} (j=0,1,...,M-1) through (2.83) and H_j, J_j and I_j (j=1,...,M), using (2.85) and (2.86);
- By the definition of the upstream boundary condition (j=M), G_M and F_M are computed;

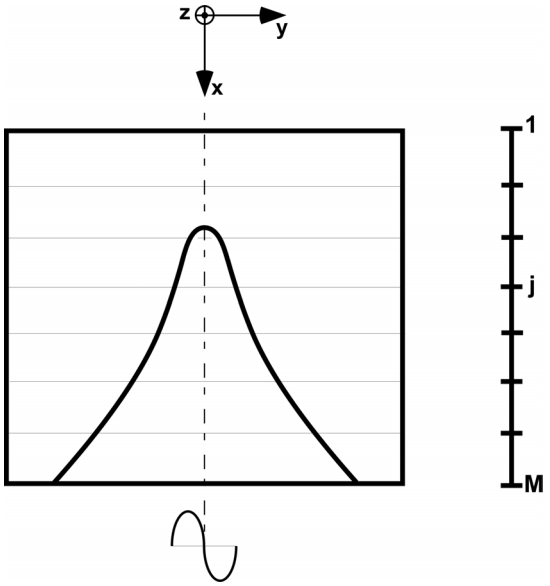

Figure 2.11: Different iterative procedure depending on the choice of first cross section.

- The second sweep is downstream-upstream, and allow one to determine the values of Q_j and h_j (j=M-1,M-2,...,1)

The coefficients F_1 and G_1 at the upstream boundary are computed as:

$$F_1 = \frac{L_2}{L_1}, \qquad G_1 = \frac{L_3}{L_1} \tag{2.90}$$

Since no-flux condition is imposed at the upstream boundary, $L_1 \neq 0$ while $L_2 = L_3 = 0$. Conversely, at the downstream boundary the stage condition leads the following relation:

$$h_M^{n+1} = \frac{R_3 - R_1\, G_M}{R_2 + R_1\, F_M} \tag{2.91}$$

Finally, after some algebra, we obtain $R_3 = H$, $R_1 = R_2 = 0$.

1st sweep: from landward to seaward - 2nd sweep: from seaward to landward

The double sweep method is based on this initial relation:

$$h_j^{n+1} = F_j\, Q_j^{n+1} + G_j \tag{2.92}$$

where F_j and G_j are variables to be determined later. By substituting (2.92) in (2.71) and (2.73) we obtain:

$$(A1_j + B1_j\, F_j)\, Q_j^{n+1} + C1_j\, Q_{j+1}^{n+1} + D1_j\, h_{j+1}^{n+1} = E1_j - B1_j\, G_j \tag{2.93}$$

From the first of the above equations, it is straightforward to obtain:

$$Q_j^{n+1} = -\frac{C1_j}{A1_j + B1_j\,F_j} Q_{j+1}^{n+1} - \frac{D1_j}{A1_j + B1_j\,F_j}\,h_{j+1}^{n+1} + \frac{E1_j - B1_j\,G_j}{A1_j + B1_j\,F_j}$$

$$h_j^{n+1} = H_j\,Q_{j+1}^{n+1} + I_j\,h_{j+1}^{n+1} + J_j \tag{2.94}$$

where H_j, I_j, J_j are defined as follows:

$$H_j = -\frac{C1_j}{A1_j + B1_j\,F_j}, \quad I_j = -\frac{D1_j}{A1_j + B1_j\,F_j}, \quad J_j = \frac{E1_j - B1_j\,G_j}{A1_j + B1_j\,F_j} \tag{2.95}$$

To eliminate Q_i^{n+1}, we multiply equation (2.93) by $(A2_j + B2_j\,F_j)$, equation 2.93 by $(A1_j + B1_j\,F_j)$ and subtract them side by side:

$$\begin{aligned}[C1_j\,(A2_j + B2_j\,F_j) - C2_j\,(A1_j + B1_j\,F_j)]Q_{j+1}^{n+1} \\ + [D1_j\,(A2_j + B2_j\,F_j) - D2_j\,(A1_j + B1_j\,F_j)]\,h_{j+1}^{n+1} \\ = (A2_j + B2_j\,F_j)(E1_j - B1_j\,G_j) - (A1_j + B1_j\,F_j)(E2_j - B2_j\,G_j)\end{aligned} \tag{2.96}$$

From the previous equation, setting $\varepsilon_j = (A1_j + B1_j\,F_j)$, h_{j+1}^{n+1} it follows:

$$h_{j+1}^{n+1} = -\frac{\varepsilon_j\,H_j + C2_j}{\varepsilon_j\,I_j + D2_j}\,Q_{j+1}^{n+1} + \frac{E2_j - B2_j\,G_j - \varepsilon_j\,J_j}{\varepsilon_j\,I_j + D2_j} \tag{2.97}$$

Moreover,

$$F_{j+1} = -\frac{\varepsilon_j\,H_j + C2_j}{\varepsilon_j\,I_j + D2_j}, \quad G_{j+1} = \frac{E2_j - B2_j\,G_j - \varepsilon_j\,J_j}{\varepsilon_j\,I_j + D2_j} \tag{2.98}$$

Equations (2.92) and (2.94) are used to compute upward the values of F_j, G_j, H_j, J_j and I_j. The procedure consists of four steps:

- By the definition of the downstream boundary condition (j=M), G_M and F_M are computed;
- In the first downstream-upstream sweep F_{j+1} and G_{j+1} (j=M-1,...,0) are evaluated through relation (2.83), H_j, J_j and I_j (j=M-1,...,1) using (2.85) and (2.86);
- By the definition of the downstream boundary condition (j=1), G_0 and F_0 are computed;
- The second upstream-downstream sweep allow one to determine the values of Q_j and h_j (j=1,...,M-2,M-1)

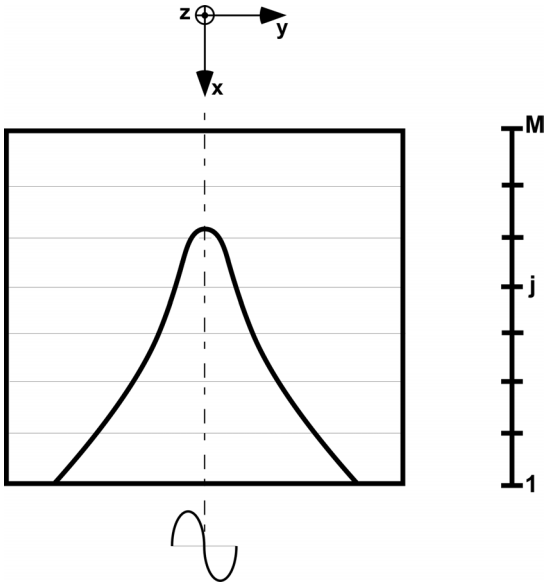

Figure 2.12: Different iterative procedure depending on the choice of first cross section.

The downstream the coefficients F_M and G_M are computed as:

$$F_M = \frac{R_2}{R_1}, \qquad G_M = \frac{R_3}{R_1} \tag{2.99}$$

Since a no-flux condition is imposed at the upstream boundary, $R_1 \neq 0$ while $R_2 = R_3 = 0$. Conversely, at the downstream boundary the stage condition leads to the following relation:

$$h_1^{n+1} = \frac{R_3 - R_1\, G_1}{R_2 + R_1\, F_1} \tag{2.100}$$

After some algebra, we finally obtain $R_3 = H$, $R_1 = R_2 = 0$.

2.4 Results

The robustness of the model has been tested by considering i) a tidal water front that propagates over a sloping beach and ii) the depletion of a 1D reservoir with a linearly sloping bed with an intermediate sawtooth-like berm. Both tests have been suggested by Balzano [1998] to evaluate the ability of a 1D model to account for wetting and drying processes.

In the first test the domain consists of a rectangular basin, 14 400 m wide, connected to the sea at one side and closed at the other sides. The domain is discretised through eleven cross sections, with a spacing of 1200 m. The time step used in the simulations is 600 s. Moreover, the Grauckler Strickler friction coefficient is set equal to 50 $m^{1/3}s^{-1}$. The tide at the seaward open boundary has an amplitude

of 2 m and a period of 43 200 s. Three slightly different bed configurations are investigated: a linearly sloping beach; a linearly sloping beach interrupted by an intermediate berm; a linearly sloping beach interrupted by an intermediate crooked (irregular) contour. Although these bed configurations do not allow for an analytical solution of the problem nor for experimental results to be used for comparison, the spatio-temporal variations of the water surface during flood and ebb phases offer the opportunity to evaluate whether the wetting and drying algorithm leads to possibly unphysical behaviors.

The panels reported in Figure 2.13 show flood and ebb water levels for the three beach profiles introduced above. In the first configuration (linearly sloping beach, upper panels), the water surface fall regularly during the ebb phase, with a wave front that recedes smoothly and bends slightly as low tide is approached. A similar behavior is evident also for the flood phase, except when the upper beach edge is approached, with a shoreline that tends to move forward irregularly. Note that the present treatment of wetting/drying, based on a sub-grid model that accounts for possible ground unevenness of mean amplitude e_s, the water level is computed also below the local mean elevation. In the presence of an intermediate berm (middle panels) the water surface rises and falls smoothly, without the wiggles, similarly to the previous case.

Finally, when a crooked (sawtooth-like) berm in inserted in the middle of a linearly sloping beach (lower panels), the free surface is only weakly affected by the presence of the bed irregularity. Indeed, the sawtooth-like berm has an amplitude comparable with that of e_s and, hence, cannot be detected by the sub-grid scale model set at the basis of the wetting/drying algorithm. Overall, the 1D model performance is satisfactory showing almost no wiggles in water levels in both flood and ebb phases.

The second test suggested by Balzano [1998], consists in the outflow from a 1D reservoir that starts from a water level of 2.0 m and lasts 100 h, having imposed a sinusoidal depletion downstream. The grid spacing is 1200 m, while the times step is 600 s. Four different values of the roughness parameter e_s has been considered: $e_s = 0.003$ m (upper left panel of Figure 2.14); $e_s = 0.3$ m (upper right panel of Figure 2.14); $e_s = 0.6$ m (lower left panel of Figure 2.14); $e_s = 2$ m (lower right panel of Figure 2.14). In all cases, the water surface does not feel the approaching bed until it reaches the lowest point of the crooked contour.

As e_s is increased, the curvature of the free surface progressively becomes negligible even when it encroaches the sawtooth-like berm. In order to let the free surface feel possible bed irregularities a value of $e_s = 0.3$ m is considered a good tradeoff between the need to ensure stable free surface solutions and the need to account for bed geometrical singularities.

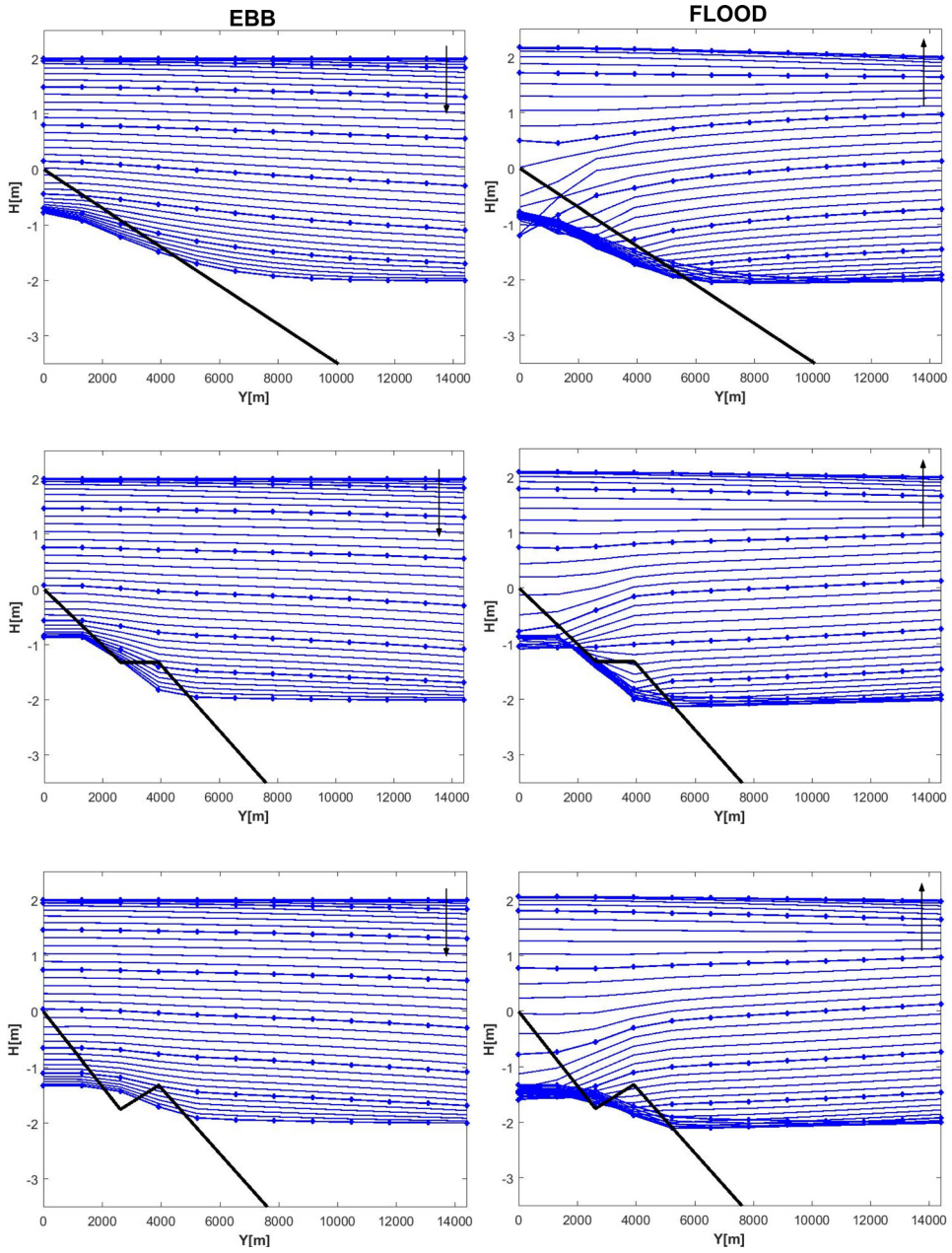

Figure 2.13: Water level oscillations on a linearly sloping beach with or without intermediate irregularities, as suggested by Balzano [1998]. Left panels: ebb phase; right panels: flood phase. Input data are: $\Delta x = 1200$ m, Δt=600 s, k_s=50 $m^{1/3}s^{-1}$, $a_0 = 2.0$ m, $T = 43\,200$ s. The roughness parameter e_s in equations (2.43), (2.44) has been set to 0.3 m. Thin lines denote water levels at every time step; thick lines correspond to water level plotted every 5 time steps (i.e., 50 min).

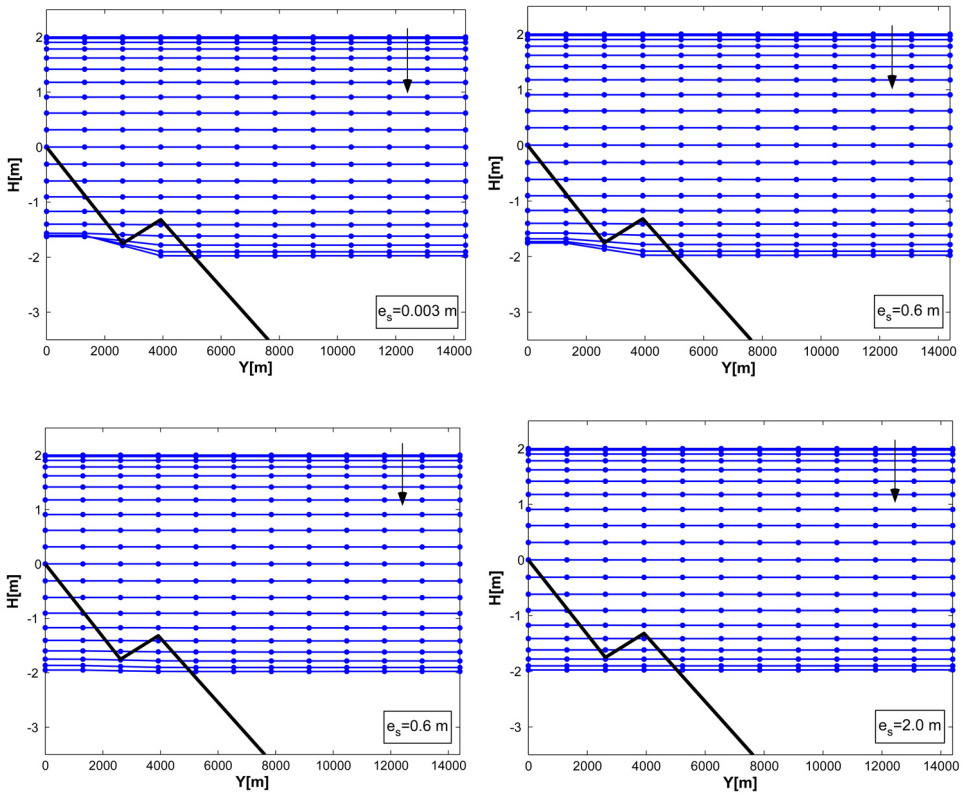

Figure 2.14: Outflow from a 1D basin with reservoir by sinusoidal depletion (reference case suggested in Balzano [1998]) for different e_s values from left to right 0.003, 0.3, 0.6, 2.0 m. These are the run input data: $\Delta x = 1200$ m, Δt=600 s, k_s=50 $m^{1/3}s^{-1}$, $a_0 = 2.0$ m, $T_{run} = 100$ h.

The 1D model was also used to simulate the tidal propagation on a rectangular basin, 200 m wide and 2000 m long. Three bed configurations were considered: a horizontal flat bed throughout the entire basin (Figure 2.15a); a convergent channel extending along the entire basin (Figure 2.15b); a convergent channel merging landward in a flat bed, thus implying a quite rapid change of cross-section geometry (Figure 2.15c). The bed elevation of the lateral boundaries in all the three cases is set at 0.0 m. The channel axis, when present, it tilted seawards with a 0.04% slope. The basin was discretised by using 21 cross sections with a spacing of 100 m. The Gauckler-Strickler friction coefficient was set to 30 $m^{1/3}s^{-1}$. The basin is closed at the landward and lateral boundaries, while the seaward boundary is subjected to a semi-diurnal tide of 0.5 m amplitude. The time-step used in the simulations is equal to 200 s.

The 1D model has been compared with a 2D model, FEM model developed at department ICEA in Padova (2DEF, Carniello et al. [2005]; Defina [2000]; Viero et al. [2013]), which uses 27 930 triangular elements to discretise the whole basin. The mesh is staggered and has a minimun element size of 1 m, and a maximum size of 20 m. The bed heights were assigned to elements automatically. Given 21 cross sections data points, a temporarily mesh was built and used to assign the elevations of each grid element of the staggered mesh. In both the 1D and 2D models, the roughness parameters e_s was set equal to 0.3 m (as suggested by the above tests). The application of the seaward boundary condition in the 2D model needs some explanation. Indeed, the tidal forcing was applied at the end of an additional sloping ramp, 100 m long, extending seaward beyond the last cross section of the 1D model. The aim is to ensure that in the 2D model the last row of elements is always wet, such that the wetting and drying processes gradually affect the tidal propagation. Conversely, in 1D hydrodynamics, it was preferred to multiply function $\Psi_{h,ch}$ for the tidal oscillation at the seaward cross section, as $\Psi_{h,ch}\, a_0 \cos \omega t$, to handle wetting and drying processes. This expedient avoids the use of an additional sloping ramp extending seaward that would have required adding other cross sections beyond the channel inlet.

The comparison between the two models is performed in terms of water levels, maximum velocity and shear stresses along the basin axis and discharges in some relevant cross sections. Additional results (see Appendix A) concern the effects on the three bathymetries of Figure 2.15 induced by the presence of tidal flats set at -0.45 m.

Figure 2.16 shows the comparison between the water oscillations computed by the present 1D model and the 2DEF at three cross sections: seaward, in the middle, and landward. For each cross section, the 2DEF water levels are monitored at the channel axis, at left lateral boundary and in the middle of the tidal flats. Obviously,

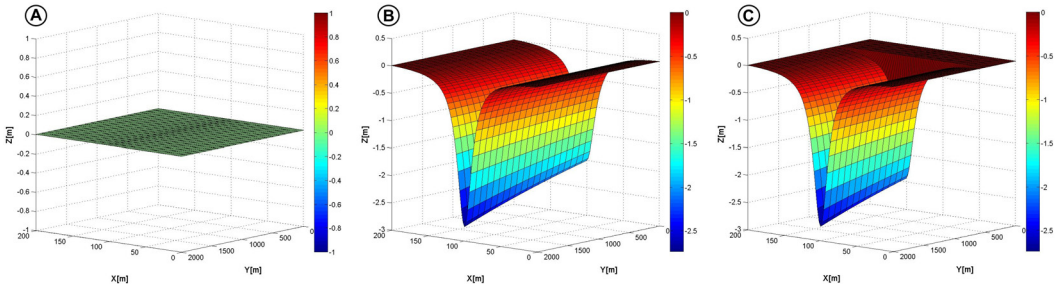

Figure 2.15: The three bathymetries used to test the present 1D model: a) channel with compact cross sections; b) channel with compound cross sections; c) channel with both compact and compound cross sections.

the 1D model provides only one cross sectional value of the water level. The flat bed topography leads to an overall 1D character of the flow. Indeed, the water levels computed by 2DEF are equal except when approaching the lateral boundary of the tidal domain (green lines) where the flow is forced to satisfy a non flux conditions for both the components of the velocity. The values of the free surface elevations at the channel axis and in the middle of the tidal flats are quite similar for both the models. Some differences are however observed at the seaward cross section, where the automatic procedure to assign height to each triangular element of the 2DEF leads to some small errors when estimating the water surface elevations. Overall, the initially sinusoidal tidal wave tends to change its shape as it propagates throughout the tidal basin, smoothing the crests and flattening the troughs as a consequence of the topographic influence. The relatively small differences exhibited by the results provided by the two models are possibly due to the different treatment of the convective terms in the two models. Indeed, the 2DEF model used a simplified lagrangian framework to compute the convective terms [Defina and Bonetto, 1998], while an eulerian approach is adopted in the 1D model.

Figure 2.17 shows the temporal distribution of the cross-sectional discharge at the above considered cross sections. All the diagrams are characterized by an evident asymmetry, with and ebb phase that is flatter and lasts longer than the flood phase which, in turn, is more peaked and shorter. Despite the constant width of the tidal domain and the flatness of the cross sections, a slight flood dominance behavior is evident from the results. The 1D model appears to reproduce correctly the trends emerging from the 2DEF calculations.

These results are confirmed by the $Q - h$ diagrams plotted in Figure 2.18. The matching between the two model remains reasonably good. The skewness of the curves is quite evident, especially at the seaward section. Note that the presence of a sloping ramp near to the seaward boundary, introduced to impose the sinusoidal wave forcing in 2DEF model and absent in the 1D model, is likely responsible for

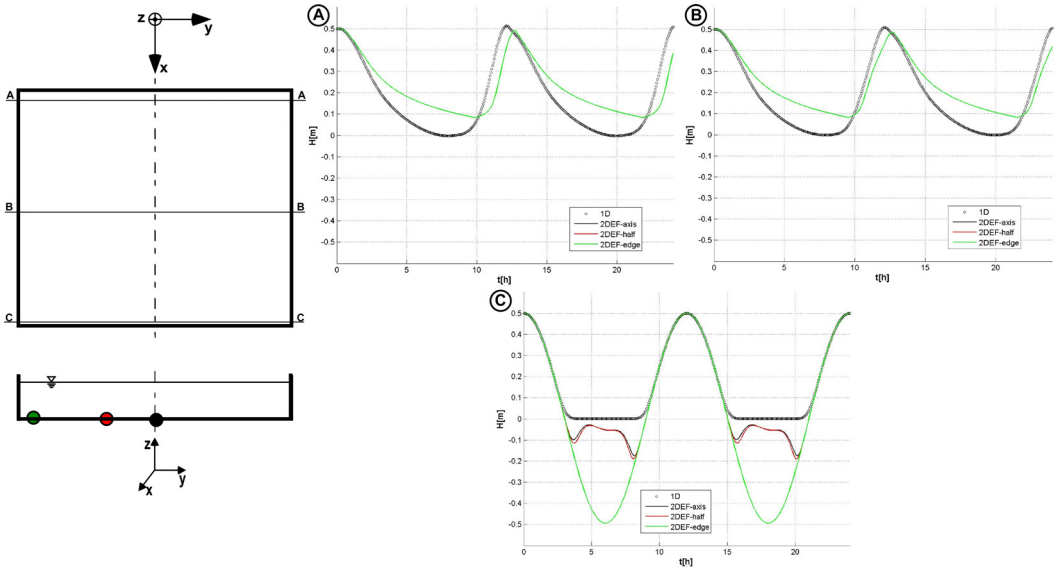

Figure 2.16: Water level oscillations computed for bathymetry 1 (z_{tf} = 0.0 m). a) landward section; b) halfway cross section; c) seaward section. The water levels are tracked on the channel axis (black), on the tidal flat edge (red) and on the lateral boundary of the tidal domain (green).

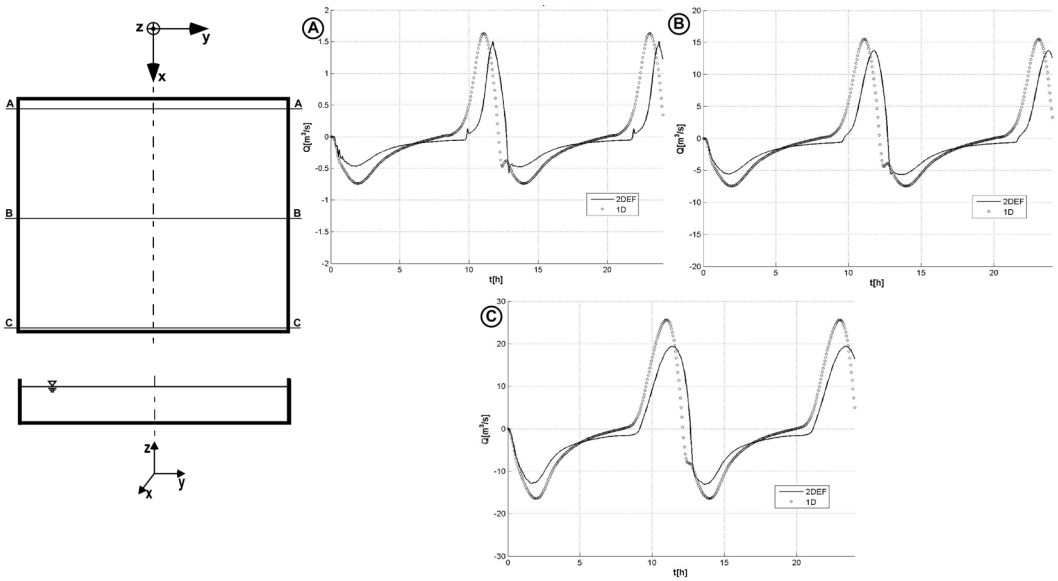

Figure 2.17: Temporal distribution of the cross-sectional discharge Q computed for bathymetry 1 (z_{tf} = 0.0 m). a) landward section; b) halfway cross section; c) seaward section.

the slightly different shapes of the $Q - h$ computed by the two models.

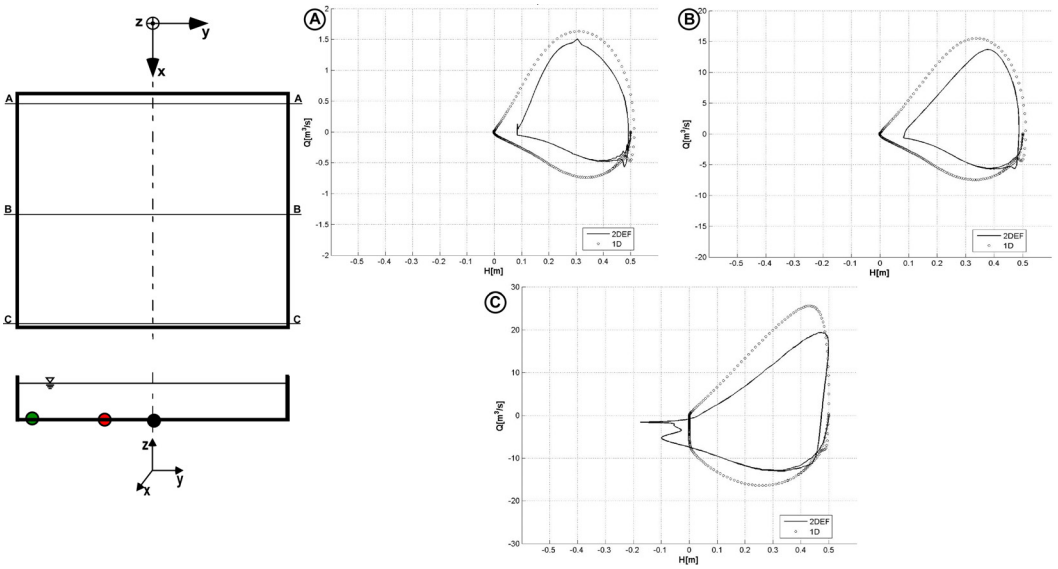

Figure 2.18: The cross sectional discharge Q is plotted as a function of the water stage h for bathymetry 1 ($z_{tf} = 0.0$ m) a) landward section; b) halfway cross section; c) seaward section.

The effect of the ramp clearly appears also in Figure 2.19, showing the maximum values of the shear stresses τ_{max} and of the velocity U_{max} calculated during a tidal cycle along the longitudinal axis of the basin. Indeed, at the seaward section both the velocity and the shear stress resulting from the 2DEF model are larger that those provided by the 1D model. Note also the spikes of both τ_{max} and U_{max} induced by the sloping ramp which bends the streamlines making the velocity and the shear stress especially during the ebb phase. Overall, the the concordance between the two models is reasonably good.

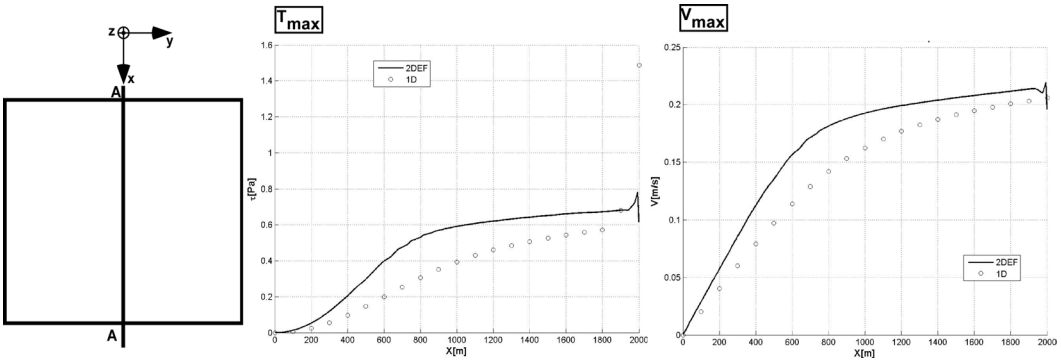

Figure 2.19: a) Maximum shear stress τ_{max} and b) velocity U_{max} computed during a tidal cycle along the longitudinal axis fo the tidal basin with bathymetry 1 ($z_{tf} = 0.0$ m).

It is worth focusing also on the energy slope distribution along the basin due to its importance for the bottom shear stress distribution as it will be discussed in Chapters 4 and 5. The flat bed resembles the initial configuration of the basin

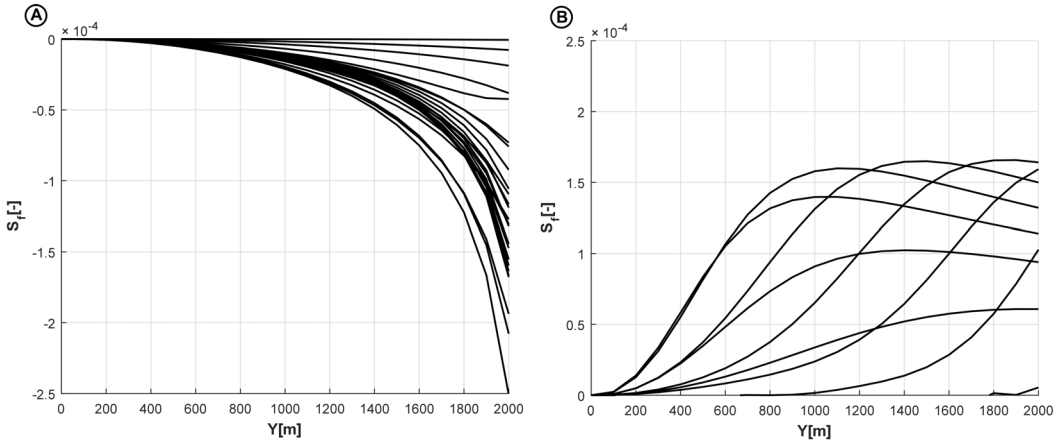

Figure 2.20: Behavior of the 1D model energy slope S_f along the channel in the bathymetry 1 a) in ebb and b) in flood phase.

before any erosional or depositional effects start to shape the channel. In this case, the 1D model energy slope is smooth along the channel in both tidal phases without any wiggles or spikes (Figure 2.20). Despite the simple domain, the energy slope values are different in the two tidal phases, higher in the ebb than in flood phase.

The overall picture emerging from the analysis of the results corresponding the bathymetry 1 (Figures 2.16, 2.17, 2.18, 2.19) are confirmed by those obtained for bathymetry 2.

In particular, Figure 2.21 shows that the differences in water levels between the two models gradually mitigate when moving landward, owing to wetting and drying effects. The channel, in fact, has a slightly descending slope and the lateral shoal are not completely flat. The tidal wave propagating over the basin tends to change its shape, smoothing the crests and flattening the troughs only on tidal flats, but not within channel. The difference between the water levels computed by the two models inside the channel are thus very small.

The temporal distributions of the cross-sectional discharge at different cross sections (Figure 2.22) confirm the good performance of the 1D model as compared to the 2DEF model. The 1D model reproduces appropriately the flood dominant behavior of the tidal wave, resulting from the concurrent action of channel convergence and tidal flats [Todeschini et al., 2008]. The flood dominant asymmetry gradually reduces moving landwards, where the channel funneling has less influence and tidal flats occupy all the basin width.

The reasonably good matching between the results provided by the 1D model and the 2DEF model, and the ability of the former to deal properly with wetting and drying situations are confirmed by the $Q - h$ diagrams (Figure 2.23) and the plots of the maximum shear stresses τ_{max} and the maximum velocity U_{max} calculated during a tidal cycle along the longitudinal axis of the basin (Figure 2.24). In

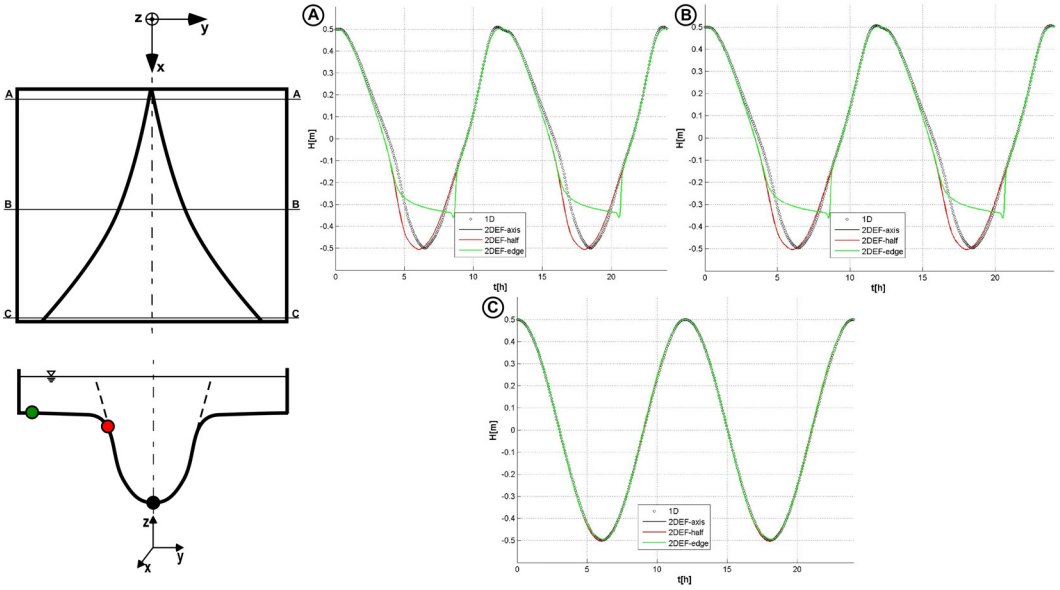

Figure 2.21: Water level oscillations computed for bathymetry 2 (z_{tf} = 0.0 m). a) landward section; b) halfway cross section; c) seaward section. The water levels are tracked on the channel axis (black), on the tidal flat edge (red) and on the lateral boundary of the tidal domain (green).

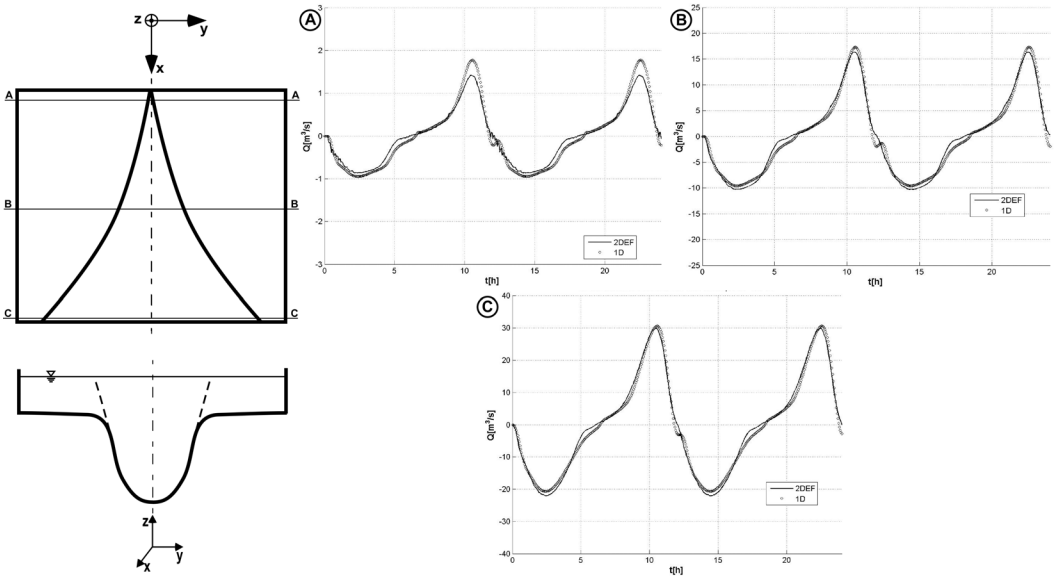

Figure 2.22: Temporal distribution of the cross-sectional discharge Q computed for bathymetry 2 (z_{tf} = 0.0 m). a) landward section; b) halfway cross section; c) seaward section.

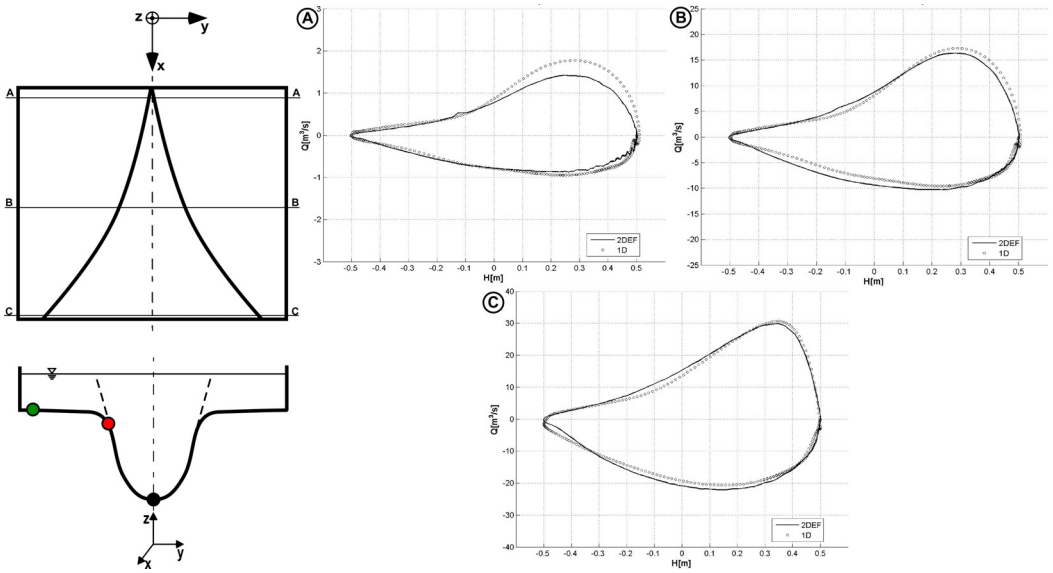

Figure 2.23: The cross sectional discharge Q is plotted as a function of the water stage h for bathymetry 2 ($z_{tf} = 0.0$ m) a) landward section; b) halfway cross section; c) seaward section.

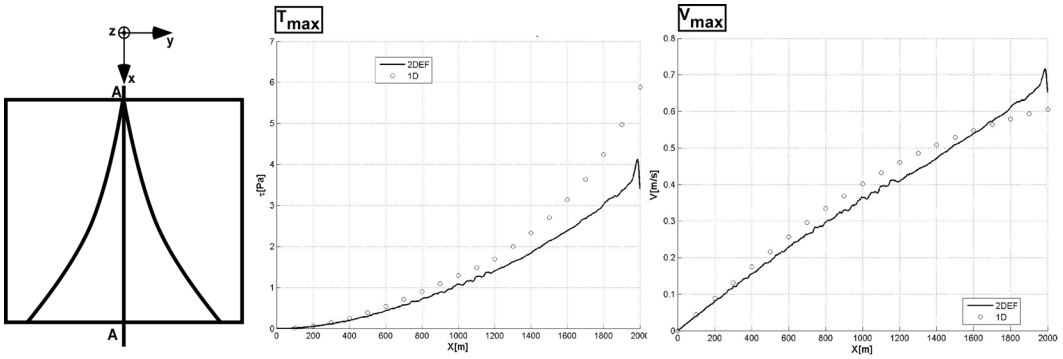

Figure 2.24: a) Maximum shear stress τ_{max} and b) velocity U_{max} computed during a tidal cycle along the longitudinal axis for the tidal basin with bathymetry 2 ($z_{tf} = 0.0$ m).

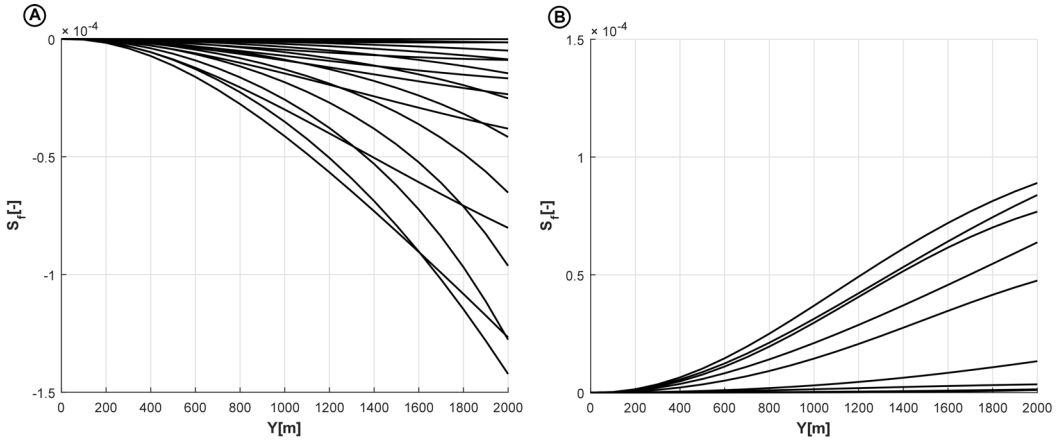

Figure 2.25: Behavior of the 1D model energy slope S_f along the channel in the bathymetry 2 a) in ebb and b) in flood phase.

particular, Figure 2.24 still emphasizes the effects of the sloping ramp introduced in the 2DEF model to apply a sinusoidal tide at the seaward boundary. This is why the overall performance of the 1D model, as compared to the 2DEF model, is quite good in the inner part of the tidal basin, while at the seaward boundary the shear stresses are overestimated and the velocities are underestimated.

As it will be shown in Chapters 4 and 5, bathymetry 2 could represent a channel in its route toward an equilibrium configuration. Despite the presence of lateral shoals, the energy slope is smooth along the channel in both tidal phases (Figure 2.25). The energy slope values are higher in the flood phase compared to the ebb phase.

Finally, let us consider the results of the two models applied to bathymetry 3. Figure 2.26 shows that the differences among the water levels computed inside the channel by the 1D model and the 2DEF model are very small. The basin is completely flat only in the landward part, where the channelized region vanishes and wetting and drying processes repeat periodically during the tidal cycle. This topographical feature is responsible for the strong mitigation experienced landward by the water levels are mitigated by the wetting and drying algorithm gradually moving landward.

Also the temporal distributions of the cross-sectional discharge (Figure 2.27) and the $Q-h$ diagrams 2.28 highlight the flood dominant behavior of the tidal basin due to channel convergence and the role played by tidal flats. However, differently from bathymetry 2, the degree of hydraulic asymmetry does not reduce landwards. Only the cross sections where the main channel disappear, merging with the tidal flats, exhibit a less evident degree of flood dominance. The matching between the 1D model and the 2DEF model is in general quite good for cross sections located along the main channel and at the main channel head, while some discrepancies appear in

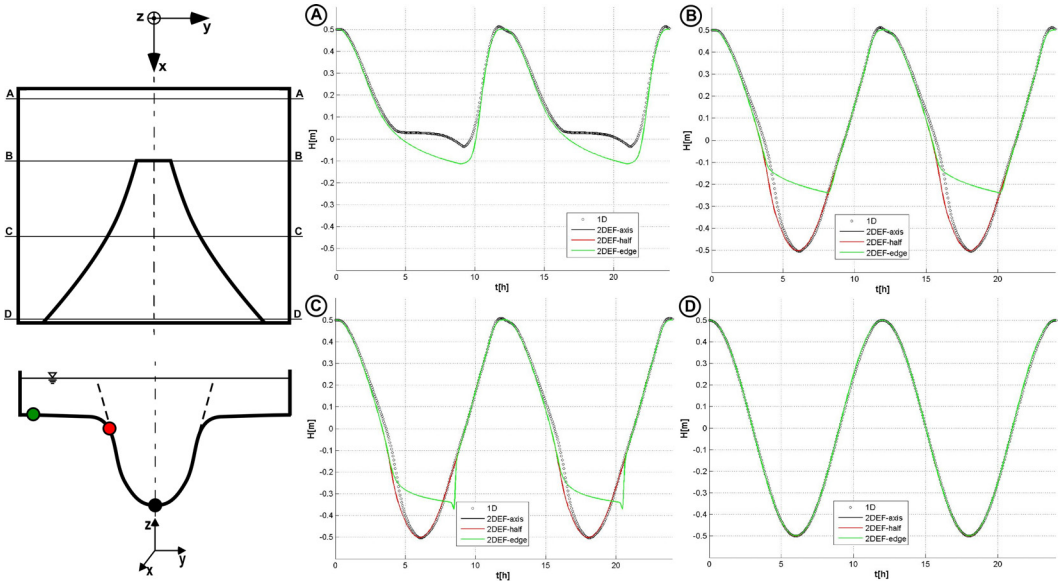

Figure 2.26: Water level oscillations computed for bathymetry 3 (z_{tf} = 0.0 m). a) landward section; b) halfway cross section; c) seaward section. The water levels are tracked on the channel axis (black), on the tidal flat edge (red) and on the lateral boundary of the tidal domain (green).

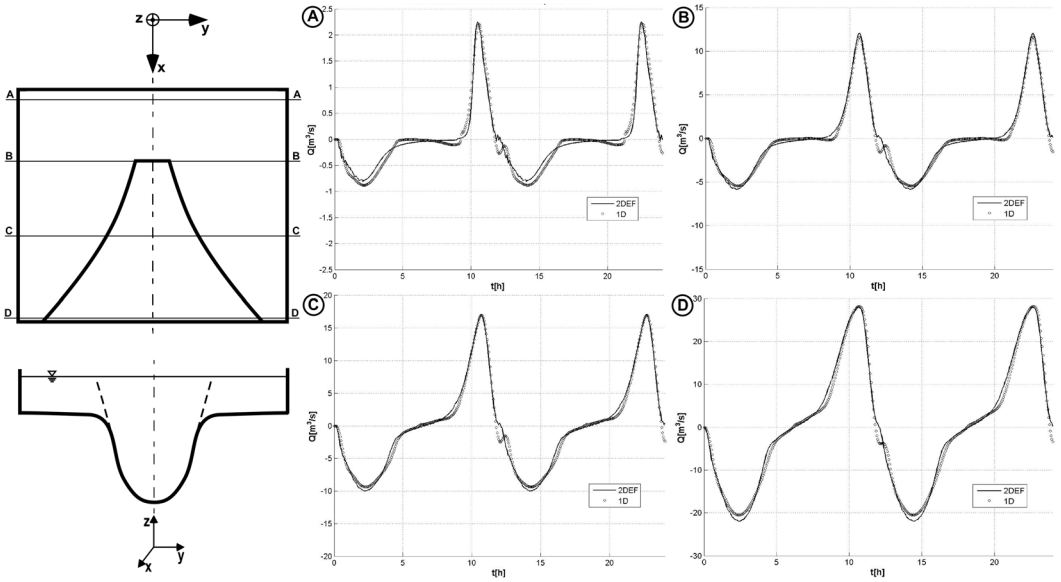

Figure 2.27: Temporal distribution of the cross-sectional discharge Q computed for bathymetry 3 (z_{tf} = 0.0 m). a) landward section; b) halfway cross section; c) seaward section.

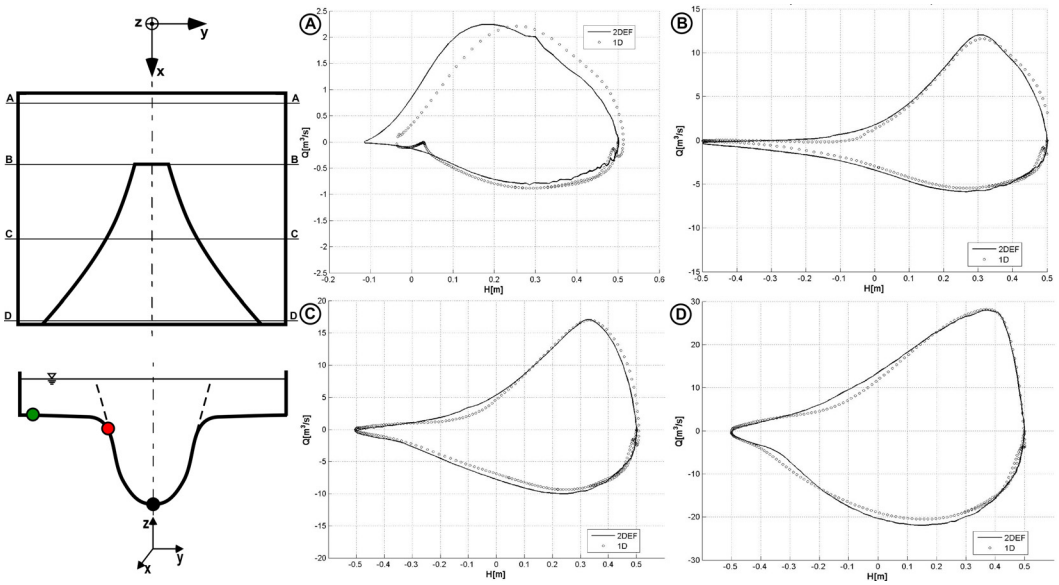

Figure 2.28: The cross sectional discharge Q is plotted as a function of the water stage h for bathymetry 3 ($z_{tf} = 0.0$ m) a) landward section; b) halfway cross section; c) seaward section.

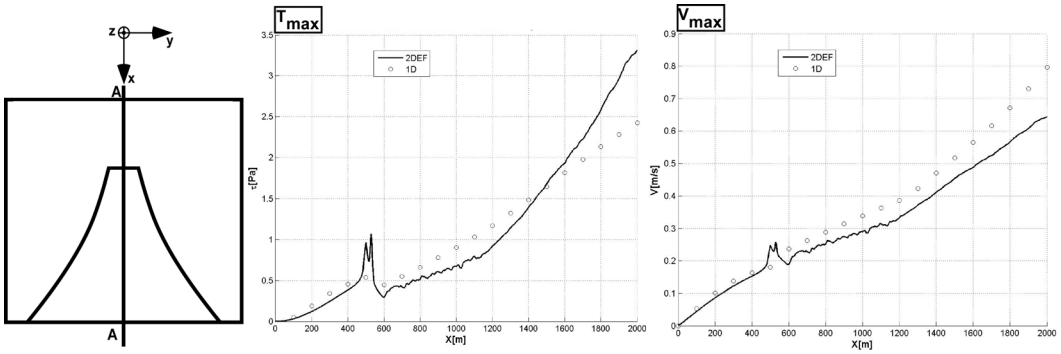

Figure 2.29: a) Maximum shear stress τ_{max} and b) velocity U_{max} computed during a tidal cycle along the longitudinal axis for the tidal basin with bathymetry 3 ($z_{tf} = 0.0$ m).

the landward portion of the tidal basin where the two-dimensional character of the flow likely play some role, completely neglected in the 1D model. Despite this, the 1D model, to the 2DEF model, appears to reproduce the along axis distribution of τ_{max} and U_{max} with a degree of accuracy (Figure 2.29) with respect similar to that observed for the previously examined bathymetries. In particular, the 1D model is able to replicate the spike at the channel head, where the transition between compact and compound cross sections leads to a jump in the bed geometry.

As it will be described in Chapters 4 and 5, the geometric discontinuity due to an abrupt change in cross sections may occur in the channel evolution. The sharp transition from a compact to a compound cross section affects the 1D model energy slope distribution along the channel in both tidal phases (Figure 2.30). Specifically, the topografic jump due to the abrupt change in the cross section triggers a peak

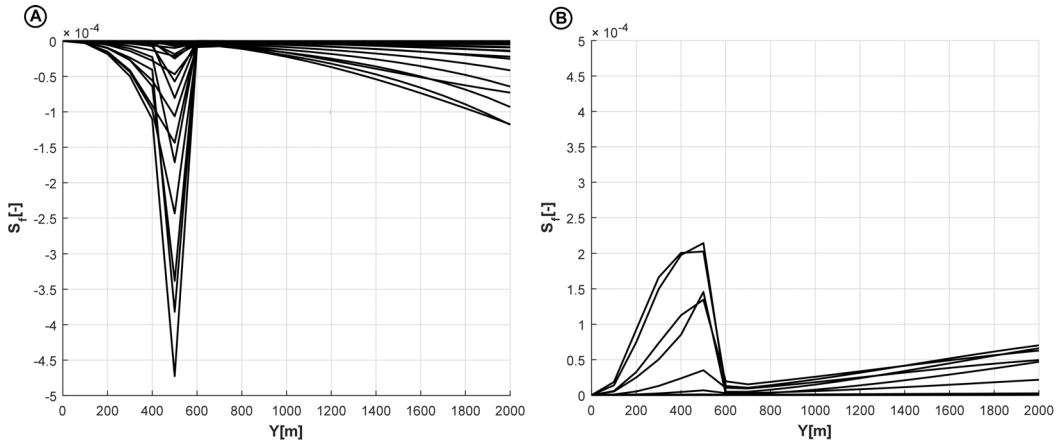

Figure 2.30: Behavior of the 1D model energy slope S_f along the channel in the bathymetry 3 a) in ebb and b) in flood phase.

in the energy slope at the toe of the jump. This unrealistic behavior of the slope energy distribution over a topografic jump may cause wiggles in the scouring at the toe of the jump as the channel is approaching an equilibrium state (see Chapters 4 and 5).

2.5 Concluding remarks

A 1D model has been developed to study the propagation of a tidal wave in a schematical rectangular basin. The model describes the flow within a main channel and, if present, over the lateral tidal flats flanking it. The wetting and dying processes are tackled using a physics-based procedure which introduces a subgrid model to account for ground irregularities [Defina, 2000].

The model has been validated considering the test cases proposed by Balzano [1998] and three additional bathymetries where geometrical complexities were gradually introduced. Overall, the model shows enough robustness and stability to be used for long-term runs.

Chapter 3

Morphodynamics

This chapter discusses the main features of the morphodynamic modeling, which relies on the 1D hydrodynamics described in the previous chapter. The aim is to develop a simple bed evolution model that includes i) erosion ($\mathcal{E}$), ii) deposition ($\mathcal{D}$) due to settling, as well as trapping and organic production due to vegetation, iii) rate of Relative Sea Level Rise (RSLR), but neglects bedload fluxes. As a first rough approximation, the sediment transport occurring in the tidal basin is assumed to be driven by a concentration constant in space and time (i.e., such that a uniform sediment input is applied throughout the entire basin surface). Despite this strong assumption, the model appears to capture the principal features exhibited in the long-term by the tidal channels observed in the field (see Chapter 5).

3.1 Modeling suspended sediment transport

The morphodynamic evolution of a tidal environment is governed by the 2D Exner equation [Lanzoni, 2008]:

$$(1-p)\frac{\partial z_b^*}{\partial t} + \frac{\partial (C\,D)}{\partial t} + \nabla_{xy} \cdot \mathcal{Q}_\mathbf{s} = 0 \tag{3.1}$$

where p is porosity, z_b^* is the local bed elevation referred to m.s.l., C is the mean concentration of sediment suspended in the water column, D is the local water depth, $\mathcal{Q}_\mathbf{s}$ the total sediment flux which accounts for both bed load Q_{sb} and suspended load Q_{ss}. Separating the effects of bed load and suspended load, the sediment balance

can be re-written as follows:

$$(1-p)\frac{\partial z_b^*}{\partial t} = \mathcal{D} - \mathcal{E} - \nabla \cdot Q_{sb} \tag{3.2}$$

where the net sediment supply reads as follows:

$$\mathcal{D} - \mathcal{E} = -\frac{\partial (C D)}{\partial t} - \nabla \cdot Q_{ss} \tag{3.3}$$

The morphodynamic evolution is hence described by two equations, one controlling the bedload fluxes and one driving the suspended sediment exchange, which reads as follows:

$$(1-p)\frac{\partial z_b^*}{\partial t} + \frac{\partial Q_{sbx}}{\partial x} + \frac{\partial Q_{sby}}{\partial y} + \mathcal{E} - \mathcal{D} = 0 \tag{3.4}$$

$$\frac{\partial (C\,D)}{\partial t} + \frac{\partial (D\,U_x\,C)}{\partial x} + \frac{\partial (D\,U_y\,C)}{\partial y} - \frac{\partial}{\partial x}\left(D\,\mathscr{K}_x\,C\right) - \frac{\partial}{\partial y}\left(D\,\mathscr{K}_y C\right) = \mathcal{E} - \mathcal{D} \tag{3.5}$$

where U_x and U_y denote the components of the depth averaged velocity vector, $\mathcal{E}$ is the erosion rate (function of the local bed shear stress and soil properties), $\mathcal{D}$ is the deposition rate (function of the local concentration, and and of the local soil properties through the settling velocity), while $\mathscr{K}_x$, $\mathscr{K}_y$ are the dispersion coefficients along the longitudinal direction x and the lateral direction y, respectively. Considering a rectangular tidal basin dissected by a main straight channel, a 1D approach can be used to describe the processes occurring within the channel and on lateral shoals. In a 1D framework, the traversal velocity U_y vanishes identically, and the above equations become:

$$(1-p)\frac{\partial z_b^*}{\partial t} + \frac{\partial Q_{sbx}}{\partial x} + \mathcal{E} - \mathcal{D} = 0 \tag{3.6}$$

$$\frac{\partial (C\,D)}{\partial t} + \frac{\partial (D\,U_x\,C)}{\partial x} - \frac{\partial}{\partial x}\left(D\mathscr{K}_x\,C\right) = \mathcal{E} - \mathcal{D} \tag{3.7}$$

The bedload rate Q_{sbx} can be computed by estimating the unit width bedload rate through the classical predictors such as the Meyer-Peter-Muller formula [Goud and Aubrey, 1985; Meyer-Peter and Müller, 1948]:

$$Q_{sb} = 8\sqrt{g\,d^3\left(\frac{\varrho}{\varrho_s} - 1\right)}(\mu\,\hat{\theta} - \hat{\theta}_c)^{3/2} \tag{3.8}$$

where d is the mean sediment diameter, $\hat{\theta}$ is the Shield parameter defined as ${u_*}^2/[(\varrho/\varrho_s - 1)\,g\,d]$, u_* is the friction velocity, $\hat{\theta}_c$ is its critical value for incipient

sediment motion, and μ is a ripple factor.

The morphodynamic model should be applied to the 3D domain coherently with 1D hydrodynamic model. According to this latter model, the tidal flow is assumed to concentrate within the main channel as far as the momentum conservation is concerned, while the lateral shoals contribute to the overall friction and act as storage volumes in the continuity equation. By analogy, the mophodynamic model would in principle describe the sediment transport within the channel and would account for the possible sediment exchange between the channel and the lateral intertidal areas. In the present modeling framework, bed load transport is neglected with respect to suspended load (Figure 3.1, Di Silvio [1978a,b]). In addition, the sediment concentration equation is simplified drastically, assuming that the suspended concentration C does keep everywhere constant in space and in time (Figure 3.2). This implies that the local deposition rate (or the total local accretion rate) varies spatially only in relation to different values of the hydroperiod (i.e., the time interval during which the bed is flooded by the tide), the soil composition (through the critical bed shear stress below which particles can settle) and of the local value of the bottom shear stress. This implies that the total local accretion rate then depends on the difference between local deposition and erosion.

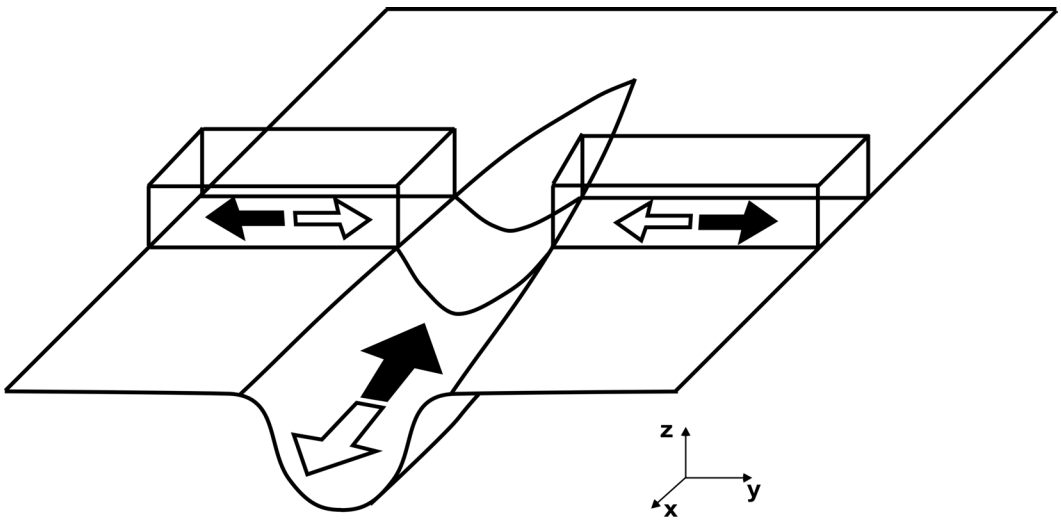

Figure 3.1: Sketch of the sediment fluxes in the main channel and on its lateral shoals (adapted from Di Silvio [1978a]).

In reality, the concentration would change both along the channel and on the intertidal areas, decreasing progressively in the landward direction and moving away from the main channel. The constant concentration assumption thus imply some overestimation of the deposition rates within the channel and the tidal flats. Keeping in mind this limitation, the bed evolution at each location of the tidal basin is

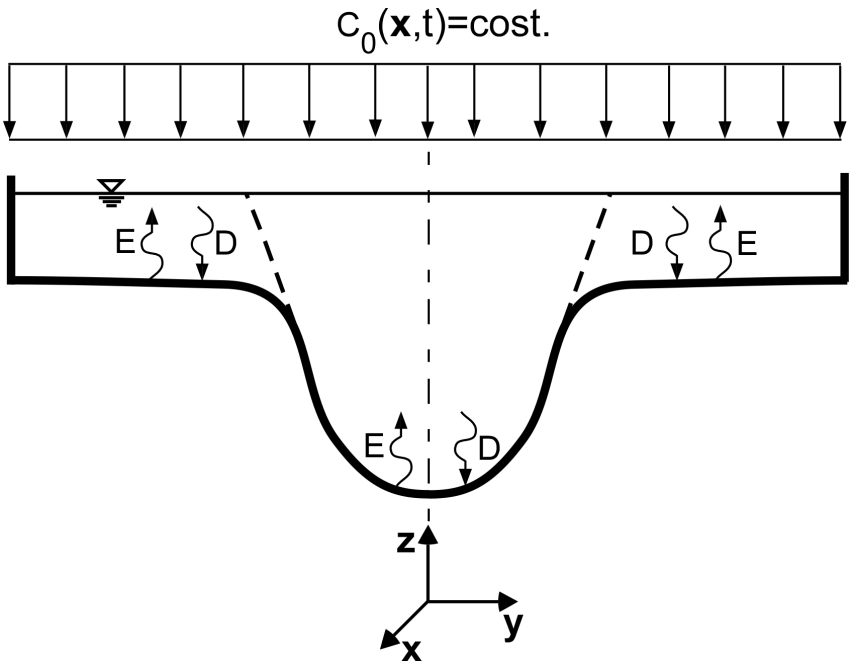

Figure 3.2: The sediment fluxes considered in the morphodynamic model, with $C_0(\boldsymbol{x}, t) = const.$ the concentration of the externally imposed input of sediment.

described by the equation:

$$\frac{\partial z_b^*}{\partial t} = \mathcal{D} - \mathcal{E} - \frac{\partial Q_{sbx}}{\partial x} \tag{3.9}$$

In the previous equations the bed elevation z_b^* is referred to the MSL; however, when RSLR is taken into account, MSL grows entailing the use of a moving reference frame. To refer the bed elevation z_b to a fixed reference system, we consider the following position assuming a constant RSLR over time:

$$\frac{\partial z_b^*}{\partial t} = \frac{\partial z_b}{\partial t} + r$$

where r is the Rate of Sea Level Rise (RSLR). Substituting the last position in the equation (3.9), the effect of RSLR is singled out in a fixed reference frame and turns into a sort of additional erosional effect constant in time and space:

$$\frac{\partial z_b}{\partial t} = \mathcal{D} - \mathcal{E} - \frac{\partial Q_{sbx}}{\partial x} - r \tag{3.10}$$

The erosion rate $\mathcal{E}$ is computed by means of the following empirical-based for-

mula [Metha, 1984]:

$$\mathcal{E} = \mathcal{E}_0 \left(\frac{\tau}{\tau_{ce}} - 1 \right) \mathcal{H} \left(\frac{\tau}{\tau_{ce}} - 1 \right) \tag{3.11}$$

where τ is the local bed shear stress, τ_{ce} is the critical threshold for erosion, $\mathcal{H}$ is the Heaviside step function, while $\mathcal{E}_0$ is the constant erosion rate derived empirically from sediment features (continuous line in Figure 3.3). Assuming that the critical threshold is distributed according to a probability density function, Carniello et al. [2012] suggested to modify the relation (3.11) introducing a smooth transition between $\tau > \tau_{ce}$ and $\tau \leq \tau_{ce}$, as depicted in Figure 3.3. The relation used to describe this smooth transition in the erosion rate is:

$$\mathcal{E} = \mathcal{E}_0 \left\{ -1 + \left[1 + \left(\frac{\tau}{\tau_{ce}} \right) \right]^{1/e} \right\} \tag{3.12}$$

where e is a suitable parameter (here set equal to 2) used to change the degree of smoothing (Figure 3.3).

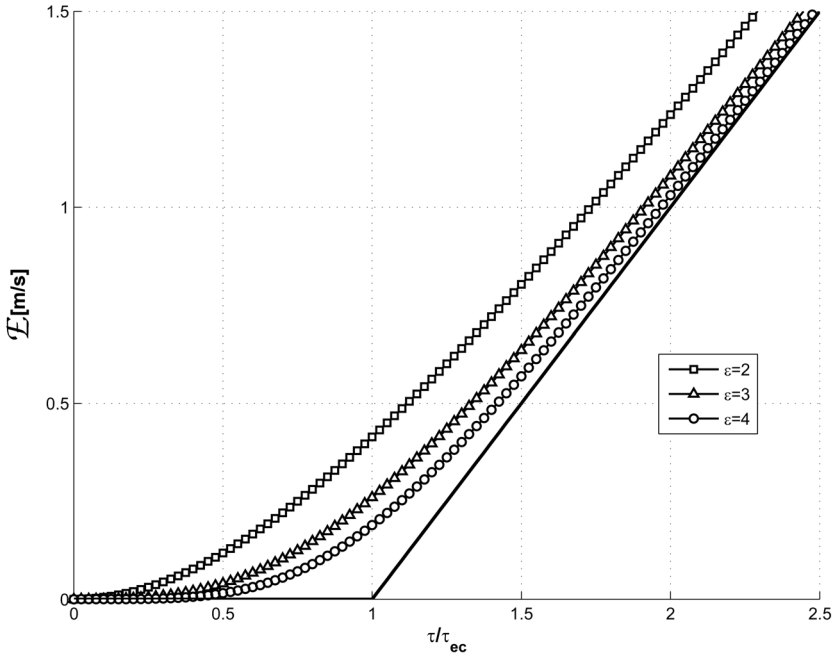

Figure 3.3: Erosion rate curves as a function of the bed shear stress. Original formulation based on a well defined threshold for incipient erosion (continuous line) and gradual transition from an immobile bed to an eroding bed as proposed by Carniello et al. [2012].

On the other hand, the overall sediment deposition rate $\mathcal{D}$ is in general the sum of three contributions:

$$\mathcal{D} = Q_s + Q_t + Q_o \tag{3.13}$$

where Q_s is the deposition rate due to sediment settling, Q_t is the deposition rate due to vegetation trapping, and Q_o the organic production rate. Clearly, when no vegetation encroaches the lateral shoals, only the settling rate contributes to deposition can be computed as [Einstein and Krone, 1962; Krone, 1962]:

$$Q_s = w_s\, C_0 \left(1 - \frac{\tau}{\tau_{cd}}\right) \mathcal{H}\left(1 - \frac{\tau}{\tau_{cd}}\right) \tag{3.14}$$

where τ_{cd} is the critical threshold for incipient deposition, w_s is the settling velocity, assumed to be constant, $C_0[-]$ is the local value of the suspended sediment concentration while $\mathcal{H}$ is the Heaviside step function (Figure 3.4). The use of equation (3.14) for cohesive sediments is debated [Winterwerp, 2007], owing to the effects of flocculation that, under some conditions, can become important. However, assuming mean sediment sizes d_{50} up to 0.05 mm, flocculation likely does not play any role and equation 3.14 is still valid [Metha, 1984].

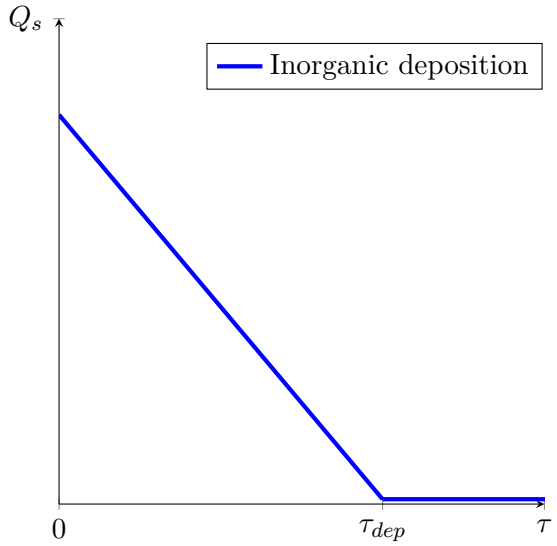

Figure 3.4: Deposition rate curve as a function of the bed shear stress.

The presence of vegetation on the intertidal platform leads to additional contributions to sedimentation, limits sediment resuspension, and increases flow resistance. In order to take into account vegetation growth, a relation for biomass has to be introduced [Mudd et al., 2004]. Biomass b is here defined as the weight per unit surface of the vegetal mass lying above the marsh surface. Its generally depends on plant species, soil salinity, hydroperiod, nutrient availability [Silvestri and Marani, 2004]. In a simplified framework in which only one vegetation species is present, namely *Spartina alterniflora* in this case [Morris et al., 2002], b is related to platform

height as follows:

$$b = \begin{cases} 0 & z_b < z_{bmin} \\ b_{max} \frac{z_{bmax} - z}{z_{bmax} - z_{bmin}} & z_{bmin} \leq z_b \leq z_{bmax} \\ 0 & z_b > z_{bmax} \end{cases} \tag{3.15}$$

where b_{max} is the maximum value that can be attained by b, while z_{bmax} and z_{bmin} denote the interval of ground elevations at which plants can survive. According to this formula biomass production peaks at z_{bmin} and then linearly decays as the platform height increases and the hydroperiod is decreases. Above z_{bmax}, the biomass vanishes because plants cannot survive any longer (Figure 3.5). The biomass relation (3.15) describes the typical behavior of species for which maximum organic production occurs at low marsh elevations like in the case of *Spartina alterniflora* [Morris et al., 2002; Mudd et al., 2004].

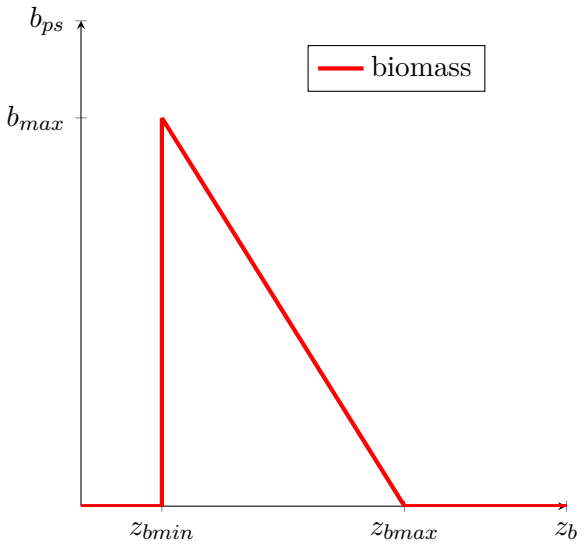

Figure 3.5: Plant biomass curve as a function of the bed elevation z_b

The organic production rate is proportional to biomass through the relation [Randerson, 1979]:

$$Q_o = Q_{b0} \frac{b}{b_{max}} \tag{3.16}$$

where Q_{b0} is the maximum rate $(m/years)$ at which the marsh elevation can increase owing to organic production.

The trapping deposition is expressed as [Palmer et al., 2004]:

$$Q_t = C_0 \, U_0 \, \eta \, d_s \, n_s \, h_s \tag{3.17}$$

where U_0 is a characteristic velocity value of the flow trough vegetation, d_s is the stem diameter, n_s the stem density per unit area and h_s is average stem height. The coefficient η represents trapping efficiency and is defined as:

$$\eta = \alpha_\eta \left(\frac{U_0 \, d_s}{\nu} \right)^{\beta_\eta} \left(\frac{d_p}{d_s} \right)^{\gamma_\eta}$$

where d_p is the particle diameter, ν kinematic viscosity, α_η, β_η, and γ_η are experimental coefficients [Palmer et al., 2004]. The stem density n_s and the average stem height h_s, the projected plant area per unit volume a_s, and the stem diameter d_s are related to biomass as follows [Mudd et al., 2004]:

$$\begin{aligned} n_s &= \alpha_n \, b^{\beta_n} \\ h_s &= \alpha_h \, b^{\beta_h} \\ a_s &= \alpha_a \, b^{\beta_a} \\ d_s &= \alpha_d \, b^{\beta_d} \end{aligned}$$

where α_n, β_n, α_h, β_h, α_a, β_a, β_d, β_d are empirical coefficients.

3.2 Results

3.2.1 Morphodynamic equilibrium considerations

The choice of the critical thresholds for erosion and deposition processes could become crucial for the final configuration of the channel, especially under the assumption of a constant sediment supply, whereby the sediment concentration C_0 keeps approximately constant in space and time. If $\tau_{ce} < \tau_{cd}$, erosion and deposition can occur at the same time; conversely, if $\tau_{ce} > \tau_{cd}$, one process rules the other out (Figure 3.6). The assumption of a constant sediment supply might be incompatible with the attainment of different equilibrium conditions on the tidal flats and within the main channel. We will return back (see Chapter 5) on this question.

Below, we investigate whether the choice of the critical thresholds for erosion and deposition allows equilibrium states for both the main channel and the adjacent tidal flats. For the sake of simplicity, only sediment settling is considered. The 1D

sediment balance equation then reads:

$$\frac{\partial z_b}{\partial t} = w_s\, C_0 \underbrace{\left(1 - \frac{\tau}{\tau_{cd}}\right) \mathcal{H}\left(1 - \frac{\tau}{\tau_{cd}}\right)}_{\mathcal{F}_d(\tau)} - Q_{e0} \underbrace{\left(\frac{\tau}{\tau_{ce}} - 1\right) \mathcal{H}\left(\frac{\tau}{\tau_{ce}} - 1\right)}_{\mathcal{F}_e(\tau)} - \frac{\partial Q_{sbx}}{\partial x} - r \tag{3.18}$$

where $\mathcal{H}(\dots)$ is the Heaviside step function used to describe erosion and deposition rates in compact form.

Denoting by $\langle \dots \rangle$ the time average over T:

$$\langle \dots \rangle = \int_{t^*}^{t^*+T} \dots \, dt \tag{3.19}$$

the tidal averaging of the sediment balance equation is:

$$z_b(t^* + T) - z_b(t^*) = w_s\, C_0 \, \langle \mathcal{F}_d(\tau) \rangle - Q_{e0} \, \langle \mathcal{F}_e(\tau) \rangle - \frac{\partial}{\partial x} \langle Q_{sbx} \rangle - \mathcal{R}\, T \tag{3.20}$$

where $\mathcal{R}$ is the RSLR in one tidal cycle, while $\langle \mathcal{F}_d(\tau) \rangle$ and $\langle \mathcal{F}_e(\tau) \rangle$ can be defined through the hydroperiod t_H as:

$$\langle \mathcal{F}_e(\tau) \rangle = t_H \left(\frac{\bar{\tau}}{\tau_{ce}} - 1\right) \tag{3.21}$$

$$\langle \mathcal{F}_d(\tau) \rangle = t_H \left(1 - \frac{\bar{\tau}}{\tau_{cd}}\right) \tag{3.22}$$

The equilibrium condition implies that $z_b(t^* + T) = z_b(t^*)$ and, consequently:

$$w_s\, C_0 \, \langle \mathcal{F}_d(\tau) \rangle = Q_{e0} \, \langle \mathcal{F}_e \rangle(\tau) + \frac{\partial}{\partial x} \langle Q_{sbx} \rangle + \mathcal{R}\, T \tag{3.23}$$

According to the diagram reported in Figure 3.6a ($\tau_{cd} < \tau_{ce}$), equilibrium would require that the term $\partial \langle Q_{sbx} \rangle / \partial x$ is negative. In the absence of any significant contribution by longitudinal bedload fluxes, as typically occurs on tidal flats, equilibrium can be attained only in the absence of any erosion, i.e. for $\bar{\tau} < \tau_{cd}$, and is such that sea level rise and deposition balance each other out:

$$\boxed{\partial \langle Q_{sbx} \rangle / \partial x \simeq 0, \quad \bar{\tau} < \tau_{cd}} \quad \Rightarrow \quad w_s\, C_0 \, \langle \mathcal{F}_d(\tau) \rangle = \mathcal{R}\, T \tag{3.24}$$

On the other hand, the possible presence of a negative longitudinal bedload flux

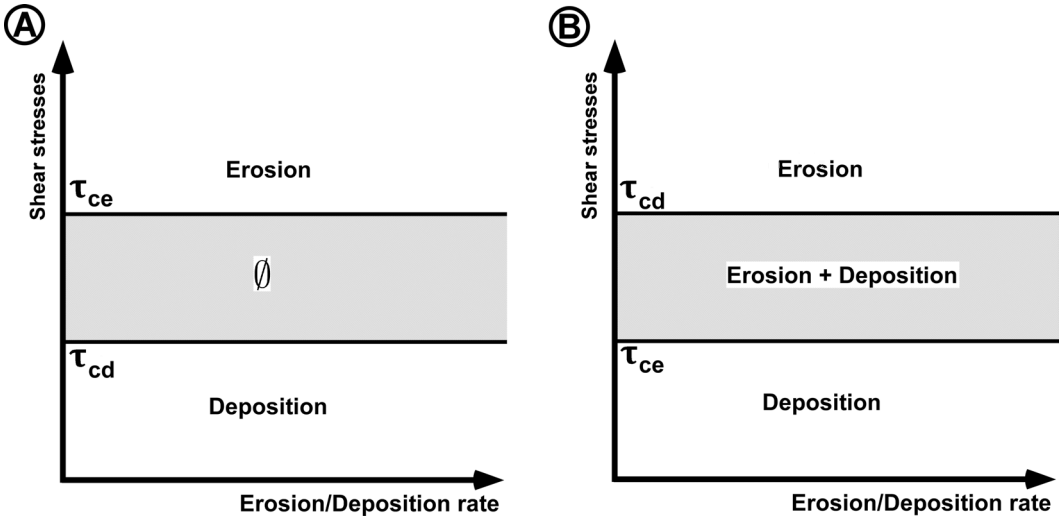

Figure 3.6: Possible combinations of erosion/deposition thresholds. a) The critical bed shear stress for deposition is higher than critical bed shear stress for erosion. An intermediate interval of shear stresses then exists, such that the bed does not experience erosion nor deposition. b) The critical bed shear stress for deposition is higher than that for erosion. An intermediate interval of shear stresses then exists, such that both processes can occur at the same time.

implies that equilibrium can exist also in the presence of erosion:

$$\boxed{\partial\langle Q_{sbx}\rangle/\partial x < 0, \quad \bar{\tau} > \tau_{ce}} \qquad -\frac{\partial}{\partial x}\langle Q_{sbx}\rangle = Q_{e0}\,\langle \mathcal{F}_e(\tau)\rangle + \mathcal{R}\,T \tag{3.25}$$

As pointed out above, bedload fluxes are likely to be negligible on intertidal areas. There tidal currents are very weak (of the order of a few cm/s, see e.g. Table A1 of Rinaldo et al. [1999]) to trigger the bedload. As a consequence, intertidal areas tend towards an equilibrium whereby deposition (controlled, through C_0 by suspended sediment supplied externally to the system and the hydroperiod) compensates RSLR (equation (3.24)). In the absence of bedload, the fate of an initially channelized region is controlled by a similar balance and the channel unavoidably destined to transform in a tidal flat. Conversely, an equilibrium can be attained in the channel provided a negative bedload flux exists that compensates the rates of erosion and sea level rise (equation (3.25)). This implies that some bedload must be feeded in the channel from upstream, a condition unlikely to occurs in tidal channels, but that can be encountered in estuaries.

Under the assumption that $\tau_{cd} < \tau_{ce}$, the existence of different equilibrium bed elevations for channelized regions and intertidal areas is ensured by relaxing the assumption of a well defined threshold for erosion, as proposed by Carniello et al. [2012] (Figure 3.3). In this case, a certain rate of erosion always occur that allows the establishment of different equilibrium conditions on tidal flats and within the channel, also in the absence of any bedload flux in the latter.

On the other hand, according to the diagram reported in Figure 3.6b ($\tau_{cd} > \tau_{ce}$), three different equilibrium conditions exist, depending on whether erosion occurs or not. In the absence of both erosion ($\bar{\tau} < \tau_{ce}$) and tidally averaged bedload transport ($\langle Q_{sbx} \rangle = 0$), only deposition takes place, and morphodynamic equilibrium requires that:

$$\boxed{\partial \langle Q_{sbx} \rangle / \partial x = 0, \quad \bar{\tau} < \tau_{ce}} \quad \Rightarrow \quad w_s \, C_0 \, \langle \mathcal{F}_d(\tau) \rangle = \mathcal{R} \, T \tag{3.26}$$

On the other hand, the condition that $\tau_{cd} > \tau_{ce}$ implies that erosion and deposition can coexist for $\tau_{ce} < \bar{\tau} < \tau_{cd}$. As a consequence, assuming a non vanishing bedload flux, the equilibrium conditions becomes:

$$\boxed{\partial \langle Q_{sbx} \rangle / \partial x \neq 0 \quad \tau_{ce} < \bar{\tau} < \tau_{cd}} \quad \Rightarrow \quad w_s \, C_0 \, \langle \mathcal{F}_d(\tau) \rangle = Q_{e0} \, \langle \mathcal{F}_e \rangle(\tau) + \frac{\partial}{\partial x} \langle Q_{sbx} \rangle + \mathcal{R} \, T \tag{3.27}$$

Finally, in the absence of any deposition term as follows

$$\boxed{\partial \langle Q_{sbx} \rangle / \partial x < 0 \quad \bar{\tau} > \tau_{cd}} \quad \Rightarrow \quad -\frac{\partial}{\partial x} \langle Q_{sbx} \rangle = Q_{e0} \, \langle \mathcal{F}_e(\tau) \rangle + \mathcal{R} \, T \tag{3.28}$$

The condition (3.26) likely controls the tidal flat equilibrium. If applied to an initially channelized region, it leads to a transition towards a tidal flat configuration. The condition (3.27) could be applied both to a tidal flat region (vanishing bedload) or to the channel bed (bedload flux different from zero). The two environments thus can tend towards different equilibrium configurations. Finally, the condition (3.28) can be applied to a channel in which erosion and sea level rise are compensated by a negative bedload flux (resulting from a landward input of sediment).

3.3 Concluding remarks

In this chapter a simplified bed evolution model is developed and its numerical solution is discussed. The model accounts for erosion, deposition and sea level rise, while neglects bed load transport. The role of suitable bed shear stress thresholds for deposition and erosion has been discussed with reference to a tidal basin feeded externally with a constant suspended sediment supply, surrogated by assuming a spatially and temporally constant concentration C_0. Under this simplified condition, it is demonstrated that the choices of the above thresholds is critical for the existence of distinct equilibrium states on the tidal flat areas and within the channel region. In particular, if erosion and deposition rule each other out, the only equilibrium configuration for an initially channelized region is to transform into a tidal flat.

Further modeling attempts should be made in the near future to include in the

morphodydnamic model bed load and suspended sediment transport, relaxing the assumption of constant suspended sediment concentration in space and time.

Chapter 4

The plano-altimetric equilibrium configuration

As stated in Chapter 3 the aim of the present work is to investigate the equilibrium configuration of tidal channels in the presence of: i) non negligible tidal propagation effects (i.e., relaxing the quasi-static assumption adopted in previous approaches); ii) external inputs of suspended sediments (surrogated through a spatially and temporally constant concentration); iii) sea level rise; iv) vegetation encroachment of the intertidal areas. These aspects of the problem are investigated with reference to a rectangular tidal basin whose final equilibrium configuration consists of a main channel, flanked by two symmetrical intertidal regions. A 1D hydrodynamic model (Chapter 2) is used to describe the hydrodynamics of the tidal basin and, in particular, the spatio-temporal distribution of the energy slope. This information is then used to compute the distribution of bed shear stresses along each lateral transect of the basin and each instant of the tidal cycle. Next, these stresses are used to compute the erosion and deposition rates within the basin, thus controlling its evolution towards a possible equilibrium configuration. The bed evolution model accounts for the main physical processes responsible for shaping the main channel and the adjacent intertidal regions, namely sediment deposition, bed particle erosion and sea level rise, possibly mediated by halophytic vegetation growth. The novel feature of this model is provided by the possibility to analyze the mutual role of tidal forcing, suspended sediment concentration (SSC), relative sea level rise (RSLR) and vegetation encroachment on the morphodynamic evolution of a tidal channel.

The chapter is organized as follows. In Section 4.1 the notion of stable cross-

sectional geometry is discussed. Section 4.2 describes how the distribution of the bed shear stresses across a given cross section can be computed, accounting also for the possible effects of the halophytic vegetation that grows on the intertidal areas as a certain bed elevation is exceeded. The numerical approach used to solve the relevant equations is described in Section 4.3. Some sensitivity and validation tests are presented in Section 4.4. Finally, in Section 4.6 some conclusive remarks are drawn.

4.1 Stable cross sections

The problem of determining a morphologically stable cross section in both fluvial and tidal settings has been investigated by many researchers [Fagherazzi and Furbish, 2001; Glover and Florey, 1951; Henderson, 1966; Pizzuto, 1990; Tubino and Colombini, 1992]. Indeed, this problem has a great relevance for engineering design purposes as well as environmental reasons (e.g., rehabilitation and re-naturalization projects, habitat suitability analysis, etc.). Here we are specifically interested in determining the cross-sectional distribution of bed shear stresses in a tidal channel.

Under uniform flow conditions, the cross-sectionally averaged shear stress $\overline{\tau}$ is given by the classical formula

$$\overline{\tau} = \varrho\, g\, R_H\, S \tag{4.1}$$

with ϱ water density, g gravitational acceleration, R_H hydraulic radius of the cross-section and S bed slope. However, another approach has to be sought to gain insight into the cross sectional distribution of bed shear stresses. In the case of a straight channel with prismatic cross section, the problem has been tackled analysing the velocity contours within the section and the related shear stress distribution [Leighly, 1932]. The flow field characteristics within the cross section are investigated drawing a network of isovels and their orthogonal rays (Figure 4.1). All the rays are converging on a specific ray which is just below the water surface and also cuts orthogonally the isovels. By construction, no shear stresses are acting on these orthogonal rays. The cross section can then be subdivided in small wedge-shaped volumes, bounded by the orthogonal rays, the water surface and the bed contour. The equilibrium of each of these volumes is assessed investigating the forces acting on its boundaries, namely gravity, acting downward, and the bed shear stresses, opposing to the flow. Note that the equilibrium of each wedge-shaped volume, enclosed only by the water surface and the orthogonal rays, is possible only by assuming that the downward action of gravity is balanced by additional shear stress arising along the dashed ray owing to the presence of secondary currents (denoted by red arrows in Figure 4.1).

Taking into account all the processes emerging from the isovel partitioning is a

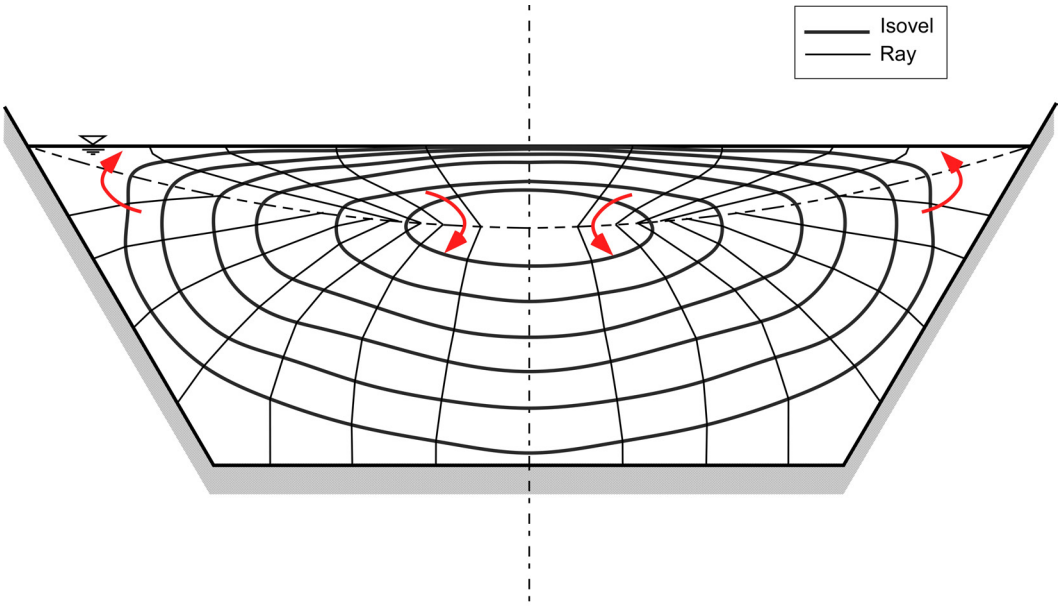

Figure 4.1: Network of isovels and their orthogonal rays (Adapted from [Leighly, 1932]).

difficult task and should be addressed numerically through suitable numerical simulations of the turbulent flow field that establishes within the cross section. In engineering applications simpler methods are usually used to reduce the effort needed to compute the shear stress distribution along the cross-sectional wet boundary. Various attempts have been made to determine such a distribution [Guo and Julien, 2005; Khodashenas and Paquier, 1998; Knight et al., 2007; Pizzuto, 1990; Ramana Prasad and Russell Manson, 2002; Yang et al., 2004]. In this regard, Khodashenas et al. [2008] reviewed six methods with increasing degree of complexity for assessing the shear stresses distribution in a generic cross section and evaluated them by means of experimental results. Here we recall the Vertical Depth Method (VDM) and the Merged Perpendicular Method (MPM). The Vertical Depth Method [Khodashenas and Paquier, 1998] is the easiest approach. The cross-sectional area is subdivided in sub-areas by means of vertical rays, and the mean shear stress acting on the wet perimeter of each sub-area is computed with the relation (4.1). The VDM method is applicable to cross sections of any shape but it neglects the momentum exchange due to secondary currents and is poorly reliable for high values of the trasversal bed slope. The Merged Perpendicular Method [Khodashenas and Paquier, 1998] uses rays orthogonal to the bed derived for the cross-sectional area subdivision. However, differently from the VDM method, some problems can arise around convex corners, where the rays can intersect. A correction is then needed, by taking the average of the two intersecting rays. The method produces a smoothing of the shear distribution around convex corners and provides a full description of the shear stress

distribution along the wetted perimeter of complex sections.

Choosing among these methods poses the question of which approach encompasses the essential physical mechanisms needed to evaluate correctly the cross sectional stability of a straight channel. As shown by Parker [1978b], computing the shear stresses according to the Vertical Depth Method also at the banks of a gravel river would force the channel to widen indefinitely. The method, in fact, is unable to describe a river with mobile bed and stable banks. To overcame this problem, Lundgren and Jonnson [1964] derived a shear stress distribution for wide cross sections that neglects secondary currents but accounts for lateral momentum exchange by turbulent diffusion. This has been the theoretical framework which has been used to allow mobile bed and stable banks to coexist in gravel rivers [Parker, 1978a,b]. The shear stress distribution developed by Lundgren and Jonnson [1964] is the key ingredient for the model we developed to obtain stable cross sections, as described below.

4.2 The shear stress distribution across the channel section

The generic transect of the tidal basin is typically characterized by a compound cross section. This general geometry is described through a local curvilinear reference frame of axis x, n, ζ, where x is the longitudinal straight coordinate coinciding with the main channel axis, n is the lateral curvilinear coordinate, locally tangent to the sediment bed, and ζ is the local normal to the bed, pointing upward (Figure 4.2). Moreover, the cross section is described in a global reference frame x, y, z, where z is the vertical axis upward oriented, while x and y define a horizontal plane set at MSL. In order to account for the the curvilinear nature of the n coordinate, a traversal metric coefficient h_n is introduced [Pletchter et al., 2013; Tubino and Colombini, 1992]:

$$h_n = 1 - \frac{\zeta}{R} \tag{4.2}$$

where the radius of curvature R reads:

$$R = -\frac{1}{\cos\alpha}\frac{\partial^2 D}{\partial n^2}, \qquad \cos\hat{\alpha} = \sqrt{1 - \left(\frac{\partial D}{\partial n}\right)^2} \tag{4.3}$$

with $\hat{\alpha}$ the angle that the vertical direction z forms with the normal to the bed ζ, and D is the local water depth.

The starting point to derive the shear stress distribution across the channel section, is the momentum balance equation along the longitudinal direction x, averaged

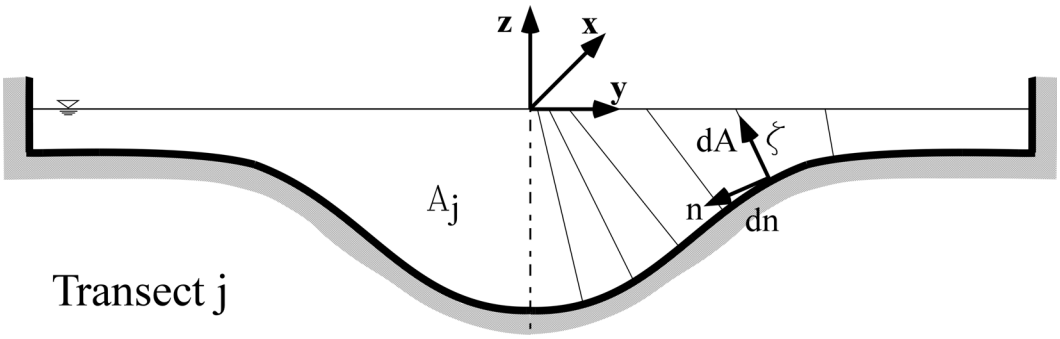

Figure 4.2: Sketch of a typical cross-section of the tidal basin, formed by a main channel flanked by intertidal areas, and notations.

over turbulence:

$$\varrho \frac{\partial u_x}{\partial t} + \frac{\varrho}{h_n}\left[\frac{\partial (h_n\, u_x^2)}{\partial x} + \frac{\partial (u_x\, u_y)}{\partial n} + \frac{\partial (h_n\, u_x\, u_z)}{\partial \zeta} - u_y^2 \frac{\partial h_n}{\partial x}\right] = \\ - \varrho \frac{\partial}{\partial x}\left(\frac{p}{\varrho} + gh\right) + \frac{1}{h_n}\left[\frac{\partial (h_n\, T_{xx})}{\partial x} + \frac{\partial T_{nx}}{\partial n} + \frac{\partial (h_n\, T_{\zeta x})}{\partial \zeta} - T_{nn}\frac{\partial h_n}{\partial x}\right] \quad (4.4)$$

where ϱ is the fluid density, u_x, u_y, u_z are the components in the x, y, z direction of the turbulence averaged velocity vector, and T_{xx}, T_{nx}, T_{nn} are components of the shear stress tensor. The local reference frame x, n, ζ allows one to track the bed shear stress along the bed accounting for its curvature.

Equation (4.4) is associated with the following kinematic and dynamic conditions to be satisfied at the bed ($\zeta = \zeta_0$) and the water surface ($\zeta = D_\zeta$):

$$\left[\frac{\partial D_\zeta}{\partial t} + u_x \frac{\partial D_\zeta}{\partial x} + \frac{u_y}{h_n}\frac{\partial D_\zeta}{\partial n} - u_z\right]_{\zeta = D_\zeta} = 0, \quad \left[\frac{\partial \zeta}{\partial t} + u_x \frac{\partial \zeta}{\partial x} + \frac{u_y}{h_n}\frac{\partial \zeta}{\partial n} - u_z\right]_{\zeta = \zeta_0} = 0, \quad (4.5)$$

$$\left[T_{\zeta x} + \frac{1}{h_n}\frac{\partial D_\zeta}{\partial n} T_{nx} - T_{xx}\frac{\partial D_\zeta}{\partial x}\right]_{\zeta = D_\zeta} = 0, \quad \left[T_{\zeta x} - \frac{1}{h_n}\frac{\partial \zeta}{\partial n} T_{nx} - T_{xx}\frac{\partial \zeta}{\partial x}\right]_{\zeta = \zeta_0} = \tau \quad (4.6)$$

where $D_\zeta = D\cos\hat{\alpha}$.

In the case of a straight tidal channel, some assumptions can be put forward to simplify the hydrodynamic problem [Lanzoni and D'Alpaos, 2015]:

1. the cross sections are shallow such that horizontal scales are much larger than the local flow depth. This implies that in the direction normal to the main flow the velocity are much smaller and the pressure can be assumed to be

distributed hydrostatically, namely:

$$\frac{\partial}{\partial x}\left(\frac{p}{\varrho}+g\,h\right)=g\frac{\partial H}{\partial x} \tag{4.7}$$

2. the flow is gradually varying in time, such that at each instant of the tidal cycle temporal acceleration is negligibly small, $\frac{\partial u_x}{\partial t}\cong 0$;
3. the cross sectional flow can be modeled as 1D, thus neglecting the role of secondary currents within the cross section;
4. longitudinal variations of the metric coefficient are negligible, $\frac{\partial h_n}{\partial x}\cong 0$;
5. momentum exchange between the isovels is negligible;
6. a logarithmic velocity profile establishes along the normal to the sediment bed;
7. the longitudinal variations of shear stresses are negligible with respect to those in the traversal and normal directions, $\frac{\partial T_{xx}}{\partial x}\cong 0$.

The $x-$momentum equation then simplifies to:

$$\frac{\partial(h_n\,u_x^2)}{\partial x}+h_n\,\frac{\partial(g\,H)}{\partial x}=\frac{1}{\varrho}\left[\frac{\partial T_{nx}}{\partial n}+\frac{\partial(h_n\,T_{\zeta x})}{\partial\zeta}\right] \tag{4.8}$$

Integrating this equation along ζ, making use of relations (4.5) and (4.6) and assuming a gently varying traversal slope (i.e., such that the normal ray to isovels can be approximated using straight lines), lead to the following integro-differential equation for determining the cross-sectional shear stress distribution [Lundgren and Jonnson, 1964]:

$$\tau=\varrho\,g\,S\,\frac{d\mathcal{A}}{dn}+\frac{\partial}{\partial n}\int_{\zeta_0}^{D_\zeta}T_{nx}d\zeta \tag{4.9}$$

where S is the energy slope, dn is the wet perimeter between two normals and $d\mathcal{A}$ is the area between two normals. In the Appendix B we explained in detail how to derive the above equation. The shear stress distribution described by equation (4.9) was widely adopted in river morphodynamics [Diplas, 1990; Ikeda et al., 1988; Parker, 1978a,b; Pizzuto, 1990; Schippa, 1992], and was recently used to address the morphodynamic evolution of cross sections in tidal environments [D'Alpaos et al., 2006; Fagherazzi and Furbish, 2001; Lanzoni and D'Alpaos, 2015; Xu et al., 2019].

4.2.1 The turbulence model

In equation (4.9) the shear stress distribution is expressed as the sum of two terms: the first depends on the energy slope S, the second term is instead due to

the turbulent mixing across the normals to the sediment bed. The latter contribution can be determined assuming the Boussinesq closure model for the shear stress components:

$$(T_{xx}, T_{nx}, T_{\zeta x}) = \varrho \nu_T \left(2\frac{\partial u_x}{\partial x}, \frac{1}{h_n}\frac{\partial u_x}{\partial n}, \frac{\partial u_x}{\partial \zeta} \right) \tag{4.10}$$

where ν_T is the eddy viscosity, here assumed to be distributed according to a parabolic function. Indeed, several researches have shown that a parabolic model describes properly the momentum exchange in channels subjected to a oscillating water level, as in tidal channels [Rodi, 1993]. The parabolic eddy viscosity is thus assumed to read:

$$\nu_T(\hat{\zeta}) = u_* \, D_\zeta \, \mathcal{N}(\hat{\zeta}), \qquad \mathcal{N}(\hat{\zeta}) = \kappa \, \hat{\zeta}(1 - \hat{\zeta}) \tag{4.11}$$

where κ is the Von Karman constant, $u_* = \sqrt{\tau/\varrho}$ is the shear stress velocity, $\hat{\zeta} = \frac{\zeta}{D_\zeta}$ is the dimensionless coordinate along the normal, D_ζ is the flow depth measured along the normal to the sediment bed and Γ is a dimensionless parabolic function. The logarithmic velocity profile along ζ reads:

$$u(\hat{\zeta}) = \frac{U}{\mathcal{C}} \mathcal{G}(\hat{\zeta}), \qquad \mathcal{G}(\hat{\zeta}) = \frac{1}{\kappa} \ln \frac{\hat{\zeta}}{\zeta_0} \tag{4.12}$$

where U is the mean velocity along the normal and $\mathcal{C}$ is the local flow conductance

$$\mathcal{C} = \frac{U}{u_*} = \frac{\chi}{\sqrt{g}} = \frac{k_s}{g} R_H^{1/6} \tag{4.13}$$

with χ and k_s the Chezy and Gauckler-Strickler friction coefficients, respectively.

Making use of these relations, allows one to write equation (4.9) in the form [Lanzoni and D'Alpaos, 2015]:

$$\tau = \varrho \, g \, S \, \frac{d\mathcal{A}}{dn} + \frac{d}{dn} \left[\mathcal{K} \frac{d\tau}{dn} \right], \tag{4.14}$$

where

$$\mathcal{K} = \frac{\Gamma(\zeta) \, D_\zeta^2}{2} \tag{4.15}$$

$$\Gamma(\zeta) = \int_0^1 \mathcal{N}(\zeta) \, \mathcal{G}(\hat{\zeta}) \, d\hat{\zeta} = \frac{1}{6} \ln\left(\frac{1}{\hat{\zeta}_0}\right) - \frac{\hat{\zeta}_0^3}{9} + \frac{\hat{\zeta}_0^2}{4} - \frac{5}{36} \tag{4.16}$$

Equation (4.14) clearly shows that the shear stress distribution across a tran-

sect is controlled by two contributions: the first depending on the cross-sectional geometry, embedded in the term $d\mathcal{A}/dn$, and the energy slope S; the second due to dispersive effects and proportional to the quantity $\mathcal{K}$ which controls the momentum exchange between adjacent cross-sectional sub-areas.

Given a certain water level in a cross section, the larger is the discharge, the higher is the energy slope and, therefore, the shear stress. On the other hand, the larger is the term $\mathcal{K}$ the higher is the momentum exchange between the various sub-areas in which the cross section has been divided. Figure 4.3 shows the different contributions concurring to the shear stress distribution when they peak during a tidal cycle. Within the channel the dispersive term is negative and, hence, subtracts momentum from the channel, reducing the shear stresses. In turn, the subtracted momentum concurs to increase shear stresses at the edge of the lateral intertidal platforms. Overall, the momentum exchange smooths the distribution of bed shear stresses over the cross section [D'Alpaos et al., 2006]. In the following we will use this shear stress distribution to drive erosion and deposition processes within a cross section.

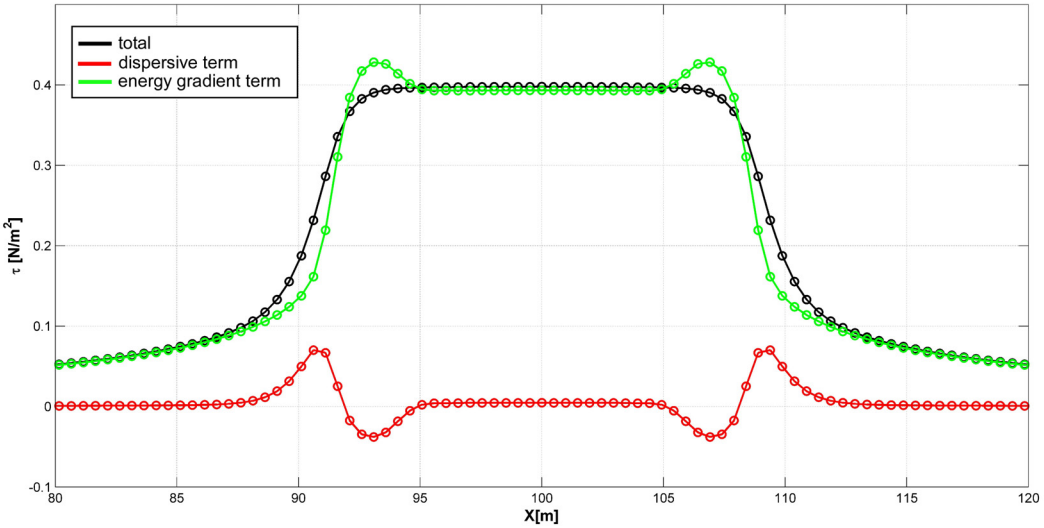

Figure 4.3: Dispersive and energy slope contributions to the cross sectional distribution of bed shear stresses as they peak during a tidal cycle.

4.2.2 Vegetation effects on velocity and shear stress distribution

When the intertidal areas adjacent to the main channel reach a high enough elevation, halophytic vegetation starts to colonize them. The presence of vegetation affects the resistance to the flow and the sediment transport, eventually influencing the morphodynamic configuration attained by the system. Several experimental and field studies have been carried out to investigate how the mutual feedbacks

among hydrodynamics, sediment dynamics and vegetation dynamics interact together, determining the morphological features emerging in river and tidal environments [Bouma et al., 2007; Caroppi et al., 2018; Solari et al., 2015; Tambroni et al., 2015].

Overall, the presence of vegetation increases the resistance to the flow, favoring flow concentration within the channel, modifies turbulent structures within vegetated patches, changing the intensity of bed shear stresses and, as described previously (chapter 3), enhancing sediment deposition. We describe in the following how the essential effects triggered by vegetation (i.e., increased friction, different shear stress distribution) are included in the present modeling framework.

Concerning shear stress distribution in (4.9), different studies have described the velocity profile over vegetated surfaces. A first approach assumes that a logarithmic velocity profile still holds, and the presence of vegetation is accounted for by increasing the resistance coefficient (i.e., accounting for the drag force due to plant stems) and by modifying the eddy viscosity formulation [Kean and Smith, 2005a]. This model was applied to the study the flow and bed shear stresses distributions in some reaches of the Rio Puerco (New Mexico, US) and Whitewater (Kansas, US) rivers, validating the model on the basis of the collected field data [Griffin et al., 2005; Kean and Smith, 2005b]. A second approach assumes that the logarithmic velocity profile does not hold anymore, thus introducing new formulations depending on the type of vegetation [Nepf and Vivoni, 2000; Nepf, 1999].

Here we follow the first approach. On the marsh region, we account for the increased resistance to the flow by simply assuming a smaller value of the Gauckler-Strickler friction coefficient k_s [Belliard et al., 2015; D'Alpaos et al., 2006], which is also assumed to lumps dispersive effects (Figure 4.4).

The additional friction due to vegetation and conceptualized through a coefficient $k_{s,v}$ is computed by taking a balance between drag, friction and gravity acting on a control volume encompassing a vegetated patch [Mudd et al., 2004]. The resulting expression is:

$$k_{s,v} = [1/2 c_D \, a_s]^{-1/2} \, D^{-2/3} \, g^{1/2} \tag{4.17}$$

where c_D and a_s are parameters for drag coefficient and stem density, respectively. The values of these parameters are here assigned on the basis of field measurements carried out in South Carolina on a marsh dominated by *Spartina alterniflora* [Mudd et al., 2004]. This approach was already adopted to study the altimetric evolution of a single transect of a tidal basin [D'Alpaos et al., 2006]. The expression (4.17) depends on the water depth, which generally varies in space and in time, thus introducing a further source of non-linearity in the model.

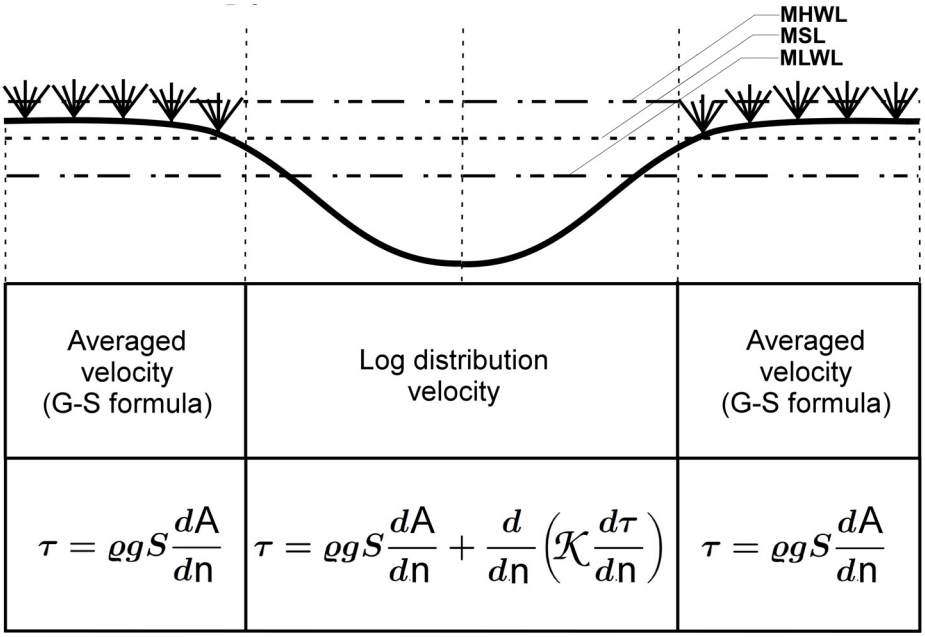

Figure 4.4: Overall framework for computing the cross-sectional distribution of bed shear stresses in the main channel and in the presence of intertidal platforms encroached by saltmarsh vegetation. Here, S is the energy slope, dn is the elementary wetted perimeter delimited by two normals to the sediment bed, $\mathrm{d}\mathcal{A}$ is the infinitesimal area between the two normals, $\mathcal{K}$ is the factor that drives the momentum exchange between the normals.

Eventually, the overall Gauckler-Strickler coefficient k_s is computed as follows [Belliard et al., 2015]:

$$k_s^{-2} = k_{s,g}^{-2} + k_{s,r}^{-2} + \phi_v \, k_{s,v}^{-2} \tag{4.18}$$

where $k_{s,g}$ and $k_{s,r}$ account for grain roughness and bedform roughness, respectively. The greater is vegetation encroachment, the larger is the friction, i.e., the smaller is k_s. Note that, the coefficient $k_{s,v}$ is mediated by a parameter ϕ_v, which is equal to the ratio b/b_{max} between the local biomass and the max biomass that plants are able to produce. Owing to the cohesive character of the sediment bed considered in the present research, bedforms are unlikely to form and, therefore, in the following, $k_{s,r}$ is set equal to zero. Moreover, in all simulations we assume that the local biomass reaches its max production, i.e. $\phi_v = 1$.

4.3 Numerical approach

4.3.1 The computational domain

The computational domain consists of a rectangular tidal basin dissected by a straight channel along the longitudinal axis. The basins is subdivided in M

transects, each one discretized with N nodes. Previous researches [D'Alpaos et al., 2006; Fagherazzi and Furbish, 2001] considered a single transect subject to a tidal forcing applied directly to the water elevation within the section. Conversely, in the present approach the various transects are considered to be connected hydraulically, as described in Chapter 2, and the tidal forcing is applied to the seaward boundary.

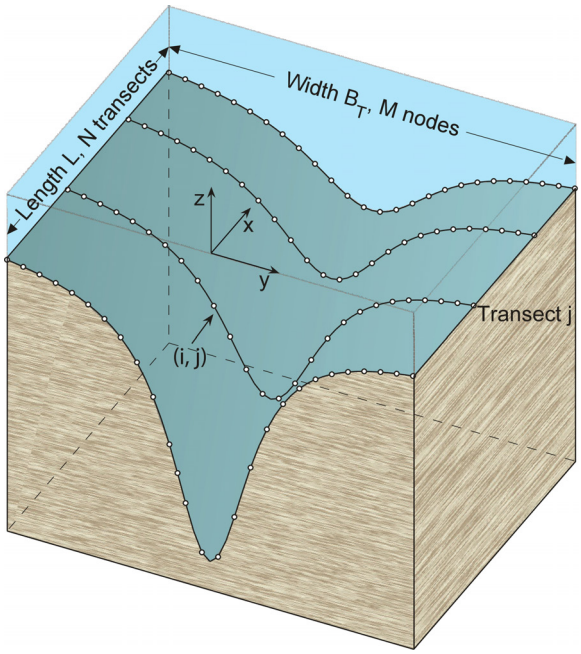

Figure 4.5: Sketch of the computational domain.

Re-gridding techniques

A proper description of the cross sectional geometry requires the use of re-gridding techniques to vary the nodal distribution along each transect, refining the mesh within the channel region. The mathematical problem of re-gridding could be tackled in a general way through the use of unstructured meshes. The numerical implementation of these techniques is described in Quarteroni [2014]. Recently, some new methods (e.g., virtual element method and mimetic finite difference) have been developed whereby the classical mesh properties, such as aspect ratio and delauney condition, do not need to be satisfied [see, e.g. Manzini, 2011; Manzini et al., 2014]. In the present contribution, non uniform spacing functions have been used to define the nodal positions along each transect. Two useful algebraic relationships for nodal

distribution are [Date, 2009]:

$$\frac{y(i)}{L} = \left[\frac{i-1}{N-1}\right]^{\hat{n}}, \qquad \frac{y(i)}{L} = 1 - \left[1 - \frac{i-1}{N-1}\right]^{\hat{n}} \tag{4.19}$$

where $\hat{n}$ is a positive number which drives the nodal density. Here we used the second relation for nodal distribution assuming $\hat{n}$ equal to 1.5 .

Initial bathymetry

The formation of a tidal channel is simulated starting from a submerged horizontal plane with a prescribed incision along the axis domain. This initial bathymetry is also used to delineate initially channeled and un-channeled regions. Three different functions have been used to define the initial incision.

- Cosine function;

$$z_b(y) = \cos(\omega y + \varphi) \tag{4.20}$$

  with $\omega = 2\pi/\mathcal{B}_T$ the angular frequency, φ the phase and $\mathcal{B}_T$ the overall width of the tidal basin.

- *Witch of Agnesi* (or versoria);

$$z_b(y) = \frac{8\,a^3}{y^2 + 4\,a^2} \tag{4.21}$$

  where the parameter a controls the curve convexity.

- Gaussian function;

$$z_b(y) = \frac{1}{\sigma\sqrt{2\,\pi}}\, e^{-\frac{(y-\mu_y)^2}{2\,\sigma_y^2}} \tag{4.22}$$

  where the mean μ_y sets the position of the symmetry axis , while σ_y controls the curve shape.

4.3.2 The Exner equation finite difference scheme

The numerical approach to be used for the solution of equation (3.10) has to deal with two time scales. A short time scale t, which spans each tidal cycle of period T, and a long time scale $\mathfrak{t}$, which covers time intervals larger than a day, eventually reaching the time span $\mathcal{T}$. The following sections describe the numerical schemes implemented with respect to this time scale distinction.

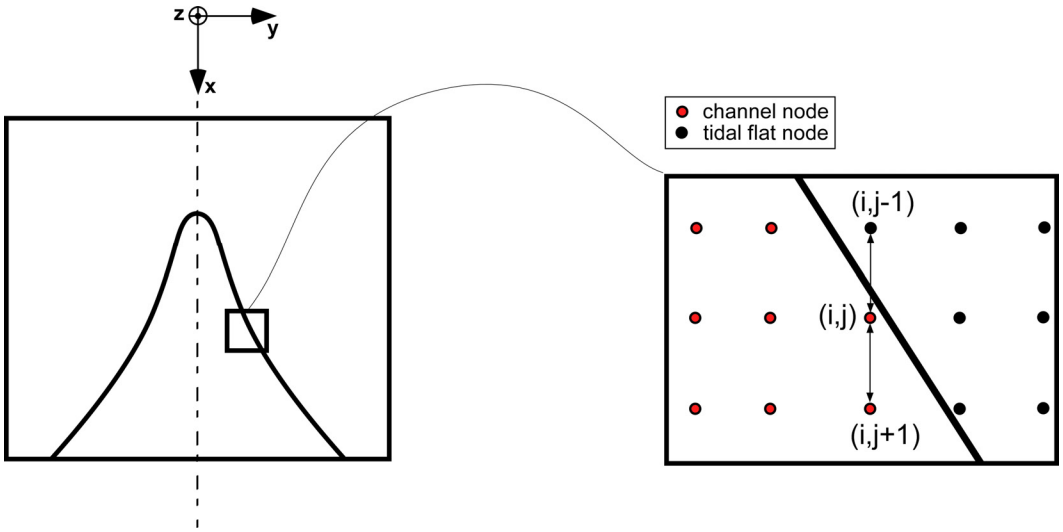

Figure 4.6: The q_b finite difference issue.

Short-term numerical scheme

For short time scales, many numerical schemes have been used to discretize the bed evolution equation (3.10) [Wu, 2008]. A quite common approach, based on a semi-implicit finite difference approximation, reads as follows:

$$(1-p)\frac{1}{\Delta t}\left\{z_{j,i}^{n+1} - \left[(1-\lambda)\, z_{j,i}^{n} + \frac{\lambda}{2}(z_{j-1,i}^{n} + z_{j+1,i}^{n})\right]\right\} + \frac{1}{2\Delta x}({Qsbx}_{j+1,i}^{n} - {Qsbx}_{j-1,i}^{n}) = \mathcal{D}_{j,i}^{n} - \mathcal{E}_{j,i}^{n} \tag{4.23}$$

where $z_{i,j}^{n}$ in the bed elevation at the generic grid node located at the position of coordinates $i\,\Delta x, j\,\Delta y$ and at time $n\,\Delta t$. Here, i and j refer to the longitudinal and lateral directions, respectively, Δx is the longitudinal grid step, Δy is the lateral grid step, and Δt is the time-step used to advance during each tidal period. Finally, λ is a weighting coefficient used to introduce (when $\lambda > 0$) dissipative interfaces which may stabilize the numerical solution. Specifically, for $0 < \lambda < 1/2$ the procedure is conditionally stable while it is unconditionally stable for $1/2 \leq \lambda < 1$ [Abbott and Basco, 1989]. On the other hand, setting $\lambda = 0$ avoids any dissipation interface, and the scheme becomes fully explicit:

$$(1-p)\frac{1}{\Delta t}(z_{j,i}^{n+1} - z_{j,i}^{n}) + \frac{1}{2\Delta x}({Qsbx}_{j+1,i}^{n} - {Qsbx}_{j-1,i}^{n}) = \mathcal{D}_{j,i}^{n} - \mathcal{E}_{j,i}^{n} \tag{4.24}$$

However, within the present hydrodynamic framework, the use of schemes such as those provided by the algebraic equations (4.23) and (4.24) to obtain a 3D description of the bed evolution can lead to flawed results. Indeed, when centered or

weighted difference approximations are adopted with respect to spatial variables, elimination of physically meaningful topographic features may be forced. Specifically, when the weighted difference discretization (4.23) is applied across the boundary between the main channel and the adjacent tidal flats (Figure 4.6), the numerical scheme favors the progressive smoothing of differences in bed elevation and drives a progressive loss of convergence in the main channel. In other words, the channel width tends to become constant along the whole tidal basin. This is due to the fact that the 1D hydrodynamic model describes the flow only within the main channel, while the tidal flats are assumed to concur only to store water and to the overall friction. Hence, even though the erosion/deposition rates, computed on the basis of the local values of the bed shear stresses, can be quite close to the actual values (as emerging from the comparison with a 2D model described in the previous Chapter), the use of three-points difference schemes such as those of equations (4.23) and (4.24) can lead to a distorted bed evolution. In summary, a 2D hydraulic approach has to be used in conjunction with the discretized bed evolution equations (4.23) and (4.24).

In order to overcome the above difficulties, we used forward difference schemes for spatial variables. Neglecting the contribution of the bed load transport and relying on fully explicit schemes, the discretized form of the bed evolution equation reads (with $p = 0$):

$$z_{j,i}^{n+1} = z_{j,i}^{n} + \Delta t \left(\mathcal{D}_{j,i}^{n} - \mathcal{E}_{j,i}^{n} \right) \tag{4.25}$$

where the values of $\mathcal{D}$ and $\mathcal{E}$ are computed by considering the bed shear stresses resulting from equation (4.14).

Clearly, the decoupled approach used here to describe separately the spatio-temporal distribution of the bed shear stresses and the corresponding bed evolution, raises the question of how one can update in time the bed domain [Roelvink, 2006]. Two methodologies are possible: *offline* bed update and *online* bed update. The first technique is based on the assumption that morphological changes occurring within a tidal cycle do not influence the hydrodynamics. If this hypothesis holds, the bed is considered fixed during a tidal cycle and the bed is updated at the end of the tidal cycle. Conversely, the *online* technique applies the scheme (4.25) at every time step, updating the bed just after the spatial distribution of the bed shear stresses is computed through the procedure described in Section 4.2.

Long-term numerical scheme

In the case of long term simulations, the bed updating approach described in the previous section generally requires too long computational times. A morphological

factor is thus commonly adopted to accelerate the bed evolution computations ([e.g., MORfological acceleration FACtor, Roelvink, 2006]). Specifically, the bed update is accelerated introducing in the sediment balance equation a coefficient, whose magnitude is a measure of the bed update acceleration. For example, running a simulation for a day and then applying a morphological acceleration factor of 30, the updated bed is assumed to describe the bathymetry that would occur after 30 days. The greater is the morphological factor, the faster is the update.

The correct use of morphological acceleration factors is still a hot topic in morphodynamics. Experimental attempts have been made to use laboratory data for model validation [Knaapen and Joustra, 2012]. Theoretical analyses have also been put forward to determine the largest value that can be attributed to the morphological factor [Carraro et al., 2018; Ranasinghe et al., 2011], and to determine new morphodynamic upscaling techniques [Carraro et al., 2018]. At the moment, a trial procedure is commonly used to tune the morphological factor for the considered model and the computational domain under investigation [Deltares, 2014].

Adopting the *offline* bed update procedure described above, the sediment balance equation is integrated over the long time scale $\mathcal{T}$:

$$\int_0^{\mathcal{T}} \frac{dz_{j,i}}{d\mathfrak{t}}\, d\mathfrak{t} = \int_0^{\mathcal{T}} (\mathcal{D}_{j,i} - \mathcal{E}_{j,i})\, dt \tag{4.26}$$

where $\mathcal{E}$ and $\mathcal{D}$ represent the long term erosion and deposition rates, respectively. The integral on the left hand side can be approximated as a sum of erosion and deposition rates over the considered time window, namely:

$$\mathcal{Z} = \sum_i^{\mathcal{T}} (\mathcal{D}_{j,i} - \mathcal{E}_{j,i})\, \Delta\mathfrak{t}_i \tag{4.27}$$

$$= \left(\sum_i^{\mathcal{T}} (\mathcal{D}_{j,i} - \mathcal{E}_{j,i})\, \Delta t_i \right) f_{MOR} \tag{4.28}$$

where $\mathcal{T} = N_{\mathcal{T}}\, \mathfrak{t}_i$.

Conversely, when using the *online* bed update, the acceleration is achieved by simply multiplying the erosion and deposition rates (4.25) by the morphological factor:

$$z_{j,i}^{n+1} = z_{j,i}^{n} + f_{MOR}\, \Delta t \left(\mathcal{D}_{j,i}^{n} - \mathcal{E}_{j,i}^{n} \right) \tag{4.29}$$

In the present thesis a *offline* approach have been used, in accordance with previous analyses on long term simulations of tidal environments [D'Alpaos et al., 2006; Fagherazzi and Furbish, 2001; Lanzoni and D'Alpaos, 2015].

4.3.3 The shear-stress distribution finite difference scheme

For each transect, the numerical integration of equation (4.14) is obtained by using a center difference scheme on a non-uniform spaced grid [Ferziger and Perić, 2002]. Following the procedure of Pizzuto [1990], we obtain:

$$\tau_j - \frac{2}{\Delta n_R + \Delta n_L}\left(\mathcal{K}_R \frac{\tau_{j+1}-\tau_j}{\Delta n_R} - \mathcal{K}_L \frac{\tau_j - \tau_{j-1}}{\Delta n_L}\right) = \varrho\, g\, S_j \frac{1}{2}\left[\frac{\mathcal{A}_{j-1}}{\Delta n_L} + \frac{\mathcal{A}_j}{\Delta n_R}\right] \tag{4.30}$$

where n_R and n_L denote the value attained by the transversal coordinate n at the right and left ends, respectively, of discretization stencil. Collecting the terms containing the shear stresses at nodes $j-1$, j, $j+1$, this equation yields:

$$\left[-\frac{2}{\Delta n_R + \Delta n_L}\frac{\mathcal{K}_L}{\Delta n_L}\right]\tau_{j-1} + \left[1 + \frac{2}{\Delta n_R + \Delta n_L}\left(\frac{\mathcal{K}_L}{\Delta n_L} + \frac{\mathcal{K}_R}{\Delta n_R}\right)\right]\tau_j + \left[-\frac{2}{\Delta n_R + \Delta n_L}\frac{\mathcal{K}_R}{\Delta n_R}\right]\tau_{j+1} = \varrho\, g\, S_j \frac{1}{2}\left[\frac{\mathcal{A}_{j-1}}{\Delta n_L} + \frac{\mathcal{A}_j}{\Delta n_R}\right]$$

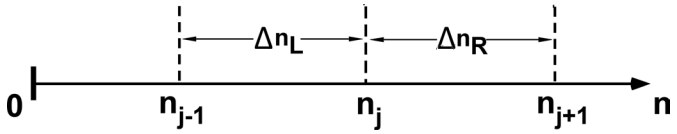

Figure 4.7: Discretization stencil. L:left; R:right.

Setting

$$\Delta n_R = P_j, \quad \Delta n_L = P_{j-1}, \quad \mathcal{K}_L = \frac{1}{2}(\mathcal{K}_j + \mathcal{K}_{j-1}) \quad \mathcal{K}_R = \frac{1}{2}(\mathcal{K}_{j+1} + \mathcal{K}_j) \tag{4.31}$$

and re-arranging all terms, the previous equation becomes:

$$\underbrace{\left[-\frac{\mathcal{K}_j + \mathcal{K}_{j-1}}{P_j + P_{j-1}}\frac{1}{P_{j-1}}\right]}_{=\widehat{A}_{j-1}}\tau_{j-1} + \underbrace{\left[1 + \frac{1}{P_j + P_{j-1}}\left(\frac{\mathcal{K}_j + \mathcal{K}_{j-1}}{P_{j-1}} + \frac{\mathcal{K}_{j+1} + \mathcal{K}_j}{P_j}\right)\right]}_{=\widehat{B}_j}\tau_j + \underbrace{\left[-\frac{\mathcal{K}_{j+1} + \mathcal{K}_j}{P_j + P_{j-1}}\frac{1}{P_j}\right]}_{=\widehat{C}_{j+1}}\tau_{j+1} = \underbrace{\varrho\, g\, S_j \frac{1}{2}\left[\frac{\mathcal{A}_{j-1}}{P_{j-1}} + \frac{\mathcal{A}_j}{P_j}\right]}_{=\widehat{R}_j}$$

namely

$$\widehat{A}_{j-1}\,\tau_{j-1} + \widehat{B}_j\,\tau_j + \widehat{C}_{j+1}\,\tau_{j+1} = \widehat{R}_j \tag{4.32}$$

The linear algebraic system resulting from the discretization of equation (4.14) must be complemented with suitable boundary conditions. Here we require that no momentum exchange is allowed at the lateral cross section boundaries:

$$\tau_j = g\,S\,D_j \qquad j = 1, n \tag{4.33}$$

where D_j is the local water depth measured along the normal passing through the node j.

The overall tridiagonal system build up by assembling all the algebraic equations (4.32) ($j = 2, n-1$) takes the form:

$$\begin{bmatrix} 1 & 0 & & & & & & \\ \widehat{A}_2 & \widehat{B}_2 & \widehat{C}_2 & & & & & \\ & \ddots & \ddots & \ddots & & & & \\ & & \widehat{A}_j & \widehat{B}_j & \widehat{C}_j & & & \\ & & & \ddots & \ddots & \ddots & & \\ & & & & \widehat{A}_{n-1} & \widehat{B}_{n-1} & \widehat{C}_{n-1} \\ & & & & & 0 & 1 \end{bmatrix} \begin{bmatrix} \tau_1 \\ \tau_2 \\ \vdots \\ \tau_j \\ \vdots \\ \tau_{n-1} \\ \tau_n \end{bmatrix} = \begin{bmatrix} \varrho\,g\,S\,D_1 \\ \widehat{R}_2 \\ \vdots \\ \widehat{R}_j \\ \vdots \\ \widehat{R}_{n-1} \\ \varrho\,g\,S\,D_n \end{bmatrix} \tag{4.34}$$

where the number of rows and columns equals the number of nodes along the cross section.

When vegetation encroaches the marsh platform, the previous linear system slightly changes, owing to the vanishing of dispersive terms over the vegetated surface (Figure 4.4). Thereby, the overall algebraic system becomes:

$$\begin{bmatrix} 1 & 0 & & & & & & & & \\ 0 & 1 & 0 & & & & & & & \\ & \ddots & \ddots & \ddots & & & & & & \\ & & \widehat{A}_j & \widehat{B}_j & \widehat{C}_j & & & & & \\ & & & \ddots & \ddots & \ddots & & & & \\ & & & & \widehat{A}_{j+m} & \widehat{B}_{j+m} & \widehat{C}_{j+m} & & & \\ & & & & & \ddots & \ddots & \ddots & & \\ & & & & & & 0 & 1 & 0 \\ & & & & & & & 0 & 1 \end{bmatrix} \begin{bmatrix} \tau_1 \\ \tau_2 \\ \vdots \\ \tau_j \\ \vdots \\ \tau_{j+m} \\ \vdots \\ \tau_{n-1} \\ \tau_n \end{bmatrix} = \begin{bmatrix} \varrho\,g\,S\,D_1 \\ \varrho\,g\,S\,D_2 \\ \vdots \\ \widehat{R}_j \\ \vdots \\ \widehat{R}_{j+m} \\ \vdots \\ \varrho\,g\,S\,D_{n-1} \\ \varrho\,g\,S\,D_n \end{bmatrix} \tag{4.35}$$

Differently from Pizzuto [1990] and Fagherazzi and Furbish [2001], who applied

the Thomas algorithm, the tridiagonal systems (4.34) and (4.35) are solved by a LU factorization [D'Alpaos et al., 2006; Lanzoni and D'Alpaos, 2015].

4.3.4 Cross-sectional geometry issues

Let us for the moment consider a quasi-static propagation of the tidal wave and disregard additional effects such as sea level rise, external suspended sediment supply and vegetation encroachment. Under these conditions, the numerical solution of equation (4.14) has been used to investigate various aspects of short tidal channels morphology D'Alpaos et al. [2006]; Fagherazzi and Furbish [2001]; Lanzoni and D'Alpaos [2015] that have been then compared with field observations [Lanzoni and D'Alpaos, 2015; Marani et al., 2002]. The computed channel cross sections were usually wide enough to satisfy the assumption of a gently varying bottom curvature set at the basis of equation (4.14) [Lundgren and Jonnson, 1964].

However, when the above mentioned additional effects are taken into account, tidal channels may become narrower and deeper, thus implying relatively smaller width-to-depth ratios. Under these conditions, the normal rays can start to intersect each other (Figure 4.8), thus complicating the identification of the various sub-areas and, consequently, the computation of the coefficient $\mathcal{K}$ driving the momentum exchange between rays. The narrower the cross sections become, the harder it becomes evaluating not only the energy slope term, because area subdivisions are unreliable, but also the dispersive term, because normal depths used to compute the coefficient $\mathcal{K}$ are also questionable. The issue arises in narrow cross sections for which the assumption of a bed gently sloping in the transverse direction does not hold any more, even though it must be noted that the interception between normal rays usually occurs for high water stages, when the velocity, and hence the shear stresses are likely to be small. Note also that the assumption of a logarithmic velocity profile along the normal to the wall can in principle be used also when normal rays intersects [Marchi, 1961]. Clearly, other processes, such as secondary currents neglected so far, may start to affect the shear stress distribution.

In order to overcome the above mentioned problems, here we consider a very simple approach. If interceptions occur, the normal rays are corrected automatically such that rays, no longer orthogonal to the bed, intercept at the water surface (red lines in Figure 4.8). Assumed a logarithmic profile is assumed up along the corrected ray, the new outline of rays and sub-areas is used to perform the computations of shear stress distribution in equation (4.9).

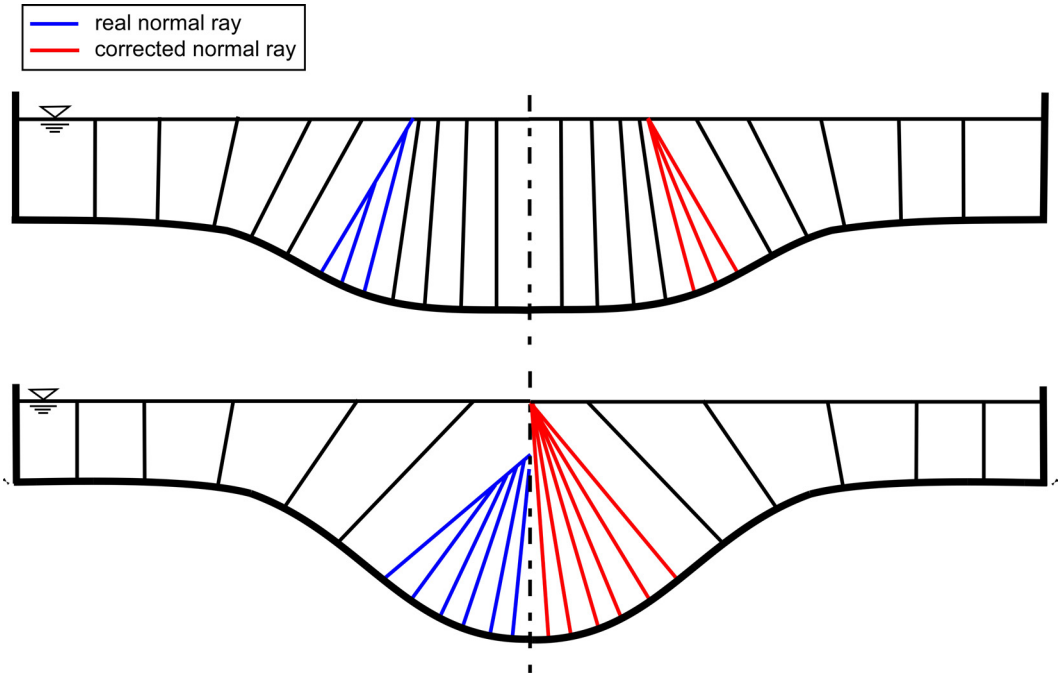

Figure 4.8: Examples of interceptions between normal rays (blue lines) and approximations used (red lines) to manage these situations.

4.3.5 Numerical code flowchart

The model is composed by four modules: the hydrodynamic module that is used to compute the 1D hydrodynamics of the tidal basin; the shear stress distribution module, that uses the energy slope provided for each cross section by the hydrodynamic module; the morphodynamic module that uses the spatial distribution of shear stress to compute accretion/erosion rates and, eventually, evolves the bed of the tidal basin (Figure 4.9).

For each simulation, the relevant input data and parameters are prescribed (Table 4.1) with reference to an initially prescribed or a previously computed bathymetry. At each time step of the long term time scale on which the tidal domain bed evolves, the hydrodynamic module is used to compute the 1D flow field that establishes in the domain under the action of the seaward imposed tidal forcing. At the other three boundaries no flux conditions are imposed and, during the the whole tidal cycle the domain bed is kept fixed (Chapter 2).

The energy slope provided by the 1D model at each instant of the tidal cycle for the various cross sections is then used to determine the cross-sectional shear stress distribution as described in Section 4.2. It is worthwhile to note that, differently from earlier researches [D'Alpaos et al., 2006; Fagherazzi and Furbish, 2001; Lanzoni and D'Alpaos, 2015], in the present approach, the value of the energy slope results from 1D hydraulic computations, rather than from an iteration procedure carried

out to ensure that a suitable discharge (computed though a quasi-static continuity balance) flows within the section.

The spatio-temporal distribution of bed shear stresses is used to estimate the local erosion and deposition rates that are eventually needed by the morphodynamic module to evolve the bed of the tidal domain (chapter 3). Specifically, relying on an *offline* technique, at the end of a tidal cycle the tidally averaged values of erosion and deposition rates are used to update the local bed elevations using an acceleration factor of 30 days.

The updated bathymetry then becomes the new computational domain and the above described procedure is repeated until the system reaches an equilibrium configuration. The overall run duration is set by a test/trial procedure such that it is long enough to let the basin reach everywhere asymptotically constant bed elevations.

The overall model can be used with three different setups.

1. Purely erosional model: sediment erosion is the only process shaping the channel;

2. Depositional model: erosion, sea level rise (SLR) and settling deposition (SSC) are the mechanisms that concur to determine the fate of the tidal basin;

3. Vegetated model: vegetation effects are included in the depositional model.

In the following sections the results of these setups will be discussed in detail. In particular, the purely erosional model will be used to validate the present framework by comparison with a previously developed model [Lanzoni and D'Alpaos, 2015] and field observations.

4.4 Model sensitivity to the acceleration of the morphological factor

The sensitivity of the present modeling framework to changes in the morphological factor has been addressed by considering a rectangular basin, 2000 m long and 200 m wide, with a small incision, 0.05 m deep, along the axis. The basin is initially set at an elevation of -0.5 m a.m.s.l., and is subjected to a semi-diurnal tide of amplitude 0.5 m, and to a RSLR rate of 3.5 mm/yr. The external suspended sediment supply is surrogated by assuming a concentration $C_0 = 10.0$ mg/l, constant in space and time as described in Chapter 3. For a given bed topography of the basin, the 1D model described in Chapter 2 was used to compute the energy slope S_f at each cross section and at each instant of the tidal cycle. The spatio-temporal distribution of S_f was then used to determine the bed shear stress distribution $\tau_{i,j}$ across each

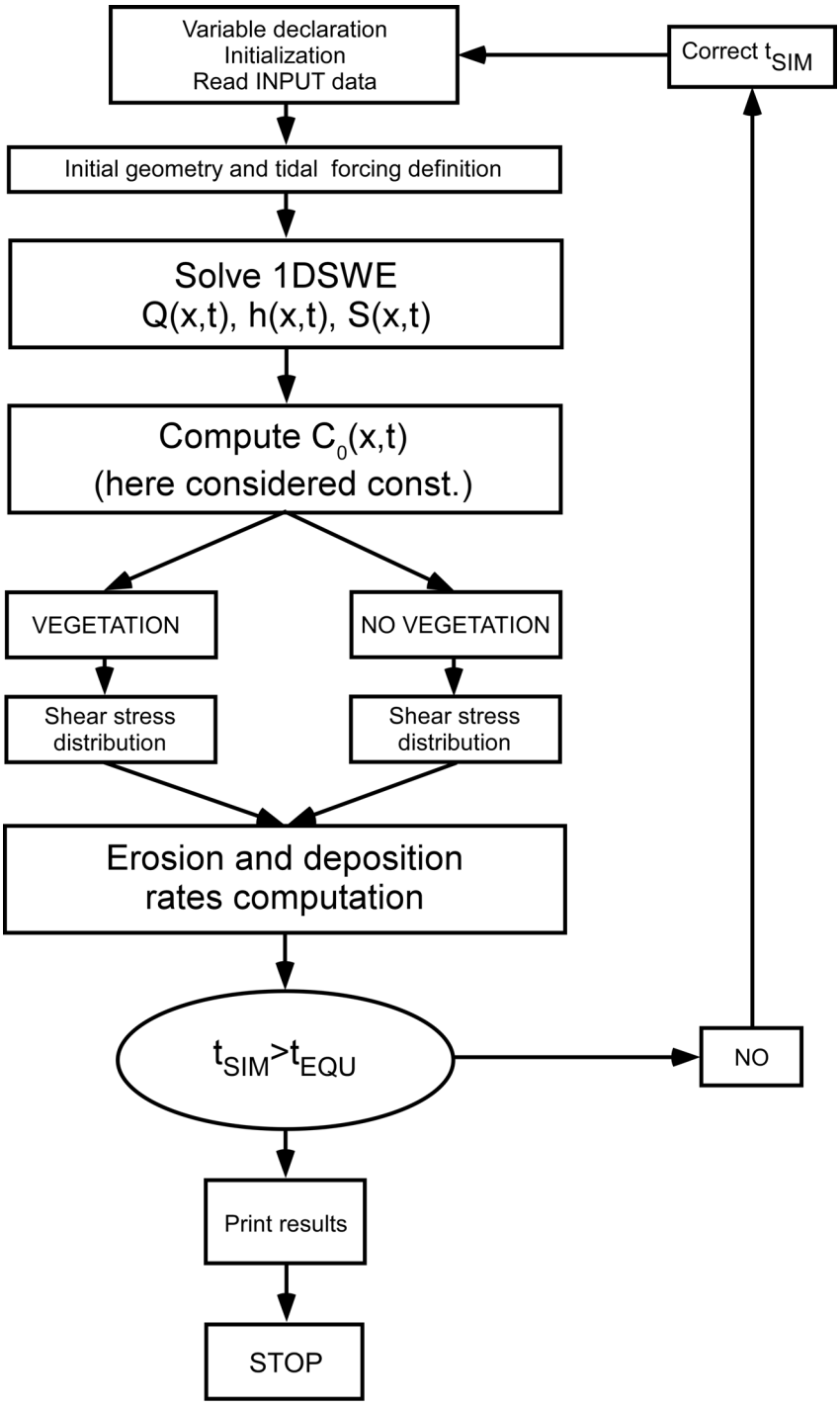

Figure 4.9: Code flowchart.

basin transect, as described in Section 4.14. Different values of the morphological factor f_{MOR} (5, 15, 30, 60, 120) were then used to accelerate the computations, starting from the same initial conditions up to an equilibrium configuration (i.e., when the mean difference in bed elevations throughout the basin at two consecutive time steps, normalized by the average depth, was smaller than a given tolerance, say 5%).

Figure 4.10a shows the bed elevation of the channel axis at the seaward end for different values of f_{MOR}. Note that bed elevations are not corrected for the sea level rise, i.e., they are computed with respect to a fixed reference frame. Erosion clearly prevails at the beginning, producing a net scour of the channel bed. As the channel deepens, shear stresses reduce and deposition starts. At the end of the simulation (300 years) all processes (i.e., erosion, deposition and sea level rise) concur to produce a dynamic equilibrium. Small differences are evident in the bed evolution when using different values of f_{MOR}. Nevertheless, the equilibrium elevation attained by the channel axis elevation (Figure 4.10b) varies relatively weakly. The decrease in the equilibrium elevation as f_{MOR} increases is approximately linear, and exceeds 10 cm only for $f_{MOR} > 30$. Based on this sensitivity analysis, we then will set $f_{MOR} = 30$ in all the following simulations.

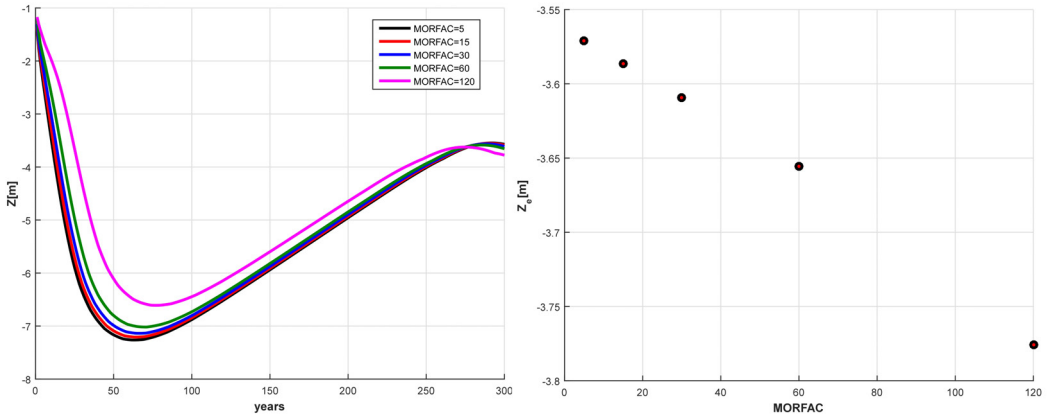

Figure 4.10: Effects on the equilibrium channel configuration of different values of the morphological factor f_{MOR}. a) Temporal evolution of the channel axis elevation at the seaward cross-section; b) Equilibrium elevation of the seaward channel axis for different f_{MOR} values.

4.5 Model validation

Model validation has been carried out by considering the purely erosional setup. The morphological time used for these simulations is 300 years, i.e., 3600 months. For any new bathymetry, the hydrodynamic model runs for two tidal cycles, in order to ensure a full adaptation of the flow field to the new bed topography. The tidally

averaged erosion and deposition rates resulting from the last of these three cycles are then multiplied for an acceleration factor of 30. The input data and parameters fixed in all runs are reported in Table 4.1.

Parameter	***Value***	***Unit***
ρ_s	2650	kg/m^3
w_s	$2 \cdot 10^{-4}$	m/s
D_{50}	0.5	mm
τ_{cd}	0.1	N/m^2
τ_{ce}	0.4	N/m^2
$\mathcal{E}_0$	$2 \cdot 10^{-4}$	$kg/m^2/s$
T	12	h

Table 4.1: Parameters adopted in the runs carried out for validating the model: ρ_s sediment density; w_s settling velocity; D_{50} mean sediment grain size; τ_{cd} critical threshold for deposition; τ_{ce} critical threshold for erosion; $\mathcal{E}_0$ empirically-based erosion rate due to sediment features.

4.5.1 General features of the morphodynamic evolution

Let us consider a tidal basin 2000 m long and 200 m wide. The basin is subjected to a sinusoidal tide with an amplitude of 0.5 m, acting at the seaward boundary. No-flux conditions are imposed at the landward and lateral boundaries. The initial bed, set at an elevation of -0.5 m a.m.s.l. is perturbed by an incision shaped by a cosine function with amplitude of 0.05 m to trigger the channel formation. Figure 4.11 shows successive stages of the tidal channel evolution. A main channel starts to grow, deepening and stretching in the landward direction and developing a certain degree of convergence. Gradually, the distinction between lateral shoals and the main channel becomes clearer. Once the main channel has reached its maximum length, it keeps on adjusting its depths. On the contrary, the elevation of the tidal flats remains constant approximately at the initial elevation, owing to the "small" values (smaller than the critical threshold for erosion) attained by the bed shear stresses acting on them. Eventually, the channel head vanishes abruptly in the landward unchanneled platform.

The various evolution stages clearly appear from the longitudinal profiles shown in Figure 4.12a. At the beginning, the channel axis deepens exhibiting an almost linear profile. As the simulation goes on, the erosion progressively leads to the incision of a deeper (and larger) channel that, as the landward head eventually tends to form an abrupt transition to the landward platform. This transition behaves as a bathymetric jump which prevents the developing of a convex profile in the upper part of the tidal basin. At the foot of this jump, wiggles are observed to form as a consequence of the abrupt changes in the energy slope associated with the

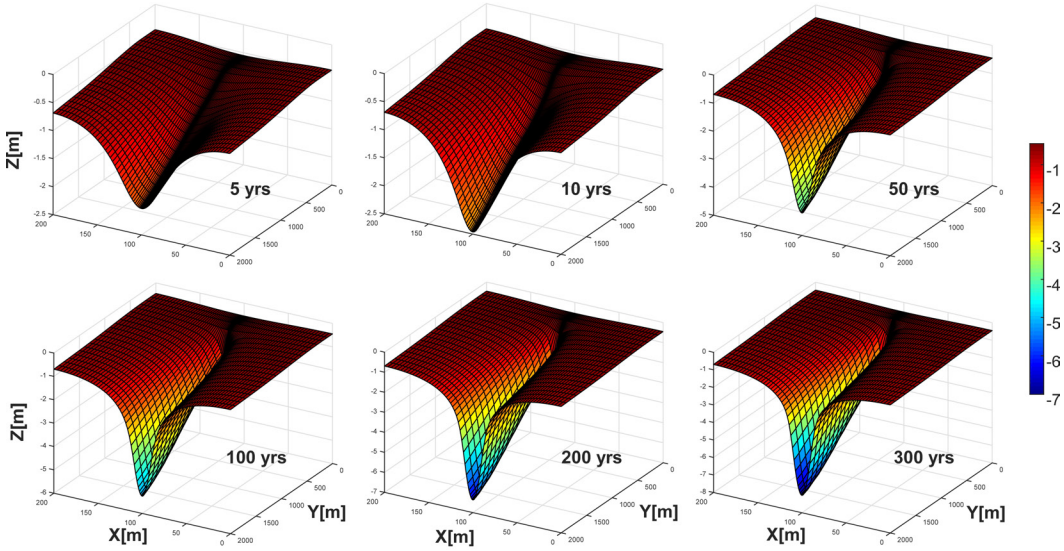

Figure 4.11: Evolution of a 2000 m long and 200 m wide tidal basin computed for purely erosional conditions. The reference case depicted here corresponds to a sinusoidal tidal forcing of amplitude 0.5 m; the initial elevation of the tidal flats flanking the main channel is −0.5 m a.m.s.l.

bathymetric jump. Except for this channel head region, the final longitudinal bed configuration resembles the analytical profiles obtained under equilibrium conditions by various authors, e.g. Friedrichs and Aubrey [1996]; Schuttelaars and De Swart [1999]; Seminara et al. [2010]; Toffolon and Lanzoni [2010] as well as experimental profiles [Tambroni et al., 2005].

The time tracking of channel axis elevation and lateral shoal elevations at the seaward cross section over the entire duration of the simulation highlights the route towards morphodynamic equilibrium (Figure 4.12b). Tidal flats do not change their initial elevation, owing to the small values attained by the bed shear stresses acting on them. Conversely, flow concentration in the initially (cosine shaped) channelized region triggers an erosion that rapidly scours the main channel bed, whose depth after a quite fast increase, later on tends asymptotically towards a constant value. Indeed, as the run proceeds, channel deepening implies a reduction of flow velocities bed shear stresses and, hence, erosion rates. When shear stresses fall below the critical threshold erosion, erosion rates slowly vanish (recall relation (3.12)). Eventually, a static equilibrium is reached [Seminara et al., 2010], whereby a no erosion condition establishes everywhere throughout the tidal basin.

4.5.2 Sensitivity analysis

The model robustness has been tested performing a sensitivity analysis involving domain dimensions (L, B_T), initial bathymetry height ($z_{in,tf}$), tidal amplitude a_0, critical shear stress (τ_{ce}), friction coefficient k_s and the basin aspect ratio as

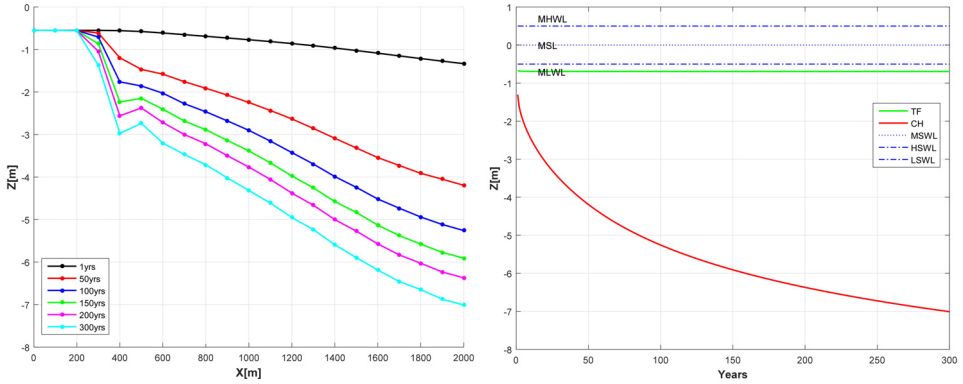

Figure 4.12: a) Longitudinal profiles obtained at different times with the purely erosional model. b) Temporal evolution of channel axis elevation and tidal flat elevation computed at the seaward boundary. Reference case as explained in the caption of Figure 4.11.

in Lanzoni and D'Alpaos [2015] (Table 4.2). The results have been compared with those obtained by Lanzoni and D'Alpaos [2015]. Their model (hereafter denoted as LD15) differs from the present one for the following aspects. The LD15 hydrodynamics is based on a 0D quasi-static approach, whereby the water level keeps horizontal when oscillating in response to the tidal forcing. Wetting and drying processes are not accounted for explicitly, but at the beginning of a given simulation, when the basin is very shallow, the tidal amplitude is increased gradually up to the prescribed value. To this aim, a suitable tidal lag is adopted. Finally, the energy slope employed to compute the shear stresses distribution across a section is determined through an iteration procedure which stops when the discharge flowing through the section (sum of the discharges in the sub-areas) equals that provided by the continuity equation.

The longitudinal profile and the width distribution computed in the various tests (Table 4.2) are represented in Figure 4.13. As the basin widens, the channel gets deeper and larger, conveying more flow in both the ebb and flood phases. Note that the typical saw-like trend characterizing the longitudinal distribution of main channel width is due to the criterion used for detecting it. Successive cross sections can exhibit the same width if the traversal slope of the channel borders remains almost the same in adjacent transects. Overall, the width distribution shows a quite linear trend, except close to the main channel head where the channel bed wets and dries during the tidal cycle and the width decreases faster than linearly, in agreement with previous findings [Lanzoni and Seminara, 2002]. Considering the tidal forcing, the larger the tidal amplitude, the deeper is the channel.

The longitudinal profile shows an approximately linear trend except towards the channel head, where it joins to the landward intertidal platform with a sharp transition. As the amplitude increases, this transition becomes sharper and some wiggles

Run	**L** $[m]$	B_T $[m]$	$z_{in,tf}$ $[m]$	a_0 $[m]$	τ_{ce} $[N/m^2]$	k_s $[m^{1/3}/s]$
$I1$	2000	100	-0.5	0.5	0.4	30
$I2$	2000	200	-0.5	0.5	0.4	30
$I3$	2000	300	-0.5	0.5	0.4	30
$I4$	2000	400	-0.5	0.5	0.4	30
$I5$	2000	500	-0.5	0.5	0.4	30
$II1$	2000	300	-0.5	0.3	0.4	30
$II2$	2000	300	-0.5	0.4	0.4	30
$II3$	2000	300	-0.5	0.6	0.4	30
$II4$	2000	300	-0.5	0.7	0.4	30
$III1$	2000	300	-0.1	0.7	0.4	30
$III2$	2000	300	-0.3	0.7	0.4	30
$III3$	2000	300	-0.7	0.7	0.4	30
$III4$	2000	300	-1.0	0.7	0.4	30
$IV1$	2000	300	-0.5	0.5	0.2	30
$IV2$	2000	300	-0.5	0.5	0.3	30
$IV3$	2000	300	-0.5	0.5	0.5	30
$IV4$	2000	300	-0.5	0.5	0.6	30
$V1$	2000	300	-0.5	0.5	0.4	20
$V2$	2000	300	-0.5	0.5	0.4	25
$V3$	2000	300	-0.5	0.5	0.4	35
$V4$	2000	300	-0.5	0.5	0.4	40
$VI1$	3000	450	-0.5	0.5	0.4	30
$VI2$	4000	600	-0.5	0.5	0.4	30
$VI3$	6000	900	-0.5	0.5	0.4	30
$VI4$	3000	75	-0.5	0.5	0.4	30
$VI5$	500	75	-0.1	0.5	0.4	30

Table 4.2: Runs used to validate the purely erosional model, as described in Lanzoni and D'Alpaos [2015].

arise at the tow of the jump. Moreover, an increasing tidal amplitude not only does lead to a deeper channel, but also to a longer channel. Looking at the width distributions, it is clear that for small tidal amplitudes the channel region extends just for half of the basin length. Above a certain amplitude, all the bathymetries have the same channel length, but different depths. A change in the initial elevation of the intertidal flats influences the initial rate of scouring. The shallower is the initial tidal basin, the deeper eventually becomes the main channel. Indeed, as no deposition is here considered, the channel has no possibilities to recover from this intense initial scour. In addition, an initially shallower tidal basin does not promote the formation of wiggles at the transition from the channel head to the landward intertidal platform. This result is due to the much intense erosion that occurs in a shallower basin, whereby a deeper main channel is generated and the final static equilibrium is reached faster. Essentially, the trends observed for the main channel width and the channel bed profile for a shallower initial basin are quite similar to those observed for a wider tidal basin. In both cases the initial channel scour is enhanced and, therefore, morphological equilibrium is reached faster. The critical threshold for erosion has interesting effects on the channel evolution. It seems to affect the equilibrium channel depth throughout most of the basins, except at the seaward boundary. As the critical threshold decreases, erosion increases making the channel to stretch landward and to get deeper. Moreover, the wiggles forming towards the channel head tend to disappear. Far enough from the channel head, the bed profile keeps an almost linear trend, the width changes slightly such that the degree of convergence does not change so much as well. Finally, the larger the friction coefficient, the deeper and shorter is the channel. As k_s increases, the profile gets smoother keeping the same linear-convex shape. On the other hand, a higher friction implies a progressive stretching of the main channel until the maximum length is attained; the bed wiggles near to the channel head increase as well.

The overall features of the channel morphologies obtained in the various tests is synthesized in the plots of Figure 4.14. They report: the cross-sectional area, A, as a function of the tidal prism, P; the mean channel depth, D, plotted versus channel width, B; the width-to-depth ratio, β, as a function of B. The first relation appears to follow the so called O'Brien-Jarrett-Marchi (OBJM) law, implying a power law relation with slope 6/7 throughout the entire main channel length. A small difference in the intersection with the A axis is however observed, suggesting larger values of A with respect to those prescribed by the empirically determined OBJM law. This difference is likely due to the different overall friction experienced by the synthetically generated topographies with respect to the calibration value determined on the basis of experimental data [D'Alpaos et al., 2009a]. The compliance with the OBJM law indicates that the cross sections within the main channel

eventually reach an equilibrium configuration. This equilibrium is invariably static, since just erosional effects are taken into account [D'Alpaos et al., 2009a].

Regarding the other two types of plot shown in Figure 4.14, we must note that widths are computed according to the criterion described in Chapter 2, while depths are those of the equivalent rectangular section having the same area and same width of the main channel cross section. Overall, the trends produced through the present model for purely erosive conditions are similar to those obtained through LD15's model. This is clearly shown in Figure 4.15 where the results of the present model under purely erosive conditions are denoted by red circles (bottom panel) while those of Lanzoni and D'Alpaos [2015] correspond to black circles (top panel). Despite the very similar trends shown by the $A - P$ plots, some systematic differences emerge in the $D - B$ and $\beta - B$ plots. This suggests that the morphologies generated with the present model are characterized by larger widths and smaller depths and, hence, larger width-to-depth ratios with respect to those produced by LD15's model. On the other hand, the comparison with the field data collected by [Marani et al., 2002], also shown in Figure 4.15 as crosses, indicates that the new synthetic cross sectional data match the field data better than the LD15's model.

In conclusion, despite the small wiggles which arise near to the channel head when the transition towards the landward intertidal platform becomes too steep, the overall geomorphic features of synthetically generated geometries match reasonably well literature data.

4.6 Concluding remarks

The theoretical framework adopted to compute the bed shear stress across any cross section of the tidal basin is found to produce realistic geometries. The novel feature is due to the hydraulic connection between the cross sections ensured by the 1D approach described in Chapter 2, which relaxes the assumption of a quasi-static propagation of the tidal wave commonly adopted in previous models and treats specifically wetting and drying processes. The need to use a suitable morphological factor to accelerate long-term simulations is also discussed and a *offline* procedure is selected for the present thesis. According to a trial procedure, MORFAC is set at 30 so that each timestep computation allows to update the bathymetry as after 30 days.

Under purely erosional conditions, used to test the model by comparison with previous numerical results and field data, a sharp edge tends to form near to the channel head, marking the transition to the upper intertidal flats located landward. In other words, the model does not produce a relatively smooth transition as that predicted by previous analytical computations [Friedrichs and Aubrey, 1996; Schut-

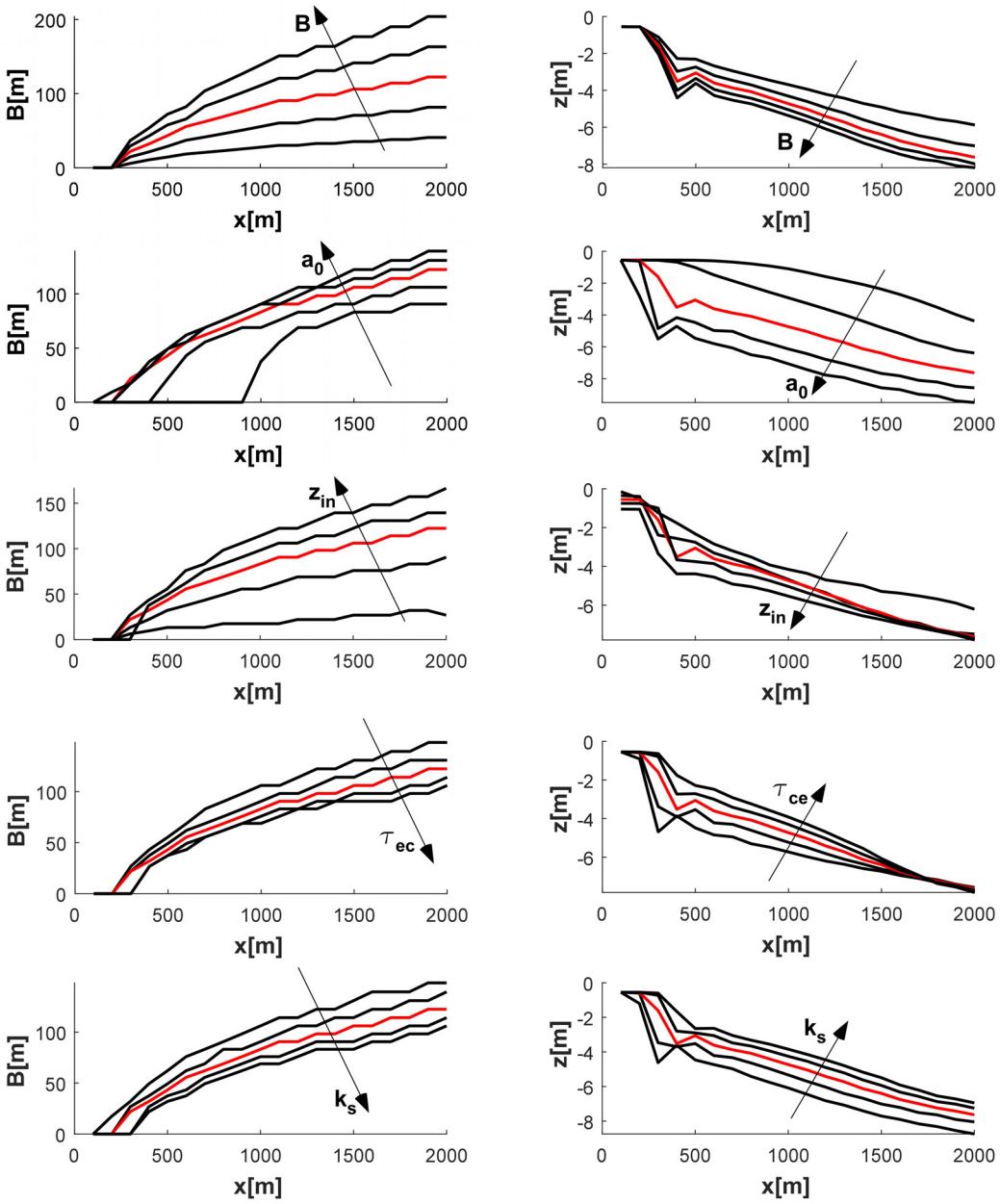

Figure 4.13: Width and bed profiles obtained using a purely erosional model. The red line denotes the reference test (see test I3 in Table 4.2). The ranges of the investigated paramenters are those reported in Table 4.2.

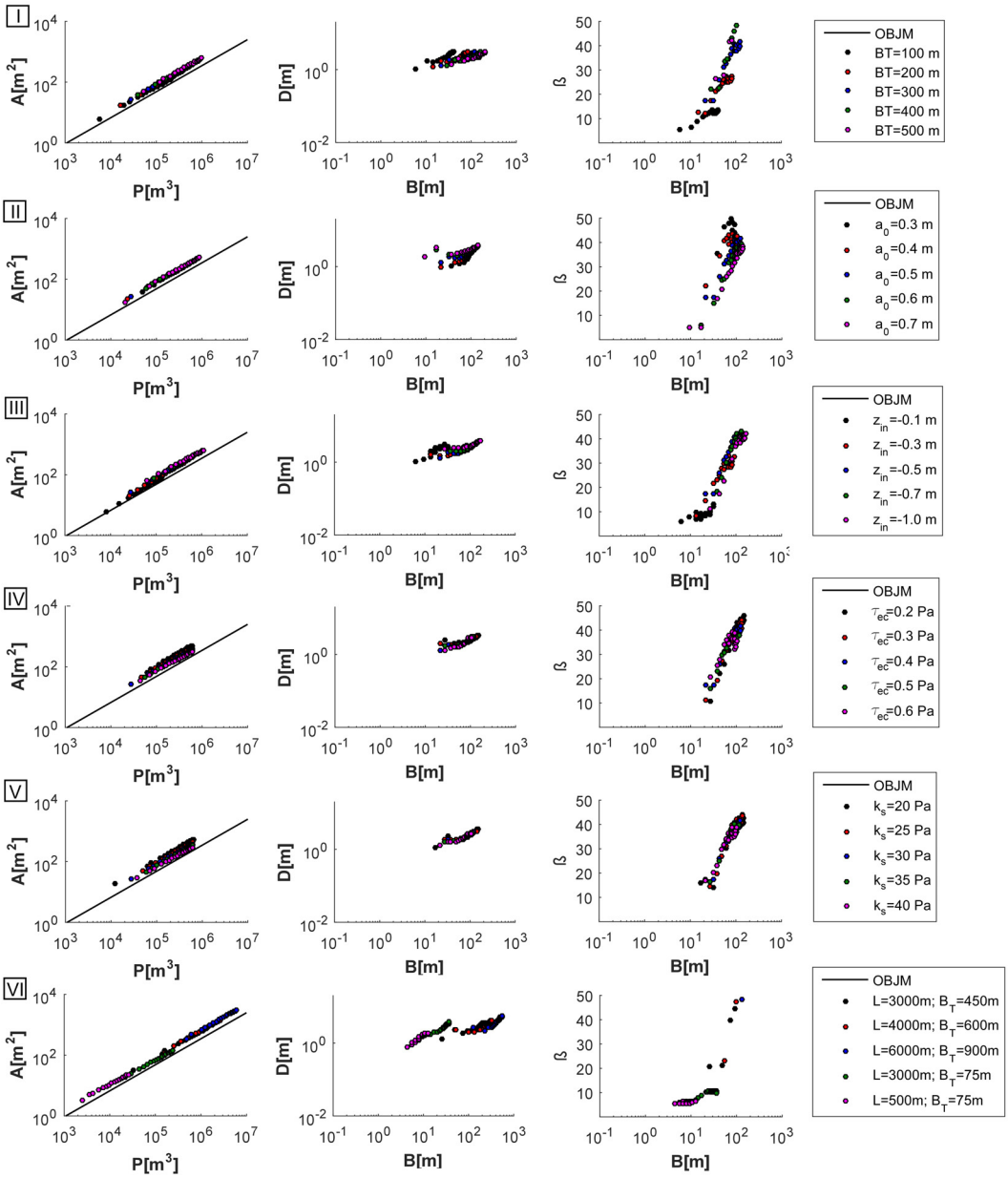

Figure 4.14: a) The cross-sectional area, A, is plotted versus the tidal prism, P, emphasizing the compliance with the O'Brien-Jarret-Marchi law; b) the mean flow depth, D, of the main channel cross section is plotted versus the corresponding width, B; c) the main channel width-to-depth, β, is plotted versus the main channel width, B relation.

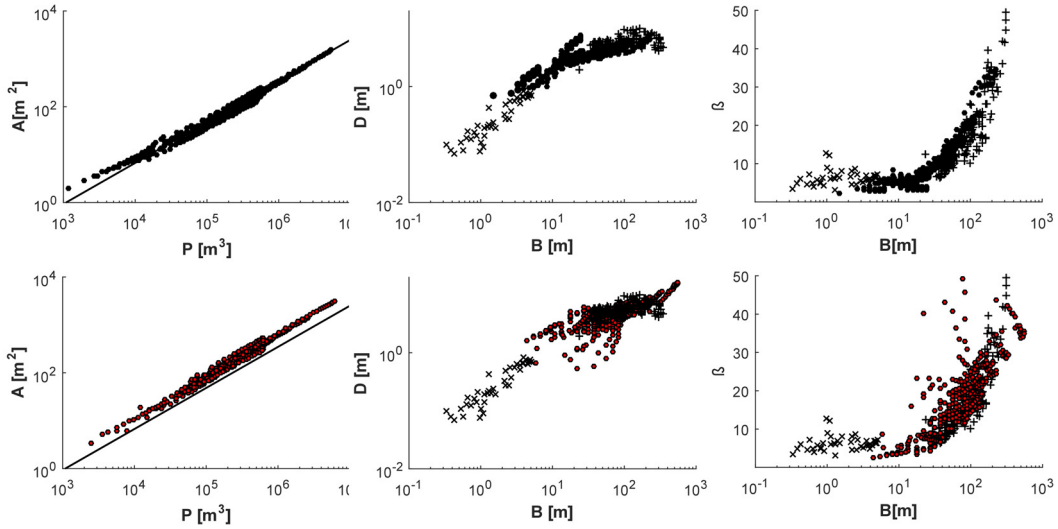

Figure 4.15: Comparison between the present computations, LD15's model and the field data measured in the Venice lagoon [Marani et al., 2002]. Red circles represent the present model results considering purely erosional effects (bottom panel). Black circles represent LD15's model results considering purely erosional effects (top panel). Field cross sectional data in Marani et al. [2002] are represented as crosses, if referred to channels dissecting salt marshes, as pluses, if referred to channels dissecting tidal flats.

telaars and De Swart, 1999; Seminara et al., 2010]. Despite these local effects, the OBJM law is satisfied along the entire channel, suggesting the establishment of morphological equilibrium conditions. This equilibrium is invariably static, because only erosional effects are accounted for. Overall, the geomorphological features of channel cross sections compare reasonably with those already found numerically or arising from field observations [Lanzoni and D'Alpaos, 2015; Marani et al., 2002]. In general, channel geometries produced by the present model cover a wider ranger of width-to-depth ratios, pointing at a wider variability of synthetically generated morphologies, in accordance with field observations.

Given these very encouraging results, in the following the modeling framework so far described will be used relaxing the assumption of purely erosive conditions. In the next chapter we will then analyze the consequences that deposition (possibly enhanced by the presence of vegetation) and sea level rise have on the tidal basin equilibrium topography.

Chapter 5

Results

This chapter reports and discusses the simulations performed considering the model setups including depositional effects (in the absence and in the presence of vegetation) and sea level rise (SLR). The aim is to analyze the effects exerted on tidal channel evolution by initial basin topography, suspended sediment concentration (SSC), the sea level rise (SLR) and the vegetation cover. Finally, the question whether an equilibrium condition can be obtained and which type of equilibrium is possibly established is addressed.

5.1 Purely erosive effects on initial conditions

Before tackling the SRL and SSC effects, it is worthwhile to analyze the consequences of using different initial slightly channelized geometries to trigger the formation of a main tidal channel. In particular, changing the shape and the dimension of the initial incision we investigate whether the system eventually forgets its initial geometry or is affected by it at equilibrium. The purely erosional model has been used to these purposes.

At the beginning of each simulation, the tidal basin is assumed to consist of a flat platform with a given elevation. This platform is incised by means of a slightly channelized region, whose depth and width are alternatively prescribed through: a cosine function of amplitude a_{in}; a gaussian function with variation coefficient CV; a *witch of Agnesi* in which a parameter a drives the convexity (Figure 5.1). All cross sections within the initially channelized region are compact cross sections according to the definition given in Chapter 2 (i.e., the transversal slope does not exceed $1-2$ %). The other parameters used in the tests are those of the *Test Case I*3 in Table

4.2.

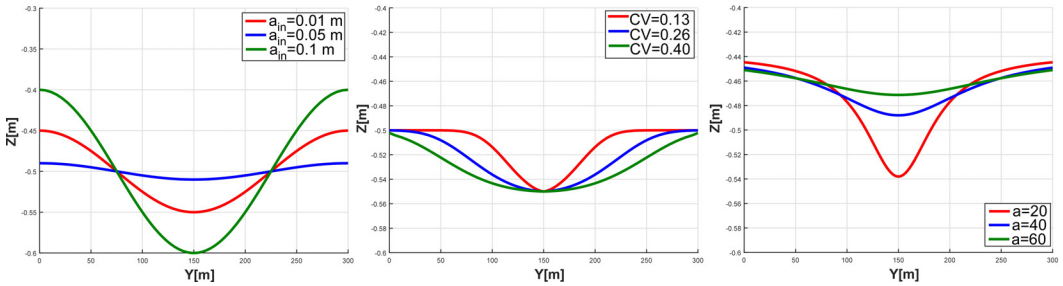

Figure 5.1: Examples of initial cross-sectional shapes used to trigger the formation of a main channel within a rectangular tidal basin. a) Cosine function; b) Gaussian function; c) *Witch of Agnesi*.

An overview of the bed topographies obtained at the end of the various simulations is presented in Figures 5.2 and 5.3. In all runs, the longitudinal distribution of the main channel width (Figures 5.2a,c,e) displays an approximately linear trend. The use of a cosine function leads to wider cross sections in the mid and landward portions of the basin, while, close to the sea, the width changes keep relatively small. Conversely, adopting the other two functions eventually produces wider channels. The longitudinal profiles shown in Figures 5.2b,d,f, indicate that initial incisions shaped according to gaussian and *witch of Agnesi* functions cause much more scouring. Anyhow, all profiles are characterized by a channel head that connects to the upper landward platform through a quite step slope, which sometimes presents weak wiggles. Specifically, the stepping transition is about 1 m high for the cosine function, while the other two shaping functions generate a step whose height is about 2 m.

The $A-P$, $D-B$, $\beta-B$ relations shown in Figure 5.3 demonstrate how the initial incision shape can exert a great influence on the final configuration. When the initial incision is shaped by a cosine function, the final depths and widths remain the same, no matter what is the cosine amplitude a_{in}. Conversely, gaussian and *witch of Agnesi* functions eventually lead to wider and deeper cross sections, depending on the value assigned to CV and a, respectively. The larger is CV (or a), the smaller is the width-to-depth ratio which ranges from $40-50$ for small CV (or a) to $10-15$ for high CV (or a). These results likely depend on the sensitivity of the final geometry to the criterion, based on transverse slope thresholds (see Chapter 2), adopted to extract automatically the cross-sectional widths. When just erosional effects are considered, the initial bed topography associated with gaussian and *witch of Agnesi* functions is thus found to affect the final channel configuration. Despite these differences, the final bed configurations always follow the OBJM law, exhibiting just a slight offset of the intercept with the A axis, as already discussed

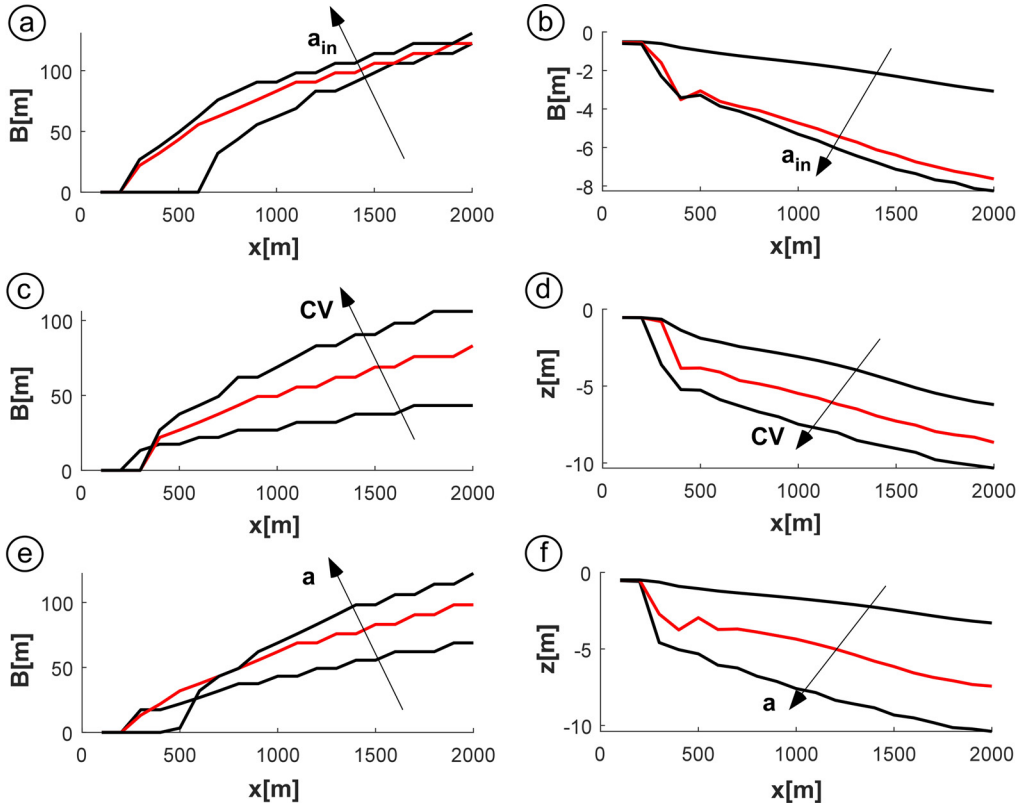

Figure 5.2: Longitudinal distribution of a,c,e) main channel with; b,d,f) channel depth at the axis. Initial channel incision prescribed through: a,b) cosine function; c,d) gaussian function; e,f) width of Agnesi. All simulations have been carried out with the purely erosional model. Parameters are those of the Test Case $I3$ in Table 4.2.

in Section 4.5. In the following, a cosine function will be always used for the initial

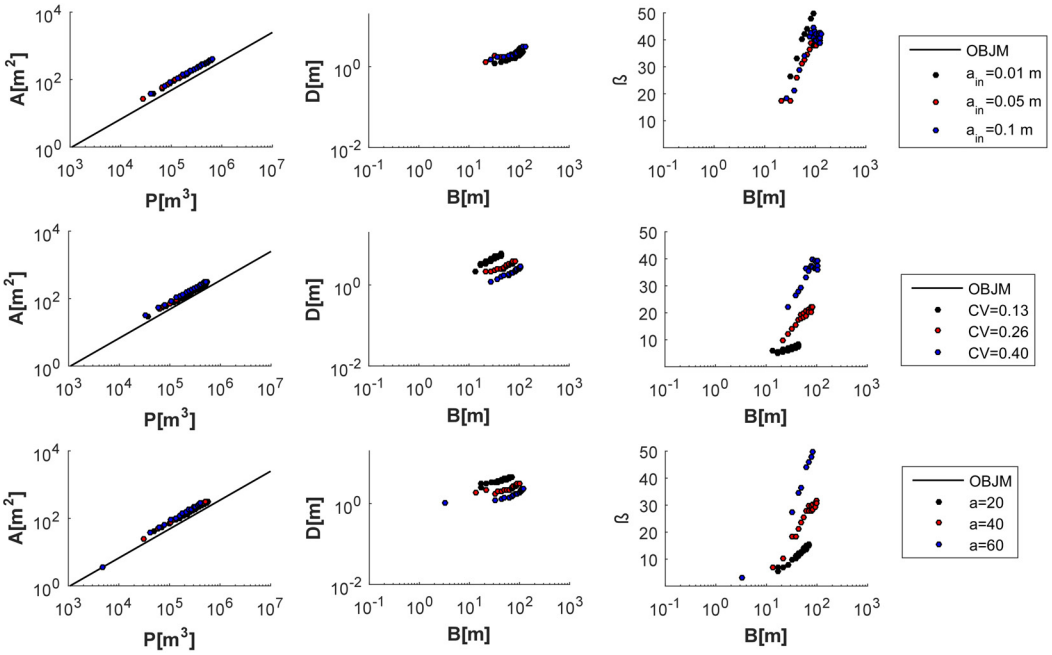

Figure 5.3: a) The cross-sectional area, A, is plotted versus the tidal prism, P; b) the mean flow depth, D, of the main channel cross section is plotted versus the corresponding width, B; c) the main channel width-to-depth, β, is plotted versus the main channel width, B relation. Simulation conditions are the same of Figure 5.2.

incision, in order to minimize as much as possible the influence of the initial bed topography on the final basin configuration.

5.2 Depositional model

The depositional model considered in this section, besides erosional effects, accounts also for sea level rise and deposition of suspended sediment, as described in Chapter 3. Here, we are interested in assessing under which conditions a dynamic equilibrium can be attained both on the main channel and the adjacent tidal flat, depending on the rate of SLR and the external availability of suspended sediment, embodied by the prescribed SSC.

5.2.1 Sediment settling and sea level rise

Let us refer to the typical parameter set of *Test Case I2* in Table 4.2. The depositional model has been implemented first considering a SLR of 3.5 mm/yrs and a SSC equal to 7.5 mg/l. The evolution of the tidal channel is represented in figure 5.4, where bed elevations are referred to the mean sea level (MSL). A flat bed with a small longitudinal cosine-shaped incision is prescribed at the beginning

of the run. Erosional effects are found to prevail at the beginning of the simulation. The initially channelized region progressively deepens, stretching throughout the basin and assumes a funnel shape. Meanwhile, the adjacent intertidal platforms, differently from the purely erosive setting, gradually increase their elevation due to sediment settling. This accretion is also related to the small values attained by bed shear stresses on the platform, implying a negligible rate of erosion. On the other hand, within the channel region, where shear stresses and, hence, erosional effects are stronger, accretion only starts after the flow depth has reached its maximum value (about -5.95 m).

Gradually, the bed variations throughout the basin become progressively smaller and the system finally tends towards an equilibrium configuration. At the seaward boundary, the intertidal platform flanking the channel reaches an elevation of 0.38 m, while the channel bed converges to an elevation of -5.95 m. The lateral tidal flats reach their equilibrium elevation before the channel bed. The concurrent presence of both depositional and erosional effects as well as of a certain rate of sea level rise, implies that the equilibrium finally established is dynamic, i.e. in a reference frame moving with MSL and averaging over a tidal cycle, erosional effects equal the depositional effects.

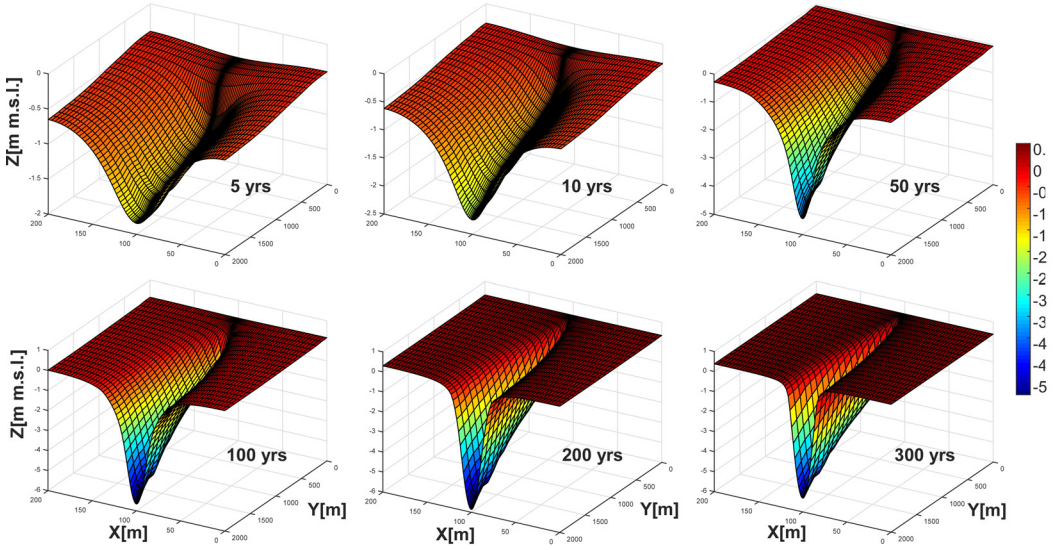

Figure 5.4: Three-dimensional view of the morphodynamic evolution of a rectangular tidal domain computed with the depositional model. Relevant parameters are those corresponding to the Test Case $I2$ of Table 4.2 and to Table 4.1. In addition, SLR =3.5 mm/yrs, SSC =7.5 mg/l).

The longitudinal profiles reported in Figure 5.5a, indicate that during the early evolutionary stages a step-like transition forms at the conjunction between the landward platform and the channel head. Downstream of this transition the channel bed progressively deepens and this deepening slows down in time. In addition, as

the landward platform accretes because of sediment settling, downstream of the step-like transition erosion can locally produce a scour that, later on, smooths out. Progressively, the bed profile tends to assume a convex shape in the upper portion of the tidal basin. The perturbations observed in the longitudinal profiles of Figure 5.5a are possibly due to wetting and drying as well as to subcritical-supercritical flow transitions near to the channel head, where the channel joins the landward tidal platform and the flow characteristics (and hence, the energy slope gradients) are poorly described by a 1D hydraulics model. Despite these issues, at the seaward boundary, the temporal evolution of the channel bed and of the tidal flats proceeds smoothly (Figure 5.5b). The intertidal platform accretes regularly from the very beginning of the simulation, finally reaching a constant elevation. The adjustment in elevation of the adjacent tidal flats, in turn, reflects into the channel bed evolution, that in a first phase decreases, reaching a minimum elevation, and then accretes progressively tending towards a constant elevation.

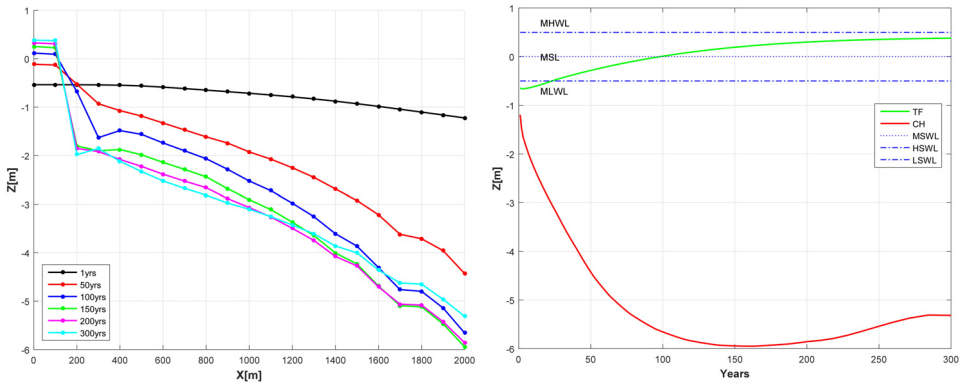

Figure 5.5: a) Longitudinal bed profiles at different stages of the tidal basin evolution; b) temporal trajectories of the elevations of two points located at the seaward boundary on the channel bed (red line) and the adjacent tidal flat (green line). The simulation is that referred to in Figure 5.4.

5.2.2 Effects of SSC and SLR variations

The results of simulations carried out varying the SSC and SLR values are shown in Figure 5.6. Overall, the greater is SSC, the shallower becomes the channel for all SLR values here considered. The increase in SSC enhances the difference in elevation between the main channel bed and the landward tidal platform, promoting the formation of a step-like transition that tends to produce a localized scour as its height increases too much. For $SSC = 5.0$ mg/l the longitudinal channel profile is relatively smooth, while for higher SSC values wiggles arise nearby the step-like transition and progressively migrate seaward, perturbating the entire channel bed. Increasing the rate of relative sea level rise, the profiles get progressively smoother and the effects of wiggles generated at the channel head tend to disappear. This

is likely due to the reduced importance of wetting and drying for higher values of the rate of RSLR. Anyhow, far enough from the channel head, the channel bed profile tends to develop a concave shape for high enough values of convergence, while an almost linear profile tends to be attained when the channel width keeps almost constant along the channel, in accordance with previous findings [Friedrichs and Aubrey, 1996; Seminara et al., 2010; Toffolon and Lanzoni, 2010]. Finally, the channel length ($\sim$ 1700 m) does not change significantly in response to SSC variations.

On the other hand, the cross sections become narrower as the SSC increases. At the seaward boundary, if the SSC doubles from 5.0 mg/l to 10.0 mg/l, the width decreases accordingly from 40 m to 20 m for all values of the considered rate of RSLR. Channel convergence tends to reduce this trend, as cross sections narrow upstream. The width distribution can be approximated with a linear trend, except near to the channel head where the spatial channel-width gradients are larger. Cross sectional widths are not influenced much by varying the rate of RSLR, at least within the investigated range.

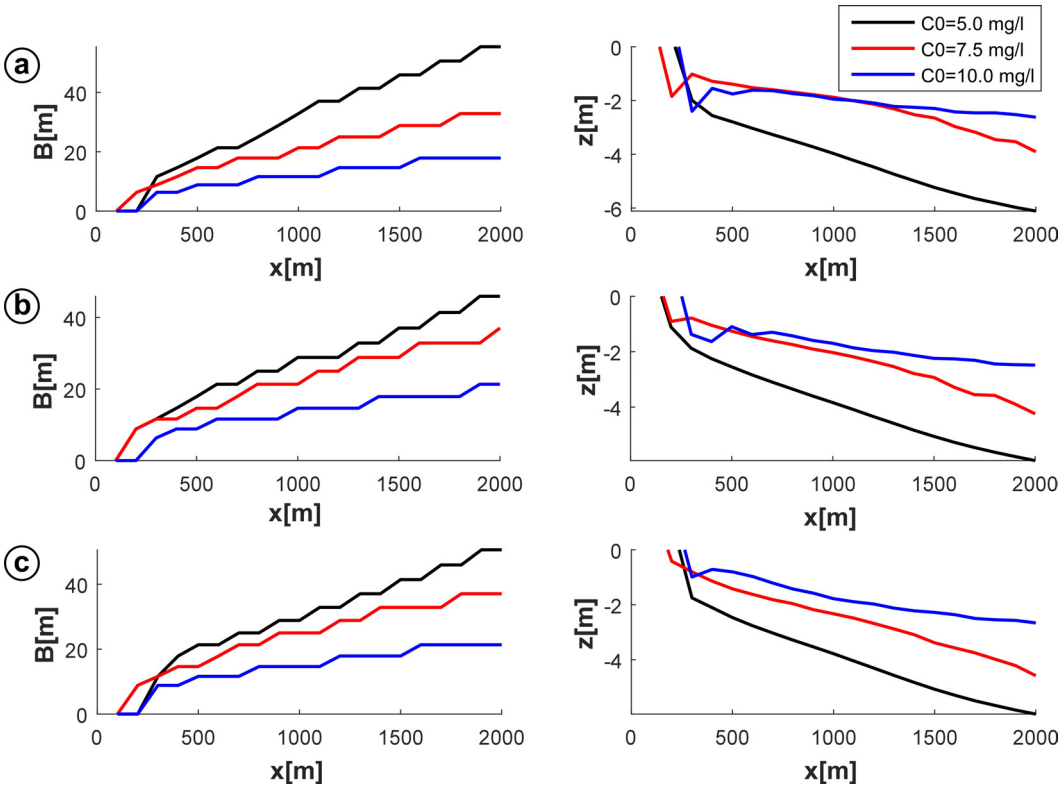

Figure 5.6: Longitudinal distributions of main channel width and bed profiles computed using depositional model for different values of the SLR. (a) $SLR = 2.5$ mm/yrs; (b) $SLR = 3.5$ mm/yrs; (c) $SLR = 4.5$ mm/yrs.

The overall effects of changes in SSC are summarized in Figure 5.7, showing the

$A - P$, $D - B$ and $\beta - B$ relations. When $SSC = 5.0$ mg/l, the OBJM law is satisfied throughout the basin. As the SSC increases behind this value, the smaller cross sections (i.e., located far from the seaward boundary) start to depart from the straight line expressing the OBJM law. This finding is due to the fact that the narrower and shallow cross sections are more frequently subjected to wetting and drying and, hence, they do not match the power law relationship in accordance with field observations [Marani et al., 2002]. On the other hand, $D - B$ and $\beta - B$ relations turn out to be only slightly influenced by the investigated SSC changes. Finally, varying SLR does not appreciably modify the above described trends.

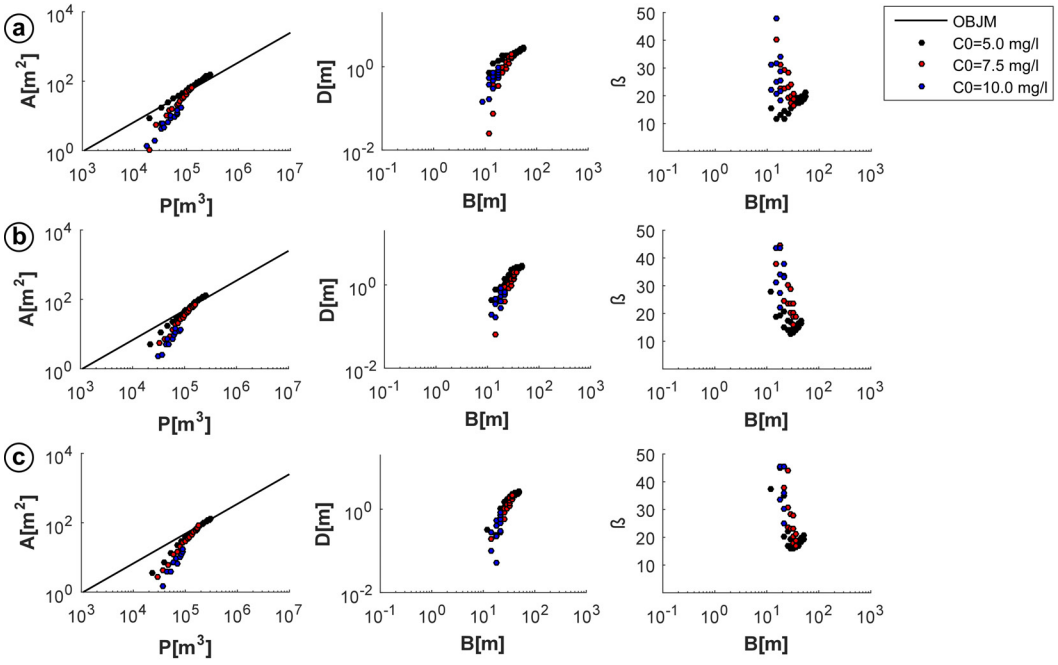

Figure 5.7: a) The cross-sectional area, A, is plotted versus the tidal prism, P; b) the mean flow depth, D, of the main channel cross section is plotted versus the corresponding width, B; c) the main channel width-to-depth, β, is plotted versus the main channel width, B relation. Simulation conditions are the same of Figure 5.6.

5.3 Vegetation effects

The parameters used to model the production of vegetation biomass are reported in Table 5.1 and were kept fixed for all runs. Note that, according to the biomass model implemented in Chapter 3, vegetation growth is max at z_{min} and then decays linearly. Despite this relationship between biomass production and elevation does not correspond to any specific halophytic species, this behavior has been adopted in many previous studies. The considered relationship between biomass and elevation, promotes vegetation growth at low elevations and, consequently, exerts a greater

influence on the channel bed evolution.

Parameter	***Value***	***Unit***
z_{max}	0.49	m
z_{min}	0.01	m
b_{max}	1000	g/m^2
Q_{b0}	2.5	mm/yrs
c_{D0}	1.1	
α_{c_D}	-0.0003	
U_0	0.1	m/s

Table 5.1: Parameters adopted to model biomass production by vegetation: z_{max} maximum stem height within the vegetation pattern; z_{min} minimum stem height within the vegetation pattern; b_{max} max biomass value; Q_{b0} max organic production rate; c_{D0} drag coefficient without vegetation; α_{c_D} fitting parameter linking drag coefficient to biomass; U_0 is a characteristic velocity value of the flow trough vegetation.

5.3.1 Comparison with the test case $I2$.

The vegetation model was run considering the set of parameters typical of *Test case* $I2$, assuming $SLR = 3.5$ mm/yr, $SSC = 7.5$ mg/l and for the vegetation properties reported in Table 5.1. The corresponding channel evolution is represented in Figure 5.8, where all bed elevations are referred to MSL. As long as bed elevation is below the minimum height allowing for vegetation growth, no difference is evident with respect to the results of Figure 5.4. When bed elevation exceeds z_{min}, vegetation encroachment enhances sediment deposition (by trapping) as well as organic soil production, fastening the accretion of the intertidal platforms until a maximum elevation of ~ 0.42 m is achieved. A faster platform accretion, in turn, echoes into channel bed evolution. In a first phase, the main channel becomes deeper, reaching a minimum elevation of ~ -5.79 m at the seaward boundary. Subsequently, in a second phase of the morphodynamic evolution, sediment deposition becomes dominant and the channel bed accretes, eventually converging to an asymptotic elevation of ~ -5.19 m.

The longitudinal channel bed profiles reported in Figure 5.9a are quite irregular. This is due to the scour (and the consequent wiggles) produced at the channel head when the height of the step-like transition towards the landward tidal platform becomes too large. Overall, the final profile tends to develop a convex profile. These findings point out the need of a better description of the processes that take place at the transition between the channel head and the landward upper tidal flats. There, frequent wetting and drying processes, and possible shifts from supercritical to subcritical flow conditions as the longitudinal slope steepens, strongly affect the 1D hydrodynamics and, consequently, the bed shear stress redistribution across the

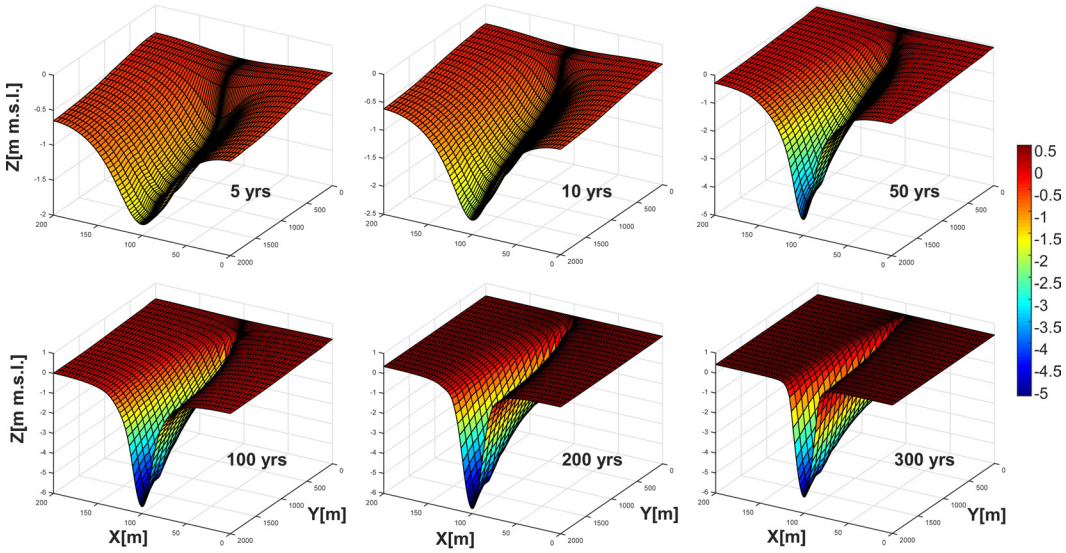

Figure 5.8: Three-dimensional view of the morphodynamic evolution of a rectangular tidal domain computed with the depositional model and allowing the growth of vegetation. Relevant parameters are those corresponding to the Test Case $I3$ of Table 4.2. In addition, SLR =3.5 mm/yrs, SSC =7.5 mg/l).

section.

Despite the perturbations arising nearby the channel head, the seaward section evolves smoothly toward an equilibrium configuration both on the marsh surface and within the channel, as shown in Figure 5.9b. As marsh elevation exceeds MSL, the accretion trend shows a kink which is due to enhanced sediment deposition induced by vegetation growth. This increased accretion reflects into channel bed evolution, such that the bed profile experiences a slight inflection before the system tends to a higher elevation.

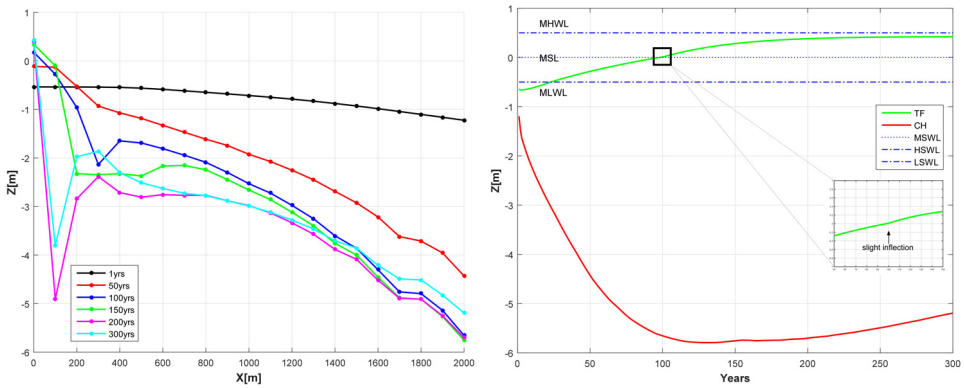

Figure 5.9: a) Longitudinal bed profiles at different stages of the tidal basin evolution; b) temporal trajectories of the elevations of two points located at the seaward boundary on the channel bed (red line) and the adjacent tidal flat (green line). The simulation is that referred to in Figure 5.8.

5.3.2 SSC and SLR variations

As for the case of pure sediment settling, simulations were run to test the effects of different SSC and SLR values. Figures 5.10 and 5.11 show the results of this numerical exercise.

According to the width distributions depicted in Figure 5.10, channel cross sections narrow as the SSC increases. However, for a given cross section, channel width does not change considerably. For example, considering a rate of RSLR equal of 3.5 mm/yrs, the inlet widths range between $28 - 33$ with a difference of 5 m in a basin 200 m wide. Moreover, the width distribution assumes an almost linear behavior except close to the channel head, where the rate of channel funneling increases. Finally, the main channel widths do not seem to be influenced significantly by the considered variations in the rate of RSLR.

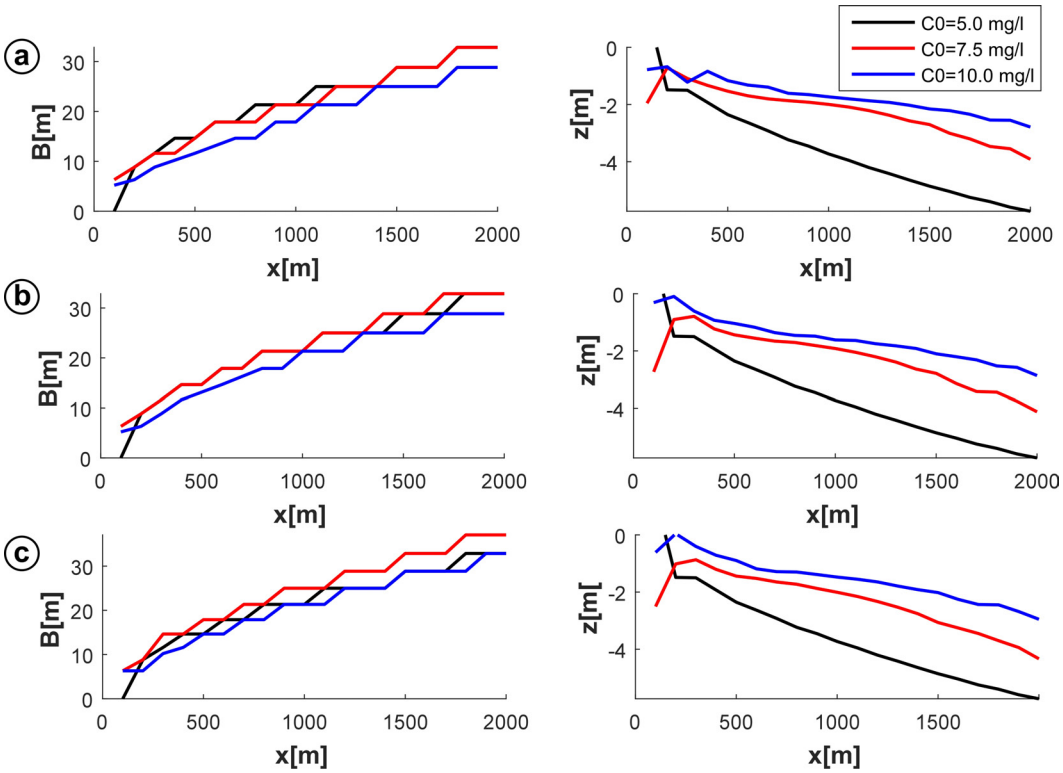

Figure 5.10: Longitudinal channel width and bed profiles obtained adding vegetation growth to the depositional model. (a) SLR=2.5 mm/yrs; (b) SLR=3.5 mm/yrs; (c) SLR=4.5 mm/yrs.

The longitudinal channel bed profiles reported in Figure 5.10, indicate that the larger is SSC, the shallower becomes the channel for every value considered for the rate of RSLR. As already observed under the pure settling scenario, an increase in the SSC enhances the difference in elevation between the landward platform and the channel head. Thus, for SSC equal to 5.0 mg/l, the channel bed profile is quite smooth, while for higher SSC values, the step-like transition at the channel

head increases its height, a scour localizes at that point and wiggles perturbate the channel bed. Increasing the rate of RSLR, these perturbations smooth progressively out. As explained, a higher rate of RSLR reduces the occurrence of wetting and drying cycles, improving the performance of the model.

An overall picture of the cross sectional morphology is represented in Figure 5.11, showing the $A - P$, $D - B$ and $\beta - B$ relations. As observed also in the case of pure settling, the OBJM law is satisfied throughout the whole channel if the SSC is equal to 5.0 mg/l. Conversely, for larger values of the SSC, the narrower cross sections located far away from the seaward boundary depart from the OBJM law, in accordance with field observations [Marani et al., 2002]. The considered variations in the rate of RSLR does not change these trends. Similarly, the $D - B$ and $\beta - B$ relations do not seem to be particularly affected by the considered variations in the SSC.

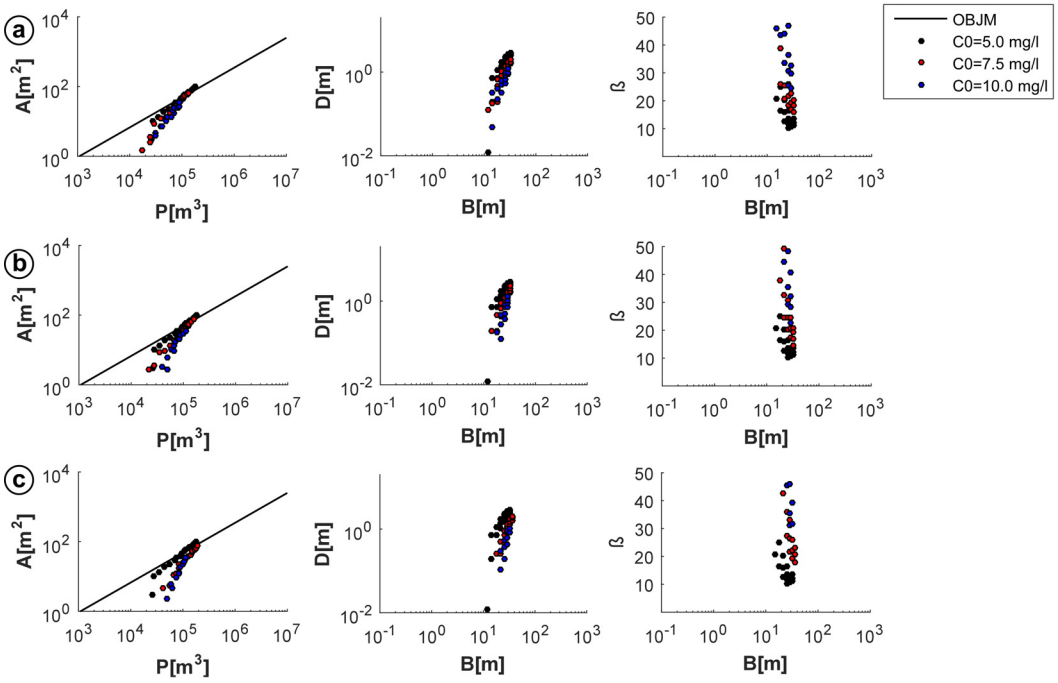

Figure 5.11: a) The cross-sectional area, A, is plotted versus the tidal prism, P; b) the mean flow depth, D, of the main channel cross section is plotted versus the corresponding width, B; c) the main channel width-to-depth, β, is plotted versus the main channel width, B. Simulation conditions are the same of Figure 5.10.

5.4 Overall comparison of the results

Figures 5.12 and 5.13 show the overall comparison among the results obtained by considering alternatively: i) only erosion (erosional scenario); ii) erosion, settling deposition and RSLR (depositional scenario); iii) erosion, settling deposition,

vegetation trapping, organic soil production and RSLR (vegetated scenario).

Because in the previous section we have seen that the considered RSL variations do not strongly affect the final equilibrium configuration of the tidal basin, in the following we refer to the case of $SLR = 3.5$ mm/yrs. We thus concentrate on the effects exerted by SSC and vegetation growth.

The width distributions reported in the left panels of Figure 5.12 indicate that variations in SSC (at least for the investigated range) induce relatively restrained changes. Specifically, at the seaward boundary the width ranges between $28 - 32$ m in the presence of vegetation, while for the depositional scenario the range widens to $21 - 46$ m. Hence, vegetation acts as a width stabilizer. On the other hand, the bed profiles depicted in the right panels of Figure 5.12 suggest that vegetation likely has two different effects, depending on the elevation of the intertidal areas adjacent to the main channel. When these lateral platforms are above MSL but close to it, as in the plots (a) of Figure 5.12 where the platform is set at 0.32 m, the additional friction due to vegetation favors the concentration of the flow within the channel. The corresponding bed profile thus gets deeper, and the channel bed elevation at the seaward boundary reaches the value -5.7 m. Conversely, when the lateral platforms are much higher than MSL, as in the plots (c) of Figure 5.12 where the platform is set at 0.45 m, the flow is already concentrated within the channel and vegetation concurs to reduce the tidal prism, both slowing down the flow on the vegetated platform and increasing its accretion rate. As a result, the longitudinal channel bed profile is characterized by much shallower sections, and indeed the elevation at the seaward section grows up to -2.9 m. The intermediate conditions represented in the plots (b) of Figure 5.12 where the tidal platform elevation is 0.42 m, leads to results very similar to those obtained for the case (c).

The different role exerted by vegetation described above, appears clearly also from the $A - P$, $D - B$ and $\beta - B$ relations shown in Figure 5.13. In the purely erosional scenario, as already pointed out in Chapter 4, the tidal prism-cross sectional area relationship invariably follows the OBJM law, even though the intercept with the vertical axis has a slightly larger value than that obtained empirically. The inclusion of additional effects such as setting deposition, sea level rise and vegetation, generally leads to a deepening of the cross sections. Indeed, in the purely erosional scenario width-to-depth ratios fall in the range $30 - 40$ while, for a SSC of 5.0 mg/l (panels (a) in Figure 5.13), this range becomes $15 - 30$ in the depositional scenario and $10 - 15$ in the presence of vegetation. Despite this, the OBJM law is still satisfied along most of the tidal channel, except for the smaller sections, where wetting and drying phenomena lead to a departure from the law [D'Alpaos et al., 2009a; Marani et al., 2002].

Differently, increasing SSC to 10.0 mg/l (panels (c) in Figure 5.13), deposition

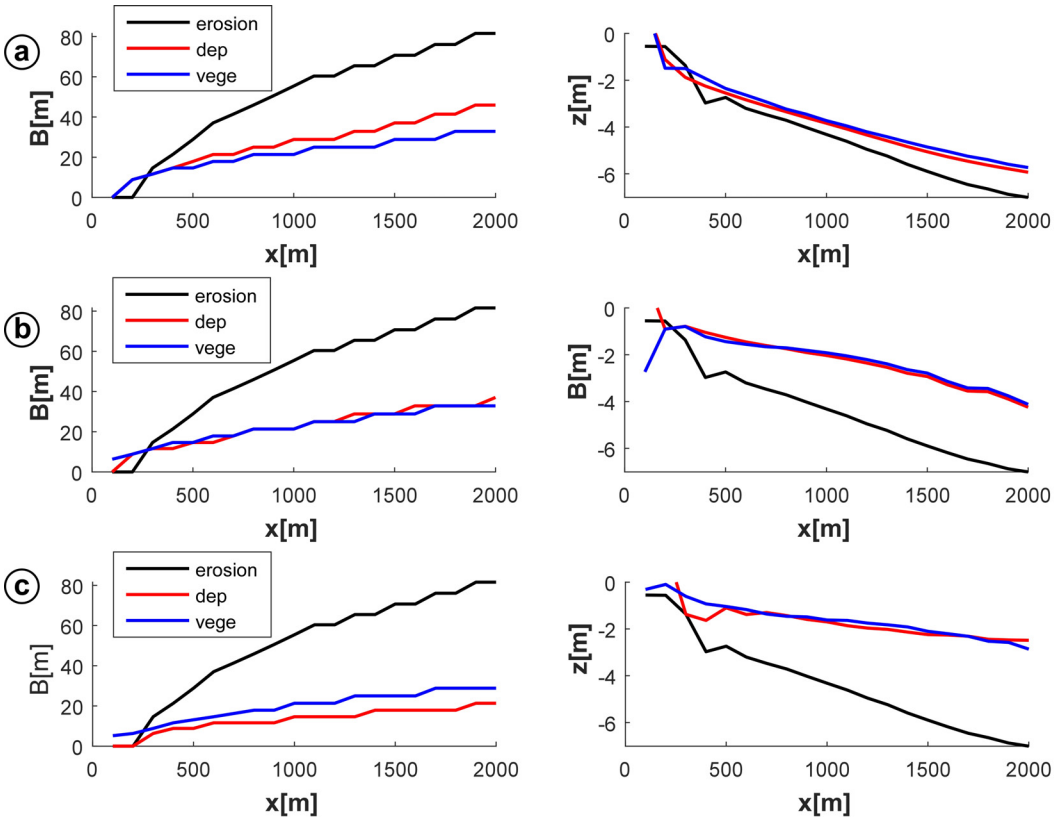

Figure 5.12: Longitudinal channel width and bed profile computed with reference to the erosional (black line), depositional (red line) and vegetated (blue line) scenarios, for different values of suspended sediment availability: (a) SSC=5.0 mg/l; (b) SSC=7.5 mg/l; (c) SSC=10.0 mg/l.

processes, enhanced by the presence of vegetation, promote a significant reduction of the tidal prism, and a departure from the OBJM law is observed not only for small cross sections but also for larger cross sections. On the other hand, the width-to-depth ratio falls in the range $15-50$ for both depositional and vegetated scenarios, while in the erosional scenario the range becomes $10-30$. In conclusion, vegetation appears to have two counteracting effects. On one hand, it tends to concentrate the flow within the channel, promoting the formation of deeper channels. On the other hand, it slows down the flow on the intertidal platform and enhances the accretion of these areas, tending to reduce the tidal prism and, consequently, fostering shallower cross sections. These two counter-acting effects due to vegetation rule out one another, depending on the elevation of the tidal platform flanking the channel. The former mechanism prevails for elevations slightly larger than MSL, while the latter dominates for tidal flat elevations much higher than MSL.

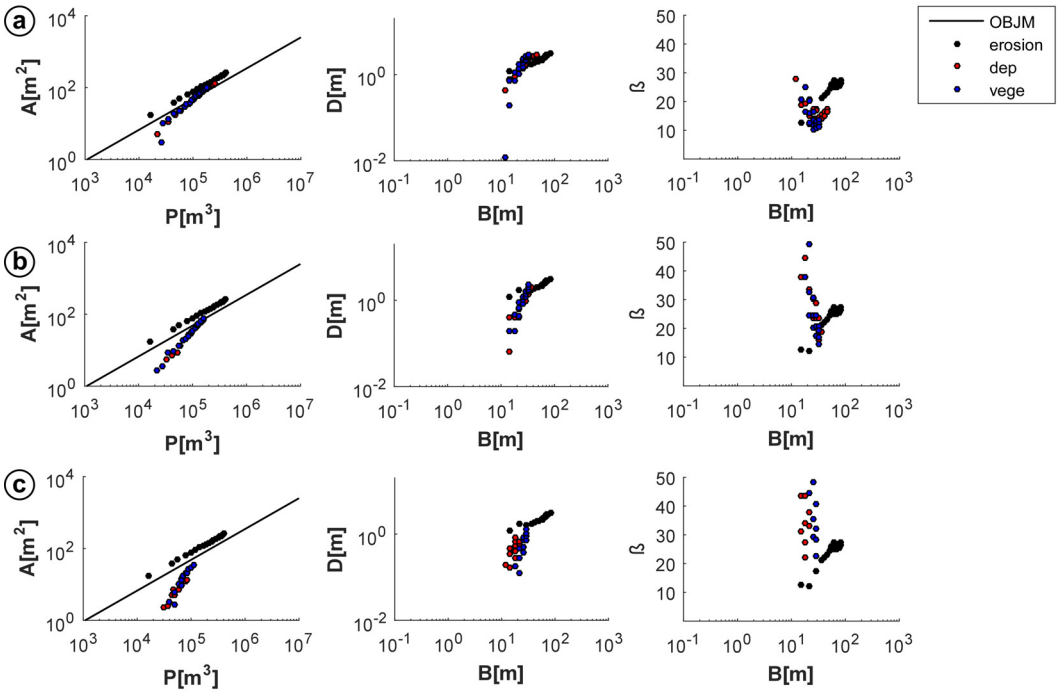

Figure 5.13: The relations $A-P$, $D-B$ and $\beta-B$ are plotted for the equilibrium channel bed topographies computed with reference to the erosional (black line), depositional (red line) and vegetated (blue line) scenarios, for different values of suspended sediment availability: (a) SSC=5.0 mg/l; (b) SSC=7.5 mg/l; (c) SSC=10.0 mg/l.

All the synthetic cross sectional morphologies computed with the present model considering SSC, SLR and vegetation growth are compared with the available field data [Marani et al., 2002]. In this regard, the $A-P$, $D-B$ and $\beta-B$ relations are shown in Figure 5.14. Looking at the panel on the left, it is clear that the OBJM law is satisfied considering the purely erosional conditions (black circles) throughout the

basin. When sediment supply, sea level rise and vegetation are taken into account, the OBJM law still holds but deviations are evident in landward cross sections, far from the inlet and highly subjected to wetting and drying processes, as observed in the field [Lanzoni and D'Alpaos, 2015; Marani et al., 2002]. Looking at the central and right panel, it is clear that the cross sections computed under purely erosive conditions (black circles) are wider and shallower ($15<\beta<20$) matching more the features of channels cutting through actual tidal flats(pluses). Conversely, introducing SSC and vegetation, the cross sections narrow and deepen ($\beta<10$) matching more the shape of channel dissecting actual salt marshes (crosses).

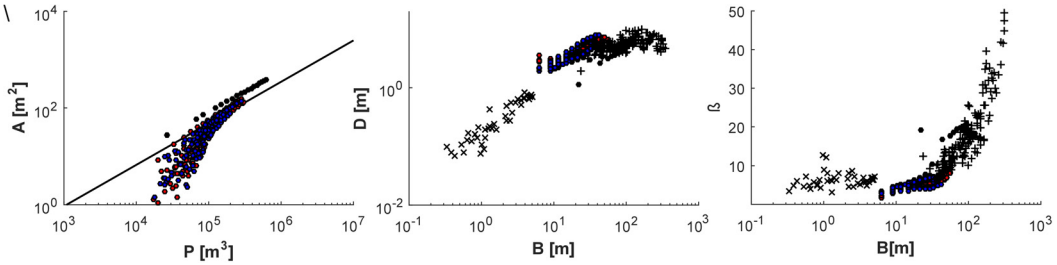

Figure 5.14: Comparison between the present computations and the field data measured in the Venice lagoon [Marani et al., 2002]. Black circles represent the results obtained considering the purely erosional setup, red circles represent the results obtained considering the depositional setup (SSC+SLR), blue circles represent the results obtained considering the vegetated setup (SSC+SLR+vegetation). Field cross sectional data in Marani et al. [2002] are represented as crosses, if referred to channel dissecting salt marshes, as pluses, if referred to channel dissecting tidal flats.

5.5 Endangering the survival of the tidal landscapes

In all simulations conducted the channel strives to reach an equilibrium between erosional and depositional processes eventually mediated by the vegetation encroachment. Once the equilibrium is reached, the follow-up question is if a sudden change in external forcings, whether RSLR or SSC, may endanger the survival of the tidal environment just formed. In this regard additional scenarios have been investigated starting from the equilibrium reached with a sediment supply equal to 7.5 mg/l and RSLR equal to 3.57 mm/yrs. The vegetation effects are also considered in these new scenarios. For sake of simplicity, the evolution is described just at the seaward cross section of the basin.

Firstly we consider the effect of a sudden change in SSC. After 300 years, the tidal environment fate is challenged by setting SSC either up to 22.5 mg/l or downot to 2.5 mg/l. If the sediment supply reduces to 2.5 mg/l keeping constant all the other parameters, the tidal system can no longer keep the pace of the RSLR and thus it is doomed to drown (Figures 5.15 c and d). In 200 years the tidal-flat elevation

drops almost to MSL and the channel becomes deeper reaching approximately an elevation of −7.50 m (Figures 5.15 c). The vegetation tends to slightly mitigate the speed at which the system sinks (Figures 5.15 d); specifically, the marshes set above the MSL, while the channel reaches approximately a higher elevation, around −7.0 m . Conversely, if the sediment supply increases up to 22.5 mg/l, the tidal system tends to infill (Figures 5.15 a and b). The tidal flats reach the max tidal elevation, while the channel progressively becomes shallower. No specific role seems to be played by the vegetation when the system infills.

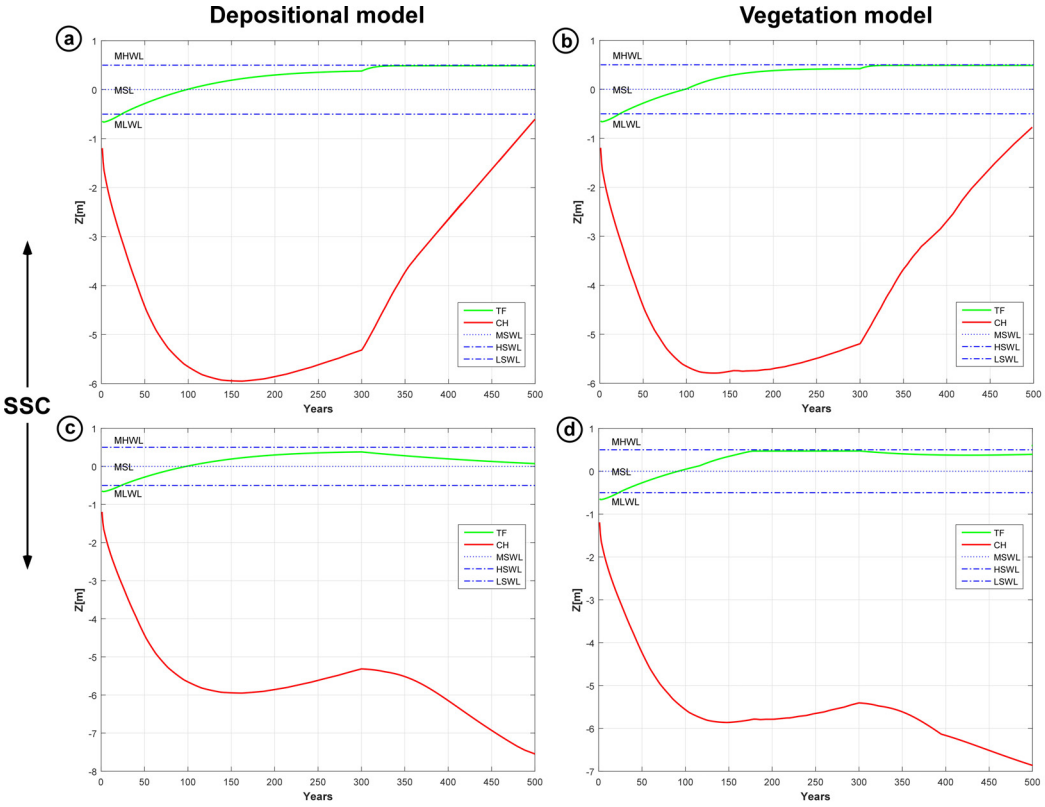

Figure 5.15: Seaward cross section evolution under a sudden change in SSC after 300 yrs: (a) SSC=22.5 mg/l; (b) SSC=22.5 mg/l; (c) SSC=2.5 mg/l; (d) SSC=2.5 mg/l.

Similar effects are reproduced when, instead of a SSC change, a sudden RSLR change is considered. After 300 years, the tidal environment fate is challenged by increasing RSLR to 10.5 mm/years or redicing it to 1.2 mm/years. In this latter case keeping constant the other forcings, the tidal system tends to infill since the sea level rise is not able to counteract the sediment input (Figures 5.16 c and d). The infilling process makes the tidal flats to reach the maximum tidal elevation and the channel to rise quickly. As shown previously considering SSC effects, the vegetation does not affect the evolution of the channel during the infilling process. On the other hand, if the relative sea level rise increases up to 10.5 mm/yrs keeping constant the

other forcings, the sediment input is not enough to keep the pace with RSLR and the system drowns (Figures 5.16 a and b). In 200 years the lateral platforms sink below MSL, while the channel drowns reaching an the elevation of about −9.0 m. The presence of vegetation reduces the speed at which the system sinks: after 200 years the marshes are still above MSL while the channel reaches an approximated elevation of −8.0 m.

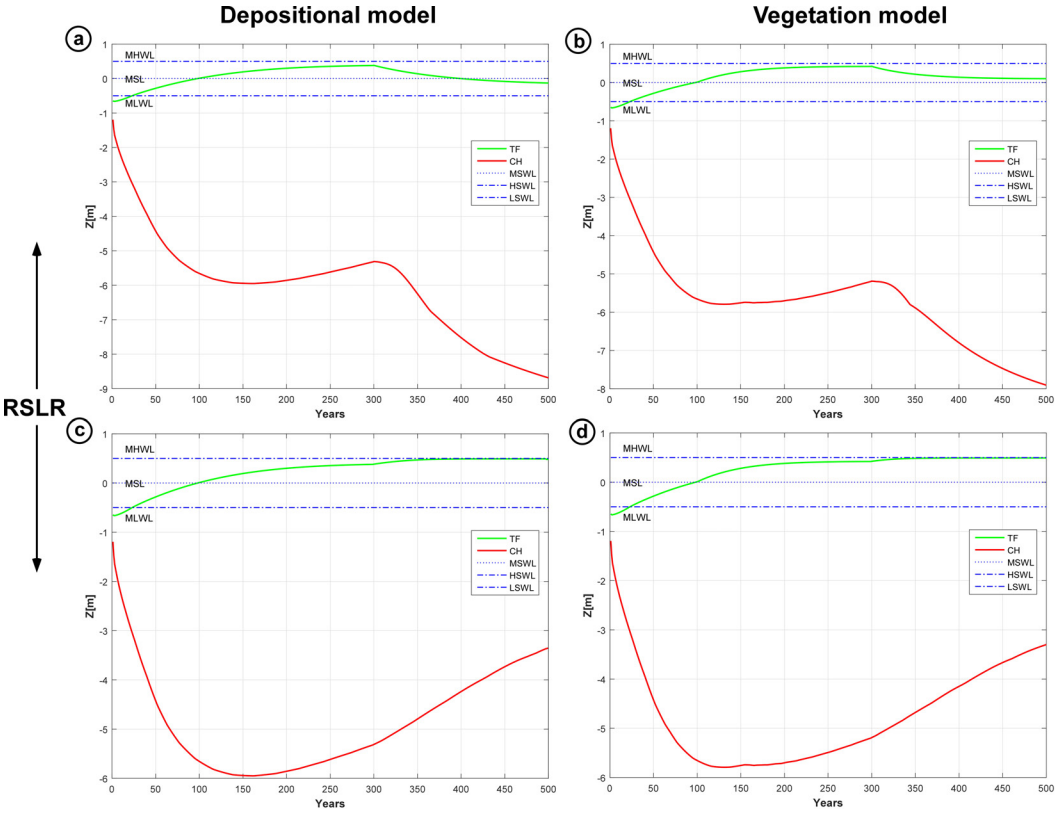

Figure 5.16: Seaward cross section evolution under a sudden change in RSLR. (a) RSLR=10.5 mm/yrs; (b) RSLR=10.5 mm/yrs; (c) RSLR=1.2 mm/yrs; (d) SSC=1.2 mg/l.

5.6 Concluding remarks

In this chapter we used the modeling framework developed so far to investigate three scenarios. The first is purely erosional (erosional scenario), in accordance with previous research approaches. The second includes erosion, settling deposition and sea level rise (depositional scenario). The third couples erosion, settling deposition, vegetation trapping, organic soil production and sea level rise (vegetated scenario).

In the erosional scenario, the consequences of different shapes of the initial incision imposed to trigger a channel have been analyzed. Cosine shaped incisions of different amplitude are found to have negligibly small effects on the final topography

of the tidal basin. Conversely, initial incisions described by gaussian or *witch of Agnesi* functions seem to have a certain influence on the final bed configuration, leading to narrower cross sections as the depth of the initial incision is reduced.

The present simulations highlight the numerical difficulties that arise near to the transition between the tidal channel head and the upper intertidal platform located landward. There, various phenomena operate: wetting and drying become more frequent, the tidal flow may be subject to hydraulic transitions from supercritical to subcritical conditions, and viceversa, and the flow field has likely a two dimensional character. These processes are particularly difficult to handle numerically when the step-like transition formed at the channel head grows substantially in height. The temporal evolution of the energy slope computed throughout a tidal cycle with the 1D hydraulic model is characterized by the formation of spikes as the bed wets/dries. These spikes are responsible for the formation of large bed shear stresses that, in turn, may alter significantly the local bed topography, with the consequent formation of a local scour and of wiggles in the longitudinal bed profile.

Despite these numerical difficulties, some preliminary conclusions could be drawn when SSC, SLR and vegetation are taken into account.

For the depositional scenario, the greater is SSC, the shallower and narrower becomes the channel. As the rate of RSLR is increased, the wiggles that may form near the channel head are progressively smoothed out. Indeed, higher SLR implies that wetting and drying occurrence reduces, improving the model performance. The vegetation cover acts as a width stabilizer, inducing small fluctuations in cross sectional width for different SSC values. Additionally, vegetation encroachment on the marsh surface produces two competing effects. On the one hand, enhanced marsh accretion associated with the increased particle trapping and with the organic production by halophytic plants, increases marsh elevation in the tidal frame, thus reducing the landscape forming tidal prism and the size of channel cross sections. On the other hand, the increased flow resistance on the vegetated marsh promotes flow concentration within the channel, leading to channel cross sections with smaller width-to-depth ratios, namely to more incised channel sections. Present simulations indicate that the second process is more important in marshes which are lower in the tidal frame, whereas the first process is more important in marshes higher in the tidal frame when most of the tidal fluxes are already confined within the channel.

When forcings are not able to offset each other, the system cannot reach an equilibrium but it evolves quickly: if the sediment input prevails, the basin tends to infill, while if the sea level rise prevails, the basin is doomed to drown. When forcings are off-balance, the effects of vegetation encroachment only retardates the attainment of the final equilibrium but does not change its nature.

Chapter 6

Conclusions

The aim of this thesis was to study the plano-altimetric evolution of a tidal channel relaxing few simplifying assumptions (i.e. the quasi-static approximation for tide propagation and the related hydrodynamic field) embedded in previous models and furthermore to consider wetting and drying phenomena and the effects of sedimentation, sea level rise and vegetation growth. The study concerns the evolution of a 3D rectangular basin cut through by a straight funneling channel, flanked by lateral intertidal platforms. The open channel flow was solved by using a one-dimensional (1D) hydrodynamic model developed to describe the flow field accounting for the contribution of the lateral shoals, to handle a large variety of channel morphology, to tackle wetting and drying processes that represent an ubiquitous feature of channels and shoals in tidal landscapes. The 1D hydrodynamics was "validated" by considering a few test cases suggested in Balzano [1998] and adopted here to benchmark the results of the new model against those of a full-fledged 2D model that solves the complete shallow water equations. Given the 1D flow field and the spatio-temporal distribution of the energy slope, the distribution of bed shear stress is computed along each transect of the tidal basin. Deposition and erosion rates are then computed by assuming a constant sediment supply (SSC) and neglecting the contribution of bed-load transport, and the bathymetry is then suitably updated to account for changes in the morphology of the landscape through the morphodynamic loop. The tidal channel evolution has been investigated in relation to three different scenarios which progressively include different processes. In the purely erosional scenario, only sediment erosion is assumed to shape the channel. In the depositional scenario, erosion sums to sea lever rise (SLR) and settling deposition driven by SSC: the intertidal platforms within the basin thus accrete as the

channel incision proceeds. Finally, in the vegetation scenario sediment trapping by vegetation and organic soil production sum to the previously considered processes.

The results of the simulations carried out to characterize the plano-altimetric evolution of a tidal channel can be summarized as follows.

- Under purely erosive conditions, the model produces a larger variety of synthetic channel morphologies which, overall, match cross sectional geometry measured in the field [Marani et al., 2002] or computed by other models [Lanzoni and D'Alpaos, 2015].

- The synthetic channel morphologies follow the OBJM law, relating the cross-sectional area A and the tidal prism P. A slight offset is observed for the interception with the A axis, implying larger values of A for a given P. This result is likely due to the friction relationship (Gauckler-Strickler) adopted in the 1D model [D'Alpaos et al., 2009a]. Other deviations are observed for small sections, far from the inlet and highly subjected to wetting and drying cycles [Marani et al., 2002].

- The geometry initially imposed to the tidal basin is found to possibly affect the final channel configuration only when considering the purely erosive scenario. The use of a cosine function to shape the initial incision introduced to trigger the tidal channel formation minimize the influence of the initial conditions.

- As soon as the intertidal platforms adjacent to the main channel grow up to mean sea level (MSL), vegetation starts to grow on them affecting friction and depositional processes. Vegetation encroachment exerts a stabilizing effect on main channel widths, which keep approximately constant if sediment supply is increased (at least for the investigated range of SSC).

- The equilibrium configuration reached by the tidal channel under the effects of sea level rise, sediment supply and vegetation is controlled by two counteracting effects associated to the presence of vegetation and treated separately by other models.

    - When the lateral platforms set at an equilibrium just above MSL (i.e., for small SSC), the increased flow resistance on the lateral intertidal platforms favors flux concentration within the channel [Temmerman et al., 2007].
    - Conversely, when the lateral platforms have elevations close to higher water levels (i.e., for large SSC), the flow turns out to be already confined within the channel and, hence, vegetation favors a decrease in the tidal

prism due to the higher salt marsh elevations [DAlpaos et al., 2005]. In this case, cross sections tend narrow and shallow and, consequently, large deviations are evident with respect to OBJM law.

Clearly, further improvements can be introduced in the present modeling framework. A more refined treatment of the step-like transition between the channel head and the upper landward tidal platform has to be developed, in order to avoid spikes in the temporal evolution of the energy slope and, therefore, unrealistic scour and deposition peaks at the channel head. Bed load transport could be accounted for when evolving the bed on the long term scale. The assumption of a constant SSC to surrogate external sediment supply could be relaxed, through a 2D description of the spatio-temporal distribution of SSC to be used when updating in time the bed topography. All these additional ingredients are deemed to improve the verisimilitude of the computed equilibrium configuration.

Appendix A

1D model validation: additional results

The 1D model described in chapter 2 has been tested setting the floodplain height of the three reference bathymetries (Figure A.1) at $z_{tf} = -0.45$ m. The comparisons between 1D and 2D models are shown in the following pages.

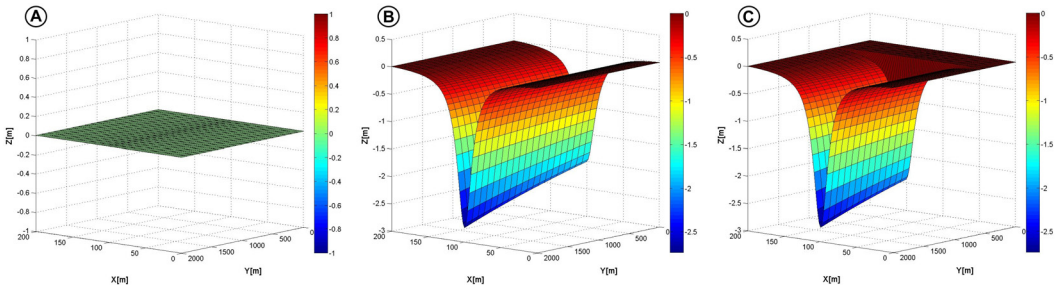

Figure A.1: The three bathymetries tested: in the panel A prismatic channel with compact cross sections, in the pannel B non-prismatic channel with compound cross sections and in the pannel C a non-prismatic channel with both compact and compound cross sections.

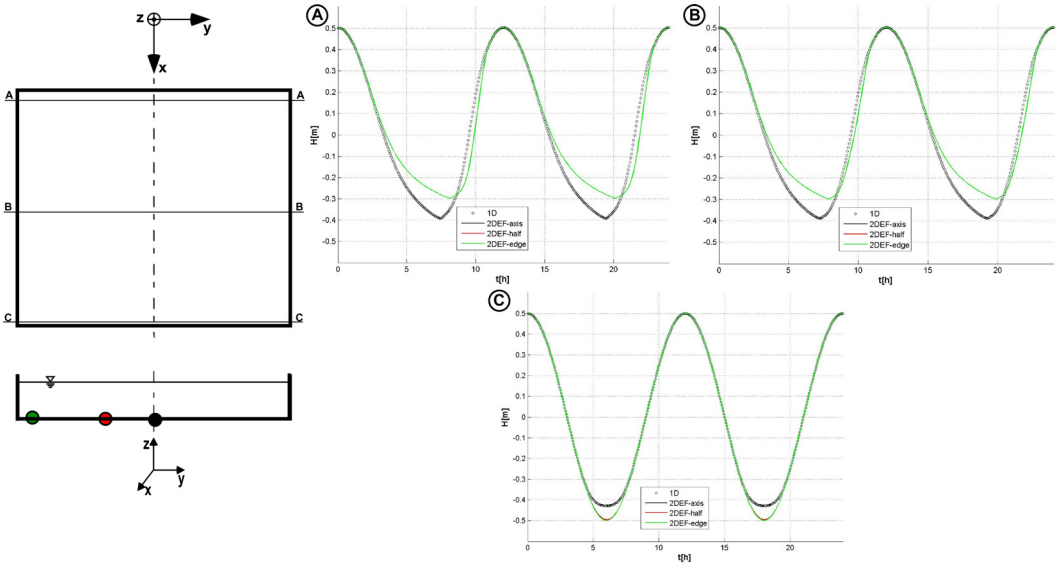

Figure A.2: Water level oscillations computed for bathymetry 1 ($z_{tf} = -0.45$ m). a) landward section; b) halfway cross section; c) seaward section. The water levels are tracked on the channel axis (black), on the tidal flat edge (red) and on the lateral boundary of the tidal domain (green).

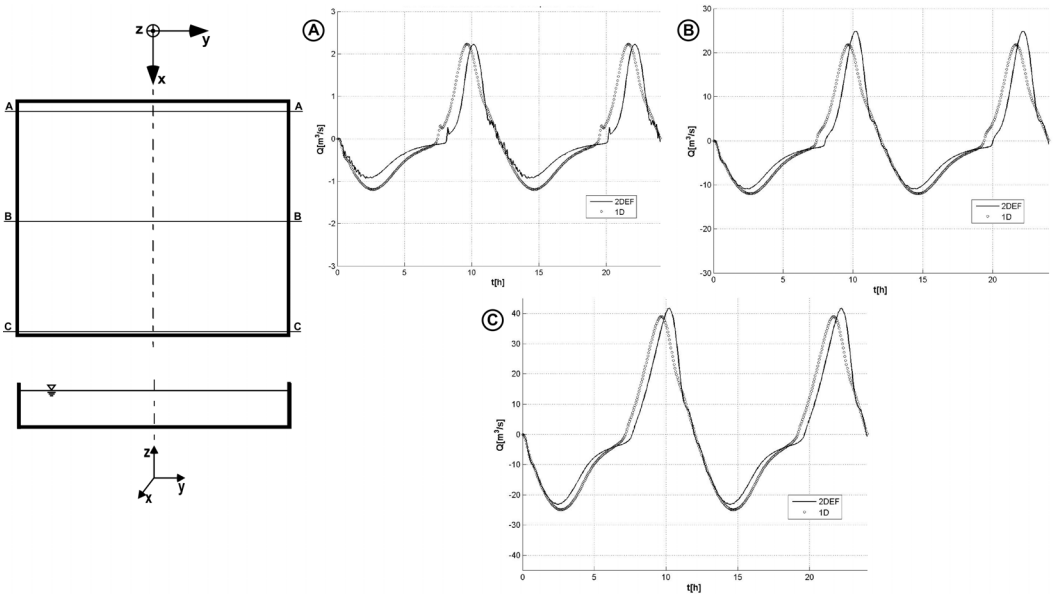

Figure A.3: Temporal distribution of the cross-sectional discharge Q computed for bathymetry 1 ($z_{tf} = -0.45$ m). a) landward section; b) halfway cross section; c) seaward section.

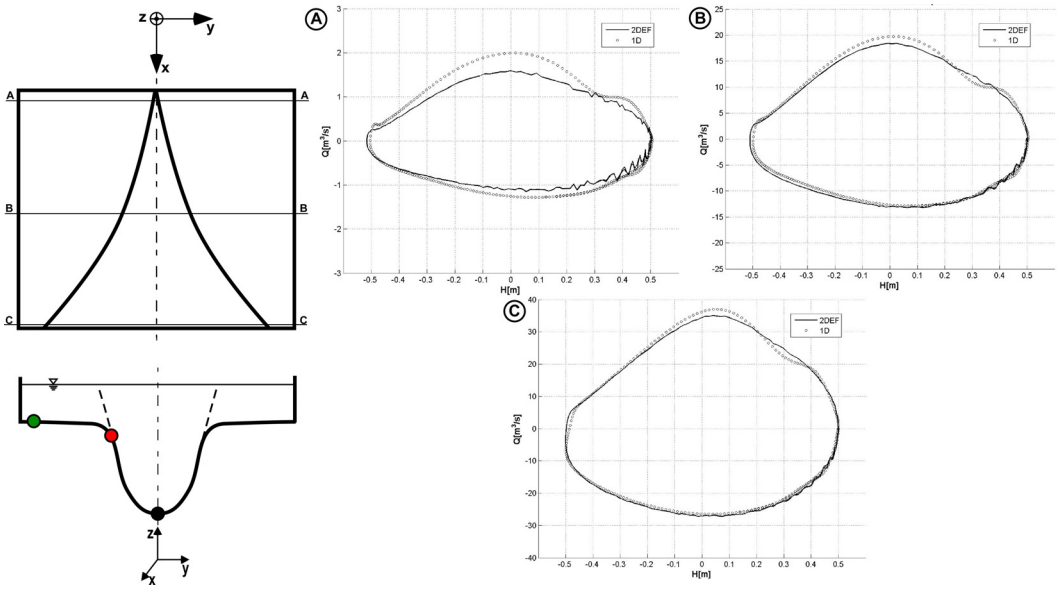

Figure A.4: The cross sectional discharge Q is plotted as a function of the water stage h for bathymetry 1 ($z_{tf} = -0.45$ m) a) landward section; b) halfway cross section; c) seaward section.

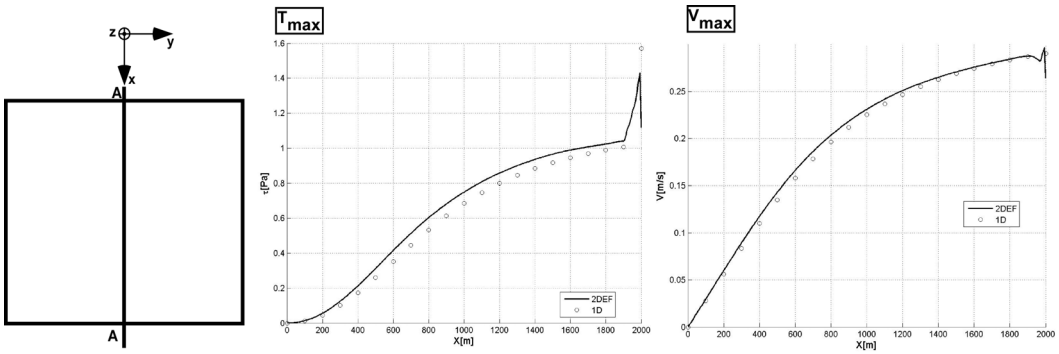

Figure A.5: a) Maximum shear stress τ_{max} and b) velocity U_{max} computed during a tidal cycle along the longitudinal axis fo the tidal basin with bathymetry 1 ($z_{tf} = -0.45$ m).

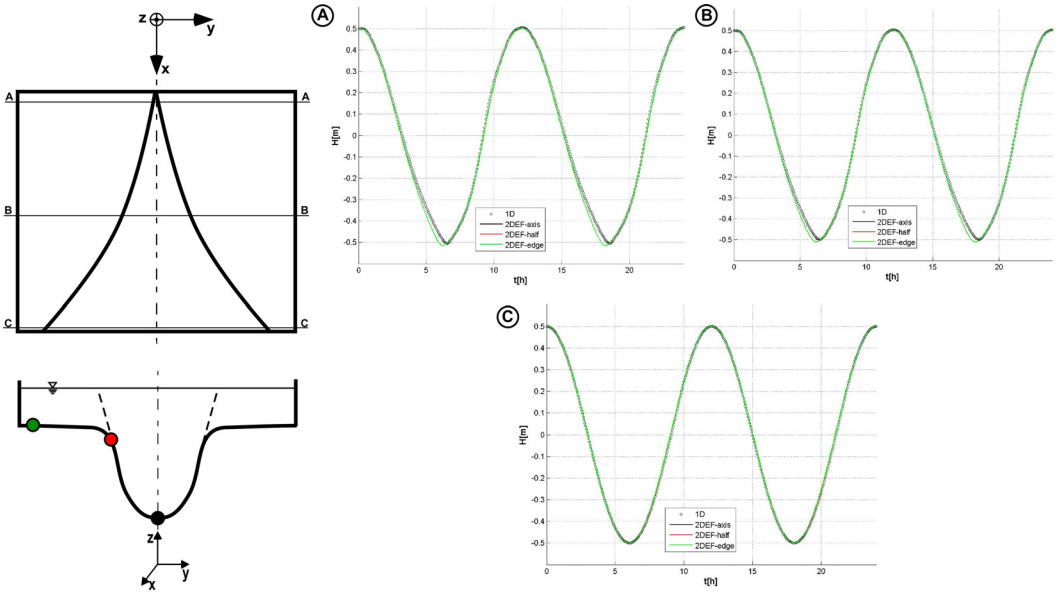

Figure A.6: Water level oscillations computed for bathymetry 2 ($z_{tf} = -0.45$ m). a) landward section; b) halfway cross section; c) seaward section. The water levels are tracked on the channel axis (black), on the tidal flat edge (red) and on the lateral boundary of the tidal domain (green).

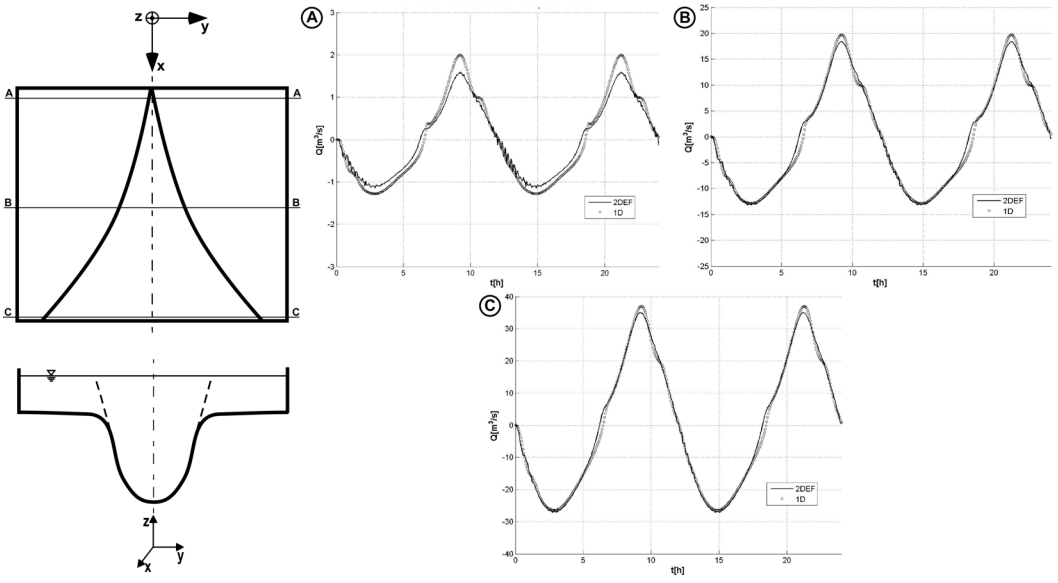

Figure A.7: Temporal distribution of the cross-sectional discharge Q computed for bathymetry 2 ($z_{tf} = -0.45$ m). a) landward section; b) halfway cross section; c) seaward section.

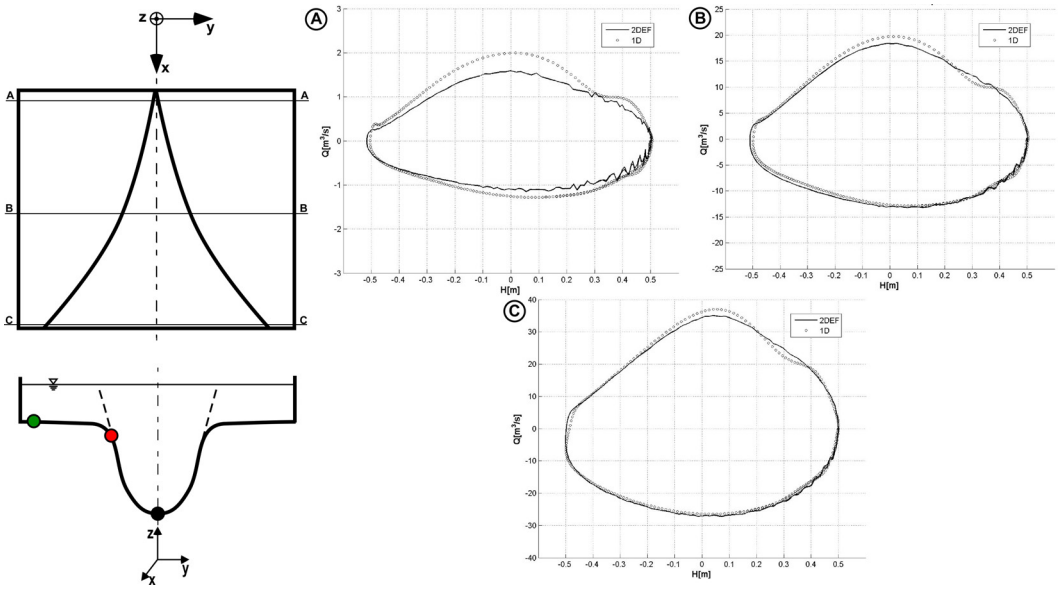

Figure A.8: The cross sectional discharge Q is plotted as a function of the water stage h for bathymetry 2 ($z_{tf} = -0.45$ m) a) landward section; b) halfway cross section; c) seaward section.

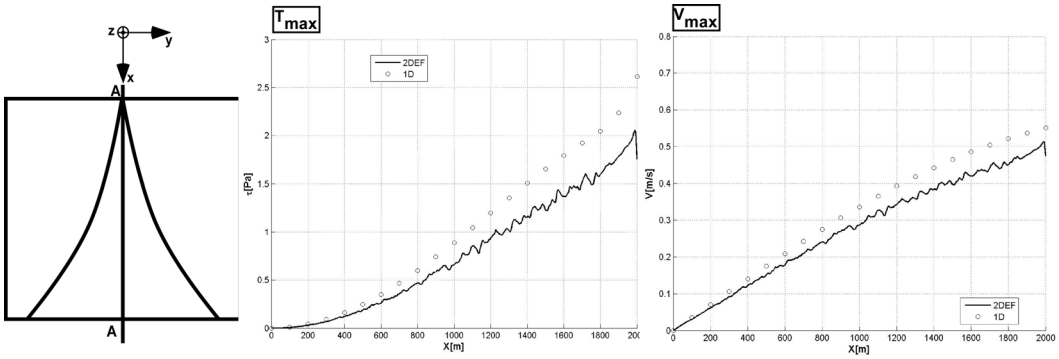

Figure A.9: a) Maximum shear stress τ_{max} and b) velocity U_{max} computed during a tidal cycle along the longitudinal axis fo the tidal basin with bathymetry 2 ($z_{tf} = -0.45$ m).

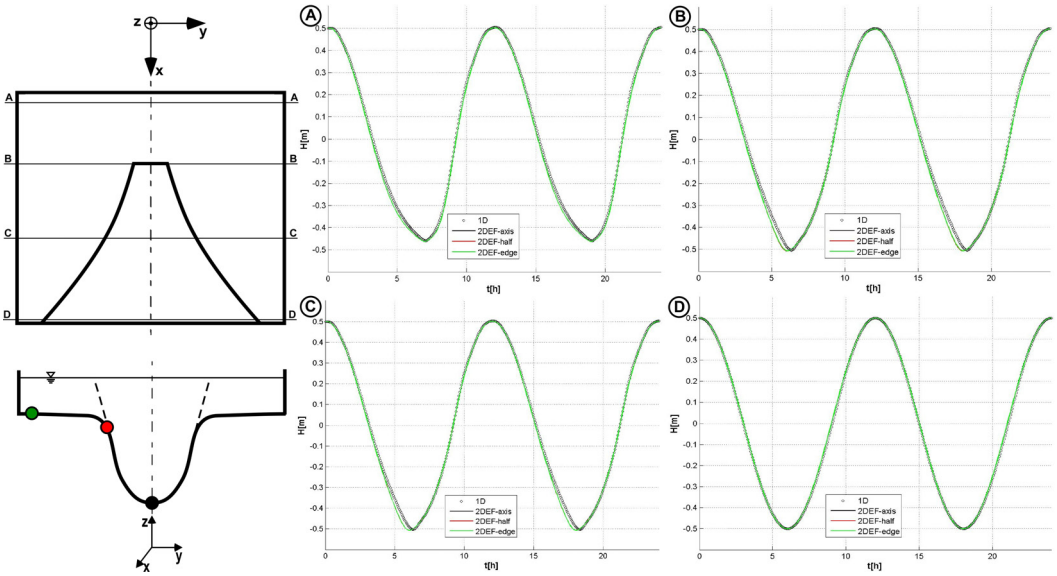

Figure A.10: Water level oscillations computed for bathymetry 3 ($z_{tf} = -0.45$ m). a) landward section; b) halfway cross section; c) seaward section. The water levels are tracked on the channel axis (black), on the tidal flat edge (red) and on the lateral boundary of the tidal domain (green).

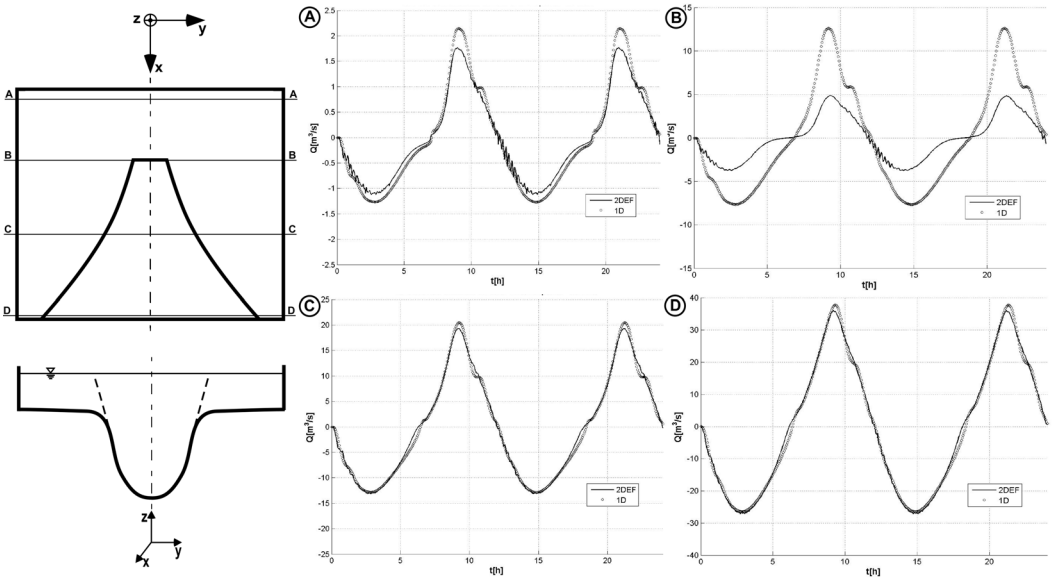

Figure A.11: Temporal distribution of the cross-sectional discharge Q computed for bathymetry 2 ($z_{tf} = -0.45$ m). a) landward section; b) halfway cross section; c) seaward section.

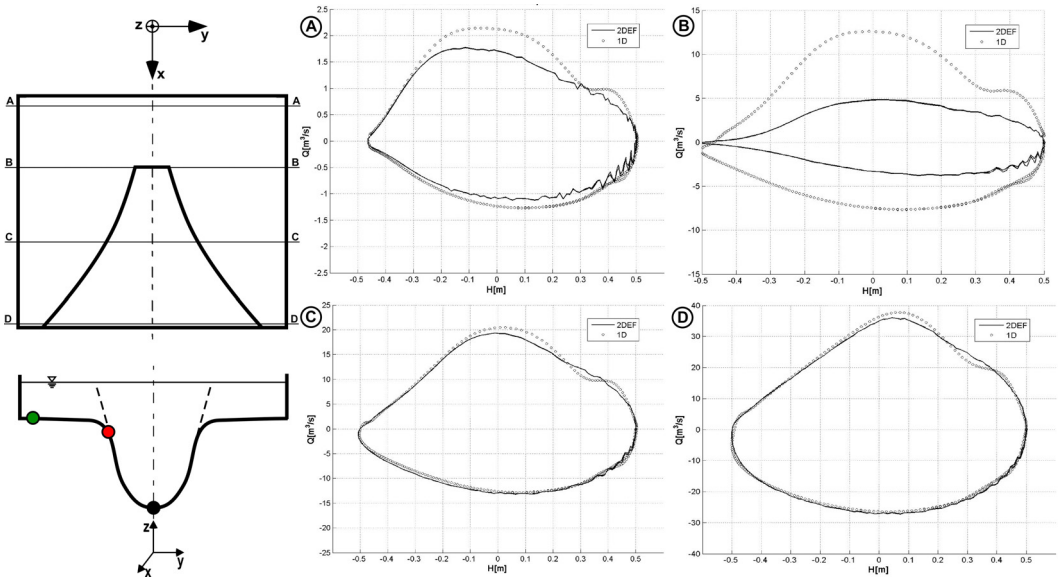

Figure A.12: The cross sectional discharge Q is plotted as a function of the water stage h for bathymetry 3 ($z_{tf} = -0.45$ m) a) landward section; b) halfway cross section; c) seaward section.

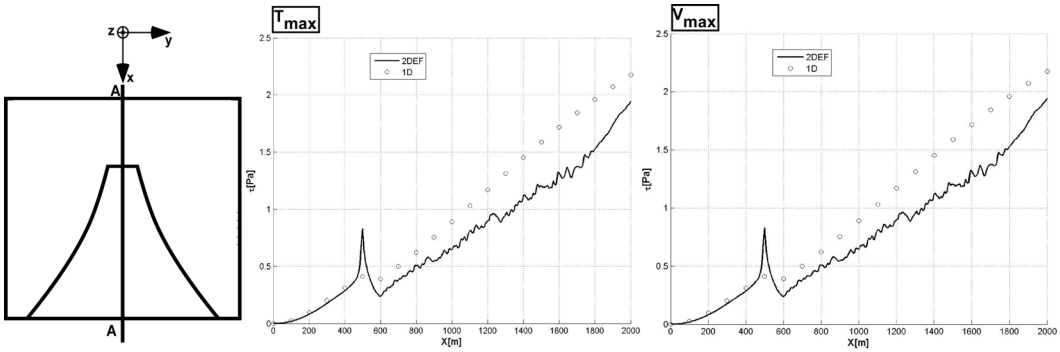

Figure A.13: a) Maximum shear stress τ_{max} and b) velocity U_{max} computed during a tidal cycle along the longitudinal axis fo the tidal basin with bathymetry 3 ($z_{tf} = -0.45$ m).

Appendix B

Shear stress distribution equation derivation

The shear stress distribution 4.9 is here derived. The momentum balance averaged over turbulence along the coordinate x reads as follows:

$$\varrho\frac{\partial u_x}{\partial t}+\frac{\varrho}{h_n}\left[\frac{\partial(h_n u_x^2)}{\partial x}+\frac{\partial(u_x\,u_y)}{\partial n}+\frac{\partial(h_n\,u_x\,u_z)}{\partial\zeta}-u_y^2\frac{\partial h_n}{\partial x}\right]= \\ =-\varrho\frac{\partial}{\partial x}\left(\frac{p}{\varrho}+gh\right)+\frac{1}{h_n}\left[\frac{\partial(h_n\,T_{xx})}{\partial x}+\frac{\partial T_{nx}}{\partial n}+\frac{\partial(h_n\,T_{\zeta x})}{\partial\zeta}-T_{nn}\frac{\partial h_n}{\partial x}\right] \quad \text{(B.1)}$$

Assuming that the horizontal scale of the hydrodynamic processes are dominant with respect to local depth ($\frac{\partial}{\partial x}\left(\frac{p}{\varrho g}+h\right)\cong g\frac{\partial H}{\partial x}$) and that the longitudinal variations of the metric coefficient are negligible ($\frac{\partial h_n}{\partial x}\cong 0$), the previous equation becomes after multiplying each side for the metric coefficient h_n:

$$h_n\varrho\frac{\partial u_x}{\partial t}+\varrho\left[\frac{\partial(h_n u_x^2)}{\partial x}+\frac{\partial(u_x\,u_y)}{\partial n}+\frac{\partial(h_n\,u_x\,u_z)}{\partial\zeta}\right]=-\varrho g h_n\frac{\partial H}{\partial x}+\left[\frac{\partial(h_n\,T_{xx})}{\partial x}+\frac{\partial T_{nx}}{\partial n}+\frac{\partial(h_n\,T_{\zeta x})}{\partial\zeta}\right]$$

Hence, the integration over depth along the normal direction, from the free surface D_ζ to the bottom bed ζ_0, reads as follows:

$$\varrho \int_{\zeta_0}^{D_\zeta} h_n \frac{\partial u_x}{\partial t} d\zeta + \varrho \int_{\zeta_0}^{D_\zeta} \left(\frac{\partial (h_n\, u_x^2)}{\partial x} + \frac{\partial (u_x\, u_y)}{\partial n} + \frac{\partial (h_n\, u_x\, u_z)}{\partial \zeta} \right) d\zeta = -$$
$$- \varrho \int_{\zeta_0}^{D_\zeta} h_n \frac{\partial H}{\partial x} d\zeta + \int_{\zeta_0}^{D_\zeta} \left[\frac{\partial (h_n\, T_{xx})}{\partial x} + \frac{\partial T_{nx}}{\partial n} + \frac{\partial (h_n\, T_{\zeta x})}{\partial \zeta} \right] d\zeta$$

Each term on the left side is computed using the Leibniz' rule as follows[1]:

$$\varrho \int_{\zeta_0}^{D_\zeta} h_n \frac{\partial u_x}{\partial t} d\zeta = \varrho \left[\frac{\partial}{\partial t} \int_{\zeta_0}^{D_\zeta} h_n\, u_x d\zeta + h_n \frac{\partial \zeta_0}{\partial t} u_x \Big|_{\zeta=\zeta_0} - h_n \frac{\partial D_\zeta}{\partial t} u_x \Big|_{\zeta=D_\zeta} \right]$$
$$\varrho \int_{\zeta_0}^{D_\zeta} \frac{\partial (h_n u_x^2)}{\partial x} d\zeta = \varrho \left[\frac{\partial}{\partial x} \int_{\zeta_0}^{D_\zeta} (h_n\, u_x^2) d\zeta + \frac{\partial \zeta_0}{\partial x} (h_n\, u_x^2) \Big|_{\zeta=\zeta_0} - \frac{\partial D_\zeta}{\partial x} (h_n\, u_x^2) \Big|_{\zeta=D_\zeta} \right]$$
$$\varrho \int_{\zeta_0}^{D_\zeta} \frac{\partial (u_x\, u_y)}{\partial n} d\zeta = \varrho \left[\frac{\partial}{\partial n} \int_{\zeta_0}^{D_\zeta} (u_x\, u_y) d\zeta + \frac{\partial \zeta_0}{\partial n} (u_x\, u_y) \Big|_{\zeta=\zeta_0} - \frac{\partial D_\zeta}{\partial n} (u_x\, u_y) \Big|_{\zeta=D_\zeta} \right]$$
$$\varrho \int_{\zeta_0}^{D_\zeta} \frac{\partial (h_n u_x\, u_z)}{\partial \zeta} d\zeta = \varrho \left[-(h_n\, u_x\, u_z) \Big|_{\zeta=\zeta_0} + \frac{\partial D_\zeta}{\partial \zeta} (h_n\, u_x\, u_z) \Big|_{\zeta=D_\zeta} \right]$$

Similarly, the depth integration on the right-hand side is computed as:

$$\varrho g \int_{\zeta_0}^{D_\zeta} \frac{\partial H}{\partial x} h_n d\zeta = \varrho g \frac{\partial H}{\partial x} \int_{\zeta_0}^{D_\zeta} h_n d\zeta$$
$$\int_{\zeta_0}^{D_\zeta} \frac{\partial (h_n T_{xx})}{\partial x} d\zeta = \frac{\partial}{\partial x} \int_{\zeta_0}^{D_\zeta} (h_n T_{xx}) d\zeta + \frac{\partial \zeta_0}{\partial x} (h_n T_{xx}) \Big|_{\zeta=\zeta_0} - \frac{\partial D_\zeta}{\partial x} (h_n T_{xx}) \Big|_{\zeta=D_\zeta}$$
$$\int_{\zeta_0}^{D_\zeta} \frac{\partial T_{nx}}{\partial n} d\zeta = \frac{\partial}{\partial n} \int_{\zeta_0}^{D_\zeta} T_{nx} d\zeta + \frac{\partial \zeta_0}{\partial n} T_{nx} \Big|_{\zeta=\zeta_0} - \frac{\partial D_\zeta}{\partial n} T_{nx} \Big|_{\zeta=D_\zeta}$$
$$\int_{\zeta_0}^{D_\zeta} \frac{\partial (h_n T_{\zeta x})}{\partial \zeta} d\zeta = (h_n T_{\zeta x}) \Big|_{\zeta=D_\zeta} - (h_n T_{\zeta x}) \Big|_{\zeta=\zeta_0}$$

Substituting the previous positions and singling out the kinematic and dynamic boundary conditions, the depth integration along the normal direction yields:

[1] Leibniz's rule yields:

$$\frac{d}{dt} \int_{a(x)}^{b(x)} f(x,t) dx = \int_{a(x)}^{b(x)} \frac{\partial f(x,t)}{\partial t} dx + f(b(x),t) \frac{db}{dt} - f(a(x),t) \frac{da}{dt} \tag{B.2}$$

$$\varrho\frac{\partial}{\partial t}\int_{\zeta_0}^{D_\zeta} h_n\, u_x d\zeta + \varrho\frac{\partial}{\partial x}\int_{\zeta_0}^{D_\zeta} h_n u_x^2 d\zeta + \varrho\frac{\partial}{\partial n}\int_{\zeta_0}^{D_\zeta}(u_x\, u_y)d\zeta +$$
$$+\varrho u_x h_n \underbrace{\left(\frac{\partial\zeta_0}{\partial t} + u_x\frac{\partial\zeta_0}{\partial x} + \frac{u_y}{h_n}\frac{\partial\zeta_0}{\partial n} - u_z\right)\Big|_{\zeta=\zeta_0}}_{=0} - \varrho u_x h_n \underbrace{\left(\frac{\partial D_\zeta}{\partial t} + u_x\frac{\partial D_\zeta}{\partial x} + \frac{u_y}{h_n}\frac{\partial D_\zeta}{\partial n} - u_z\right)\Big|_{\zeta=D_\zeta}}_{=0} =$$
$$= -\varrho g\frac{\partial H}{\partial x}\int_{\zeta_0}^{D_\zeta} h_n d\zeta + \frac{\partial}{\partial x}\int_{\zeta_0}^{D_\zeta}(h_n T_{xx})d\zeta + \frac{\partial}{\partial n}\int_{\zeta_0}^{D_\zeta} T_{nx}d\zeta +$$
$$+ h_n \underbrace{\left(\frac{\partial\zeta_0}{\partial x}T_{xx} + \frac{T_{nx}}{h_n}\frac{\partial\zeta_0}{\partial x} - T_{\zeta x}\right)\Big|_{\zeta=\zeta_0}}_{=-\tau} - h_n \underbrace{\left(\frac{\partial D_\zeta}{\partial x}T_{xx} + \frac{T_{nx}}{h_n}\frac{\partial D_\zeta}{\partial n} - T_{\zeta x}\right)\Big|_{\zeta=D_\zeta}}_{=0}$$

Hence, taking out the simplifications and assuming negligible the temporal acceleration, the previous equation becomes:

$$\varrho\frac{\partial}{\partial x}\int_{\zeta_0}^{D_\zeta}(h_n\, u_x^2)d\zeta + \varrho\frac{\partial}{\partial n}\int_{\zeta_0}^{D_\zeta}(u_x\, u_y)d\zeta = -\tau - \varrho g\frac{\partial H}{\partial x}\int_{\zeta_0}^{D_\zeta} h_n d\zeta + \frac{\partial}{\partial x}\int_{\zeta_0}^{D_\zeta}(h_n\, T_{xx})d\zeta + \frac{\partial}{\partial n}\int_{\zeta_0}^{D_\zeta} T_{nx}d\zeta$$

Moreover, we assume that the stream flow and shear stress variations experienced along the longitudinal direction are much smaller than those occurring in the traversal and vertical direction, which means:

$$\frac{\partial}{\partial x}\int_{\zeta_0}^{D_\zeta}(h_n\, T_{xx})d\zeta \cong 0$$
$$\frac{\partial}{\partial x}\int_{\zeta_0}^{D_\zeta}(u_x\, u_y)d\zeta \cong 0$$

Considering these two positions, the depth averaged equation along the normal direction reads:

$$\tau = -\varrho g\frac{\partial H}{\partial x}\int_{\zeta_0}^{D_\zeta} h_n d\zeta - \varrho\frac{\partial}{\partial x}\int_{\zeta_0}^{D_\zeta} h_n u_x^2 d\zeta + \frac{\partial}{\partial n}\int_{\zeta_0}^{D_\zeta} T_{nx}d\zeta$$

Looking at this equation, we note that $\int_{\zeta_0}^{D_\zeta} h_n d\zeta$ is a local hydraulic radius $\frac{d\mathcal{A}}{dn}$, where $d\mathcal{A}$ is the area between two successive normals. Then, the velocity along the normal is written as $u = \hat{\beta}U$, where U is the mean velocity along the normal and $\hat{\beta}$ is a corrector coefficient, which is $\cong 1$ when the velocity profile is log-distributed. Since the cross section may be also compound, a Coriolis coefficient α is introduced to take into account non-uniform velocity distribution in the cross-sectional area. Given these considerations, the last equation yields what we were looking for:

$$\tau = \varrho g S \frac{d\mathcal{A}}{dn} + \frac{\partial}{\partial n} \int_{\zeta_0}^{D_\zeta} T_{nx} d\zeta \tag{B.3}$$

$$S = -\frac{\partial}{\partial x}\left(H + \alpha_{cor} \frac{U^2}{2g} \right) \tag{B.4}$$

Bibliography

M. B. Abbott and D. R. Basco. *Computational fluid dynamics: an introduction for engineers*. John Wiley & Sons, New York (US), 1989.

J. R. L. Allen. Salt-marsh growth and stratification: A numerical model with special reference to the severn estuary, southwest britain. *Marine Geology*, 95(2):77–96, 1996.

W. Artichowicz and P. Mikos-Studnicka. Comparison of average energy slope estimation formulas for one-dimensional steady gradually varied flow. *Archives of Hydro-Engineering and Environmental Mechanics*, 61(3-4):89–109, 2014.

W. Artichowicz and D. Prybytak. Impact of energy slope averaging methods on numericalsolution of 1d steady gradually varied flow. *Archives of Hydro-Engineering and Environmental Mechanics*, 62(3-4):101–119, 2015.

A. Balzano. Evaluation of methods for numerical simulation of wetting and drying in shallow water flow models. *Coastal Engineering*, 34:83–107, 1998.

J.P. Belliard, M. Toffolon, L. Carniello, and A. D'Alpaos. An ecogeomorphic model of tidal channel initiation and elaboration in progressive marsh accretional contexts. *Journal of Geophysical Research: Earth Surface*, 120(6):10401064, 2015.

M. Bendoni, S. Francalanci, L. Cappietti, and L. Solari. On salt marshes retreat: Experiments and modelingtoppling failures induced by wind waves. *Journal of Geophysical Research: Earth Surface*, 119:603–620, 2014.

M. Bendoni, R. Mel, L. Solari, S. Lanzoni, S. Francalanci, and H. Oumeraci. Insights into lateral marsh retreat mechanism through localized field measurements. *Water Resources Research*, 52(2):1446–1464, 2016.

T. J. Bouma, L. A. van Duren, S. Temmerman, T. Claverie, A. Blanco-Garcia, T. Ysebaert, and P. M. J. Herman. Spatial flow and sedimentation patterns

within patches of epibenthic structures: Combining field, flume and modelling experiments. *Continental Shelf Research*, 27:1020–1045, 2007.

R. E. Bowen, A. Frankic, and M. E. Davis. Human development and resource use in the coastal zone: Influences on human health. *Oceanography*, 19:62–71, 2006.

A. Canestrelli, A. Defina, and L. D'Alpaos. Long-term evolution and morphodynamic equilibrium of a tidal channel flanked by tidal flats. In C. M. Dohmen-Janssen and S. J. M. H. Hulscher, editors, *Proceedings of 5th IAHR Symposium on River, Coastal and Estuarine Morphodynamics: RCEM 2007*, volume 1, pages 145–154. CRC Press Taylor & Francis Group, 2007.

L. Carniello, A. Defina, S. Fagherazzi, and L. D'Alpaos. A combined wind wavetidal model for the venicelagoon, italy. *Journal of Geophysical Research*, 110,F04007: 1–15, 2005.

L. Carniello, A. Defina, and L. D'Alpaos. Modeling sand-mud transport induced by tidal currents and wind waves in shallow microtidal basins: Application to the venice lagoon (italy). *Estuarine, Coastal and Shelf Science*, 102-103:105–115, 2012.

G. Caroppi, P. Gualtieri, N. Fontana, and M. Giugni. Vegetated channel flows: Turbulence anisotropy at flowrigid canopy interface. *Geoscience*, 8(259):116, 2018.

F. Carraro, D. Vanzo, V. Caleffi, A. Valiani, and A. Siviglia. Mathematical study of linear morphodynamic acceleration and derivation of the masspeed approach. *Advances in Water Resources*, 117:40–52, 2018.

J. A. Church, P. U. Clark, A. Cazenave, J. M. Gregory, S. Jevrejeva, A. Levermann, M. A. Merrifield, G. A. Milne, R. S. Nerem, P. D. Nunn, A. J. Payne, W. T. Pfeffer, D. Stammer, and A. S. Unnikrishnan. Sea level change. In T.F. Stocker, D. Qin, G.-K. Plattner, M. Tignor, S. K. Allen, J. Boschung, A. Nauels, Y. Xia, V. Bex, and P. M. Midgley, editors, *Climate Change 2013: The Physical Science Basis. Contribution of Working Group I to the Fifth Assessment Report of the Intergovernmental Panel on Climate Change*, chapter 13, pages 1137–1216. Cambridge University Press, 2013.

G. Coco, Z. Zhou, B. van Maanen, M. Olabarrieta, R. Tinoco, and I. Townend. Morphodynamics of tidal networks: Advances and challenges. *Marine Geology*, 346:1 – 16, 2013. ISSN 0025-3227.

J. A. Cunge. Applied mathematical modeling of channel flow. In K. Mahmood and V. Yevjevich, editors, *Unsteady flow in open channels*, volume 1, pages 379–406, 1975.

J. A. Cunge, F. M. Holly, and A. Verwey. *Practical aspect of computational river hydraulic*, volume 3 of *Monographs and surveys in water resources engineering*. Pitman Pub., London, 1980. 420 pp.

A. DAlpaos, S. Lanzoni, M. Marani, S. Fagherazzi, and A. Rinaldo. Tidal network ontogeny: Channel initiation and early development. *Journal of Geophysical Research*, 110(F02001):1–14, 2005.

A. D'Alpaos, S. Lanzoni, S. M. Mudd, and S. Fagherazzi. Modelling the influence of hydroperiod and vegetation on the cross-sectional formation of tidal channels. *Estuarine coastal and shelf science*, pages 1–14, 2006.

A. D'Alpaos, S. Lanzoni, M. Marani, and A. Rinaldo. On the o'brien-jarret-marchi law. *Rendiconti Lincei. Scienze Fisiche e Naturali*, 20:225–236, 2009a.

A. D'Alpaos, S. Lanzoni, M. Marani, and A. Rinaldo. On the tidal prismchannel area relations. *Journal of Geophysical Research: Earth Surface*, 115(F01003): 1–13, 2009b.

A. D'Alpaos, M. Toffolon, and C. Camporeale. Ecogeomorphological feedbacks of water fluxes, sediment transport and vegetation dynamics in rivers and estuaries. *Advances in Water Resources*, 93:151–155, 2016.

R. W. Dalrymple, B. A. Zaitlin, and R. Boyd. Estuarine facies models; conceptual basis and stratigraphic implications. *Journal of Sedimentary Research*, 62(6): 1130–1146, 1992.

A. W. Date. *Introduction to computational fluid dynamics*. Cambridge University press, Cambridge, 2009.

H. J. de Vriend, M. Capobianco, T. Chesher, H. E. de Swart, B. Latteux, and M. J. F. Stive. Approaches to long-term modelling of coastal morphology: a review. *Coastal Engineering*, 21:225–269, 1993.

A. Defina. Two-dimensional shallow flow equations for partially dry areas. *Water Resources Research*, 36(11):3251–3264, 2000.

A. Defina and I. Bonetto. Rappresentazione dei termini di accelerazione convettiva in un modello bidimensionale della propagazione di onde lunghe in acque basse. In *Atti del XXVI Convegno di Idraulica e Costruzioni Idrauliche*, 1998.

Deltares. *Delft3D-Flow. User manual*. Deltares, 2014.

DHI. *MIKE11: A modelling system for Rivers and Channels. User Guide*. DHI, 2017a.

DHI. *MIKE21: Flow Model:Hydrodynamic Module. User Guide.* DHI, 2017b.

G. Di Silvio. La riproduzione su modelli fisici e matematici dei fenomeni di dispersione in ambienti fluviali e costieri. In *Atti del XVI Convegno di Idraulica e Costruzioni Idrauliche*, 1978a.

G. Di Silvio. Modelli matematici per lo studio della propagazione di onde lunghe e del trasporto di materia nei corsi dacqua e nelle zone costiere. In *Atti Del Convegno su Metodologie Numeriche per la Soluzione di Equazione Differenziali DellIdrologia e DellIdraulica*, 1978b.

G. Di Silvio. Delimitazione topografica di una laguna a marea: implicazioni idrodinamiche e morfologiche. In *Convegno di Studi nel Bicentenario della Conterminazione Lagunare*, pages 307–324. Istituto Veneto di SS.LL.AA, 1992.

P. Diplas. Characteristic of self-formed straight channels. *Proc. A.S.C.E. Journal of Hydraulic Engineer*, 116:707–728, 1990.

J. J. Dronkers. *Tidal computations in rivers and coastal waters.* North Holland Publishing Company, Amsterdam, 1964.

H. A. Einstein and R. B. Krone. Experiments to determine modes of cohesive sediment transport in salt water. *Journal of Geophysical Research*, pages 1451–1461, 1962.

S. Fagherazzi and D. Furbish. On the shape and widening of salt marsh creeks. *Journal of geophysical research*, 106:pp. 991–1003, 2001.

S. Fagherazzi, A. Bortoluzzi, W. E. Dietrich, A. Adami, S. Lanzoni, M. Marani, and A. Rinaldo. Tidal networks, 1, automatic network extraction and preliminary scaling features. *Water Resources Research*, 35(12):3891–3904, 1999.

J. H. Ferziger and M. Perić. *Computational method for fluid dynamics.* Springer, New York, 2002.

D. L. Fread, M. Jin, and J. M. Lewis. An lpi numerical implicit solution for unsteady mixed-flow simulation. In *North American Water and Environment Congress & Destructive Water*, pages 1–7. ASCE, 1996.

M. A. Freitag and K. W. Morton. The preissman box scheme and its modifcation for transcritical flows. *International Journal for Numerical Methods in Engineering*, 70:791–811, 2007.

J. R. French and T. Spencer. Numerical simulation of vertical marsh growth and adjustment to accelerated sealevel rise, north norfolk, u.k. *Earth Surface Processes and Landforms*, 18(1):63–81, 1996.

R. H. French. *Open Channel Hydraulics*. McGraw-Hill Book Company, Singapore (SGP), 1986.

C. Friedrichs and J. Perry. Tidal salt marsh morphodynamics: A synthesis. *Journal of Coastal Research*, pages 7–37, 2001.

C. T. Friedrichs and D. G. Aubrey. Characterization of cohesive sediment properties and transport processes in estuaries. In S. Pattiaratchi, editor, *Mixing in Estuaries and Coastal Seas*, volume 50, chapter 24, pages 405–429. American Geophysical Union, 1996.

F. J. G. Gibbons. A hydrodynamic flood routing model for one dimensional flow. Master's thesis, University of the Witwatersrand, Johannesburg (RSA), 1986.

R. E. Glover and Q. L. Florey. Stable channel profiles. Hydraulic laboratory report, hyd no. 325, U.S. Dept. of the Interior, Bureau of Reclamation, Design and Construction Division, Denver (US), 1951.

M. R. Goud and D. G. Aubrey. Theoretical and observational estimates of nearshore bedload transport rates. *Marine Geology*, 64(1-2):91–111, 1985.

E. R. Griffin, J. W. Kean, K. R. Vincent, J. D. Smith, and J. M. Friedman. Modeling effects of bank friction and woody bank vegetation on channel flow and boundary shear stress in the rio puerco, new mexico. *Journal of Geophysical Research*, 110(F4):1–15, 2005.

J. Guo and P. Y. Julien. Shear stress in smooth rectangular open-channel flows. *Journal of Hydraulic Research*, 131(1):30–37, 2005.

F. M. Henderson. *Open channel flow*. Collier Macmillan publishers, London, 1966.

Z. J. Hughes. *Tidal Channels on Tidal Flats and Marshes*, chapter 11, pages 269–300. Springer Netherlands, 2012.

S. Ikeda, G. Parker, and Y. Kimura. Stable width and depth of straight gravel rivers with eterogeneous material. *Water Resources Research*, 24:713–722, 1988.

J. T. Jarrett. Tidal prism-inlet area relationships. Gen. Invest. Tidal Inlets Rep. 3, 1976.

T. C. Johnson, M. J. Baines, and P. K. Sweby. A box scheme for transcritical flow. *International Journal for Numerical Methods in Engineering*, 55(8):892–912, 2002.

J. W. Kean and J. D. Smith. Flow and boundary shear stress in channels with woody bank vegetation. In S. J. Bennett and A. Simon, editors, *Riparian Vegetation and Fluvial Geomorphology, Water Science and Application*, volume 8, chapter 6, pages 237–252. American Geophysical Union, 2005a.

J. W. Kean and J. D. Smith. Generation and verification of theoretical rating curves in the whitewater river basin, kansas. *Journal of Geophysical Research*, 110(F4): 1–17, 2005b.

R. S. Khodashenas and A. Paquier. A geometrical method for computing the distribution of boundary shear stress across irregular straight open channel. *Journal of Hydraulic Research*, 37(3):381–388, 1998.

R. S. Khodashenas, K.E.K. Abderrezzak, and A. Paquier. Boundary shear stress in open channel flow: A comparison among six methods. *Journal of Hydraulic Research*, 46(5):598–609, 2008.

M. L. Kirwan and S. Temmerman. Coastal marsh response to historical and future sea-level rise acceleration. *Quaternary Scince Review*, 28:1801–1808, 2009.

M. L. Kirwan, G. R. Guntenspergen, A. D'Alpaos, J. T. Morris, S. M. Mudd, and S. Temmerman. Limits on the adaptability of coastal marshes to rising sea level. *Journal of Geophysical Research*, 37(L23401):1–5, 2010.

M. A. F. Knaapen and R. Joustra. Morphological acceleration factor: usability, accuracy and run time reductions. In *Proceedings of XIXth TELEMAC-MASCARET User Conference*, 2012.

D. W. Knight, M. Omran, and X. Tang. Modeling depth averaged velocity and boundary shear in trapezoidal channels with secondary flows. *Journal of Hydraulic Engineering*, 133(1):3947, 2007.

R. B. Krone. Flume studies of the transport of sediment in estuarial sholaing processes. Technical report, Eng. Lab., Berkley University, USA, 1962.

R. B. Krone. A method for simulating historic marsh elevations. In N. C. Kraus, editor, *Coastal sediments ́87*, pages 316–323. America Society of Civil Engineers, 1987.

S. Lanzoni. Mathematical modelling of bedload transport over partially dry areas. *Acta Geophysica*, 56(3):734–752, 2008.

S. Lanzoni and A. D'Alpaos. On funneling of tidal channels. *Journal of Geophysical Research: Earth Surface*, pages 1–20, 2015.

S. Lanzoni and G. Seminara. Long-term evolution and morphodynamic equilibrium of tidal channels. *Journal of Geophysical Research*, 107(C1, 3001):1–13, 2002.

D. S. L. Lawrence, J. R. L. Allen, and G. M. Havelock. Salt marsh morphodynamics: an investigation of tidal flows and marsh channel equilibrium. *Journal of Coastal Research*, 20(1):301–316, 2004.

J. B. Leighly. *Toward a theory of the morphologic significance of turbulence in the flow of water in streams*, volume 6, pages 1–22. University of California Press, 1932.

A. Luijendijk, G. Hagenaars, R. Ranasinghe, G. Baart, F. Donchyts, and S. Aarninkhof. The state of the worlds beaches. *Scientific Report*, 8:1–11, 2018.

H. Lundgren and I. Jonnson. Shear and velocity distribution in shallow channels. *Proc. ASCE J. Hydraulic Division*, pages 1–21, 1964.

G. Manzini. The mimetic finite difference method. In J. Fořt, J. Fürst, Halama, Herbin J., R., and F. Hubert, editors, *Finite Volumes for Complex Applications VI Problems & Perspectives*, Springer Proceedings in Mathematics, page 119134. Springer, 2011.

G. Manzini, A. Russo, and N. Sukumar. New perspectives on polygonal and polyhedral finite element methods. *Mathematical Models & Methods in Applied Sciences*, 24(8):16211663, 2014.

M. Marani, S. Lanzoni, D. Zandolin, G. Seminara, and A. Rinaldo. Tidal meanders. *Water Resources Research*, 38(11):1–7, 2002.

M. Marani, S. Lanzoni, S. Silvestri, , and A. Rinaldo. Tidal landforms, patterns of halophytic vegetation and the fate of the lagoon of venice. *Journal of Marine System*, 51:191–210, 2004.

M. Marani, A. D'Alpaos, S. Lanzoni, L. Carniello, and A. Rinaldo. Biologically-controlled multiple equilibria of tidal landforms and the fate of the venice lagoon. *Geophysical Research Letters*, 34(L11402):1–5, 2007.

M. Marani, A. D'Alpaos, S. Lanzoni, L. Carniello, and A. Rinaldo. The importance of being coupled: Stable states andcatastrophic shifts in tidal biomorphodynamics. *Journal of Geophysical Research*, 115(F04004):1–15, 2010.

M. Marani, A. D'Alpaos, S. Lanzoni, and M. Santalucia. Understanding and predicting wave erosion of marsh edges. *Geophysical Research Letters*, 38(L21401): 1–5, 2011.

E. Marchi. Il moto uniforme delle correnti liquid nei condotti chiusi e aperti. *L'Energia elettrica*, 38(4):393–409, 1961.

E. Marchi. Sulla stabilità delle bocche lagunari a marea. *Rend. Fis. Accad. Lincei*, 9:137–15, 1990.

G. Mariotti and S. Fagherazzi. A numerical model for the long-term evolution of salt marshes. *Journal of Geophysical Research: Earth Surface*, 115(F01004):1–15, 2010.

G. Mariotti and S. Fagherazzi. Critical width of tidal flats triggers marsh collapse in the absence of sea-level rise. *Proceedings of the National Academy of Sciences*, 110(14):53535356, 2013a.

G. Mariotti and S. Fagherazzi. A two-point dynamic model for the coupled evolution of channels and tidal flats. *Journal of Geophysical Research: Earth Surface*, 118: 13871399, 2013b.

S. C. Medeiros and S. C. Hagen. Review of wetting and drying algorithms fro numerical tidal flow models. *International Journal for Numerical Methods in Fluids*, 71(6):473–487, 2013.

E. A. Meselhe and F. M. Holly Jr. Invalidity of preissmann scheme for transcritical flow. *Journal of Hydraulic Engineering*, 123(7):652–655, 1997.

A. Metha. *Characterization of cohesive sediment properties and transport processes in estuaries*, pages 290–315. Springer-Verlag, 1984.

E. Meyer-Peter and R. Müller. Formulas for bed-load transport. In *Proceedings of IAHSR 2nd meeting*, 1948.

J. T. Morris, P. V. Sundareshwar, C. T. Nietch, B. Kjerfve, and D. R. Cahoon. Responses of coastal wetlands to rising sea level. *Ecology*, 83(10):2869–2877, 2002.

S. M. Mudd, S. Fagherazzi, M. Morris, and D. Furbish. *Flow, sedimentation and biomass production on a vegetated salt marsh in South Carolina: toward a predictive model of marsh morphologic and ecologic evolution*, pages 165–188. American Geophysical Union, 2004.

H. Nepf and E. Vivoni. Flow structure in depth-limited, vegetated flow. *Journal of Geophysical Research*, 105(C12):28547–28557, 2000.

H. M. Nepf. Drag, turbolence, and diffusion in flow through emergent vegetation. *Water Resources Research*, 35(2):479–489, 1999.

M. P. O'Brien. Estuary tidal prisms related to entrance areas. *Civ. Eng.*, 1(8): 738–739, 1931.

M. R. Palmer, H. M. Nepf, T. Petterson, and J. Ackerman. Observations of particle capture on a cylindrical collector: implications for particle accumulation and removal in aquatic systems. *Journal of Geophysical Research*, pages 76–85, 2004.

G. Parker. Self-fromed straight rivers with equilibrium banks and mobile bed. part 1. the sand-silt river. *Journal of Fluid Mechanics*, 89:109–125, 1978a.

G. Parker. Self-formed straight rivers with equilibrium banks and mobile bed. part 2. the gravel river. *Journal of Fluid Mechanics*, 89:127–146, 1978b.

S. Pennings, M. Grant, and M. Bertness. Plant zonation in lowlatitudes salt marshes: Disentangling the roles of flooding, salinity and competition. *Journal of Ecology*, 93(1):159167, 2005.

M. Pivato, L. Carniello, I. Moro, S. Silvestri, and P. D'Odorico. On the feedback between water turbidity and microphytobenthos growth in shallow tidal environments. *Earth Surface Processes and Landforms*, 44:1192–1206, 2019.

J. E. Pizzuto. Numerical simulation of gravel river widening. *Water Resources Research*, 26(9):1971–1980, 1990.

R. H. Pletchter, J. C. Tannehill, and D. A. Anderson. *Computational fluid dynamics and heat transfer*. Series in computational and physical processes in mechanics and thermal sciences. CRC Press, Boca Raton, Florida, 2013. 753 pp.

D. Pritchard and A. Hogg. Cross-shore sediment transport and the equilibrium morphology of mudflats under tidal currents. *Journal of Geophysical Research*, 108(C10, 3313):1–11, 2003.

D. Pritchard, A. Hogg, and J. W. Roberts. Morphological modelling of intertidal mudflats:the role of cross-shore tidal currents. *Continental Shelf Research*, 22: 1887–1895, 2002.

A. Quarteroni. *Numerical models for differential problems*. Springer-Verlag, Milano, 2014.

B. V. Ramana Prasad and J. Russell Manson. Discussion of a geometrical method for computing the distribution of boundary shear stress across irregular straight open channels. *Journal of Hydraulic Research*, 40(4):537539, 2002.

R. Ranasinghe, C. Swinkels, A. Luijendijk, D. Roelvink, J. Bosboomb, M. Stive, and D. Walstra. Morphodynamic upscaling with the morfac approach: Dependencies and sensitivities. *Coastal Engineering*, 58(8):806–811, 2011.

P. Randerson. *A simulation model of salt-marsh development and plant ecology*, pages 48–67. Saxon House, 1979.

A. Rinaldo. Equilibrio fisico e idrogeologico della laguna. Una Agenda 21 per Venezia, Progetto Venezia, 1997.

A. Rinaldo, S. Fagherazzi, S. Lanzoni, and M. Marani. Tidal networks 2. watershed delineation and comparative network morphology. *Water Resources Research*, 35 (12):3905–3917, 1999.

W. Rodi. Elements of theory of turbulence. In A.B. Abbott and W.A. Price, editors, *Coastal,estuarial and harbour engineers' reference book*, pages 45–59. CRC Press, 1993.

J. A. Roelvink. Coastal morphodynamic evolution techniques. *Coastal Engineering*, 53:277–287, 2006.

C. Sart, J. P. Baume, P. O. Malaterre, and V. Guinot. Adaptation of preissman's scheme for transcritical open channel flows. *Journal of Hydraulic Research*, 48(4): 428–440, 2010.

L. Schippa. Modellazione della sezione trasversale in alveo rettilineo. In *XXIII Convegno di Idraulica e di Costruzioni idrauliche*, Firenze, 31 Agosto - 4 Settembre 1992.

H. M. Schuttelaars and H. E. De Swart. Initial formation of channels and shoals in a short tidal embayment. *Journal of Fluid Mechanics*, 386:15–42, 1999.

G. Seminara, S. Lanzoni, N. Tambroni, and M. Toffolon. How long are tidal channels? *Journal of Fluid Mechanics*, pages 1–16, 2010.

S. Silvestri and M. Marani. *SaltMarsh Vegetation and Morphology: Basic Physiology, Modelling and Remote Sensing Observations*, pages 5–25. American Geophysical Union, 2004.

L. Solari, G. Seminara, M. Marani, S. Lanzoni, and A. Rinaldo. Sand bars in tidal channels part 2. tidal meanders. *Journal of Fluid Mechanics*, 451:203238, 2002.

L. Solari, M. Van Oorschot, B. Belletti, D. Hendriks, M. Rinaldi, and A. VargasLuna. Advances on modelling riparian vegetation - hydromorphology interactions. *River Research and Applications*, 32(2):164–178, 2015.

N. Tambroni and G. Seminara. A one-dimensional eco-geomorphic model of marsh response to sea level rise: Wind effects, dynamics of the marsh border and equilibrium. *Journal of Geophysical Research*, 117(F03026):1–25, 2005.

N. Tambroni, P. K. Stansby, and G. Seminara. On the formation ofouter-deltas at tidal inlets. In *Atti XXIX Convegno di Idraulica e Costruzioni Idrauliche*, pages 1–8, 2004.

N. Tambroni, M. Bolla Pittaluga, and G. Seminara. Laboratory observations of the morphodynamic evolution of tidal channels and tidal inlets. *Journal of Geophysical Research*, 110(F04009):1–23, 2005.

N. Tambroni, J. Figueredo da Silva, R. W. Duck, S. J. McLelland, C. Venier, and S. Lanzoni. Experimental investigation of the impact of macroalgal mats on the wave and current dynamics. *Advances in Water Resources*, 93:326–335, 2015.

P. Tassi and C. Villaret. *Reference manual Sisyphe.* EDF R&D, 2017.

S. Temmerman, T. J. Bouma, J. Van de Koppel, D. Van der Wal, M. B. De Vries, and P. J. M. Herman. Vegetation causes channel erosion in a tidal landscape. *Geology*, 35(7):631–634, 2007.

I. Todeschini, M. Toffolon, and M. Tubino. Long-term morphological evolution of funnel-shape tide-dominated estuaries. *Journal of Geophysical Research*, 113 (C05005):1–14, 2008.

M. Toffolon and S. Lanzoni. Morphological equilibrium of short channels dissecting the tidal flats of coastal lagoons. *Journal of Geophysical Research*, 115(F04036): 1–15, 2010.

M. Tubino and M. Colombini. Correnti uniformi a superficie libera e sezione lentamente variabile. In *XXIII Convegno di Idraulica e di Costruzioni idrauliche*, Cosenza, 20-22 Settembre 1992.

USACE. *HEC-RAS: River Analysis System.* US Army Corps of Engineers - Hydrologic Engineering Center, 2016.

J. van de Koppel, D. van der Wal, J. P. Bakker, and P. M. Herman. Self-organization and vegetation collapse in salt marsh ecosystems. *The American Naturalist*, 165 (1):E1–12, 2005.

C. Venier, J. Figueiredo da Silva, S. J. McLelland, R. W. Duck, and S. Lanzoni. Experimental investigation of the impact of macroalgal mats on flow dynamics and sediment stability in shallow tidal areas. *Estuarine, Coastal and Shelf Science*, 112:52–60, 2012.

D. P. Viero, A. DAlpaos, L. Carniello, and A. Defina. Mathematical modeling of flooding due to river bank failure. *Advances in Water Resources*, 59:82–94, 2013.

C. Vreugdenhil. *Numerical methods for shallow-water flow*. Water Science and Technology Library, Springer Netherlands, 1992.

J. C. Winterwerp. On the sedimentation rate of cohesive sediment. In *Proceedings of 7th International conference on Estuarine and coastal fine sediments dynamics(INTERCOH), Gloucester Point, Virginia, USA*, volume 1, pages 209–226, 2007.

W. Wu. *Computational River Dynamics*. Taylor & Francis Group, London(UK), 2008.

F. Xu, G. Coco, J. Tao, Z. Zhou, C. Zhang, S. Lanzoni, and A. D'Alpaos. On the morphodynamic equilibrium of a short tidal channel. *Journal of Geophysical Research: Earth Surface*, 124(2):639–665, 2019.

S.-Q. Yang, J.-X. Yu, and Y.-Z. Wang. Estimation of diffusion coefficients, lateral shear stress, and velocity in open channels with complex geometry. *Water Resources Research*, 40(W05202):1–8, 2004.

Z. Zhou, G. Coco, I. Townend, M. Olabarrieta, M. Wegen, Z. Gong, A. DAlpaos, S. Gao, B. E. Jaffe, G. Gelfenbaum, Q. He, Y. P. Wang, S. Lanzoni, Z. B. Wang, H. Winterwerp, and C. Zhang. Is morphodynamic equilibrium an oxymoron? *Earth-Science Reviews*, 165:257–267, 02 2017.